ALMA MATER STUDIORUM – UNIVERSITÀ DI BOLOGNA

DOTTORATO DI RICERCA IN

Ingegneria Energetica, Nucleare e del Controllo Ambientale

Ciclo XXVIII

Settore Concorsuale di afferenza: 09/C2

Settore Scientifico disciplinare: ING-IND/10

Optical techniques for experimental tests in microfluidics

Presentata da: **Giacomo Puccetti**

Coordinatore Dottorato:

Chiar.mo Prof. Vincenzo Parenti Castelli

Relatore:

Chiar.mo Prof. Gian Luca Morini

Correlatore:

Dott.ssa Beatrice Pulvirenti

Esame finale anno 2016

A tutti quelli che credono nei loro sogni.
A mio padre e mia madre.

Acknowlegements

First of all, I would to express my gratitude to my supervisor Professor Gian Luca Morini, who guided me during the doctoral course giving me fundamental suggestions. Thank you also for the revision of this dissertation. I am very thankful also to Dr. Beatrice Pulvirenti for all her helps, suggestions and discussions. Many thanks to Prof. Christian Kähler for the opportunity of the visiting period as a PhD student at the LRT-7 department of Fluid Mechanics and Aerodynamics of Universität der Bundeswehr München, Germany. I enjoyed to work on the fascinating field of Thermochromic Liquid Crystals. Special thanks to Dr. Massimiliano Rossi for his constant presence and teachings during my period in Munich and his help after it. My gratitude goes also to Dr. Pamela Vocale for all her efforts in our joined works and publications. I should like to extend my warm thanks to all the people who directly or indirectly have contributed in the achievement of the results here reported, starting from Dr. Roberta Randi and Dr. Fabrizio Tarterini for SEM images, Prof. Laura Calzà for the images with microscopy confocal fluorescence and Mr. Maurizio Chendi and Dr. Stefania Falcioni for the technical support in laboratory. I am thankful to Prof. David Newport from the Department of Mechanical, Aeronautical and Biomedical Engineering of the University of Limerick, Ireland and to Prof. Marcos Rojas-Cárdenas from the Institut Clement Ader of the University of Toulouse, France, who accepted to review this dissertation. Last but not least, I am grateful to all the people who stayed at my side during my doctoral studies, especially to my parents and my girlfriend who shared with me beautiful and difficult moments along these three years of study and research.

Abstract

This PhD dissertation deals with the use of optical, non-invasive measurement techniques for the investigation of single and two-phase flows in microchannels. Different experimental techniques are presented and the achieved results are critically discussed.

Firstly, the inverse use of the micro Particle Image Velocimetry technique for the detection of the real shape of the inner cross-section of an optical accessible microchannel is shown by putting in evidence the capability of this technique to individuate the presence of singularities along the wetted perimeter of the microchannel. Then, the experimental measurement of the local fluid temperature using non-encapsulated Thermochromic Liquid Crystal particles is discussed. A deep analysis of the stability of the color of these particles when exposed to different levels of shear stress has been conducted by demonstrating that these particles can be used for simultaneous measurements of velocity and temperature in water laminar flows characterized by low Reynolds numbers (Re $<$ 10). A preliminary experiment where the TLC thermography is coupled to the APTV method for the simultaneous measurement of the three-dimensional velocity and temperature distribution in a microchannel is shown. Finally, an experimental analysis of the different flow patterns observed for an adiabatic air-water mixture generated by means of a micro T-junction is discussed. The main air-water mixture features have been deeply observed in 195 different experimental conditions in which values of superficial velocity ranging between 0.01 m/s and 0.15 m/s for both the inlet flows (air and water) are imposed. The flow patterns of the air-water mixture are strongly influenced by the value of the water superficial velocity; on the contrary, the air superficial velocity plays a secondary role for the determination of the characteristics of the bubbles (*i.e.* length).

Sommario

La presente tesi di Dottorato è volta all'utilizzo di tecniche ottiche sperimentali non invasive per lo studio di flussi monofase e bifase all'interno di microcanali. Diverse tecniche sperimentali sono presentate ed i risultati ottenuti vengono discussi in maniera critica.

Inizialmente, viene mostrato l'utilizzo inverso della tecnica μPIV per il rilevamento della reale forma della sezione di passaggio di un microcanale avente accesso ottico, mettendo inoltre in evidenza come tramite questa tecnica sia possibile individuare la presenza di singolarità geometriche lungo il perimetro bagnato della sezione. L'attenzione viene quindi rivolta all'utilizzo di particelle di Cristalli Liquidi Termocromici non incapsulati per la misura della temperatura locale di un flusso liquido all'interno di un microcanale. In particolare viene analizzata la stabilità del colore riflesso da parte di queste particelle quando sottoposte a diversi valori di sforzo di taglio, dimostrandone il loro corretto impiego come tracciante per la misura contemporanea del campo di temperatura e velocità per un flusso d'acqua avente un numero di Reynolds inferiore a 10. Un esperimento preliminare in cui la termografia tramite TLC è accoppiata al metodo APTV per la misura simultanea del campo tridimensionale di temperatura e velocità viene quindi mostrato. In fine, viene presentata un'analisi sperimentale sui diversi modelli di flusso osservati per una miscela adiabatica di aria ed acqua all'interno di una micro giunzione a T. Le principali caratteristiche della miscela bifase sono state osservate per 195 differenti condizioni sperimentali in cui la velocità superficiale delle correnti di acqua ed aria in ingresso è stata fatta variare tra 0.01 m/s e 0.15 m/s. Le caratteristiche delle bolle ed i modelli di flusso della miscela aria-acqua sono fortemente influenzati dal valore della velocità superficiale dell'acqua mentre la velocità superficiale dell'aria assume un ruolo secondario.

Contents

Acknowlegements i

Abstract/Sommario iii

List of figures/tables xvii

Nomenclature xxi

Introduction 1

1 State of the art of experimental techniques for velocity and temperature measurements inside microchannels 7

1.1 Measurements of the dimensions of microchannel inner geometry 7

1.2 Local velocity measurements 10

1.2.1 Micro Particle Image Velocimetry (µPIV). 10

1.2.2 Micro Particle Tracking Velocimetry (µPTV). 11

1.2.3 Astigmatism Particle Tracking Velocimetry (APTV) 12

1.2.4 Micro Particle Streak Velocimetry (µPSV). 12

1.2.5 Laser Doppler Velocimetry (LDV). 13

1.2.6 Micro Molecular Tagging Velocimetry (µMTV) and other techniques. 13

1.3 Local temperature measurements 18

1.3.1 Thermocouples. 18

1.3.2 Thin film thermocouples (µTFTCs). 19

1.3.3 Thin film resistances (µRTDs). 20

1.3.4 Semiconducting temperature sensors (SCs). 20

1.3.5 Infrared Thermography. 21

1.3.6 Fluorescence and phosphorescence 23

1.3.7 Thermochromic Liquid Crystals (TLCs). 25

1.3.8 Other optical techniques. 26

2 The µPIV technique and its use as an inverse technique 27

2.1 Introduction 27

2.2 Aim of the work 30

2.3 µPIV Experimental Apparatus 32

2.3.1 Test section . . . 32
2.3.2 Illuminating system, optical path and fluorescent seeding . . 33
2.3.3 Spatial Resolution . . . 37
2.3.4 Depth of Correlation . . . 39
2.3.5 Time delay between a couple of images . . . 41
2.3.6 Effects of the Brownian motion . . . 42
2.4 Methodology . . . 43
2.4.1 Mixture dilution . . . 43
2.4.2 Volume flow rate and Reynolds number . . . 43
2.4.3 Determination of the bottom wall and top wall position . . . 44
2.4.4 Experimental determination of velocity profiles . . . 45
2.4.5 Numerical determination of the velocity field . . . 48
2.4.6 Comparison between experimental measurements and numerical data . . . 49
2.5 Results and discussion . . . 53
2.5.1 Results for the straight channel . . . 53
2.5.2 SEM analysis on straight channel . . . 61
2.5.3 µPIV measurement for a micro T-junction . . . 63
2.6 Conclusions . . . 71
2.7 Perspectives . . . 71

3 Non-encapsulated Thermochromic Liquid Crystals 73
3.1 Introduction . . . 73
3.2 Aim of the work . . . 76
3.3 Fundamentals of thermochromic liquid crystals . . . 77
3.3.1 TLC colorimetry . . . 81
3.3.2 Non-encapsulated TLC particles . . . 84
3.4 Experimental Apparatus . . . 87
3.4.1 Microchannel, heating system and injection . . . 87
3.4.2 Image acquisition system . . . 88
3.5 Methodology . . . 93
3.5.1 Experimental approach . . . 93
3.5.2 Experimental Procedure . . . 95
3.6 Results and discussion . . . 97
3.7 Preliminary results on temperature measurements . . . 104
3.7.1 Experimental Apparatus . . . 104
3.7.2 Methodology . . . 106
3.7.3 Results and discussion . . . 108
3.8 Device design for investigations on temperature gradients . . . 111
3.8.1 The heating of the device . . . 118
3.9 Conclusions . . . 120
3.10 Perspectives . . . 121

4 Optical detection of air and water mixtures **123**
4.1 Introduction . . . 123
4.2 Aim of the work . . . 126
4.3 Experimental Apparatus . . . 128
4.4 Methodology . . . 133
4.4.1 Experimental determination of the velocity and length of the bubbles . . . 140
4.5 Results and discussion . . . 142
4.6 Conclusions . . . 149
4.7 Perspecitves . . . 150

5 Conclusions and Perspectives **153**
5.1 General conclusions . . . 153
5.2 Perspectives . . . 156

A A1: Additional Pictures **159**

B A2: List of Publications **163**

Bibliography **187**

List of Figures

1.1 Schematic sketch of the working principle of one-dimensional MTV. 15

1.2 Simplified description of the working principle of Thin Film Thermocouples (a), Thin Film Resistances (b) and Semiconducting Temperature sensors (c) (Morini et al., 2011). 21

1.3 Schematic representation of the radiative contributions recorded by the IR camera. Image adapted from Liu and Pan (2016). 22

2.1 Layout of the experimental apparatus: 1) Microchannel 2) Inverted microscope 3) Laser 4) Beam-forming optics 5) Dichroic mirror 6) Objective lens 7) CCD Camera 8) Syringe containing the working fluid seeded with fluorescent particles 9) Syringe pump 10) Synchronization unit 11) Software unit 12) Remote laser control. *(dimensions not in scale)*. 32

2.2 Picture of the straight microchannel under investigation. 33

2.3 Drawing of the involved beam-forming lenses. 33

2.4 Picture of the involved beam-forming lenses. 34

2.5 The experimental apparatus. 35

2.6 The experimental apparatus. 35

2.7 Schematic sketch of the depth of correlation due to the volume illumination. 39

2.8 Picture of the fluorescent particles, dispersed in the working fluid, acquired in gray-scale. 46

2.9 Black and white picture resulting from the subtraction of the gray-scale image by the mean obtained image. 46

2.10 Grid made up by the interrogation cells. 47

2.11 Example of a vector map. 47

2.12 Sketch of the trapezoidal cross-section of the microchannel. In the picture N_p represents the horizontal planes and N_v the vectors on each row of each plane. Figure A refers to the preliminary experimental campaign in which 11 horizontal planes were considered. Figure B refers to the refined research in which the number of horizontal planes is increased up to 19. The central plane is highlighted in red for both the cases. For image clarity, the number of vectors n_v is reduced in both the figures. Φ are the angles under investigation. 50
2.13 Schematic representation of the three indexes associated to the vector map. 51
2.14 Schematic representation of the methodology adopted. 52
2.15 Results for the squared straight channel for Φ angles of 90° (A,B,C), 88 (D,E,F)° and 86° (G,H,I). 53
2.16 Enlargement of fig. 2.15 E. 54
2.17 Picture of the microchannel under investigation: the two horizontal shaded lines are the lateral boundaries of the channel. 57
2.18 Results for the squared straight channel for Φ angles of 88° over 15 of 19 planes. 58
2.19 Reconstruction of the three-dimensional velocity distribution realized by collecting together all the bi-dimensional velocity data in each plane. 59
2.20 Error map obtained from the comparison between experimental velocity points and ones obtained with a numerical simulation in which a trapezoidal shape with Φ angles of 88° is assumed as the geometry of the microchannel cross-section. 60
2.21 SEM image with a magnification of 800 ×. 61
2.22 SEM image with references. 62
2.23 Reconstruction of the three-dimensional shape of the fluorescent fluid. 64
2.24 Reconstruction of the three-dimensional shape of the fluorescent fluid with references 65
2.25 Sketch of the trapezoidal section with references. 66
2.26 Different configurations utilized for the μPIV measurements inside the micro T-junction. 67
2.27 Vector map of the experimental velocity distribution for the configuration 1 with references. 68
2.28 Vector map of the experimental velocity distribution for the configuration 2 with references. 68
2.29 Comparison between experimental and numerical data for the configuration 1. The different positions refer to the image depicted in fig. 2.27. 69
2.30 Comparison between experimental and numerical data for the configuration 2. The different positions refer to the image depicted in fig. 2.28. 70

3.1 Schematic representation of phase transitions typical of thermochromic liquid crystals (Image adapted from Hallcrest LCR (2014)). 77
3.2 TLC in a smectic phase. 78
3.3 TLC in the nematic phase. 78
3.4 Thermochromic liquid crystal structure in the cholesteric phase. p is the pitch of the helical path. 79
3.5 Example of the color play shined from non-encapsulated TLCs particles (made with Hallcrest bulk material "R20C10W"). 80
3.6 Non-encapsulated TLC particles at a fixed temperature (20.2 °C) inside a microchannel: the suspended flowing particles are marked by the circles with an arrow while stuck particles are marked from the gray dotted circles. The top right box shows a zoom of a TLC particle in which both the real edge of the particle and its central core are visible. As it is shown from the inset, only the central core of the particle reflects light depending on its temperature, while the peripheral area is almost transparent. 85
3.7 Experimental test rig layout. *(dimensions not in scale)* 87
3.8 Bottom view (A) and top view (B) of the microchannel carved into the copper substrate and sealed to a microscope slide. In the picture B is visible the hole carved into the copper substrate for housing the mini Pt1000. 88
3.9 Picture of the coupling between the microchannel and the Peltier heating device. 89
3.10 Front picture of the experimental apparatus. 90
3.11 Rear picture of the experimental apparatus. 90
3.12 Non-encapsulated TLC particles (*Hallcrest UNR25C5W*) at 20.6 °C. 91
3.13 Non-encapsulated TLC particles (*Hallcrest UNR25C5W*) at 22.2 °C. 91
3.14 Relative velocity between a spherical particle and an unperturbed shear flow, (A) for a particle that follows faithfully the flow and (B) for a particle stuck to a surface. 93
3.15 *On the left*: Sketch of a longitudinal section of the microchannel. In the blue box a sketch of a TLC particle stuck to the bottom wall exposed to the flow. *On the right*: Distribution of shear rate at the bottom wall for an unperturbed flow at Re=7.5. 95
3.16 Color shined by non-encapsulated TLC particles at different temperature when no shear flow is imposed on them. In the row A) particles with a color range of 5 K (*Hallcrest R20C5W*) while in row B) particles with a color range of 10 K (*Hallcrest R20C10W*). 96
3.17 Image of a single non-encapsulated TLC particle (ΔT=10K) exposed to different wall shear rate for different values of imposed temperature. 97

3.18 Temperature response as a function of the average wall shear rate for TLCs with ΔT = 10 K (A), ΔT=5K (B) and ΔT=1K (C). The continuous line represent the average temperature imposed by the Peltier element and the dashed lines represent the uncertainty of the thermal control. 98
3.19 Difference between the mean measured temperatures (dots) and the temperature imposed by the Peltier device normalized with the temperature working range of 10 K. 99
3.20 Difference between the mean measured temperatures (dots) and the temperature imposed by the Peltier device normalized with the temperature working range of 5 K. 100
3.21 Difference between the mean measured temperatures (dots) and the temperature imposed by the Peltier device normalized with the temperature working range of 1 K. 100
3.22 Pictures of particles stuck to the glass bottom wall of the microchannel under different flow rate conditions of the working fluid: specifically, in the picture B the flow rate is higher than in picture A. In the figure are shown all the effects related to the flowing of the working fluid on the particles stuck to the wall. The destruction of a particle is highlighted inside the yellow circle, while the red arrow marks the spreading of the TLC material on the glass wall. In the green box is possible to see the particles' detachment when the flow rate of the working fluid is increased. 102
3.23 Destroyed non-encapsulated TLC particles (%) depending on the wall shear rate. The dotted line corresponds to wall shear rate of 400 s^{-1}. 103
3.24 Layout of the experimental apparatus for the TLC temperature measurements with the addition of the cylindrical lens. 104
3.25 Schematic sketch of the working principle of particles' defocusing in the APTV method. Image adapted from Segura (2014). 105
3.26 Astigmatic images of the non-encapsulated TLC particles used for the simultaneous measurement of 3D temperature and velocity field in the microchannel. 107
3.27 Trend of the bulk temperature $T_b(x)$ in the streamwise direction for a microchannel with three wall heated at a constant temperature. . 108
3.28 Simultaneous three-dimensional measurement of the temperature and velocity field for a flow in microchannel with a three walls heated at a constant temperature. 109
3.29 Picture of the new channel under study: the heating zone represents the zone where the flexible heater will be placed (Puccetti et al., 2015).111
3.30 Trend of the temperature in the central point of the channel cross-section, for devices realized in aluminum and copper, in steady state conditions. 115

3.31 Trend of the temperature in the central point of the channel cross-section, for a device realized PMMA, for different values of flexible heater power, in steady state condition. 116

3.32 Trend of the temperature in the central point of the channel cross-section as function of time, for a device realized PMMA and a thermal power of the flexible heater equal to 0.08 W. 118

3.33 Flexible electrical heater. 119

4.1 Classification of typical two-phase flow patterns observed in microchannels. The image is adapted from (Shao et al., 2009). 125

4.2 Example of air/water flow patterns observed in literature for an air-water mixture inside a micro mixer: in orange are drawn the flow pattern transitions found by Hassan et al. (2005), with dotted green lines the transitions observed by Chung and Kawaji (2004). The highlighted area represents the region under investigation in this work. The image is adapted from Shao et al. (2009). 127

4.3 Layout of the experimental apparatus: 1) Microchannel 2) Inverted microscope 3) Mercury lamp 4) Objective lens 5) High-speed Camera 6) Software unit 7) Supplementary LCD monitor 8) Water system supply 9) Air system supply 10) Shut-off valve 11) Differential gauge pressure 12) Signal amplifier 13) Multimeter 14) Analog Input Module 15) Software unit. *(dimensions not in scale)* 128

4.4 Picture of the microchannel mounted on the inverted microscope. In the picture are reported the inlet flows of water and air, as well as, the outlet branch. 129

4.5 Picture of the differential pressure gauge connected to the air inlet branch. In the picture are also highlighted the shut-off valve connected to the pressure measurement system and the outlet reservoir. 130

4.6 Picture of the entire experimental apparatus. 131

4.7 Detailed view of the experimental apparatus. 131

4.8 Pressure trend during the phase of air charge for $U_W = 0.13$ m/s and $U_A = 0.12$ m/s. 133

4.9 Mixing zone of the T-junction at different frames: the air flow (white flow) enters from the top vertical branch while the water flow enters from the left horizontal branch (water flow is transparent). The right branch is the branch of the outlet flow. 134

4.10 Bubble along the outlet branch detected in more than one frame. . 136

4.11 Bubble along the outlet branch detected in one frame. 136

4.12 Raw images of the detected front and back sides of a bubble belonging to the "Middle Taylor" flow pattern. 137

4.13 Conversion of the images from a grayscale into a black and white images. A) A threshold filter was applied in order to convert light gray pixels into white pixels and dark gray pixels into black pixels. B) A segmentation filter was later applied in order to fill the white area through the conversion of the black pixels into white pixels. . . 139

4.14 Final image of a bubble with lines drawn in correspondence of its contours: in red is detected the inner core of the bubble, while in yellow the outer shape. 140

4.15 Experimental flow pattern map observed. In light green the area of superficial flow velocities in which the Short Taylor regime has been observed, in light yellow the one belonging to Middle Taylor regimes, in orange is outlined the Long Taylor regimes and finally in light purple the Taylor-Annular regime. 143

4.16 Example of bubbles belonging to the four different flow patterns observed, obtained by merging different frames. For clarity of image, some frames are skipped in the reconstruction of "Long Taylor" and Taylor-Annular bubbles. 144

4.17 Velocity of the bubbles for the different flow patterns as a function of the sum of superficial velocities of air and water. 146

4.18 Relationship between the length of the bubbles and the superficial velocity of the water for some points belonging to each flow pattern condition. (0.02 m/s $\leq U_A \leq$ 0.15 m/s) In blue is drawn the fitting. . 146

4.19 Void fraction determined experimentally as a function of the superficial velocity of water. 147

4.20 Time-averaged volumetric void fraction as a function of the homogeneous void fraction. 147

4.21 Relationship between the static pressure along the branch of the inlet air supply and the sum of the superficial velocities of the water and air flows for some points belonging to different flow rate conditions. In blue is drawn the fitting line of the same. 148

4.22 Water droplet in silicone oil during the instant of break up. 151

4.23 Complete detection of a water droplet in silicone oil. 151

A.1 Picture of threads of fluorescent particles diluted into the working fluid after a long resting time. 159

A.2 Objectives used in chapter 2 and 4. 159

A.3 Picture of the thermochromic liquid crystals stored inside a syringe. From this picture is clearly visible the turbidity of the liquid crystals' material when it is in its smectic phase. 160

A.4 *On the left* Picture of the microchannel realized in a copper substrate and coupled with a Peltier device. The microchannel is housed in a raised mounting plate due to the insertion of the filter under the objective lens. The objective lens (M = 20× NA = 0.4) coupled with the filtering system (linear glass polarizer and achromatic quarter wave plate) is shown *on the right*. 160
A.5 System for the calibration of the thermocouples 161

List of Tables

1.1 Summary of the experimental techniques for geometry detection. . 9
1.2 Summary of the experimental techniques for velocity detection. . . 17
1.3 Summary of the experimental techniques for the fluid temperature detection. 26

2.1 Characteristics of the main components of the experimental test-rig. 36
2.2 Diffraction size of a point-wise light source in relation to the optical characteristics, in the last column are reported the results for the objective lens employed in the present experimental apparatus for a $\lambda = 560$ nm. 37
2.3 Actual diameter dimension (d_e/M) of the image of a fluorescent particle with a diameter of d_p in relation to the optical characteristics, in the last column are reported the results for the objective lens employed in the present experimental apparatus. The dimensions are in µm. 38
2.4 Depth of correlation as a function of different diameters of fluorescent particles and optical characteristics of the objective lens. The wavelength of the light emitted from the particles is set equal to 560 nm, the objective lenses with magnification of 10 × and 20 × are supposed to be immersed in air, while the lens with M = 60 × is taken as an oil immersion lens ($n_0 = 1.51$). In the last column are reported the results for the objective lens employed in the present experimental apparatus. The dimensions are in µm. 41
2.5 Characteristics of fluorescent particles and seeding concentration used in tests. 44
2.6 NRMS error ϵ_{n_p} for each plane under investigation and resulting $\bar{\epsilon}$ error as a function of the inner geometry of the microchannel. . . . 55
2.7 NRMS error ϵ_{n_p} between the experimental results and a theoretical trapezoidal shape with Φ angels of 88°, over 19 different planes along the depth of the channel. 57
2.8 Comparison between nominal, predicted and real values of the microchannel cross-section. 62
2.9 Results for the straight branch of the micro T-junction. 65

2.10 Measurements of the actual depth of the three branches at the junction. 65
2.11 Results for the three branches of the micro T-junction. 66
2.12 Calculation of the Φ angles of the straight branch. 67
2.13 Calculation of the Φ angles of the branches close to the junction. . . 67

3.1 Summary table of the principal components of the experimental setup. 92
3.2 Main properties of the PMMA used during the simulations. 116
3.3 Maximum Temperature of fluid flow as function of different values of the imposed heat flux Q at the wall both for a non-uniform distribution and for uniform distributions of the convective heat transfer coefficient h on the external surface of the device. 117

4.1 Summary table of the principal components of the experimental setup. 132
4.2 Range of superficial velocity of air and water for which the different flow patterns are established and average values of bubbles velocity for the different flow patterns in the reported range of superficial velocities and measured void fraction α. 145
4.3 Averaged values of the length of the bubbles and dimensionless length of the bubbles over the range of superficial velocity of water and air analyzed for each flow regime. 145

Nomenclature

Roman Letters

A	Area	(m^2)
c	Volume	(µl)
C	Concentration	(ppm)
c_p	Specific heat at constant pressure	(J/kgK)
Ca	Capillary number	(-)
d	Thickness / Diameter	(m)
D_h	Hydraulic diameter	(m)
F	Focal plane	(-)
h	Depth	(m)
	Convective heat transfer coefficient	(W/m^2K)
k	Thermal Conductivity	(W/mK)
L, l	Length	(m)
$\dot{m}$	Mass flow rate	(kg/s)
N	Number of	(-)
n	Refractive index	(-)
	Particles number	(-/ml)
Nu	Nusselt number	(-)
P, p	Pressure	(Pa)
P	Heated perimeter	(m)
p	Helical pitch	(m)
Pr	Prandtl number	(-)
Q	Volumetric flow rate	(m^3/s)
	Heat power	(W)
Ra	Rayleigh number	(-)
Re	Reynolds number	(-)
S, s	Displacement	(m)
T	Temperature	(K)
t	Time	(s)
u, v	Velocity components	(m/s)
V	Dimensionless velocity	(-)
W	Average velocity	(m/s)
w	Width	(m)

Greek Letters

α	Volumetric void fraction	(-)
β	Aspect ratio	(-)
	Homogeneous void fraction	(-)
	Thermal expansion coefficient	(1/K)
$\dot{\gamma}$	Shear rate	(s^{-1})
δ	Differential length	(m)
ε	Threshold parameter	(-)
	Uncertainty value	(-)
	Error	(-)
λ	Wavelength	(µm, nm)
μ	Dynamic viscosity	(kg/ms)
ν	Kinematic viscosity	(m^2/s)
ρ	Density	(kg/m^3)
σ	Surface tension	(N/m)
τ	Time	(s)
	Shear stress	(Pa)
Φ	Angle	(°)

Subscripts

*	dimensionless
-	average

Subscripts

0	concerning the medium in which the lens is immersed
	orthogonal to molecular long axis
	at x = 0
A	air
Al	aluminum
B	bubble
b	bulk
c	back
Cu	copper
e	parallel to molecular long axis
em	emission
ex	excitation
ext	external
f	front
	fluid

Subscripts

G	gas
g	glass
in	inner
L	liquid
max	maximum
p	particle
	horizontal plane
pix	pixel
s	solid
	surface
sol	solution
tot	total
v	vector
x,y,z	Cartesian coordinate
W,w	water
w	wall

Acronyms

2D	Two-dimensional
3D	Three-dimensional
µ	micro
µPIV	Micro Particle Image Velocimetry
APTV	Astigmatism Particle Tracking Velocimetry
CCD	Charged-Coupled Device
CG	Cover Glass (thickness)
CMOS	Complementary Metal-Oxide Semiconductor
DeLIF	Dual emission Laser Induced Fluorescence
DOC	Depth Of Correlation
HSI	Hue, Saturation, Intensity
IR	Infra Red
LC	Liquid Crystal
LDV	Laser Doppler Velocimetry
LIF	Laser Induced Fluorescence
LIFPA	Laser Induced Fluorescence Photobleaching Anemometry
M	Magnification
MTT	Molecular Tagging Thermometry
MTV	Molecular Tagging Velocimetry
NA	Numerical Aperture
NRMS	Normalized Root Mean Square

PIV	Particle Image Velocimetry
PMMA	Poly(Methyl Methacrylate)
POD	Proper Orthogonal Decomposition
PSV	Particle Streak Velocimetry
PTV	Particle Tracking Velocimetry
RGB	Red Green Blue
RTD	Resistance Temperature Detector
SC	Semi-Conductive Sensor
SEM	Scanning Electron Microscopy
SIV	Scalar Image Velocimetry
TFTC	Thin Film Thermocouple
TLC	Thermochromic Liquid Crystal
UV	Ultra Violet
WD	Working Distance

Introduction

Microfluidics is an interdisciplinary field devoted to the study of the manipulation and control of small amount of fluids (from milliliters to pico-liters) flowing in systems having dimensions ranging from tens to hundreds of micrometers for single phase flows (Kandlikar and Grande, 2003; Tabeling, 2005; Whitesides, 2006; Kandlikar, 2012) and up to millimeters for two-phase flows (Serizawa et al., 2002; Mehendale et al., 2000; Kandlikar et al., 2013). In these microsystems the features of convective flows can deviate from the well known behavior observed for flows in conventional systems. In fact, when the system dimensions are reduced to the microscale, the surface forces become predominant over volume forces and this fact determines a change on the basic transport phenomena (Tabeling, 2005; Bruus, 2008). The huge interest on the analysis of single phase and two-phase convective flows through microchannels have determined an increasing number of microfluidics applications in many fields, spacing from biomedical applications to the technological field (Abgrall and Gué, 2007; Kumar et al., 2011).

Drug delivery (Saltzman and Olbricht, 2002; Goettsche et al., 2005), DNA manipulation (Wong et al., 2003), detection of antigens for immunological analysis (Bessette et al., 2007; Chen et al., 2011) and detection of cancer cells with related treatment (Chen et al., 2012; Khan et al., 2013) are just some examples of fields in which microfluidic devices found currently employment for bio-medical applications. Additionally, direct applications of microfluidic systems on patients can be possible, as described in the work of Ziaie et al. (2004), in which, the authors present different techniques for the machining of bio-compatible micro devices. The authors, furthermore, draw the attention to the microfluidic hydrogel systems for the detection of the glucose and to the application of these systems as integrated devices for the insulin delivery to patients affected by diabetes.

As described by Yager et al. (2006), due to the overall dimensions of the microfluidics devices coupled with their availability for specific diagnostics (the so called lab-on-a-chip) without an employment of heavy and bulky instrumentation, lab-on-a-chip devices can be regarded as a personal points of care which anybody can hold in his own home, like glucose detectors, or, for more complex devices, can find also in small doctor's offices rather than going in large specialized clinics (Altieri and Camarca, 2001; Jones and Meier, 2004; Nichols, 2007). Yager et al. (2006) have lastly concluded that, when the cost of these point-of-care

microfluidic devices will be affordable also for the countries historically poor, the lab-on-a-chip systems will have a large distribution with a greater impact all over the world.

Not only biomedical applications have been developed in these last decades. In microchannels, the surface-to-volume ratio between the channel surface in which the fluids flow and its volume, increases. Thus, all the forces that scale with the surface become more important than the volume forces. Therefore heat and mass transfer can be enhanced in microfluidic systems both in presence of two-phase and single phase flows because these devices are characterized by large exchange surfaces combined with limited volumes (ultra compact exchangers) (Tabeling, 2005; Kumar et al., 2011). As a consequence of these features microfluidic devices, such as, micro heads of inkjet printers (Meinhart and Zhang, 2000), micro pumps (Yoshida, 2005), micro heat exchangers (Mehendale et al., 2000; Morini, 2004; Brandner et al., 2007), micro mixers (Lee et al., 2011), micro reactors (Kumar et al., 2011) and micro systems for cooling of electronic devices (Kandlikar et al., 2013) are currently applied in several industrial fields.

As always happens for all the new technologies, in order to further develop them and to enhance their effectiveness and reliability, the availability of supporting experimental data and numerical models become essentials. However, in microfluidics, due to the small dimensions of the devices, in order to limit the disturbance of the measurements on the flow, direct experimental measurements on flow characteristics (*i.e.* velocity and temperature distributions) can be only achieved using sensors placed on the surface of the microchannel or through the employment of a dispersion of particular tracers having micron and sub-micron dimensions. In this case the estimation of the flow features is then shifted to the evaluation of the properties and/or the motion of these tracers within the fluid. In many cases, nevertheless, the only experimental raw data are not sufficient to have accurate information about local characteristics of the transport phenomena, since the small dimensions of the devices inhibit the possibility to obtain a complete set of experimental data. In fact, direct observations are not everywhere possible due to the impossibility to access to some particular regions or due to shadowing effects linked to the presence of obstructions, fittings, walls and so on. Therefore the complete analysis of the flow behavior inside a microchannel can be regarded as an assimilation of gappy data. In these conditions, it becomes mandatory to couple numerical simulations to experimental tests in order to retrieve the desired information as observed by Morini and Yang (2013). In particular in these cases, the set of measurement data are used as boundary conditions for the solution of the numerical problems in order to reconstruct the fluid features within the whole microdevice; in this sense, inverse techniques (Özisik and Orlande, 2000) can be efficiently employed with this aim in microfluidics.

Inverse techniques and data assimilation are concepts widely used from quite a long time for the analysis of the systems that are too broad to be accurately experimentally evaluated in each part of them. Assimilation data analysis were routinely employed in meteorology (Derber, 1989; Stauffer and Seaman, 1994;

Bouttier and Courtier, 2002), oceanography (Robinson and Lermusiaux, 2000) and heart science (Reichle, 2008). The idea to merge numerical models with experimental observations and to use their coupling to refine the set of data by deducing information related to the regions not directly monitored or erroneously observed, has been applied also in fluid dynamics (Gunes et al., 2006; Raben et al., 2012; de Baar et al., 2014) with the aim to demonstrate that numerical simulations can integrate the set of experimental measurements within the fluid region. As an example, specific gappy data methodologies based on the use of proper orthogonal decomposition (POD) (Venturi and Karniadakis, 2004; Venturi, 2006) or Kriging interpolation (Gunes et al., 2006) have been proposed in order to reconstruct the velocity field of a flow around and past a cylinder. In particular these methodologies were analyzed by the aforementioned authors for an increasing level of missing data. The missing data were artificially generated by the authors by removing simulated results in random positions within the flow region. For all the missing levels of data, Venturi and Karniadakis (2004) and Gunes et al. (2006) demonstrated that the gappy data methodologies are able to recover the erased data with excellent efficiency. More recently, Raben et al. (2012), adopted an adaptive gappy POD in order to replace and reconstruct the erroneous data obtained via experimental PIV measurements of a water turbulent flow along a vertical channel. Also in this work, to demonstrate the reliability of the methodology, missing data in correspondence of erroneous measurements were obtained through a randomly removal of some experimental data. The authors showed in conclusion as the reconstructed velocity field was in good agreement with the original one. de Baar et al. (2014) used a Kriging interpolation of stereoscopic PIV observations in order to refine the data acquired over 12 planes in which the measurements of the three dimensional velocity field generated by a micro air vehicle were taken. Through the Kriging interpolation the authors were able to reconstruct the data over intermediate planes in way to decrease the space between the measurements. In order to evaluate the reconstructed data, the authors made PIV observations in correspondence to the fictitious planes and compared those experimental observations with the reconstructed data. A qualitative good agreement was found by de Baar et al. (2014) between the data generated through the Kriging interpolation and the observed data which confirms that assimilation data can be very useful in all the situations in which a complete set of experimental data becomes impossible to obtain due to big (or small) dimensions of the system: in this sense, microfluidics presents similar problems to extended systems like the oceans, atmospheric regions and so on. In addition, when the experimental data are used as starting point for the deduction of the behavior of the flow in regions not monitored directly, the accuracy of the experimental data becomes crucial in order to perform a correct reconstruction of the trend of the physical quantities in the areas in which these quantities were not observed. Even though these considerations can be considered valid in general, for microfluidics applications the accuracy of the experimental data becomes more and more important.

In microfluidics, even very trivial boundary conditions, like the correct knowledge of the cross-section geometry of a channel can be problematic to be measured and this can determine a non negligible influence on the interpretation of the measured quantities which can lead to a misunderstanding about achieved results (Shao et al., 2009; Kumar et al., 2011; Morini et al., 2011). For this reason, the proper understanding of the surrounding conditions, such as the shape and dimension of the microchannel coupled with the boundary conditions imposed to the flow, becomes an extremely important issue to keep under control in order to give to the experimental data the correct meaning. However, for some of these conditions there are cases in which it is not possible to perform a direct evaluation of them, as for the inner geometry of a commercial microchannel. Commercial microchannels have usually closed boundaries and therefore it is not possible to perform an accurate direct optical evaluation (*i.e.* SEM analysis) of their cross-section without destroying the microdevice. Hence, in order to avoid the destruction of the channel, the evaluation of the shape and dimensions of the inner geometry of the microchannel can be an example of application of inverse techniques in microfluidics in which, for example, μPIV measurements can be used in order to reconstruct the geometry of the channel as shown in the second Chapter of this dissertation.

Similarly, the direct experimental determination of the fluid temperature inside a microchannel is also a critical issue, since the dimensions of common temperature detectors are larger or at most comparable with the dimension of the inner cross-section of a microchannel. Hence, with these devices, reliable results are achievable only for temperature measurements on the channel surface. To overcome this problem, efforts have been made from several research groups in order to develop suitable techniques able to measure directly the fluid temperature. However, none of them can be actually considered better than others and their application is restricted to particular flow conditions, such as, a limited working temperature, or still present high uncertainties as in the case of IR thermography. One of the most promising temperature measurement technique useful for microfluidics applications is the TLC thermography based on non-encapsulated TLC particles. Nevertheless, the employment of unsealed TLC particles as particle tracers in velocimetry technique like PIV, APTV and so on, has not been completely investigated up to now and in particular, no experimental results on their mechanical stability when exposed to large shear stress have been yet reported. For this reason, in the third Chapter of this dissertation, the experimental technique for temperature measurements based on TLCs thermography is presented and detailed information about the behavior of non-encapsulated TLCs exposed to increasing shear rates are provided.

More in detail, this dissertation is focused on the use of optical, non invasive measurement techniques for the investigation in microchannels of local velocity and temperature distribution of single phase flows and for the flow patterns obtained in presence of two-phase flows. First of all, in order to summarizes

the state of art of the different experimental techniques currently employed for measuring the microchannel dimensions, as well as the velocity and the temperature distribution of a flow inside a microchannel, a review on these techniques is presented in the first Chapter. Then, three different experimental techniques for optical investigations in microfluidics are presented and critically discussed. For each experimental technique the test rig utilized and the procedure involved are illustrated and the main results achieved are described.

In the second Chapter, the inner cross-section of a microchannel is reconstructed by using a series of velocity data observed experimentally for a liquid flow in laminar regime through a straight microchannel. The experimental velocity distribution within the channel is observed by means of the technique named micro Particle Image Velocimetry (μPIV), that is nowadays one of the most reliable technique for velocity measurements in microfluidics. Firstly, the experimental data acquisition and how they can be employed for the inverse determination of the inner section of the microchannel is described. Specifically, the geometry of the cross-section is obtained by minimizing the difference existing between the velocity profiles experimentally measured and the theoretical profile obtained solving the Navier-Stokes equation for a fixed cross-section geometry. In this way, μPIV is applied as an inverse technique. The results obtained with this technique are compared with observations of destructive SEM tests which confirm the accuracy of the results obtained.

In the third Chapter, an experimental method for measuring the local temperature of a liquid flow inside microchannels is presented. The methodology relies on the use of Thermochromic Liquid Crystals (TLCs) in their non-encapsulated form. The chapter begins with an introduction about the TLCs highlighting their working principles and how the color of those particles can be properly detected and linked to the fluid local temperature (calibration procedure). Then, the pro's and con's concerning the non-encapsulated TLC are underlined. One of the aspects investigated in this dissertation is the behavior of the non-encapsulated TLC when exposed to different levels of shear stress. In Section 3.5 the experimental results of the sensitivity of non-encapsulated TLC particles to shear stress are reported. Two main conclusions are reached: first, the non-encapsulated TLC particles can be subjected to certain shear stress levels before starting to break down, second, TLC particles maintain their color until the shear stress is lower of the limit value at which corresponds the TLC particle destruction. Finally, a preliminary experiment in which non-encapsulated TLC thermography is coupled to the Astigmatism Particle Tracking Velocimetry (APTV) for the simultaneous measurement of the three-dimensional velocity and temperature distribution in a microchannel is shown.

The fourth Chapter concerns the experimental evaluation of the air bubble generation inside a water flow in a microchannel. The bubble generator is a micro

T-junction realized in fused silica in which the water flow (continuous phase) is driven in the same direction of the outlet flow while the air flow (dispersed phase) is injected orthogonally to the continuous phase. Firstly, the experimental apparatus is presented, then the procedure of the images' post processing, acquired with a high speed camera, is described. The post-processed images enable the evaluation of the main physical quantities related to the air water mixture, such as the velocity and the length of the bubbles and the mixture void fraction. The experiments are repeated for 265 different conditions of flow rate imposed to the incoming liquid and gaseous flows, corresponding to superficial velocities ranging between 0.005 m/s and 0.15 m/s. Finally a flow pattern map composed by 195 experimental observations is proposed.

Chapter 1

State of the art of experimental techniques for velocity and temperature measurements inside microchannels

1.1 Measurements of the dimensions of microchannel inner geometry

The knowledge of the microchannel geometry has a huge impact for the determination of the fluid dynamic characteristics of a microflow, like pressure drops, friction factors and so on. In fact, modifications of the channel geometry in the range of microns can induce not negligible modifications on the main flow parameters (velocity gradients and pressure drops). All the detection techniques available for the analysis of the surfaces with spatial resolution in the order of 0.1 - 1 μm require an optical access. The most reliable technique for geometrical investigation with a resolution lower than 1 μm is the Scanning Electron Microscope (SEM). Even if this investigation is undoubtedly accurate (Celata et al., 2007; Tang et al., 2007) it presents some substantial limitations. A direct optical access is required as well as a conductive substrate is needed. If the channel material is not conductive, such as the glass, the channel has to be previously treated with the deposition of a metallic layer (usually gold). Hence, SEM analysis allow only the investigation of an uncovered surface. For this reason, SEM investigation is a powerful tool during the channel realization, if this implies a first etching on a substrate with a subsequent bounding, while it is not at all useful for the investigation of already bonded microchannels, as for commercial microchannels or for a different manufacturing process, as for the cylindrical microchannels. In the latest cases, indeed, only the inlet and outlet cross-section geometry can be investigated, without destroying the devices, with this technique (Morini et al.,

2011).

In order to overcome the limitations presented by SEM investigations other techniques with a lower resolution have been proposed. As an example, the confocal fluorescence microscopy can be used in order to detect the inner geometry of a channel with optical access. In this case the channel is completely filled with a fluorescent dye and illuminated through its whole volume. Then, through the scanning of the fluorescent region it is possible to reconstruct the shape of the filling fluid and consequently, if the fluid fills completely the channel, it is possible to reconstruct the shape of the channel cross-section. An application of this technique is shown in the Section 2.5.3 of this dissertation in which the confocal fluorescence microscopy is used for the determination of the cross-section microchannel geometry of a micro T-junction. Another optical technique, able to identify the cross-section geometry of a microchannel, is presented in the second Chapter of this dissertation. The working principle of the original technique proposed by Silva et al. (2009) is to use the local velocity measurements of a flow inside a microchannel (*i.e.* by using μPIV or μPTV) in order to reconstruct the cross-section geometry of the microchannel in which the fluid flows. However, the geometry reconstruction obtained by this technique has a degree of accuracy strongly linked to the accuracy of the local velocity measurements achieved by the selected velocimetry technique.

For microchannels without any optical access, the average inner diameter of the channel can be evaluated from a careful estimation of the fluid flow rate through the microchannel. More precisely, Asako et al. (2005) have proposed to use a mass flow rate measurement in order to determine the average value of the inner hydraulic diameter of microchannels. The method proposed by these authors relies on the assumptions of a Poiseuille flow inside a microchannel, a constant mass flow rate along the measurement period, constant fluid properties and a known length of the microchannel. Under these assumptions it is possible to obtain an indication of the average hydraulic diameter of a set of microchannels from the measurements of the mass flow rate through the microchannels.

Asako et al. (2005) applied this principle in order to evaluate accurately the inner diameter of fused silica microchannels having a declared nominal inner diameter of 150 μm. The evaluation of the mass flow rate was carried out by weighing the total amount of water flowing through the channels for a time period of 10 minutes. The quantity of the water evaporated during the test was also considered from the authors. In order to give a reliable estimation of the channel diameter, the measurements were repeated for different lengths of the microchannels under investigation and the mean value of the estimated diameter was assumed to be the real diameter of the microchannels. Asako et al. (2005) demonstrate that the evaluation of the average inner diameter of a tube by using this technique is affected by an uncertainty of the order of $\pm$ 0.2 μm.

Even if, the procedure shown by Asako et al. (2005) is a smart method for the integral evaluation of the inner cross-section for microchannels without optical access, it presents some substantial limitations. First of all, the value of the inner

diameter determined with this technique is an average value along the whole length of the tube. In fact, the geometry of the microchannel is assumed to be regular and constant along the axial direction, hence with this technique it is impossible to evaluate possible local imperfections of a microchannel along its axial direction. In addition, this method gives an information about the hydraulic diameter of the section, that for the cases in which the geometry is not circular, it can be obtained with different cross-section shapes. (*i.e.* for a rectangular channel the same hydraulic diameter can be obtained with many values of the aspect ratio). This means that this techniques cannot be useful when the goal is to reconstruct exactly the real geometry of a microchannel but only when the goal is to determine the "characteristic" dimension of the channel (*i.e.* its hydraulic diameter). However, even if the hydraulic diameter is extensively used as reference dimension for the evaluation of fluid-dynamic behavior of laminar flows through non-circular channels both in macro and micro systems, many authors have demonstrated that alternative definitions of the characteristic length of a channel (like the squared root of the cross-section area of a channel) could allow a more appropriate scaling of the flow characteristics when the dimensions are changed (Duan and Muzychka, 2007).

The Asako et al. (2005) technique can enable to obtain also the indication of a different "characteristic length" (as the square root area of the channel cross-section) if there is an appropriate model which link mass flow rate to pressure drop for a fixed geometry (*i.e.* the Duan and Muzychka (2007) model). However, in this case the "shape" of the cross-section must be known.

A summary of the experimental techniques for the cross-section geometry detection of a microchannel is reported in Table 1.1.

Table 1.1: Summary of the experimental techniques for geometry detection.

Technique	Specification	References
SEM	Typical resolution: 5-8 nm @ 3 kV 2-3 nm @ 30 kV	*ZEISS EVO SEM*
Confocal Fluorescence Microscopy	Nominal length: 300 µm Uncertainty: ± 3-5 %	(-)
Weighting of accumulated liquid volume	Nominal diameter: 150 µm Uncertainty: ± 0.2 µm (± 0.16 %)	Asako et al. (2005)

1.2 Local velocity measurements

To develop a microfluidic device, experimental techniques able to detect the flow motion inside microchannels have a relevant role in order to show the flow behavior through the channel network. Different techniques have been proposed in order to track the local velocity distribution of microflows. Generally these methods are based on optical techniques that require a transparent access to the fluid (Sinton, 2004), nevertheless, less common techniques can perform velocity and flow patterns measurements inside micro- and mini- channels having opaque walls. Examples of these techniques are nuclear magnetic resonance or magnetic resonance imaging (Powell, 2008), positron emission particle tracking (Fan et al., 2006), radiographies with neutrons and x-rays (Sakai et al., 2003) and ultrasonic pulsed Doppler velocimetry (Peters et al., 2010). However these techniques are complex, expensive and with low spatial resolution, hence their employment is not widely widespreaded as for optical techniques. For a deepened analysis of those techniques the reader can refer to the review work of van Dinther et al. (2012).

As described also by Sinton (2004) the main feature of the optical techniques for flows visualization, is to slightly alter the fluid composition in order to be able to detect its movement (*i.e.* velocity distribution) avoiding disturbance on the behavior of the original flow. A brief description of the most used optical techniques for the measurement of local velocity inside microchannels is now summarized.

1.2.1 Micro Particle Image Velocimetry (µPIV).

The micro Particle Image Velocimetry (µPIV) technique is probably the most widely used technique for local velocity measurements of a flow inside microchannels, as it can be evidenced by the large number of papers in which this technique has been used for measuring the local velocity in microdevices (see reviews of Lindken et al. (2009) and Lee and Kim (2009)). This technique shares the same working principle of the macro PIV technique, *i.e.* the detection of the motion of tracer particles dispersed inside the working fluid. The seeding particles are chosen in order to have the same density of the working fluid in order to obtain a complete correspondence between the motion of the working fluid and the seeding without to introduce significant disturbance on the fluid motion. In this way the detection of the particles' displacement per unit time enables directly to calculate the related flow velocity. More precisely, the µPIV technique uses the Eulerian scheme to detect particles' displacement, therefore, does not follow the displacement of each single particle but use the mean motion of a group of particles in a small detection area called interrogation cell. The interrogation cell must be small enough in order to give a local velocity information but also large enough to contain a minimum number of particles that give substantial information. A series of images (at least two) is required in order to associate to

each interrogation cell the corresponding velocity vector. Indeed, the association of a velocity vector to each cell is obtained with a cross-correlation procedure of the particles' displacement through the acquired series of images. In order to gain the information from sub-micron particles (this is the typical dimension of the seeding used in μPIV) a magnification of the recorded images is required, therefore the sample under investigation is visualized by using an epi-fluorescent microscope in which a magnification lens is present along the light path. This entails a volumetric illumination of the flow, hence, the focal plane in which the fluorescent particles are detected is determined from the focal plane of the objective lens rather than from a thin laser sheet as happens in conventional PIV observations. For this reason, in μPIV, not only the particles that are on the objective focal plane give a useful signal but also the particles that are within a fixed layer centered on the focal plane and characterized by a thickness, called depth of correlation (DOC), give back an additional signal used in the cross-correlation procedure. A deeper analysis on the μPIV system is however postponed to the second Chapter of this dissertation, in which the main features of the experimental technique and all the main developments obtained to nowadays after the first works of Santiago et al. (1998) and Meinhart et al. (1999) are discussed.

1.2.2 Micro Particle Tracking Velocimetry (μPTV).

As for the μPIV technique, also the μPTV technique uses particles dispersed inside the working fluid in order to detect the motion of the flow. However in this case a Lagrangian approach is adopted: the displacement of each single particle is tracked, in all the field of view, from different images acquired with a constant time delay. Therefore, a velocity vector is associated to the single particle displacement. For this reason simplified tracking methods can also be used, even if, the related uncertainties associated to the velocity measurements are higher compared to employment of cross-correlation methods utilized in the μPIV technique (Cierpka and Kähler, 2012). However, the μPTV technique introduces some advantages with respect to the PIV technique as underlined by Sato et al. (2003); Cierpka and Kähler (2012) and Cierpka et al. (2012). First of all, a lesser number of particles is required. This gives a drastic advantage in order to reduce the bright noise induced by particles out of focus inside the depth of correlation and this fact decreases the effects of bias errors. In addition, for flows in steady state conditions the spatial resolution can be increased with respect to μPIV methods. In fact, through an acquisition of a higher number of images the distance between velocity vectors is reduced, where for μPIV method this is not possible since the spatial resolution is determined by the size of the interrogation cell. In addition since common μPIV methods employ a time-average cross-correlation of acquired data, temporal variations of the fluid velocity, such as pulsating flows, cannot be detected while through tracking methodologies this becomes possible (Sato et al., 2003). In last instance, as shown by Sato et al. (2003) through spatially-averaged methods of PTV the bias errors induced by the Brownian motion of the particles

can be eliminated also for velocity measurements with time resolution. The μPTV has been successfully applied for velocity measurement of electrokinetic-driven flows inside microchannels (Devasenathipathy et al., 2002).

1.2.3 Astigmatism Particle Tracking Velocimetry (APTV)

Recently, Cierpka et al. (2010) have developed a PTV technique for the detection of the three-dimensional velocity field of a flow inside a microchannel, in which the information given by out-of-focus particles are used in order to obtain the displacement of the particles along the direction perpendicular to the observation plane. This technique is called Astigmatism Particle Tracking Velocimetry (APTV) and it is simply realized by adding a cylindrical lens along the light path between the classical spherical lens of the microscope and the CCD or CMOS sensor for image acquisition (Cierpka et al., 2012; Rossi and Kähler, 2014). Three fundamental advantages are related to the APTV method: first, this technique gives fundamental information about the three-dimensional characteristics of the flow, second, it reduces sensibly the bias error induced by out-of-focus particles and third, the measurement of the three-dimensional velocity field is possible with the employment of a single camera (Cierpka et al., 2010). About this last characteristic it is possible to highlight that the 3D velocity field can be also reconstructed through stereoscopic μPIV technique as proposed by Lindken et al. (2006). However, in this case two different cameras with a tilt angle between them are required in order to acquire simultaneously the images via a stereo lens with a magnification of 1 × or 2 ×. Nevertheless, the low numerical aperture of the stereo lenses entails a large depth of correlation (60 ± 10 μm for a lens of M = 1 × and 15 ± 5 μm for a lens of M = 2 ×) reducing consequently the spatial resolution in the direction normal to the fluid flow and therefore the reliability of this technique.

More recently, Segura et al. (2015) have demonstrated the viability of the APTV method using non-encapsulated thermochromic liquid crystal (TLC) particles, in such way to perform with the employment of a single camera, simultaneous measurements of 3D velocity and temperature distribution of a fluid in microfluidic applications. Nevertheless, the discussion about the achieved uncertainties when the APTV method is coupled with the TLC thermography is let to Section 3.7, in which simultaneous measurements of three-dimensional velocity and temperature distribution are performed for a fluid flow inside a microchannel.

1.2.4 Micro Particle Streak Velocimetry (μPSV).

μPSV employs a dispersion of a fluorescent dye inside the working fluid which gives back a bright signal after being excited from a light source. The images of the particles are acquired from a CCD camera that integrate different frames recorded with a constant time delay in a single image. In this way it is possible to visualize the fluid motion inside the microfluidic device through the streaks

obtained via the fluorescent dye. Even if quantitative velocity measurements are possible with μPSV, the accuracy of the results is strongly lower compared to the accuracy achieved through μPIV and μPTV techniques (Sinton, 2004). In the past, PSV technique has been used for tracing the fluid motion either for electrokinetic flows (Taylor and Yeung, 1993; McKnight et al., 2001; Oddy et al., 2001) than for pressure driven flows (Taylor and Yeung, 1993; Brody et al., 1996) inside microchannels.

1.2.5 Laser Doppler Velocimetry (LDV).

Laser Doppler Velocimetry (LDV) or Laser Doppler Anemometry (LDA) is based on the counting of the Doppler signal gave back from reflective particles when illuminated by a laser beam. Two or more laser beam are required in order to detect flow velocity, since the velocity of the seeding particles is determined through the evaluation of distance of the interference fringes generated by reflective particles in the unit time. As for the others techniques, LDV is born for velocity determinations in conventional channels. The application of LDV to microflows is described in the technical note of Tieu et al. (1995). More recently, Onofri (2006) published a work in which a slight modification of standard LDV technique was used in order to study the velocity distribution of a flow inside a microchannel having a depth of 80 μm. Onofri (2006) used three laser beams formed by splitting the beam generated by a laser diode to illuminate titanium oxide nano particles with a diameter of 0.3 - 0.7 μm. The accuracy of LDV system shown by Onofri (2006) is in the order of 5 % with respect to the measured velocity.

1.2.6 Micro Molecular Tagging Velocimetry (μMTV) and other techniques.

Micro Molecular Tagging Velocimetry (μMTV), and more in general molecular based techniques use luminescent molecules, such as fluorescent or phosphorescent dye artificially dispersed or created inside the working fluid, in order to detect the fluid velocity distribution. Hence, these luminescent molecules are activated in a fixed region by a light source (lasers, halogen lamps, UV light sources, etc...) and their velocity is evaluated by measuring the molecules' displacement in a known time interval. To be eligible for μMTV, the molecular tracers have to respect two fundamental requirements: first, in order to furnish reliable information on the fluid motion, the forces acting on the molecules of the dye must be the same forces acting on the molecules of the fluid (Sinton, 2004) and second, the life time of the luminescent molecules must be long enough to be detected in the selected time delay (Hu and Koochesfahani, 2006; Koochesfahani and Nocera, 2007). Generally, as stated also by Koochesfahani and Nocera (2007), fluorescent dye give a signal with strong intensity but for a short time (1 - 10 ns) since the non-radiative decay rate is usually negligible compared to the radiative decay rate, while phosphorescent dye give a signal with a weaker intensity but for longer

time (up to the second). Hence, the proper choice of the molecular fluorescent dye depends on the typology of application in which velocity measurements are carried out and in its turn determines the kind of light excitation.

The major advantage of the MTV technique, is that molecular tracers can be successfully employed in order to track situations in which the drift motion of the seeding micro particles induced from the shear forces of the flow could compromise the correct detection of the same fluid motion, like for gaseous flows.

Paul et al. (1998), applied for the first time a *photoactivatable caged-fluorescent dye* for the visualization of pressure-driven and electrokinetically-driven flow inside a microchannel. In the specific case, the experiments were carried out inside fused silica capillaries with polyimide cladding having inner diameters of 75 µm and 100 µm. The fluorescent caged dye was premixed into a water flow and then driven inside the capillary. The fluorescence was then induced using two lasers: a UV laser beam (λ = 355 nm) was focused inside the microchannel in order to realize a laser sheet of 20 µm of thickness for uncaging the dye, then a double Nd:YVO_4 blue laser (λ = 473 nm) was used for exciting the dye. The light emitted by the fluorescent dye was filtered and subsequently acquired by a CCD camera. The Scalar Image Velocimetry (SIV) method developed by Dahm et al. (1992) was used in order to recover the velocity information of a pressure driven flow, while the motion of electrokinetically driven flow was directly observed through the mean displacement of the fluorescent dye. Finally the authors highlighted that the achieved spatial resolution achievable with this technique can be estimated in the order of 5 µm for in-plane measurements while the depth of field was about 20 µm.

Maynes and Webb (2002) used a *phosphorescent dye* in water solution to measure the velocity inside a fused silica microchannel with an inner diameter of 705 µm. The working principle of the technique shown by Maynes and Webb (2002) (fig. 1.1) is similar to the one adopted by Paul et al. (1998) with the difference of that the dye used by Maynes and Webb (2002) was phosphorescent and not caged, hence, a single UV laser (λ = 308 nm) was used in order to excite the dye. Also in this case the exciting light was focused inside the microchannel in order to have a laser beam with a radius of approximately 20 µm. A spatial resolution of 10 µm was achieved by the authors. The technique proposed by Maynes and Webb (2002) was applied in order to evaluate the fluid velocity inside a microchannel for Reynolds numbers ranging from 600 up 5000. The comparison with the expected theoretical flow velocity, has shown a particular good agreement with the experimental data obtained for Reynolds numbers below 2000.

Wang (2005) proposed a technique called Laser Induced Fluorescence Photobleaching Anemometry (LIFPA) in order to measure the fluid velocity in microchannels. The key point of this technique is to correlate the fluorescence intensity of the dye with the velocity of the fluid. This principle is based on the consideration that the photobleaching effect is characterized by a fluorescence intensity which decreases exponentially in time (Wang, 2005).

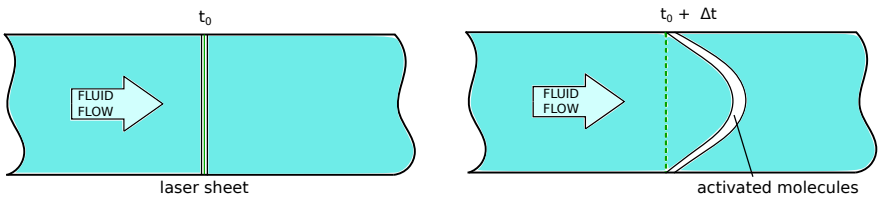

Figure 1.1: Schematic sketch of the working principle of one-dimensional MTV.

By inducing the photobleaching effect with an external source (*i.e.* external radiation in the range of absorption of the fluorescent dye) is possible to make a relationship between the fluorescent intensity of the dye and the fluid velocity. More precisely, a longer time under the photobleaching effect (lower velocity of the fluid) corresponds to a weaker signal of the dye fluorescence intensity. Hence, molecular dyes dispersed in streams with higher velocity have a higher fluorescence intensity with respect to slower molecular dyes (Kuang et al., 2009). In order to demonstrate experimentally the availability of the LIFPA technique for velocity measurements, Wang (2005) applied the LIFPA technique for the velocity measurement of an electroosmotic flow in a microchannel (width = 100 µm and depth = 50 µm) in which a flow of deionized water with a dispersion of fluorescein sodium (absorption wavelength λ_{abs} = 488 nm) is driven. In order to induce photobleaching, a UV laser beam (λ = 337.5 - 356.4 nm) is focused inside the microchannel to obtain a laser sheet of 25 µm. The signal coming from the fluorescent dye is recorded by an oscilloscope. However, in these conditions the author was able to estimate the bulk fluid velocity only.

In order to extend the LIFPA technique for the measurement of local velocity, Kuang et al. (2009) proposed a LIFPA technique via epi-fluorescence confocal microscopy. The working principle was the same of the LIFPA technique developed by Wang; through the epi-fluorescence confocal microscopy the authors were able to perform point-wise measurements with a spatial resolution below 1 µm. For the experimental demonstration, the authors used Coumarin 102 (λ_{abs} = 400 nm) as fluorescent dye dispersed into a solution of methanol. Violet laser (λ = 405 nm) was used as the photobleaching light source and a photodiode detector as the detection system. The experiments were carried either in a circular microchannel than in a rectangular microchannel and the bi-dimensional velocity distribution in both systems were found by the authors to be in good agreement with theoretical velocity values. Recent developments were carried out from the same team in order to perform through the LIFPA technique the measurement of velocity fluctuations inside microchannels (Zhao et al., 2015, 2016).

Another example of the use of photobleaching technique through confocal microscopy for velocity measurements is reported in the work of Schembri et al. (2015) in which an aqueous flow of fluorescein isothiocyanate is driven

inside borosilicate flat microchannels (heights of 50 µm and 1000 µm) and a laser with a wavelength of 488 nm is used as the light source for the molecules' photobleaching.

The MTV technique has been successfully applied by Samouda et al. (2015) for the measurement of the bidimensional velocity profile of a gaseous flow inside a minichannel. The authors used acetone in order to seed an argon flow and a quadrupled Nd:YAG laser as exciting light source. Through a focusing system, the laser beam diameter was reduced to 35 µm. With the experimental configuration adopted and through an original data reduction analysis, the final spatial resolution achieved by authors was in the order of 15 µm. The results reported by Samouda et al. (2015) are very important since up to now, for confined gaseous flows inside microchannels, all the employed experimental techniques have highlighted difficulties on the measurement of the velocity field. However, one relevant problem of the MTV technique applied to gaseous flows is the diffusion of the molecular dyes inside the gas, especially when the gaseous flow becomes more and more rarefied (Frezzotti et al., 2015). Hence, in order to provide a numerical tool for describing the molecular diffusion of tracer inside the gas flow and then perform correctly the experimental measurements of the velocity profile, Frezzotti et al. (2015) executed a Monte Carlo direct simulation (DSMC) of the flow of the mixing (molecular tracer + working fluid). Either the free motion of the molecules than the collision between them were taken into account in the simulation performed by the authors.

Therefore, through the assumptions of a simple advection-diffusion model for the tagging molecules and one-dimensional flow geometry, the displacement of the molecular dye $s_x(y,t)$ along the streamwise direction (x direction) can be expressed as (Frezzotti et al., 2015):

$$\frac{\partial s_x(y,t)}{\partial t} = u_x(y) + \mathscr{D}_{12}\frac{\partial^2 s_x(y,t)}{\partial y^2} \tag{1.1}$$

where $u_x(y)$ is the steady, fully developed velocity distribution of the gas far from the boundaries and $\mathscr{D}_{12}$ is the diffusion coefficient of the dye molecules in the carrying gas.

The implementation of the solution of Eq. (1.1), such as the one provided by Frezzotti et al. (2015), is an example in which the numerical simulation is used in order to complete the experimental data. Indeed, as shown by Si Hadj Mohand (2015), Eq. (1.1) must be coupled to MTV measurements in order to obtain a more accurate experimental information on the gas velocity distribution inside a microchannel also in conditions of low pressure of the gaseous flow.

Other optical techniques have been used in order to detect the motion of a fluid flow inside a microchannel such as shadowgraph-like imaging methods (Mauger et al., 2014) and Optical Feedback Interferometry (OFI) (Campagnolo et al., 2013), but the problems met with these techniques have limited their diffu-

sion through the microfluidics community.

In conclusion it can be summarized that, even though the μPIV can be considered the most well established technique for velocity measurements of liquid flows inside microchannels, other techniques such as the μPTV have been considerably developed in recent years. In particular APTV method gives advantages if the goal is to reconstruct 3D velocity field in comparison to similar analyses performed with 3D-μPIV.

Moreover, regarding to gaseous flows inside microchannels, the recent development of μMTV techniques seems to highlight how these techniques can allow to obtain in the future accurately velocity measurements for gas flow even in rarefied conditions.

A summary of the main experimental techniques for the velocity detection in microchannels, is reported in Table 1.2.

Table 1.2: Summary of the experimental techniques for velocity detection.

Technique	Specification	References
μPIV	In-plane spatial resolution: depending on the size of interrogation cell and magnification involved	Westerweel (1997)
	Out-of-plane spatial resolution: depending on DOC	Rossi et al. (2012)
	Typical uncertainties: 1 - 3 %	Puccetti et al. (2014) Vocale et al. (2014)
APTV	Typical uncertainties: 5 % for out-of-plane velocity components ~ 1 % for in-plane velocity components	Cierpka et al. (2012)
μPSV	Typical uncertainties: 10 - 17 %	Taylor and Yeung (1993)
LDV	Typical uncertainty: ~ 5%	Onofri (2006)
μMTV	Typical uncertainties for liquid flows: 1 - 4.5 % at the centerline velocity	Maynes and Webb (2002)
	Typical uncertainties for gaseous flows: 6 - 10 % at the centerline velocity	Samouda et al. (2015)
LIFPA	Typical uncertainty: ~ 4%	Kuang et al. (2009)

1.3 Local temperature measurements

The measurement of the local temperature in a flow through a microchannel is still a critical issue although a lot of efforts have been made during the period ranging from the last decade of the past century to now. The main problem about the measurement of the local temperature in microchannels is related to the typical dimensions of these channels. Indeed, classical sensors, such as thermocouples or thermistors, have dimensions comparable to the overall inner diameter of microchannels and consequently they cannot be used inside the microchannels without blocking the flow or, at least, without alter the fluid behavior in correspondence of the sensor. For this reason common thermocouples can be employed only for measuring directly the temperature at inlet or outlet section of the microchannel (Morini et al., 2006; Tang et al., 2007; Demsis et al., 2009), where particular care has to be taken in the thermal insulation of the device in order to prevent thermal losses (Morini et al., 2011). In general, even if micro flow sensors for measuring the temperature inside microchannels were suggested in the past (Lammerink et al., 1993; Nguyen, 1997), their implementation in microchannels results to be too much intrusive to leave the flow unperturbed and consequently perform accurate measurements of the local temperature of a microflow. For these reasons, temperature measurements inside microchannels have been performed through the employment of techniques in which the temperature of the fluid is indirectly evaluated sometimes by using some properties of the flow influenced by the temperature, sometimes by introducing in the flow small seeding particles used as local sensors and sometimes by reconstructing the temperature within the flow starting from the knowledge of the temperature distribution on the external surface of the microchannel (inverse techniques).

A review of the thermometric techniques applied to the microscale, has been made by Kim et al. (2015) and Morini et al. (2011). By following these reviews, the main sensors used for the detection of the surface temperature along a microchannel can be divided in thin film thermocouples (μTFTC), thin film thermal resistance (μRTD) and semiconducting sensors (SC). On the contrary, if the aim is to investigate the temperature distribution within the flow, attention must be paid to the thermometric techniques based on optical investigations like infrared thermometry and techniques which employ a tracer dispersed inside the flow, such as, the laser induced fluorescence (LIF) and the molecular tagging thermometry (MTT) or thermometry through thermochromic liquid crystals (TLCs).

1.3.1 Thermocouples.

As previously listed, thermocouples can be used in order to retrieve the temperature of the fluid through an indirect estimation starting from data acquired along the boundary of the microchannel. Bavière et al. (2006), for the indirect determination of the temperature of a fluid flow inside a microchannel, used 4

T-type thermocouples placed inside the brass microchannel walls orthogonally to the streamflow. The thermocouples were placed at 500 µm away from the wall of the microchannel and were equally spaced each other. Demineralized water was used as testing fluid, while the heat power was provided by 8 cartridge heaters housed in the brass substrate of the device. The temperature measurements carried by the thermocouples were used in order to reconstruct the temperature of the microchannel wall. The bulk temperature distribution of the fluid was then estimated by means of a simple balance between the wall and the fluid. The authors demonstrated that by knowing the wall temperature and the heat flux at the fluid-solid interface, it was possible to calculate by using an energy balance both the heat transfer coefficient and the bulk temperature along the axial direction of the microchannel.

Sui et al. (2011), used three T-type thermocouples for measuring the wall temperature of a sinusoidal copper microchannel having a rectangular cross-section with sides of 205 µm and 404 µm. Two additional thermocouples were placed in the inlet and outlet plenums. The average temperature of the wall was later calculated through a one-dimensional heat conduction model. The heat power was delivered by a cartridge heater housed in the copper substrate. They reconstruct the axial trend of the bulk temperature along the channel by using the wall temperature and the heat flux at the wall.

Sadaghiani and Koşar (2016) used local temperature measurements acquired through four thin thermocouples attached on the outer surface of a stainless steel micro tube in order to evaluate the inner temperature of the microchannel wall. Also in this work the one-dimensional heat conduction model, was used in order to evaluate the temperature of the inner wall of the microchannel. The outer diameter was measured by the authors using a precision caliber while the inner diameter was controlled (at the inlet and outlet surfaces) using a *Leica DMLM* microscope. The estimation of the temperature of the microchannel inner wall was later used by the authors in order to calculate the bulk temperature and the convective heat transfer coefficient.

1.3.2 Thin film thermocouples (µTFTCs).

Thin film thermocouples are able to measure the local temperature by using the Seebeck effect, that is a thermoelectric effect that arises when two different particular metals are joined together in two different points exposed to two different temperatures. Typically, µTFTCs are made using a deposition of a chromel - alumel alloy on a conductive substrate (Zhang et al., 2006; Choi and Li, 2007; Mutyala et al., 2014). Choi and Li (2007), proposed a K-type µTFTC made with a deposition of a chromel layer and an alumel layer on a nickel substrate, the junction size was of 25 µm × 25 µm with a thickness of 150 nm. The good sensitivity of the sensor was shown by a Seebeck coefficient of 40.4 µV/°C for temperature up to 800°C. Also a fast response of the sensor (28 ns) was reported by the authors. The major advantages of µTFTC are the robustness, the large operative range

and the possibility to deposit the sensor directly on the surface of the device that must have a surface as smooth as possible.

1.3.3 Thin film resistances (μRTDs).

The working principle of μRTDs is based on the dependence of the electric resistance of a material with temperature. A lot of different materials can be employed in order to build μRTD devices (Morini et al., 2011), most of them are metals such as platinum (Schöler et al., 2005), silver (Wu et al., 2009), thin films of gold and chromium (Choi et al., 2009) and aluminum (Wang et al., 2013) but also poly-silicon doped with boron can be used (Wu et al., 2001). Wu et al. (2009) used a silver wire with dimensions of 60 μm × 50 μm entirely deposited along the development of the microchannel, in order to measure the temperature of polymerase chain reactions inside a PDMS microchannel. During the calibration of the silver wire the authors found a good linearity between the temperature of the sensors and its resistance in the range of 45 - 105 °C. The steady-state temperature uncertainty was in the order of ± 0.5°C. μRTD sensors have the advantage to be easy to be produced during the microchannel fabrication and they show generally a linear dependence between the temperature and their electrical resistivity (Morini et al., 2011). μRTD can be used for surface temperature measurements in microchannels.

1.3.4 Semiconducting temperature sensors (SCs).

Semiconductor sensors (SCs) for temperature measurements, consist of a wide array of sensors coming from the microelectronics field. SCs sensors generally refer to CMOS (Complementary Metal-Oxide Semiconductor) technology and, as reviewed by Bianchi et al. (1998), for the temperature measurements purpose can be divided in MOS transistor (Miribel-Català et al., 2001), bipolar transistors, diodes (Chin et al., 2001; Guha et al., 2007; Han and Kim, 2008) and technologies which coupling the working principle of MOS and bipolar transistors (Filanovsky and Lee, 1999). The working principle of the semiconductor sensors is based on the dependence of the voltage drop of the device in relation to the temperature of the same when a constant current is circulating inside it. Therefore, through a proper calibration of SC sensors is possible to measure accurately the temperature of small surfaces. As outlined by Han and Kim (2008), the great advantage in the use of an array of diodes with respect to μTFTCs or μRTD relies on the management of connective wires. Each single thermocouple or thermistor needs the employment of two/four wires in order to bring the information from the sensor to the acquiring system; this could result in a large quantity of wires when multiple information about the temperature in different positions is needed. With a diodes array, however, the amount of connective wires can be reduced. For example, Han and Kim (2008) proposed a diode array composed by 1024 temperature measuring points (each single diode had a dimension of 50 μm × 50

μm) in which only 64 connective wires are employed. The whole device had an overall area of 12 mm × 12 mm, where the sensitive area was of 8 mm × 8 mm. The device proposed by Han and Kim (2008) has shown a linear voltage drop depending to the temperature felt in the range of 0 - 100 °C and an accuracy of ± 0.5 °C. Also SC devices are used for surface temperature measurements.

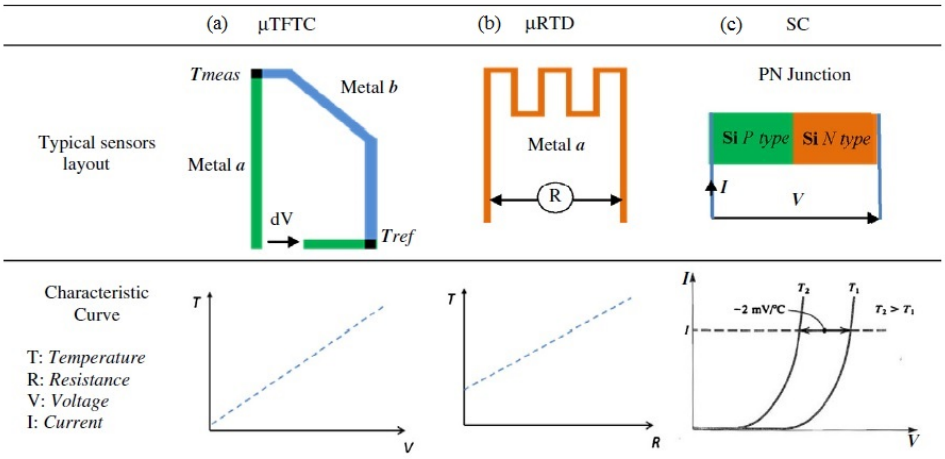

Figure 1.2: Simplified description of the working principle of Thin Film Thermocouples (a), Thin Film Resistances (b) and Semiconducting Temperature sensors (c) (Morini et al., 2011).

1.3.5 Infrared Thermography.

The infrared thermometry is an optical technique based on the principle that all objects with a temperature higher than 0 K emit an infrared radiant heat which is dependent on the temperature of the object. Through the employment of an infrared camera is possible to estimate the temperature of a surface without using any device in contact on it if the surface emission is known. Infrared thermometry is a well established technique used for measuring the temperature of surfaces where the employment of standard temperature devices are problematic or for those surfaces in which the extension is too large to require the employment of a large number of temperature sensitive devices. However, due to the continuous enhancement of the sensitivity and resolution of the infrared sensors, the infrared thermography has been successfully utilized also for temperature measurements in microsystems (Ashauer et al., 1997; Hetsroni et al., 2011). As outlined by Hetsroni et al. (2011), the main drawback of the infrared thermography in microfluidics is related to the signal resolution. In fact, since in microsystems the geometries are very small, the signal could be affected from a high value of noise and, in general, from the thermal radiation of other adjacent objects that could give a bias error on the temperature measurements. Particular care has to be taken during the procedure of data assimilation and during the

post processing. Thermographic measurements can be either performed on the external surface of the microchannel (Hetsroni et al., 2003) than directly on a fluid flowing inside a microchannel, in which, an infrared transparent window for the optical access is present (Mishan et al., 2007; Liu and Pan, 2016). In the first case the estimation of the fluid temperature can be achieved through an inverse analysis, starting from the temperature measurement on the outer surface of the microchannel. From an experimental point of view, particular care has to be taken regarding to the superficial treatments of the surface of the microfluidic device, specifically the reflection of the outer surface must be reduced as much as possible. In addition also the background has to be kept at a constant temperature. Both the microchannel emissivity and the background emissivity have to be precisely known (Hetsroni et al., 2003, 2011).

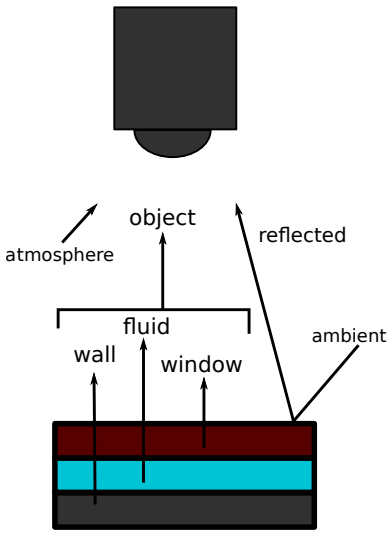

Figure 1.3: Schematic representation of the radiative contributions recorded by the IR camera. Image adapted from Liu and Pan (2016).

An example of infrared thermography applied directly to a fluid flow inside a microchannel can found in the work of Liu and Pan (2016). In this work, the authors, have performed thermal investigations on single-phase flows and two-phase flows inside a rectangular microchannel of a 1 mm in width and 250 µm in depth obtained from an aluminum substrate. The microchannel walls were coated in order to achieve a known emissivity of 0.95. The microchannel was then enclosed with a germanium plate in order to allow a transparent access for wavelengths in the range of 8 - 14 µm, coherent with band of the IR thermal sensor. The employed camera was a high speed IR camera with a resolution of 640 × 120 pixels at 200 Hz of frame rate, the resolution of the camera was in the order of 50 µm. The total radiation gained from the camera includes also the contributions of reflections on the sample surface due to the presence of objects around the sample under investigation and the contribution from the atmosphere (see fig. 1.3). In order to evaluate the accuracy of the temperature measurements

through IR thermography Liu and Pan compared the obtained calibrated measurements with the temperature measured from a micro thermocouple directly inserted inside the microchannel. The comparison was made with fluid flowing conditions. Based on the thermocouple temperature measurements, the authors corrected the temperature of the fluid measured with IR thermography putting a constant correction coefficient. Through the employment of this coefficient, the error bands on the measured temperature, were estimated to be in the order of 7.8 %. Other IR measurements of the fluid local temperature in microfluidic systems were made by Buffone and Sefiane (2004), Dhavaleswarapu et al. (2009) and Fabien et al. (2011).

1.3.6 Fluorescence and phosphorescence

Another viable solution for the temperature estimation, is to use a material having some properties which show a specific temperature dependence, dispersed into the fluid that enables the employment of specific optical techniques similarly to what done for the velocimetry measurements. Usually these materials are tracer particles having a comparable density to the working fluid. Furthermore, differently to the particles involved for the velocimetry, the particles involved for thermometric purposes have specific observable properties that change according to the surrounding temperature field, like their fluorescence intensity, hue or color. In the case of Laser Induced Fluorescence (LIF) technique, the fluid is seeded with a fluorescent dye (*e.g.* fluorescein or rhodamine B) that changes its fluorescence intensity as a function of the temperature (Crimaldi, 2008). Usually the exciting light is delivered from a laser system (Crimaldi, 2008), but nevertheless in simpler cases an arc mercury lamp can be equally involved (Ross et al., 2001). The main drawback of this method, is that the accuracy of this technique is strongly affected by the intensity of the light excitation and by the concentration of the seeding. Hence, an improvement of the LIF technique is given by the dual-emission LIF method (DeLIF), also known as two-color LIF method. In the DeLIF method two different dyes are involved instead of only one as happens in the standard LIF technique: one dye shows a temperature dependent behavior, while the second one is a temperature-insensitive dye and it is used for the normalization of the signal given by the temperature-sensitive one (Coppeta and Rogers, 1998; Sakakibara and Adrian, 1999, 2004; Someya et al., 2005). In addition, differently from the macroscopic applications, in microfluidic applications is not possible to illuminate the flow with a thin laser sheet, this means that the dye gives back a signal for all the depth of the illuminated volume (Motosuke et al., 2009). Nevertheless, in microfluidics, there could be situations in which is desirable to detect the temperature gradients along the depth direction of the sample, and this cannot be performed with a signal integrated along all the depth of the illuminated volume. Experiments in which both the velocity and the temperature distribution of a liquid in motion were detected, are reported in the works of Someya et al. (2011) and Vogt and Stephan

(2012). Someya et al. (2011) have performed an experiment in which they have measured the 2D velocity field and temperature distribution in a mixed natural convection regime driven by a combination of a Marangoni force and buoyancy in a rectangular tank. They used a temperature dependent luminophore that was incorporated into spherical particles with a diameter of 15 μm, while the working fluid was silicone oil with a kinematic viscosity of 10 cSt. In the work of Vogt and Stephan (2012), microcapsules, with diameters of the order of 9 μm and filled with two different dyes, were used for measuring the velocity field and the temperature distribution of a flow driven by natural convection and for a flow in a mini tube (inner diameter in the order of 1 mm). The authors applied a ratiometric LIF method for their analysis since only one dye was temperature sensitive while the second one showed a smaller temperature dependence. In the experiments carried by Vogt and Stephan (2012) the working fluid was a mixture of water (73 % in volume) and glycerin (27 % in volume).

The methods based on phosphor thermometry are similar to the LIF methods. The phosphor thermometry typically uses rare-earth ion centers in ceramic hosts as seeding. The advantage of the phosphor thermometry, with respect to LIF methods, is that it uses the decay mechanism of phosphor emission; this make this method insensitive to the non-uniform excitation and to the dye concentration (Khalid and Kontis, 2008). Phosphorescent alcohol solutions are currently involved in the so called Molecular Tagging Thermometry (MTT) technique with the aim to use molecular tracers for measuring simultaneously the flow temperature and velocity distribution. The term "molecular tagging thermometry" was coined by Thomson and Maynes (2001) in order to underline the similarity with the MTV technique for the velocity measurement. Differently from LIF techniques, MTT techniques rely on the phosphorescent emission instead of the fluorescent one. Hence, since the phosphorescent emission lasts for longer time than the fluorescence, only one kind of molecular dye have to be dispersed inside the working fluid for carrying out both temperature and velocity measurements of the flow. Thomson and Maynes (2001) used a phosphorescent dye dispersed in an aqueous solution for the measurements of the temperature and velocity of a laminar flow of water inside a channel with diameter of 5 mm. For carrying out these measurements, a series of coupled images with a short time delay between them have been acquired after laser excitation (UV laser) of the molecular dye. The temperature was measured from the first image by means of a previously performed calibration between the phosphorescence intensity and the temperature of the dye, while the velocity distribution was derived through the MTV method summarized in Section 1.2.6. With the adopted configuration the authors were able to measure the flow temperature between 23 °C and 53 °C with an uncertainty of 1 K. Nevertheless, they concluded that by reducing the working temperature range, the resolution of this technique can be increased both from an increasing of the CCD camera offset and from an increase of the fluid temperature. Hu and Koochesfahani (2006) underline that due to the long life of phosphorescent emission, the temperature sensitivity of the MTT technique

can be modified by changing the time delay between the excitation caused by the laser burst and the phosphorescent images acquisition. In this way the intensity change of the phosphorescence emission related to a temperature change of 1 K can become ten times higher to the temperature sensitivity of the fluorescence involved in LIF techniques.

1.3.7 Thermochromic Liquid Crystals (TLCs).

Thermochromic liquid crystals refers to the class of liquid crystals which change the reflected light color depending to their temperature. Basically, the changing of the reflected light depends on the inner structure of the TLCs that in its turn is influenced from their temperature. Typically, in correspondence of the lower temperature working point, TLCs reflect a red light while for the maximum temperature working point they reflect the blue light. The intermediate temperatures are detected by the reflection of green hue and by the related shades between red and green and blue and green. TLCs were usually produced either as microencapsulated beads used as fluid tracer or as an unsealed material used in thin film covers for surface temperature measurements. Only few works have shown the use of TLCs as suspended non-encapsulated particles in flows. The major advantage of unsealed TLC particles, is that the colors reflected from them are more brighter compared to the ones reflected from the microencapsulated TLCs. This means that the fluid temperature can be detected distinctly from each particle (typical diameters of the non-encapsulated particles are in the order of 10 - 13 μm) enabling an accurate estimation of the local temperature. The main drawback related to the non-encapsulated particles is their mechanical and chemical stability if subjected to certain external forces. Non-encapsulated TLC particles are destroyed when strong values of shear stresses are exerted on them and suffer from the exposure to oxidant components such air. In addition, the power intensity of the proper light sources and the weak sensitivity of RGB color cameras limit the employment of the TLC particles only to flows with low velocity (Segura et al., 2015). Nevertheless, the relative simplicity of the required experimental apparatus, coupled with the possibility to simultaneously perform three-dimensional velocity measurements using a single camera by means of the APTV method (see Section 3.7), makes TLCs thermography really interesting and its development could bring it to become the principal technique for local temperature measurements in microchannels. An extended discussion about the working principles of the TLCs and on the techniques utilized in order to correlate the temperature measurements with the colors reflected by TLCs can be found in the Chapter 3 of this dissertation, which is focused on the reliability of unsealed TLCs for temperature and velocity measurements inside microchannels.

1.3.8 Other optical techniques.

Other complex techniques have been proposed in order to measure the local temperature in microfluidic systems. For instance it can be mentioned the optical interferometry developed by Newport et al. (2004) and Garvey et al. (2007) and the Raman thermometry used by Vehring and Schweiger (1992); Davis et al. (1993) and Smith et al. (2006).

A summary of the main experimental techniques for the local temperature detection in microchannels is reported in Table 1.3.

Table 1.3: Summary of the experimental techniques for the fluid temperature detection.

Surface temperature measurements			
Technique	**Range**	**Typical uncertainty**	**References**
Thermocouples	0 - 200 °C	± 0.25 % FS	Morini et al. (2006)
µTFTCs	20 - 800 °C	Thermal Sensitivity: 40.4 µV/°C	Choi and Li (2007)
µRTDs	45 - 105 °C	Accuracy: ± 0.5 K	Wu et al. (2009)
SCs	0 - 100 °C	Accuracy: ± 0.5 K	Han and Kim (2008)

Flow temperature measurements			
Technique	**Range**	**Typical uncertainty**	**References**
IR	32 - 46°C	~ 8%	Liu and Pan (2016)
LIF	Microencapsulated fluorescent dyes:		
	20 - 50 °C	± 1.6 - 9.4 K	Vogt and Stephan (2012)
	Dissolved dyes:		
	21 - 25 °C	± 0.2 K	Sakakibara and Adrian (2004)
MTT	23°C - 53 °C	± 1.0 K	Thomson and Maynes (2001)
TLC	Microencapsulated TLCs:		
	36.3°C - 43.7 °C	± 0.4 - 2.4 K	Basson and Pottebaum (2012)
	Non-encapsulated TLCs, single temperature tracking:		
	24 °C - 37 °C	~ 5 %	Segura et al. (2013)

Chapter 2

A μPIV based method for the determination of the microchannel cross-section geometry

2.1 Introduction

As indicated by Cierpka and Kähler (2012), μPIV and its further developments, represents the state of the art on the experimental measurements of the velocity field of liquid flows in microchannels (Sinton, 2004; Lindken et al., 2009; Cierpka and Kähler, 2012). The working principle of the μPIV technique is basically the same of the PIV technique (Adrian, 1991) used for velocity measurements in channels with standard dimensions, but in μPIV, the use of an optical microscope with magnification lenses becomes essential due to the reduced dimensions of the system and tracer particles (Sinton, 2004; Lindken et al., 2009). The introduction of an objective lens along the optical path, changes the way in which the fluorescent particles dispersed inside the working fluid are detected. The laser beams used to illuminate the sample produces a volumetric illumination of the whole region under investigation, differently to what happens for macroscopic measurements, in which, a laser sheet is used in order to detect the displacement of the tracer particles in the time interval selected (Meinhart et al., 1999, 2000a;

This chapter is based on the publications:
Puccetti G., Pulvirenti B. and Morini G.L., 2014, Experimental determination of the 2D velocity laminar profile in glass microchannels using μPIV, *Energy Procedia*, **45**:538-547. http://dx.doi.org/10.1016/j.egypro.2014.01.058

Puccetti G., Pulvirenti B. and Morini G.L., 2014, Use of the μPIV technique for an indirect determination of the microchannel cross-section passage geometry, *IOP: Confernce Series*, **501**(1):012027. http://dx.doi.org/10.1088/1742-6596/501/1/012027

Rossi et al., 2012). In µPIV, the plane in which the tracer particles are detected has a fixed thickness linked to the focal plane of the lens. For this reason, with this system also the particles out of the focal plane contribute to the signal acquired in a single image without to add significant information (Meinhart et al., 2000a; Olsen and Adrian, 2000b). The thickness of the detection plane takes the name of "Depth of Correlation" (DOC) and it depends by the characteristics of the objective lens and from the features of the seeding particles. (Meinhart et al., 2000a; Olsen and Adrian, 2000b; Bourdon et al., 2004, 2006; Rossi et al., 2010a, 2012). The correct evaluation of DOC is an open question as underlined by Rossi et al. (2012); they underline that a correction in the definition of the DOC must be considered if the experimental apparatus involved for µPIV measurements uses objective lenses with high numerical aperture (NA).

Historically, the first work in which the µPIV technique was applied for the determination of the velocity field of a fluid inside a microchannel, is due to Santiago et al. (1998) where the Hele-Shaw flow around an elliptical cylinder with a main diameter of 30 µm was experimentally evaluated. The authors employed polystyrene particles with a nominal diameter of 300 nm as tracers and used a mercury lamp as continuous illumination system. Meinhart et al. (1999) performed a similar experimental analysis by using a double pulsed Ng:YAG laser as illumination source. Coherently to the selected illuminating system, fluorescent particles with a nominal diameter of 200 nm having a peak excitation wavelength of 540 nm were used for the analysis of the flow field inside a rectangular microchannel with a cross-section of 30 µm × 300 µm. Using a double pulsed laser light source, the exposure time can be reduced in comparison to the employment of continuous illumination system like mercury or halogen lamps. In fact, with a continuous light system, a CCD camera with a mechanical or electronic shutter must be involved to acquire back-to-back images and this limits the maximum velocity of the investigated flow. For this reason, the double pulsed monochromatic laser illumination and in particular the Nd:YAG laser became the standard illuminating source in most µPIV applications as underlined by Wereley and Meinhart (2005).

Starting from the work of Santiago et al. (1998) a lot of efforts were made by the researchers in order to further develop this technique (Lee and Kim, 2009). Klank et al. (2002) used the µPIV technique to reconstruct the three-dimensional flow field inside a silicon microchannel having dimensions of 600 µm x 60 µm (width and depth) by means of 2D velocity measurements obtained on 5 parallel planes at different channel depths. Each plane was respectively acquired at a distance of 10 µm from each other. In order to enhance the quality of their results, Klank et al. (2002) performed a stereoscopic recombination of the µPIV data.

Shinohara et al. (2004) proposed a study in which the µPIV measurements were performed by involving a high-speed camera with a CMOS sensor. In his work, the authors used particles with a diameter of 1 µm illuminated by a Nd:YAG CW laser and dispersed into a deionized water flow in counter-current direction with respect to a flow of butyl acetate. With the adopted experimental configu-

ration, Shinohara et al. (2004) were able to analyze experimentally the dynamic phenomena at the interface between the two fluids.

Lindken et al. (2006) applied a stereoscopic system to the conventional μPIV apparatus in order to perform 3D stereoscopic μPIV measurements. In this way the authors were able to collect the information of all the three velocities components of two water flows through a T micro-mixer. Particular care was taken by the authors during the calibration process of their apparatus.

Zheng and Silber-Li (2008), showed quantitative results on the comparison between theoretical velocity profiles and experimental μPIV measurements obtained in a microchannel with low aspect ratio (β= 0.35, width and depth respectively of 54.0 μm and 19.1 μm). The authors evaluated the 2D velocity field in 14 different planes along the channel depth and reported an average relative deviation between experimental results and theoretical data of the order of 1% for the planes in the middle of the channel, up to 10% for planes close to the bottom glass wall and an average relative deviation up to 5% for planes close to the top PDMS wall.

The works reported previously, represent just some examples of the development of the μPIV over the last years. Further different application methodologies of the μPIV technique can be found in the works of Cummings (2000); Ovryn (2000); Tseng et al. (2002); Park et al. (2004); Liu et al. (2005); Augustsson et al. (2011); Cierpka et al. (2012); Anastasiou et al. (2013); Ashwood et al. (2015) and more in general in the reviews of Lindken et al. (2009) and Lee and Kim (2009). μPIV applications for measurement in micro T-junctions were additionally reported in Fujisawa et al. (2006); Hoffmann et al. (2006); Lindken et al. (2006)and van Steijn et al. (2007). For a further and deeper reading about the algorithms and correlations used in μPIV applications the readers are invited to refer to the works of Meinhart et al. (2000b); Olsen and Adrian (2000a); Wereley et al. (2002) and Meinhart and Wereley (2003)

2.2 Aim of the work

In microfluidics, the reduction of the scale dimensions improve the surface-to-volume ratio and this fact makes the surface effects more relevant in comparison to the volume effects (Bruus, 2008; Tabeling, 2005). For this reason, the shape and size of the cross-section of a microchannel, play an important role on the fluid-dynamic behavior (*i.e.* pressure drop) and an incorrect evaluation of the inner geometry of the microchannel could lead to a disagreement between theoretical results and experimental measurements (Lee et al., 2005). However, the evaluation of the real inner geometry inside a microchannel is not a trivial point, as also reported by Morini et al. (2011) and still represents a research goal in microfluidics.

Stone et al. (2002), showed an application of the µPIV technique for the estimation of the inner shape of a microchannel. The authors, used the comparison between the analytical solution of the flow field and their experimental results obtained with µPIV to find the position of the walls. In order to refine the comparison between experimental measurements and analytical data, a second order polynomial function was used in order to fit the experimental points close to the walls. Then, the recognition of the wall position was achieved through the assumption of zero velocity at the solid boundary: in this way, the point in which the velocity vanishes, represents the point in which the wall is located.

Silva et al. (2009) adopted a similar methodology for the determination the irregular inner cross-section of a microchannel realized in PMMA. For the reconstruction of the velocity profile close to vertical walls, Silva et al. (2009) fitted the experimental results obtained via µPIV measurements, with a second order polynomial. The determination of the wall position was obtained with the assumption of no-slip boundary condition by finding the polynomial roots.

Rossi et al. (2010b) have reported a study on the main parameters involved for the reconstruction of the wall topology through an inverse use of the common µPIV technique. The authors used seeding particles with a nominal diameter of 560 nm and carried out their studies inside a microchannel with a rectangular cross-section of 127 µm x 2500 µm. Rossi et al. (2010b) concluded that the accuracy of this kind of measurement, is mostly related to the accuracy of the detection of the displacement of the tracer particles, that is, in its turn, essentially dependent from the depth of the measurement volume and the exposure time delay.

The aim of this section, is to show a methodology in which the µPIV technique can be utilized in order to detect the real shape of the inner cross-section of a microchannel. The methodology showed in this section, is in principle similar to the reconstruction techniques previously mentioned (Stone et al., 2002; Silva et al., 2009). Even if the methodology described here, differs from the aforementioned works for the way in which the cross-section is reconstructed. In particular, the methodology proposed in this section relies on the minimization

of the local difference between the velocity profile experimentally acquired and the velocity profile obtained from the numerical solution of the Navier-Stokes equation by varying the cross-section geometry. In this way, no further fitting of the experimental points close to the walls is required.

Rectangular microchannels are very popular in microfluidics, however, the manufacturing of the microchannel can introduce a series of irregularity on the geometry of the channel cross-section which could have a significant effect on the velocity profile, especially for Stokes flows in micropassages. As mentioned in Section 1.1, the real cross-section geometry can be accurately checked by using scanning electron microscope (SEM) analysis. With this technique is possible to achieve a high spatial resolution also for very small geometries. However, one of the major disadvantage of this technique is that inner geometries cannot be detected without destroying the device, since SEM analysis requires a direct sight of the channel cross-section under investigation. SEM analysis is very powerful when a direct optical access there exist; on the contrary for sealed channels, like in the case of commercial microchannels, this technique can be applied only by destroying the device. In order to overcome this problem, in this section it is proposed that an inverse use of μPIV technique can allow a reconstruction of the channel geometry without to destroy the channel. Specifically, the focus of this work is centered on commercial microchannels realized through a laser etching of substrate made by fused silica glass.

The chapter is structured as follows: first of all, the experimental apparatus used is presented, then, the developed procedure is described. The application of the procedure to a straight microchannel is presented in Section 2.5.1 where the experimental reconstruction of the velocity field inside the channel and the comparison with the SEM analysis data are discussed. In Section 2.5.3 the analysis is repeated for a T-junction and a comparison with results indication obtained via confocal fluorescence microscopy for the same micro T-junction is shown.

2.3 µPIV Experimental Apparatus

The lay-put of the µPIV apparatus used in the tests described in this section is shown in fig. 2.1.

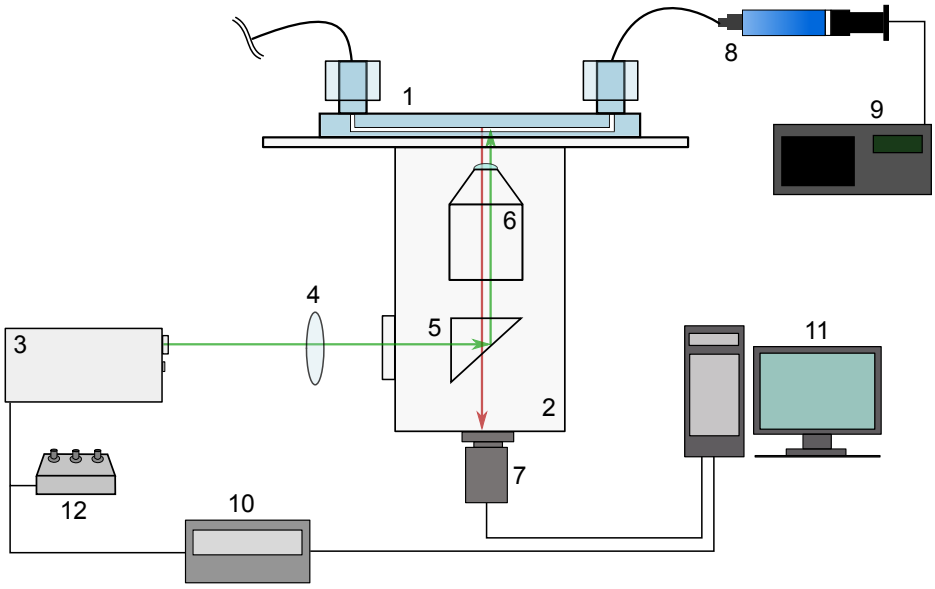

Figure 2.1: Layout of the experimental apparatus: 1) Microchannel 2) Inverted microscope 3) Laser 4) Beam-forming optics 5) Dichroic mirror 6) Objective lens 7) CCD Camera 8) Syringe containing the working fluid seeded with fluorescent particles 9) Syringe pump 10) Synchronization unit 11) Software unit 12) Remote laser control. *(dimensions not in scale).*

2.3.1 Test section

The glass microchannel under investigation (1 in fig. 2.1) is placed upon an inverted microscope (2, *Nikon* Eclipse TE 2000-U). The microchannel was manufactured through a laser etching in a high quality fused silica glass and sealed with the same material through a thermal bonding. As declared by the manufacturer, the material used for built the microchannels resulted to be transparent from the deep-ultraviolet to the mid-infrared light. The glass chip is 2" long (50.8 mm) and 1" wide (25.4 mm) (see fig. 2.2) while the straight channel is characterized by a squared cross-section with a side of 300 µm and the length of the channel is almost 38 mm.

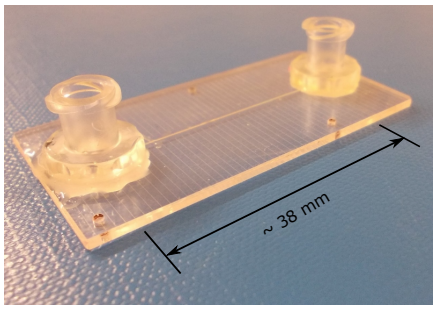

Figure 2.2: Picture of the straight microchannel under investigation.

2.3.2 Illuminating system, optical path and fluorescent seeding

As stated in the introduction of this chapter, in µPIV applications a pulsed monochromatic laser light is usually adopted in order to illuminate the fluorescent particles dispersed in the working fluid (Wereley and Meinhart, 2005; Lindken et al., 2009). Also in the test rig of fig. 2.1 the illuminating source is provided by a double pulsed Nd:YAG monochromatic ($\lambda = 532$ nm) laser (3, *Litron Laser nano s 30-15*). Each pulsation has a duration of 5 ns, while the time delay between two pulses can be varied and ranges from hundreds of nanoseconds up to few seconds. The light is delivered to the optics of the inverted microscope via a system of lenses (4) that modifies the laser beam in order to fill correctly the back side of the objective lens. The beam-forming optics (4a,4b,4c), as shown in fig. 2.3 and fig. 2.4, is composed by a double-concave lens, a diffuser plate and a double-convex lens. The two rounded lenses have the purpose to correctly collimate a laser beam with objective lens, while the the diffuser plate is used to brake the coherence of the light avoiding possible speckle effects. This system of lenses, is required when the laser beam is directly sent to the optics of the microscope without using any optical fiber connections. Then, the illuminating laser beam ($\lambda = 532$ nm) is reflected upwards by a dichroic mirror (5) and reaches the microchannel after passing through the objective lens (6). The objective of the microscope (*Nikon Plan APO*) is equipped with an air immersion lens with a magnification M = 20 × and numerical aperture NA = 0.75.

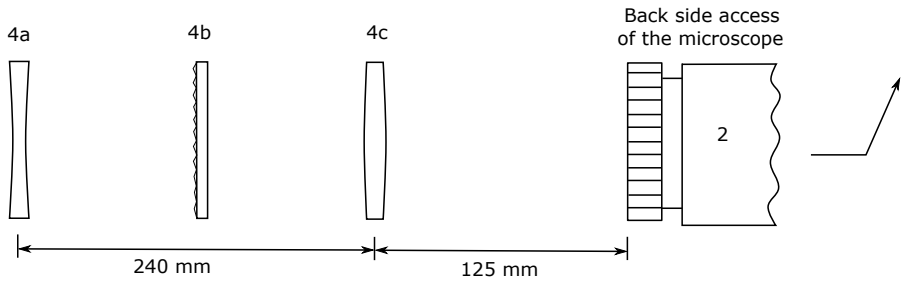

Figure 2.3: Drawing of the involved beam-forming lenses.

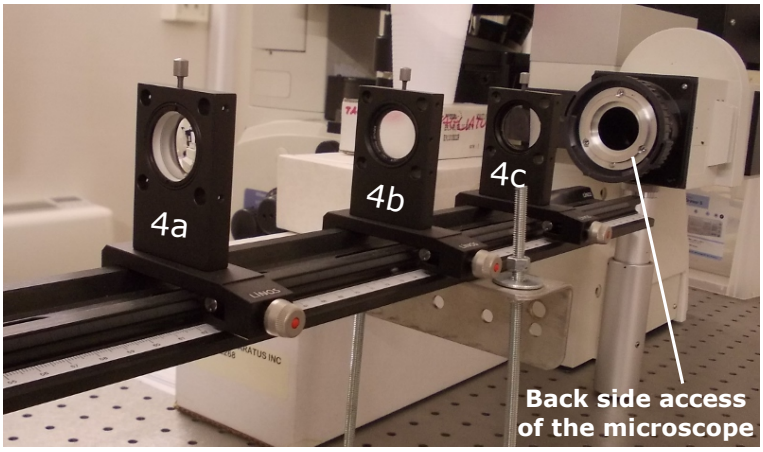

Figure 2.4: Picture of the involved beam-forming lenses.

Since the detection of the particles' location relies on the acquisition of the fluorescent signal emitted from these particles, the wavelength absorption range of the selected fluorescent particles have to match the light wavelength emitted by the laser. Therefore, based on the wavelength of the laser, particles (*Invitrogen Molecular Probes FluoSphere*) with a diameter of 1.0 µm, with an orange coloration, a carboxylate coating and peaks of excitation \ emission equal to 540 nm \ 560 nm are selected. The fluorescent seeding dispersed into the working fluid, absorbs the incoming laser light and re-emits a light with a higher wavelength (emission peak λ_{em} = 560 nm). The emitted light, therefore, crosses a dichroic mirror (5, *Nikon TRITC HYQ* EX 540/25, DM 565, BA 605/55) and is recorded by a sensitive large-format interline-transfer CCD camera (7, *PCO Seniscam QE*). The interline transfer feature of the CCD camera allows to record two subsequent frames, within an adjustable time-delay which ranges from thousands of seconds up to hundreds of nanoseconds.

The working fluid seeded with the fluorescent particles is stored in a syringe (*Hamilton Gastight #1010*) (8) with a volume of 10.0 ml. The pressure required to push the working fluid through the microchannel is supplied by a syringe pump (*Harvard Apparatus PHD 4400*) (9). The laser, the CCD camera and the software unit (11) are connected to a synchronization unit (*Dantec Dynamics Flow Map 1501*) (10), that provides the correct tuning between the laser bursts and the acquisition of the images. The intensity of the two lasers and the repetition rate of laser bursts are controlled via a remote laser controller (12).

Pictures of the experimental apparatus can be seen in in fig. 2.5 and fig. 2.6. A summary of the main technical feature of the components of the experimental apparatus described above is given in Table 2.1.

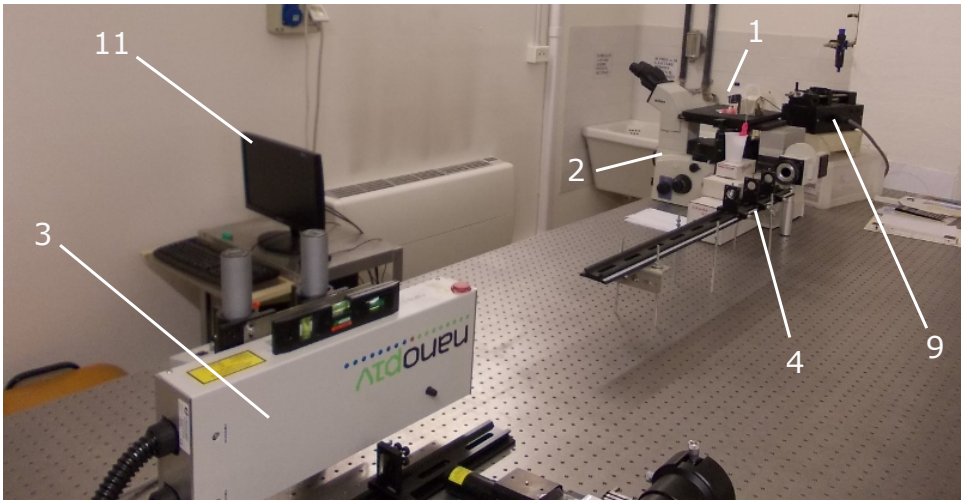

Figure 2.5: The experimental apparatus.

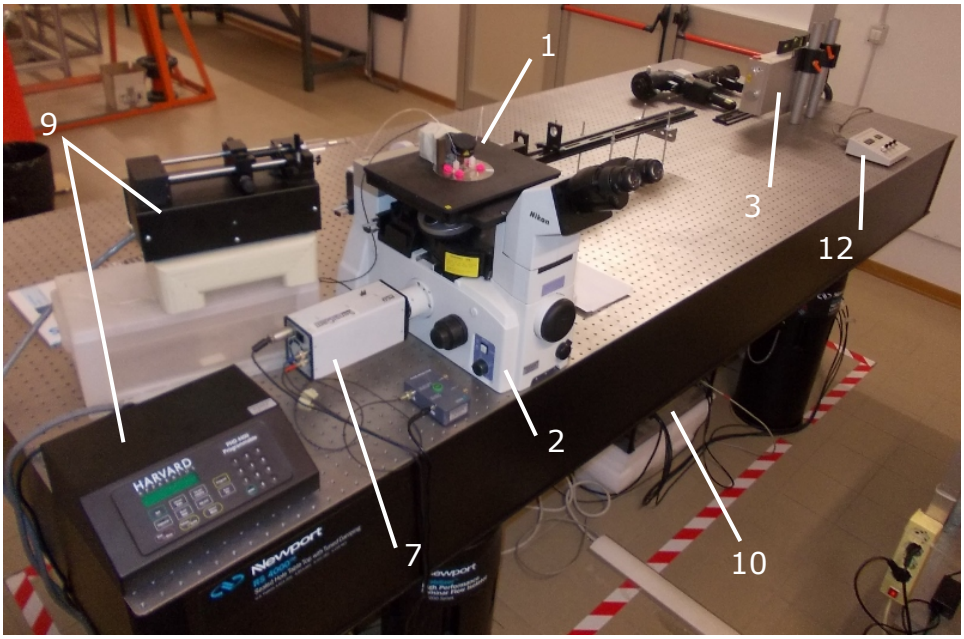

Figure 2.6: The experimental apparatus.

Table 2.1: Characteristics of the main components of the experimental test-rig.

Ref.	Component	Description
1	Microchannel	Fused Silica Glass Straight Channel: 300 × 300 μm^2, L = ~ 38mm T-junction: 300 × 300 μm^2, L = ~ 38 mm, ~ 13 mm
2	Inverted Microscope	Eclipse TE 2000-U (*Nikon*)
3	Laser	*Litron* Laser nano s 30-15, LPU 450 Nd:YAG, λ= 532 nm Max output: 30 mJ Liquid cooling
4a	Double-concave lens	*Edmund Lens* NT47-917 R_1 = -R_2 = -39.78 mm EFL = -25 mm Coating: Vis 0° Diameter = 25 mm
4b	Diffuser Plate	*Edmund Lens* NT47-991 Diffusing Angle = 1° Diameter = 25 mm
4c	Double-convex lens	*Edmund Lens* NT32-718 R_1 = -R_2 = 103 mm EFL = 100 mm Coating: M_gF_2 Diameter = 25 mm
5	Fluorescent system filter	*Nikon TRITC HYQ* Excitation Filter = 530 - 560 nm Dichroic Mirror = 575 nm Barrier Filter = 595 - 650 nm
6	Objective lens	Nikon Plan APO Magnification = 20 × Numerical Aperture = 0.75
7	CCD Camera	PCO Sensicam QE Resolution = 1376 × 1040 pixel Dynamic range: 12bit
9	Syringe Pump	*Harvard Apparatus* PHD 4400 Programmable Minimum flow rate = 0.0001 μl h^{-1} Maximum flow rate = 220.82 ml min^{-1} Uncertainty ± 0.35%
10	Synchronization Unit	*Dantec Dynamics* Flow Map 1501
-	Seeding particles	*Invitrogen* Molecular Probes FluoSphere Diameter = 1.0 μm Orange fluorescent coloration Coupling surface: Carboxylate Ex: 540 nm, Em: 560nm

2.3.3 Spatial Resolution

A critical aspect of the velocimetry techniques for microchannels is the minimum spatial resolution achievable. In µPIV the Eulerian scheme is used in order to associate a velocity vector to a detection area called interrogation cell (or window). As a consequence of this, smaller dimensions of the interrogation cell correspond to higher obtained spatial resolution. However, the dimensions of the interrogation cell cannot be decreased as desired since the velocity vector associated to the cell is coupled through a cross-correlation process based on the displacement of the fluorescent particles inside the cell during the time interval between two coupled images. For this reason, in order to obtain reliable measurements, a minimum number of particles must be contained within the cell and the maximum displacement of these particles cannot be larger than of 1/4 of the cell dimension (Westerweel, 1997). These limitations make constraints to the dimension of the dispersed particles, to their resolution obtained through the optics of the microscope and to the minimum dimension of the interrogation cells.

The minimum size of a point-wise light source obtained by means of a fixed circular magnification system (M > 1) can be expressed as follows (Olsen and Adrian, 2000a; Wereley and Meinhart, 2005):

$$d_s = 2.44\,(M+1)\,\frac{\lambda}{2\mathrm{NA}} \tag{2.1}$$

where M is the magnification of the objective lens, NA is its numerical aperture and λ is the wavelength of the emitted light. The different values of the diffraction size of a point-wise light source as a function of the characteristics of the optical devices are reported in Tab. 2.2, in which, d_s is calculated for different combinations of M and NA for a fixed wavelength of the particle light equal to 560 nm which is the wavelength of the light emitted by the fluorescent particles utilized in this study. In the analyses reported in this chapter, an objective lens with a magnification M of 20 × and a numerical aperture NA of 0.75 is involved (last columns of the Table 2.2, 2.3 and 2.7).

Table 2.2: Diffraction size of a point-wise light source in relation to the optical characteristics, in the last column are reported the results for the objective lens employed in the present experimental apparatus for a λ = 560 nm.

M	**10**	**20**	**60**	**20**
NA	**0.25**	**0.4**	**1.4**	**0.75**
d_s (µm)	30.1	35.7	29.8	19.1
d_s/M (µm)	3.0	1.8	0.5	1.0

The diameter of a fluorescent particle recorded by the CCD camera, can be calculated following the statements of Adrian and Yao (1985) as a function of the magnification M and of the diameter of the fluorescent particles used as tracers (d_p):

$$d_e = \left[d_s^2 + M^2 d_p^2 \right]^{1/2} \tag{2.2}$$

Results in terms of the ratio between the dimension of the diameter of the particles and the magnification of the lens (d_e/M) are reported in Tab. 2.3 for different typologies of objective lenses and for different sizes of the dispersed particles.

Table 2.3: Actual diameter dimension (d_e/M) of the image of a fluorescent particle with a diameter of d_p in relation to the optical characteristics, in the last column are reported the results for the objective lens employed in the present experimental apparatus. The dimensions are in µm.

	Objective lens characteristics (M / NA)			
	10	**20**	**60**	**20**
d_p	**0.25**	**0.4**	**1.4**	**0.75**
0.5	3.0	1.9	0.7	1.0
1.0	3.2	2.0	1.1	1.4
2.0	3.6	2.7	2.1	2.2

From the results reported in Tab. 2.3 is clearly visible as the employment of a lens with a low value of M and a low numerical aperture, determines an increase of the diffraction effect on the dimension of the particle. On the contrary, the use of objective lenses with high magnifications and numerical apertures, reduces the diffraction effects and the dimensions of the recorded particles becomes closer to their real dimensions. The effect of the numerical aperture of the lens can be deduced from Tab. 2.3 by the comparison of results obtained for a lens with a magnification M = 20 × and different numerical apertures, *i.e.* NA = 0.4 and NA = 0.75. For example, by considering the dimension of the particles used in this work (*i.e.* d_p = 1.0 µm), with an objective lens having a magnification M = 20 × and a numerical aperture NA = 0.4, the effective dimension of the particle acquired by CCD is equal to 2.0 µm, while the dimension of the same particle obtained through a lens with the same magnification but with a higher numerical aperture can be reduced to 1.1 µm for NA = 60. Therefore, it can be concluded that in order to properly gain a bright signal from particles with dimensions of the order of 1 µm and below it, and to increase the spatial resolution of the µPIV technique, objective lenses with a high magnification and with a high numerical aperture are generally needed.

Finally it can be stated that, when the particles are detected by using at least 3-4 pixels of the CCD sensor, the uncertainty associated to the position of the cross-correlation peak is in the order of 10 % of the particles diameter (d_e)

acquired by the camera. With reference to the setup and to the particles used in this work, the uncertainty associated to the cross-correlation peak position can be estimated in the order of about 138 nm, which is one order of magnitude below to the minimum dimension visualized by the microscope.

2.3.4 Depth of Correlation

Another important parameter for the correct evaluation of the accuracy of the velocity data obtained by using the µPIV technique in this work, is the depth of correlation DOC (cited in literature also with z_{corr} or $2z_{corr}$) linked to the experimental setup of the µPIV apparatus presented here. The DOC is a direct consequence of the volume illumination utilized for the µPIV measurements and depends on the optical components involved in the experimental apparatus (Lindken et al., 2009; Silva et al., 2009; Rossi et al., 2012). More precisely, the depth of correlation gives an indication about the depth of the illuminated volume in which the fluorescent particles are able to give a contribution to the correlation procedure (Olsen and Adrian, 2000b). If the particles' dimension and consequently the size of the interrogation cell determines the spatial resolution of the in-plane measurements, the DOC determines the spatial resolution of the out-of-plane velocity measurements (see fig. 2.7).

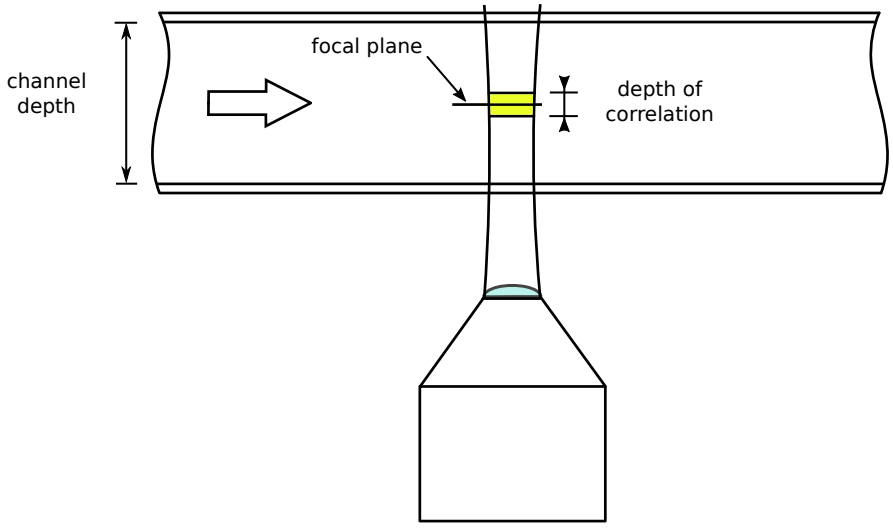

Figure 2.7: Schematic sketch of the depth of correlation due to the volume illumination.

The first analytical expression of the depth of correlation for µPIV experiments was derived in 2000 by Olsen and Adrian (2000b). Starting from this first work, the accurate evaluation of the DOC was thoroughly studied by different research groups that proposed different improvements or modifications of the original formulation (Olsen and Adrian, 2000b; Meinhart et al., 2000a; Bourdon et al.,

2004, 2006; Rossi et al., 2012).

Coherently with the formulation proposed by Bourdon et al. (2006) the depth of correlation can be written as:

$$\mathrm{DOC} = 2\left\{\frac{\left(1-\sqrt{\epsilon}\right)}{\sqrt{\epsilon}}\left[\frac{n_0^2 d_p^2}{4\mathrm{NA}^2}+\frac{5.95(M+1)^2\lambda^2 n_0^4}{16M^2\mathrm{NA}^4}\right]\right\}^{0.5} \tag{2.3}$$

where ϵ is a threshold parameter that takes into account the maximum contribution given by out-of-focus particles with respect to the in-focus particles in the correlation process; generally, ϵ is taken equal to 0.01. d_p is the diameter of the fluorescent particle, λ is the wavelength of the light emitted from the particles, n_0 is the refractive index of the medium in which the lens is immersed (in this case the objective is an an air immersion lens and n_0 is equal to 1), M is the lens magnification and NA is its numerical aperture.

In order to take into account the effect of the refraction introduced by the medium in which the particles are dispersed, Rossi et al. (2012) proposed to multiply the expression of the depth of correlation by the ratio between the refractive index of the working fluid n_w (usually water, n_w = 1.333) and the refractive index of the immersion medium of the lens n_0:

$$\mathrm{DOC} = \frac{n_w}{n_0}\left\{\frac{\left(1-\sqrt{\epsilon}\right)}{\sqrt{\epsilon}}\left(\frac{n_0^2}{\mathrm{NA}^2}-1\right)\left[d_p^2+1.49\,\lambda^2\left(\frac{n_0^2}{\mathrm{NA}^2}-1\right)\right]\right\}^{0.5} \tag{2.4}$$

In Table 2.4 are reported different values of the DOC, calculated either with Eq. (2.3) and Eq. (2.4), achieved through the use of different fluorescent particles and objective lenses. The results are obtained using a value of ϵ = 0.01 and particles with an emitting light of about 600 nm (orange particles). The objectives with a magnification of M = 10 × and M = 20 × have an air immersion lens (n_0 = 1) while the objective with a magnification of 60 × have a higher NA value, typical of oil immersion lenses (n_0 = 1.51).

For the experimental configuration involved in this work, the evaluation of the DOC gives a value of around 6 µm by using Eq. (2.3) and around 4 µm with Eq. (2.4).

From the data reported in Tab. 2.4 is clearly visible as through the correlations reported, the employment of an objective lens with a higher numerical aperture gives smaller values of the DOC for a fixed dimension of the particle diameter. However, Rossi et al. (2012), evaluated the accuracy of the theoretical calculation of the DOC using the correlation reported previously in Eq. (2.4) concluding that it usually underestimates the actual DOC, especially when an objective lens with a high numerical aperture is involved. Therefore, it is possible that the actual DOC related to the µPIV experimental apparatus used for this work is larger than the one showed here. This is an important feature to take into account when the experimental results will be analyzed.

Table 2.4: Depth of correlation as a function of different diameters of fluorescent particles and optical characteristics of the objective lens. The wavelength of the light emitted from the particles is set equal to 560 nm, the objective lenses with magnification of 10 × and 20 × are supposed to be immersed in air, while the lens with M = 60 × is taken as an oil immersion lens (n_0 = 1.51). In the last column are reported the results for the objective lens employed in the present experimental apparatus. The dimensions are in µm.

		Objective lens characteristics (M / NA)			
		10	**20**	**60**	**20**
	d_p	**0.25**	**0.4**	**1.4**	**0.75**
Results	0.5	36.6	14.0	2.9	4.3
with	1.0	38.0	15.4	4.0	5.5
Eq. (2.3)	2.0	43.3	20.1	6.9	8.9
Results	0.5	41.7	15.2	0.6	2.8
with	1.0	43.8	17.0	1.1	4.1
Eq. (2.4)	2.0	51.4	23.3	2.2	7.4

2.3.5 Time delay between a couple of images

In order to obtain reliable results, the maximum particles displacement must not exceed a quarter of the size of the interrogation cell. Following this empirical rule, for a fixed dimension of the interrogation cell, *i.e.* the in-plane spatial resolution required, the time delay between two subsequent images $\Delta\tau_s$ used for the cross-correlation procedure, can be selected according to the flow rate investigated by using the following relationship (Morini, 2008b):

$$\Delta\tau_s = \frac{l^*}{f\, W_{\max}} \tag{2.5}$$

where l^* is the minimum dimension of the interrogation cell along the flow direction, $W_{\max}$ is the maximum velocity of the particles and f is a coefficient between 2 and 4 which takes into account the possible overlap between the interrogation cells.

For the analyses shown in this chapter, due to the flow rates involved (in the range of 8 ml/h and 10 ml/h), the time delay between the coupled images is imposed equal to 50 µs.

2.3.6 Effects of the Brownian motion

The working principle of the µPIV relies on the ability of tracer particles to follow faithfully the fluid motion; for this reason particles with diameters below the micron are usually employed. However, even if tracers with smaller diameters enables higher resolution, when the particles' diameter is reduced below the micron, the random collision between the tracer and the fluid molecules could introduce bias errors due to the random thermal motion of the particles. This effect is known as Brownian motion and for the µPIV applications, the uncertainty about the particles' position due to the Brownian motion can expressed as (Santiago et al., 1998):

$$\epsilon_x = \frac{1}{W}\sqrt{\frac{2D}{\Delta\tau_s}} \qquad \text{where} \qquad D = \frac{kT}{3\pi\mu d_p} \tag{2.6}$$

where W is the velocity of tracer particles, k is the Boltzmann's constant (k = 1.38 10^{-23} J/K), T is the local fluid temperature expressed in Kelvin and μ is the dynamic viscosity of the fluid.

This effect in practice cannot be neglected when the size of the particles is below 0.5 µm and the flow velocity is below 1 mm/s (Wereley and Meinhart, 2005). Hence, when particles in the order of hundreds of nanometers are used for tracing flows with low velocity, one way to overcome the effect of Brownian motion is to increase the number of particles that contribute to the cross-correlation procedure. This can be achieved by increasing the number of couple of images that are used for the time-averaged cross correlation.

For the µPIV application shown in this dissertation, the working fluid is water, the seeding particles have a diameter of 1 µm and the average fluid velocity is between 0.03 m/s - 0.04 m/s; a time-averaged cross-correlation made on 500 couples of images is adopted. It can be concluded that the effect of the Brownian motion on the detection of particles position in the present study can be considered negligible.

2.4 Methodology

2.4.1 Mixture dilution

An important parameter to be considered, is the concentration of the seeding particles in the working fluid. As highlighted by Lindken et al. (2009), there is an optimal value of the dispersion of the fluorescent tracer particles: the particle concentration must be larger than a minimum value in order to obtain a good signal from each interrogation cell, but at the same time, the concentration must not to be too high in order to avoid as much as possible the presence of an unwanted bright noise. Therefore, before to start with experiments, the optimal value of the fluorescent particles concentration in the working fluid was determined. From the preliminary analysis of the noise of the images acquired, a volume (c) of 25 µl of original mixture per 10.0 ml of working fluid (deionized water) is found to be the optimal value of the seeding concentration. It is possible to calculate the resulting concentration (C) of the particles in the medium as follows:

$$C = \frac{V_{p,tot}}{V_{sol}} \tag{2.7}$$

where:

$$V_{p,tot} = \frac{4}{3}\pi N \left(\frac{d_p}{2}\right)^3 \tag{2.8}$$

$$N = n_p c \tag{2.9}$$

$V_{p,tot}$ is the total volume of the tracer particles and V_{sol} is the total volume of the solution. Here, V_{sol} is taken equal to the total volume of the deionized water since the total volume of particles $V_{p,tot}$ is five order of magnitude lower than V_{sol}. The total number of the fluorescent particles dispersed into the working fluid can be estimated as product between n_p, the number of microsphere per volume of aqueous suspension (usually expressed in particles per ml), and c, the volume of aqueous suspension in which the particles are dispersed. In equation (2.8) d_p represents the particles diameter.

All the significant parameters of the solution are summarized in Tab. 2.5 together with the diameter and the peaks of excitation λ_{ex} and emission λ_{em} of the selected fluorescent particles.

2.4.2 Volume flow rate and Reynolds number

The flow rates imposed during the tests have been selected coherently with the setup of the experimental apparatus. More in detail, the optimal value of the flow rate of the working fluid is linked to the concentration of the seeding, to the time delay between the laser pulses and to the size of the interrogation cells.

As stated by Westerweel (1997) and Silva et al. (2009), the displacement of the fluorescent particles between two recorded images must not exceed a quarter of the length of the interrogation cell. In addition, the number of in-focus particles in each interrogation cell have to be enough in order to give a reliable value of the velocity vector associated to the interrogation cell (Silva et al., 2009). Therefore, on the basis of the laser time pulse imposed, it is possible to demonstrate that with the apparatus described in the previous section, a good spatial resolution and a good accuracy in terms of velocity values for water flows is characterized by Reynolds numbers lower than 10. This range of Reynolds numbers is typical for microfluidics applications with liquid flows (*i.e.* lab-on-a-chip).

2.4.3 Determination of the bottom wall and top wall position

Before to start with the velocity measurements it is important to individuate clearly the position of the walls of the channel perpendicular to the light path (bottom and upper walls). In order to individuate the bottom wall, the particles stuck to the wall, are used. Once detected the particles stuck, the focal plane is moved upward and downward in order to individuate the position of the focal plane in correspondence of which the bright spots generated by the fluorescent beads becomes smaller (minimum diameter) and brilliant (maximum brightness). When these conditions are reached, the stuck particles are correctly in-focus and with them, with a good approximation, the bottom wall. It is worth to notice that smaller the particles are, compared to the depth dimension of the microchannel, more the detection of the bottom wall is accurate. The same procedure is repeated for the determination of the position of the upper wall. It is important to underline that the distance between the bottom and upper walls determined by means of the displacement of the focal plane must be corrected by taking into account the water refractive index. In this case, the distance determined by moving the focal plane has been multiplied by the water refractive index (*i.e.* $n_w = 1.333$) in order to obtain the real distance between the walls of the channel. Once fixed the two position of the horizontal walls, the position of the intermediate planes can be easily derived with respect to these references.

Table 2.5: Characteristics of fluorescent particles and seeding concentration used in tests.

d_p	n_p	λ_{ex}	λ_{em}	c	N	$V_{p,tot}$	V_{sol}	C
(µm)	(part./ml)	(nm)	(nm)	(µl)	(#)	(µl)	(ml)	(ppm)
1.0	2.7×10^{10}	540	560	25	6.75×10^{8}	0.35	10	35.33

2.4.4 Experimental determination of velocity profiles

Each experimental campaign starts with the preparation of a new mixture as described in the Section 2.4.1. A fresh dilution of fluorescent particles inside the working fluid is required since due to a repeated usage of the mixture coupled with a long resting time of it, the particles tend to coalesce all together creating a thread of seeding particles. The thread of fluorescent particles can get stuck to the microchannel walls, giving consequently a contribution to the unwanted bright noise of the images. A picture of threads of fluorescent particles dispersed into the working fluid after a long resting time is shown in appendix A (fig. A.1).

The measurement of the velocity profile is carried out for several planes obtained by moving the focal plane of the microscope between the bottom and the upper walls. For each plane, a series of couple of images is recorded with a fixed time delay of 50 μs. Also the optimal number of the coupled images have been determined. This is done by taking into account that through an increasing of the couple of the averaged images, it is possible to increase the number of in-focus particles for each interrogation cell without increase the bright noise coming from a higher dispersion of fluorescent beads inside the working fluid. Since the cross-correlation procedure for a large series of images entails an increasing computing time, the best number of the acquired images has been selected as tradeoff between accuracy and computing time. A series of 500 coupled images for the average correlation of the couple of images acquired for each plane has been chosen. All the images are firstly acquired in a gray scale as shown in fig. 2.8. In order to enhance the accuracy of the cross-correlation process the images are pre-processed. First of all a mean image is created by averaging the brightness value of each pixel in each image. Then, the obtained mean image is subtracted to each image acquired in gray scale. With this subtraction a double outcome is achieved: firstly, the contrast between the background and the bright spots is increased and in second instance, if some constant bias error is present (like the signal due to particles or thread of particles stuck to the wall), this pre-processing step removes it. The subtraction process of the images with the averaged one gives a series of images in which the background becomes very different from the bright spots due to the moving particles, as clearly visible in fig. 2.9. Then, the pre-processed black and white images are subdivided into several interrogation cells. In this analysis the size of the interrogation cell equal to 64×64 pixel with an overlap of 50% of each cell with the neighboring ones has been chosen. A picture with the indication of the interrogation cells is shown in fig. 2.10. Finally, the average of 500 couple of images has been made and a vector map, in which each vector is representative of the velocity associated to each interrogation cell, is created. Specifically, for each plane the vector map contains 39 different row vectors along the streamwise direction, and for each row vector, the bi-dimensional velocity profile is expressed by 26 vectors. Figure 2.11 shows a typical vector map extracted with the method described on the plane under investigation. In order to enhance the readability of the figure, in the picture the

number of row vectors along the streamwise direction has been reduced and the velocity vectors have been scaled with a magnification factor. The acquisition, the pre-processing and the average correlation of images were performed using the software *Flow Manager* developed by *Dantec Dynamics*.

The data produced by the average correlation process are expressed as a pixel displacement per unit time. Therefore, in order to compare the experimental data with the numerical simulations, the data contained in the vector map are converted in meter per second by using the following relationship:

$$u(y,z) = \frac{\Delta s_{pix}}{\Delta \tau} \frac{L}{L_{pix}} \tag{2.10}$$

where $u(y,z)$ is the dimensional local fluid velocity, Δs_{pix} is the average displacement of the fluorescent particles expressed in pixel, $\Delta \tau$ is the time delay between two consecutive images, L is the width of the channel expressed in meter and L_{pix} is width of the channel in pixels.

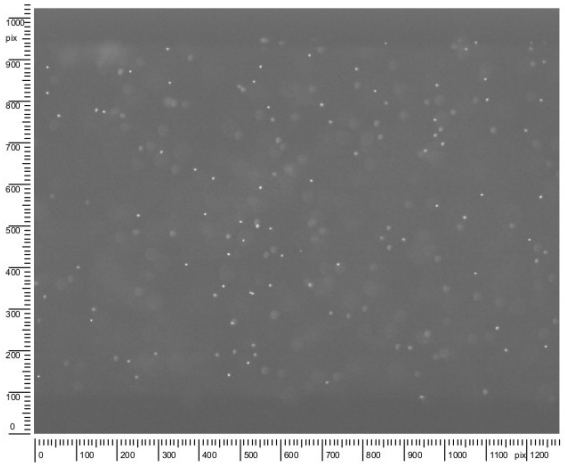

Figure 2.8: Picture of the fluorescent particles, dispersed in the working fluid, acquired in gray-scale.

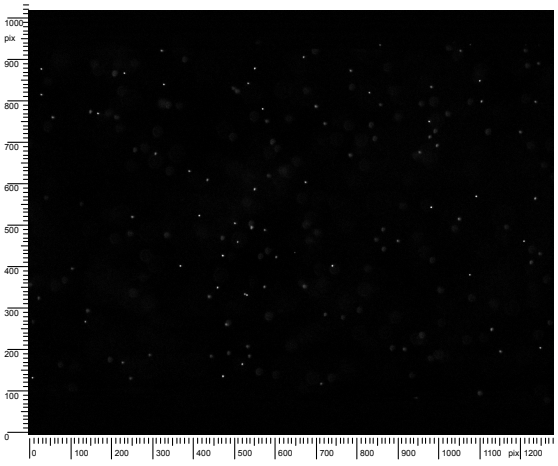

Figure 2.9: Black and white picture resulting from the subtraction of the gray-scale image by the mean obtained image.

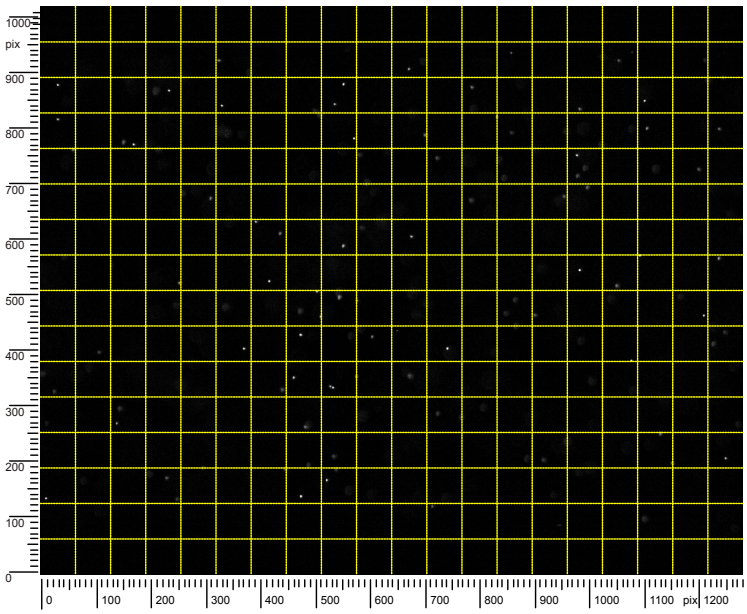

Figure 2.10: Grid made up by the interrogation cells.

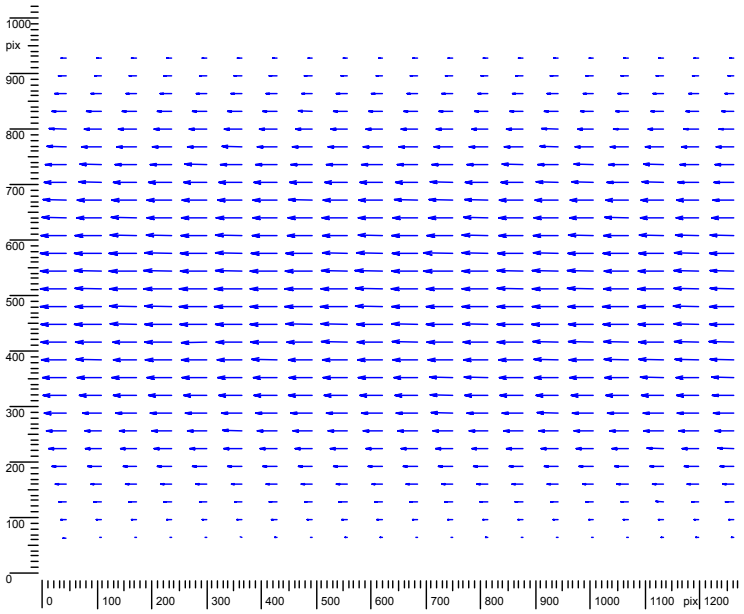

Figure 2.11: Example of a vector map.

2.4.5 Numerical determination of the velocity field

The reconstruction of the inner cross-section of the microchannel is achieved via the systematic comparison between experimental velocity measurements obtained with μPIV technique and the numerical data obtained by solving the momentum balance for laminar flow by varying the different shape of the microchannel cross-section. From a theoretical point of view, the water flow through a microchannel can be modeled as follows.

Consider a steady state, fully developed, forced laminar flow in a microchannel with a constant rectangular cross-section along the streamwise direction. Under the assumptions of Newtonian fluid with constant properties, negligible natural convection, isothermal flow and constant pressure gradient along the streamwise direction, the dimensionless Navier-Stokes momentum equation, in an orthogonal Cartesian system in which x is the coordinate along the streamwise direction and z the coordinate along the channel depth, can be written as:

$$\frac{\partial^2 V}{\partial y^{*2}} + \frac{\partial^2 V}{\partial z^{*2}} + P_d^* = 0 \tag{2.11}$$

where the equation is written in dimensionless form by introducing the following parameters:

$$y^* = \frac{y}{L} \qquad z^* = \frac{z}{L} \qquad V(y^*, z^*) = \frac{v(y,z)}{W} \qquad P_d^* = \frac{D_h^2}{\mu W}\frac{dp_d}{dx} \tag{2.12}$$

L is the width of the microchannel cross-section, $v(y,z)$ is the dimensional value of the local velocity, W is the average value of the velocity, D_h is the hydraulic diameter and dp_d/dx is the imposed pressure gradient along the streamwise direction.

For a channel with a rectangular cross-section of width L and depth (short side) H the no-slip boundary conditions at the walls can be written as:

$$V(0, z^*) = V(1, z^*) = 0 \tag{2.13}$$

$$V(y^*, 0) = V(y^*, \beta) = 0 \tag{2.14}$$

in which β is the channel aspect ratio defined as $\beta = H/L$.

Then, for microchannels with a rectangular geometry, the analytical solution of Eq. (2.11) coupled with the boundary conditions expressed by Eq. (2.13) and Eq.

(2.14) can be obtained by using the integral transform technique as reported by Morini and Spiga (1998):

$$V(y^*,z^*) = \sum_{n=1,odd}^{\infty}\sum_{m=1,odd}^{\infty} v_{n,m} sin\left(n\pi y^*\right) sin\left(\frac{m\pi}{\beta}z^*\right) \tag{2.15}$$

where the coefficients $v_{n,m}$ are defined as follows:

$$v_{n,m} = \frac{\pi^2}{4nm\left(\beta^2 n^2 + m^2\right)} \frac{1}{\sum_{i=1,odd}^{\infty}\sum_{j=1,odd}^{\infty} \frac{1}{i^2 j^2\left(\beta^2 i^2 + j^2\right)}} \tag{2.16}$$

This analytical solution is only valid for microchannels with a rectangular cross-section; for microchannels with different cross sectional geometry, Eq. (2.11) must be solved numerically by using commercial PDE solvers (Comsol, FlexPDE) or CFD software (Fluent, Open Foam). In this work the solution of Eqs. (2.15) - (2.16), for trapezoidal shaped channels, has been obtained by using the PDE solver FlexPDE.

Finally, in order to make the numerical results comparable with the experimental measurements the dimensional expression of the velocity has been obtained from the numerical solution by multiplying the dimensionless velocity distribution with the average velocity (W), which is derived from the ratio between the imposed water volumetric flow rate Q and the channel cross-section area A:

$$v(y,z) = V(y^*,z^*)W = V(y^*,z^*)\frac{Q}{A} \tag{2.17}$$

2.4.6 Comparison between experimental measurements and numerical data

The numerical velocity profiles inside the channel are firstly calculated by assuming for the microchannel a squared geometry as declared by the manufacturer (Translume). Later, the squared geometry is slightly modified in a trapezoidal one by decreasing the value of the acute angles (Φ) (see fig. 2.12). 6 different shapes are analyzed and referring to fig. 2.12, Φ angles of 90°, 89°, 88°, 87°, 86° and 85° are considered. In this stage, both apex angles are considered equal.

The experimental measurements are acquired for N_p planes along the depth of the channel. Specifically, a preliminary experimental campaign is carried involving 11 planes at different depths (fig. 2.12 A). The planes are selected starting from the channel middle plane (the position if this plane can be obtained by knowing the position of the bottom and upper walls of the channel, as explained

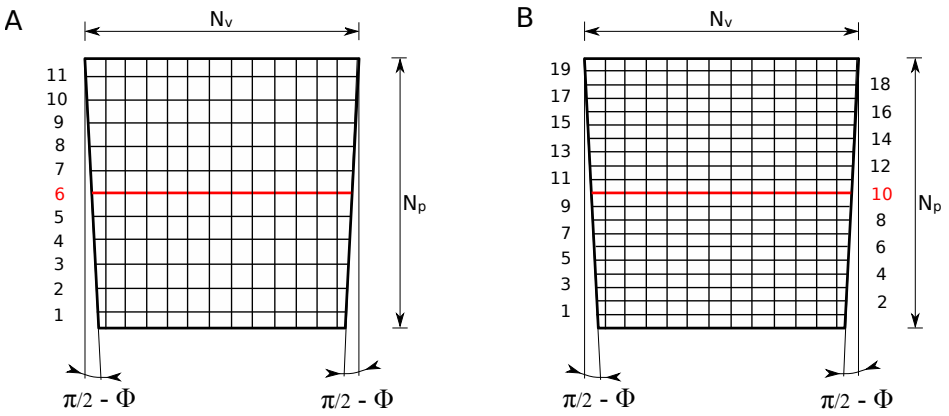

Figure 2.12: Sketch of the trapezoidal cross-section of the microchannel. In the picture N_p represents the horizontal planes and N_v the vectors on each row of each plane. Figure A refers to the preliminary experimental campaign in which 11 horizontal planes were considered. Figure B refers to the refined research in which the number of horizontal planes is increased up to 19. The central plane is highlighted in red for both the cases. For image clarity, the number of vectors n_v is reduced in both the figures. Φ are the angles under investigation.

previously). A relative distance between neighboring planes of almost 27 µm has been considered. The number of planes is the result of a trade-off between accuracy and computing time. The accuracy on the z coordinate associated to the planes is obviously related to the accuracy of the evaluation of the position of the bottom and upper planes and it depends also from the capability of the microscope to control the vertical displacement of the focal plane. In this case, with the Nikon Eclipse TE 2000-U the vertical position of the focal plane, can be controlled with an accuracy below 1 µm.

As outlined by figure 2.11 for each plane an experimental velocity map, with 39 longitudinal velocity profiles, have been recorded. Since the flow is in steady state conditions and the inner geometry of the microchannel is constant along the streamwise direction, each longitudinal velocity profile contains the same amount of information. In this way, in principle, for each plane 39 identical longitudinal velocity profiles are obtained. Now, each velocity vector is associated to three indexes:

- m, represents the longitudinal profile
- n_v represents the position along the width of the microchannel (y-coordinate)
- n_p represents the position along the depth of the microchannel (z-coordinate)

Therefore the single value of velocity will be indicated as $u^m_{n_p,n_v}$. A schematic representation is depicted in figure 2.13.

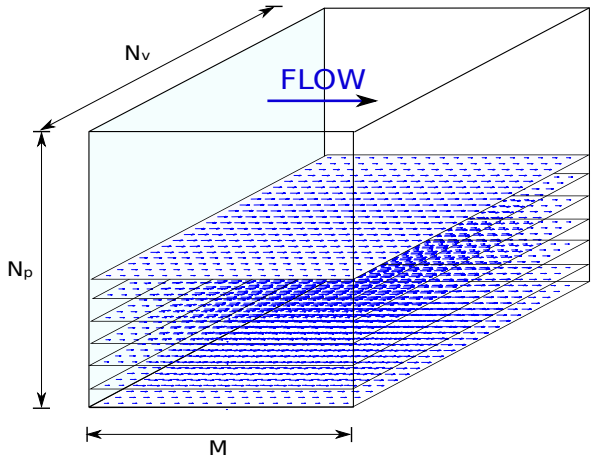

Figure 2.13: Schematic representation of the three indexes associated to the vector map.

The comparison between numerical data and experimental measurements is made as follows:

- For each velocity vector associated to the interrogation cell, the relative error $\epsilon^m_{n_p,n_v}$ between the theoretical and experimental velocity is calculated as follows:

$$\epsilon^m_{n_p,n_v} = \frac{u^m_{n_p,n_v} - v_{n_p,n_v}}{v_{n_p,n_v}} \tag{2.18}$$

  where $u^m_{n_p,n_v}$ is the experimental velocity calculated in the *v-th* position of the *m-th* row vector on the *p-th* plane while v_{n_p,n_v} is the corresponding theoretical velocity. In this way, M vectors containing Nv relative errors between the experimental measurements and the velocity profile numerically calculated, have been created.

- Then, for each m-th vector, the Normalized Root Mean Square error is calculated and finally the experimental velocity profile which corresponds to the m-th vector with the lowest NRMS error ϵ_{n_p} is selected.

$$\epsilon_{n_p} = \min_m \left(\sqrt{\frac{1}{N_v} \sum_{n_v=1}^{N_v} \left(\epsilon^m_{n_p,n_v}\right)^2} \right) \tag{2.19}$$

- As a final step, the NRMS error of each plane along the depth of the microchannel, evaluated following the Eq. (2.19), is averaged through all the planes.

$$\bar{\epsilon} = \frac{\sum_{n_p=1}^{N_p} (\epsilon_{n_p})}{N_p} \tag{2.20}$$

For laminar flows, small differences in terms of inner geometry can generate large variations on the local values of the velocity in the channel. For this reason, it becomes possible to couple the μPIV velocity evaluation with the numerical analysis of the velocity field in the channel. By using the numerical approach, the cross-section of the channel is changed until the value of $\bar{\epsilon}$ is minimized. The above described procedure is schematically described in figure 2.14.

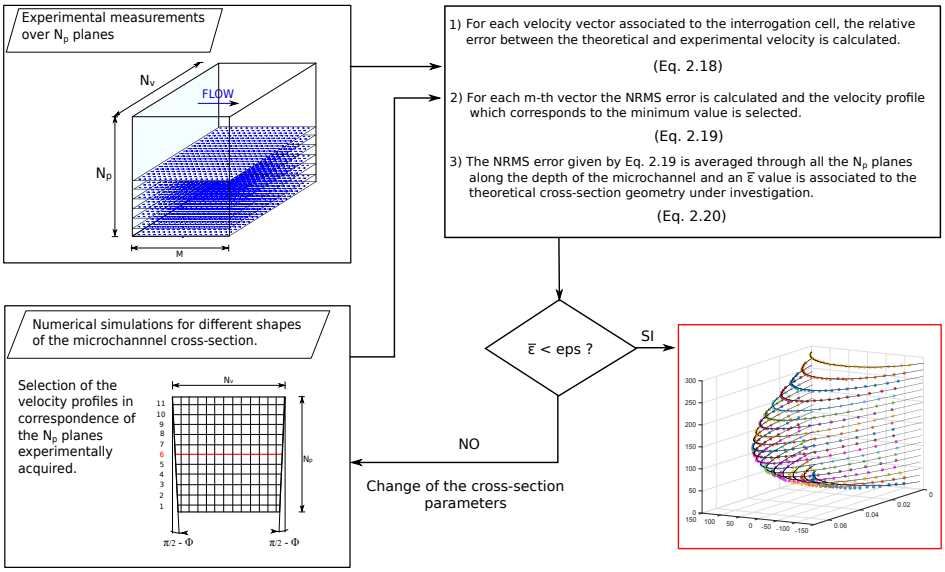

Figure 2.14: Schematic representation of the methodology adopted.

2.5 Results and discussion

2.5.1 Results for the straight channel

In fig. 2.15 the experimental velocity profile obtained by means of the µPIV apparatus is compared with the theoretical velocity profile obtained by solving Eq. (2.11) with the boundary conditions given by Eq. (2.13) and (2.14) by varying the cross-section of the channel from square (figure A,B,C) to trapezoidal with apex angles of 88° (figure D,E,F) and 86° (figure G,H,I).

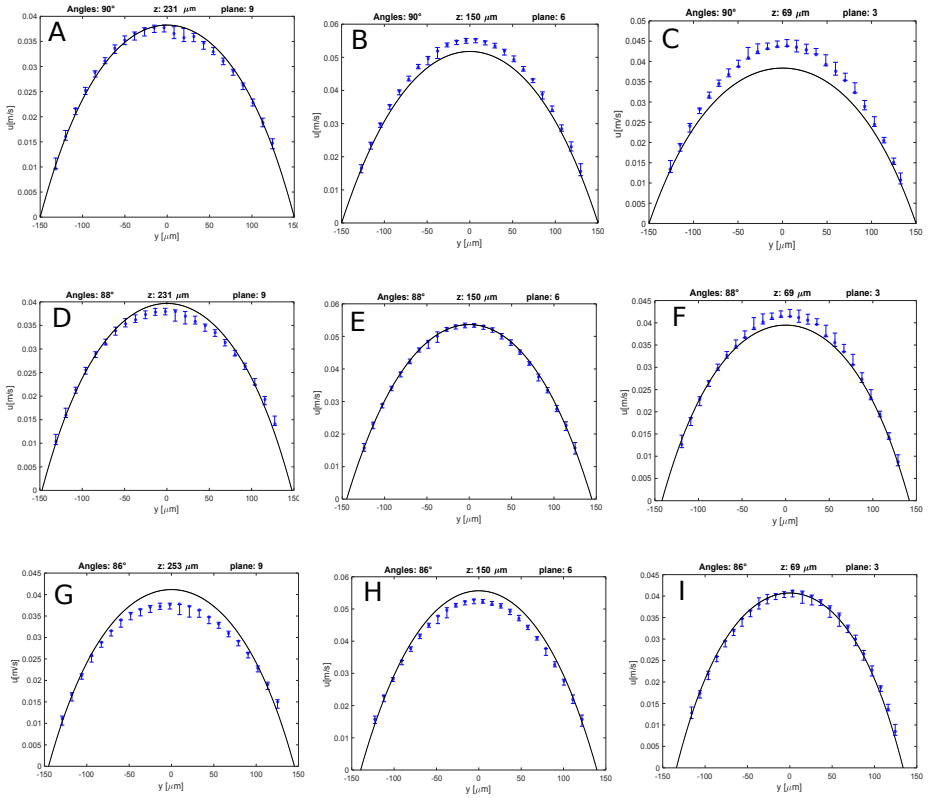

Figure 2.15: Results for the squared straight channel for Φ angles of 90° (A,B,C), 88 (D,E,F)° and 86° (G,H,I).

In figure 2.15, for each geometry the comparison has been shown for three different planes: $n_p = 9$ (A,D,G), $n_p = 6$ (B,E,H) and $n_p = 3$ (C,F,I). As shown in fig. 2.15 A and referring to fig. 2.12 A, the position of plane #9 is close to the upper wall of the channel. On the contrary, plane #6 is in the center and plane #3 is close to the bottom wall. More precisely the distance from the bottom wall and plane #9 is 231 µm, the distance between plane #6 and the bottom wall is equal to 150 µm and plane #3 is 69 µm far from the bottom wall. In figure 2.15, the continu-

ous line is the theoretical velocity profile, the blue points are the experimental velocity data of the m-th vector selected by using Eq. (2.19) and the blue bars represent the whole spread of the validated velocity measurements obtained for a specific n_v position for all the M vectors. Of course, the choice of the m-th vector changes when the numerical velocity data are calculated for a different shape of the cross-section. For this reason, the displacement of the blue points inside the range of the measured velocity is different when the experimental measurements are compared with numerical simulations in which the theoretical shape of the cross-section is different. In addition, during the validation procedure, some velocity profiles could be erased due to their lack of physical meaning. In particular the data affected to the possible erasing are the data closer to the boundary walls where the measurements are less reliable. For this reason fig. 2.15 A,D,G show 23 experimental velocity measurements for each profile while fig. 2.15 B,E,H show 24 experimental velocity measurements and fig. 2.15 C,F,I show 25 experimental velocity measurements. For clarity, an enlargement of fig. 2.15 E is shown in fig. 2.16.

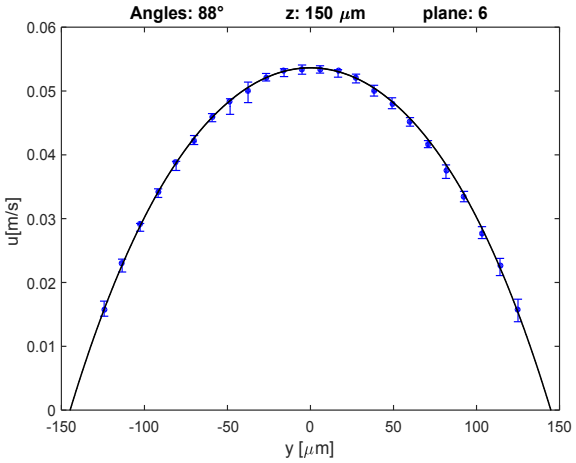

Figure 2.16: Enlargement of fig. 2.15 E.

A different elaboration of the data shown in fig. 2.15, is given in Tab. 2.6 where the NRMS error ϵ_{n_p} is shown for all the different planes as a function of the different cross-section geometry (apex angle Φ). The experimental data belonging to plane # 1 and plane # 11 are not taken into account, since too close to the solid walls, where various reasons contribute to the mismatching between experimental and numerical results, including the bright noise due to the particles stuck to the walls. In addition if the distance between the measurement plane and the channel boundary is within the dept of correlation of the measurements (see Section 2.3.4) erroneous results will be achieved. Therefore, it exist a minimum distance from the horizontal boundaries of the microchannel at which the measurements can be correctly performed and this distance is exactly related to the DOC of the measurements. However, for the purpose of the methodology here exposed,

experimental measurements close to the walls are not necessarily required since this method relies on the evaluation of the global distribution of the flow velocity field, that is directly dependent to the shape of the microchannel cross-section. For this reason, the evaluation of the velocity distribution in the central area of the cross-section can be in principle sufficient in order to retrieve preliminary information on the channel geometry. Nevertheless, experimental measurements close to the channel boundaries can give important information about local imperfections of the same as it will later clarified.

Table 2.6: NRMS error ϵ_{n_p} for each plane under investigation and resulting $\bar{\epsilon}$ error as a function of the inner geometry of the microchannel.

		NRMS error ϵ_{n_p} (%) for different Φ angles (°)					
Plane n_p (#)	z (µm)	90	89	88	87	86	85
10	258	9.7	10.4	10.3	12.6	14.2	15.5
9	231	3.4	3.5	4.3	5.7	7.9	10.3
8	204	3.5	3.0	2.7	4.7	7.4	9.2
7	177	3.9	1.8	1.7	3.5	7.0	9.0
6	150	5.5	1.8	1.2	2.6	5.4	8.9
5	123	7.6	2.9	1.0	1.9	4.4	8.4
4	96	9.4	3.9	2.3	2.1	3.2	6.6
3	69	10.4	5.7	3.6	2.1	2.0	4.5
2	42	17.8	13.0	9.1	7.0	4.6	3.9
	$\bar{\epsilon}$ (%)	7.9	5.1	4.0	4.6	6.2	8.5

From the data reported in Table 2.6, is clear that for the square geometry (Φ = 90°) the matching between experimental velocity profiles and numerical data is not optimal, especially for the planes close to the bottom wall where the NRMS error ϵ_{n_p} drastically increases. As it is visible from figures 2.15.B and 2.15.C, the experimental velocity data are generally higher compared to the theoretical profiles: this suggests that the real cross-section area tends to be reduced with respect to the square close to the bottom wall. This deduction is confirmed by the data of Tab. 2.6 when a trapezoidal cross-section with $\Phi < 90°$ is considered. With a slightly trapezoidal shape of the channel cross-section (Φ = 88°) the error $\bar{\epsilon}$ reaches indeed a minimum value of 4 %. Through a further reduction of the Φ angles, the $\bar{\epsilon}$ error becomes progressively larger, this could be interpreted as a signal that the imposed geometry of the channel tends to move away from the real one.

Focusing the attention on the data reported in Tab. 2.6 for Φ = 88°, it can be noted how the NRMS error ϵ_{n_p} between the numerical data and the experimental velocity is lower for central planes and increases close to the boundary walls. The main explanation behind this is related to the way in which the experimental velocity is derived. As already outlined, the fluorescent particles that give their

contribution to the cross-correlation procedure are contained in a fluid volume having a depth equal to the DOC value (see equations (2.3) and (2.4)). Hence, lower is the velocity gradient through the depth of correlation and more reliable is the result of the cross-correlation, on the contrary, if a strong velocity gradient is present along the depth in which the particles give a strong contribution to the cross-correlation process, lesser reliable the result will be. Similar considerations can be made by considering the effect on the velocity accuracy of the size of the interrogation cells and the velocity gradients present in each velocity profile. In addition, going closer to the top plane the light intensity decreases due to the increasing thickness of the water crossed by the light. All these considerations explain the amplitude of the bars reported in fig. 2.15: the width of the range of the measured velocities is lower for higher velocities (*i.e.* close to the central region of the channel, graphs B, E, H) while increases going closer to the solid walls where the velocity gradients are higher.

Particular care has to be taken regarding to the results obtained for plane # 2. The numerical results are carried for perfect trapezoidal shapes with sharp angles. Therefore, local imperfections of the inner geometry, as instance the presence of rounded corners instead of sharp ones, can be responsible of a substantial difference between the local velocity profiles obtained in the simulations and the measured velocity. For this reason, the large values of $\bar{\epsilon}$ associated to the data of plane #2 highlight a presence of a superficial irregularity not accounted in the geometry simulated here. In other words, the real geometry seems to be characterized by a trapezoidal geometry with an apex angle of 88° but close to the bottom wall some irregularity is expected to be present (*i.e.* curved surfaces, rounded corners or local asperities). In addition, the mismatching between experimental and numerical results can be also linked to the presence of a tilting of the cross-section with respect the horizontal plane. For this reason, particular care has been used during these tests in order to check the placement of the microfluidic device on the mounting plate of the inverted microscope. In particular, it must be verified that the bottom wall of the device is perpendicular to light path. Another possible source of difference with the numerical solution is the presence of an asymmetry of the cross-section (*i.e.* different apex angles on the right and left sides of the channel). This feature can be qualitatively checked by observing if shadowing effects are introduced by the system of illumination close to the lateral side of the microfluidic device. The presence of flat shadows close to the lateral boundaries can give an idea about the symmetry of the cross-section. In particular, larger is the shadow area and greater is the sloping of the lateral sides. About the microchannel under investigation in this dissertation, a similar thickness of the shadow associated to the later walls is found (fig. 2.17), suggesting consequently a symmetric geometry of the channel. Additionally the thickness of the shaded edges are relatively small, this indicates that the sloping of the boundaries presents a relative small deviation from the nominal value of 90° (which can be coherent with the value of 88° obtained with the described procedure).

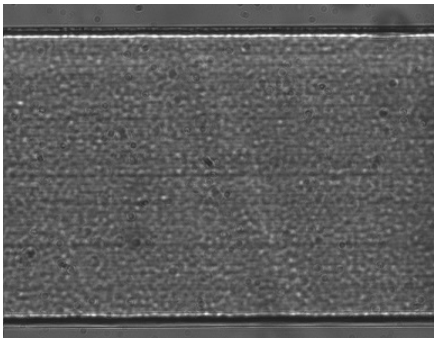

Figure 2.17: Picture of the microchannel under investigation: the two horizontal shaded lines are the lateral boundaries of the channel.

In order to refine the achieved results, an additional experimental campaign has been carried out over 19 different horizontal planes, having a distance of around 15 µm between them (fig. 2.12 B). Hence, the results are compared the with numerical simulations obtained for $\Phi = 88°$. Particular care in the arrangement of the experimental campaign has been taken with respect to the power of the laser bursts that were slightly and progressive increased as the thickness of water crossed by the light before to reach the focal plane increases. As it is visible from the comparison shown in fig. 2.18 and from the data reported in Tab. 2.7 the matching between experimental data and numerical profiles shows a good agreement especially for the central planes (from #7 to #14 in Tab. 2.7 and from d to m in fig. 2.18) where the NRMS error ϵ_{n_p} is always lower the 2 %. As expected, going closer to the boundary walls, the error ϵ_{n_p} grows up. However, if for planes #17 - #19 closer to the upper wall of the microchannel the value of ϵ_{n_p} is now acceptable, the error linked to planes #3 - #1 close to the bottom wall is too much high to be attributed to the uncertainty of the µPIV technique. This confirms the presence of some local imperfection in the shape of the trapezoidal cross-section close to the bottom wall of the channel.

Table 2.7: NRMS error ϵ_{n_p} between the experimental results and a theoretical trapezoidal shape with Φ angels of 88°, over 19 different planes along the depth of the channel.

n_p (#)	1	2	3	4	5	6	7	8	9	10
z (µm)	17	32	47	62	76	91	106	121	135	150
ϵ_{n_p} (%)	> 10	9.8	6.8	5.7	3.2	2.6	1.4	1.0	1.0	1.1
n_p (#)	11	12	13	14	15	16	17	18	19	
z (µm)	165	180	194	209	224	238	253	268	283	
ϵ_{n_p} (%)	1.3	1.2	1.0	1.3	1.8	1.6	2.5	2.6	3.1	

The quality of the results is also underlined by the narrower dispersion (bars in fig. 2.18) of the experimentally measured velocities achieved on the different planes, if compared with the bars shown in fig. 2.15 and 2.16.

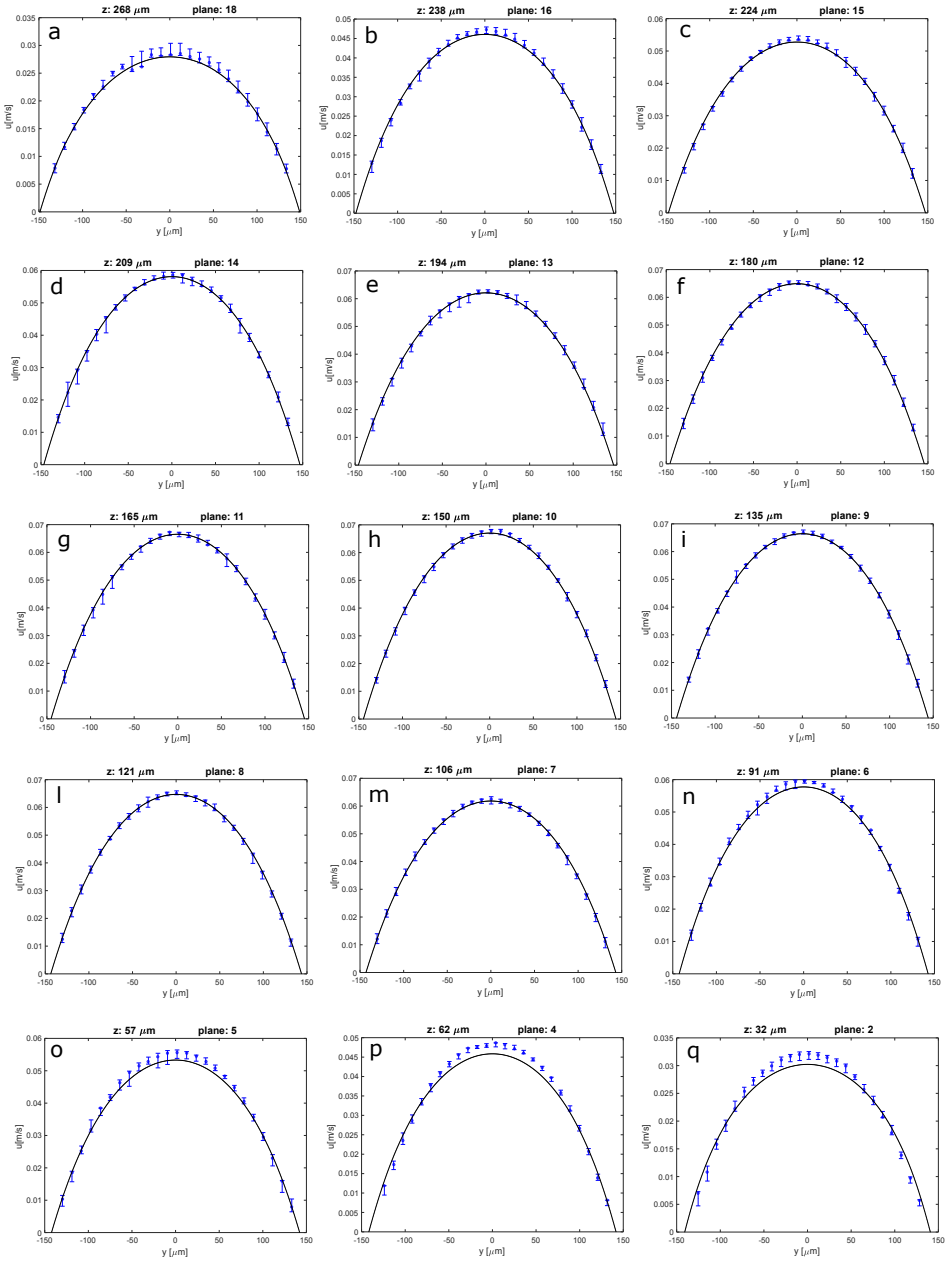

Figure 2.18: Results for the squared straight channel for Φ angles of 88° over 15 of 19 planes.

A graphical reconstruction of the three-dimensional velocity distribution on the whole microchannel cross-section is shown in fig. 2.19. The three-dimensional reconstruction is here obtained by collecting together all the bi-dimensional velocity profiles obtained for each plane considered.

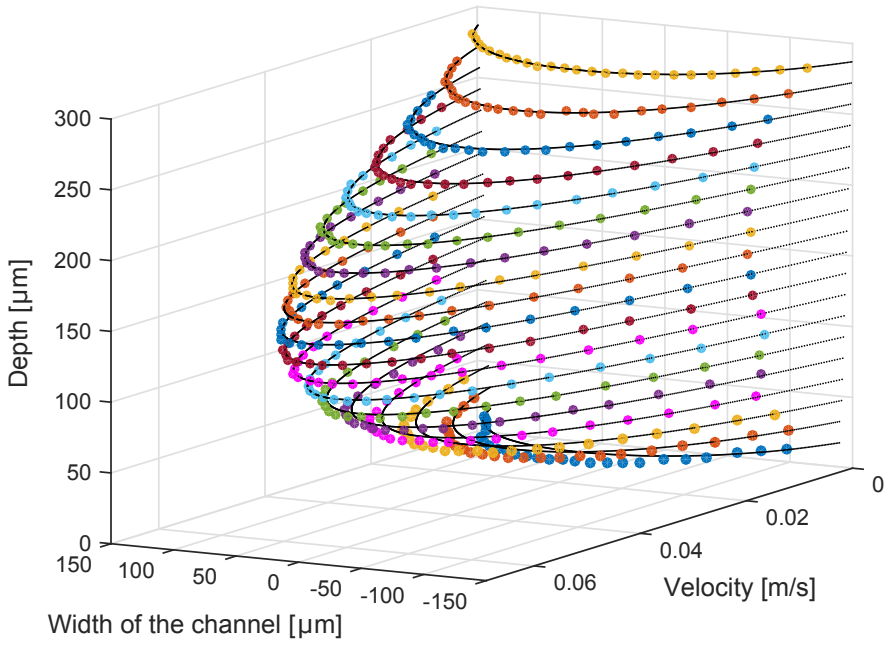

Figure 2.19: Reconstruction of the three-dimensional velocity distribution realized by collecting together all the bi-dimensional velocity data in each plane.

The data shown in Table 2.7 confirms that close to the bottom wall of the channel a poor agreement between the experimental velocity and the numerical data is obtained. The NRMS error grows up reaching a value beyond 10 % for plane # 1 (see Tab. 2.7). This difference cannot be explained even if one considers the DOC effects on the accuracy of the µPIV results close to the wall and/or the noise coming from the particles stuck to the wall. The existence of a localized geometrical singularity close to the bottom wall of the channel is highlighted by the data depicted in fig. 2.20 in which the local relative velocity error is plotted on the whole cross-section points.

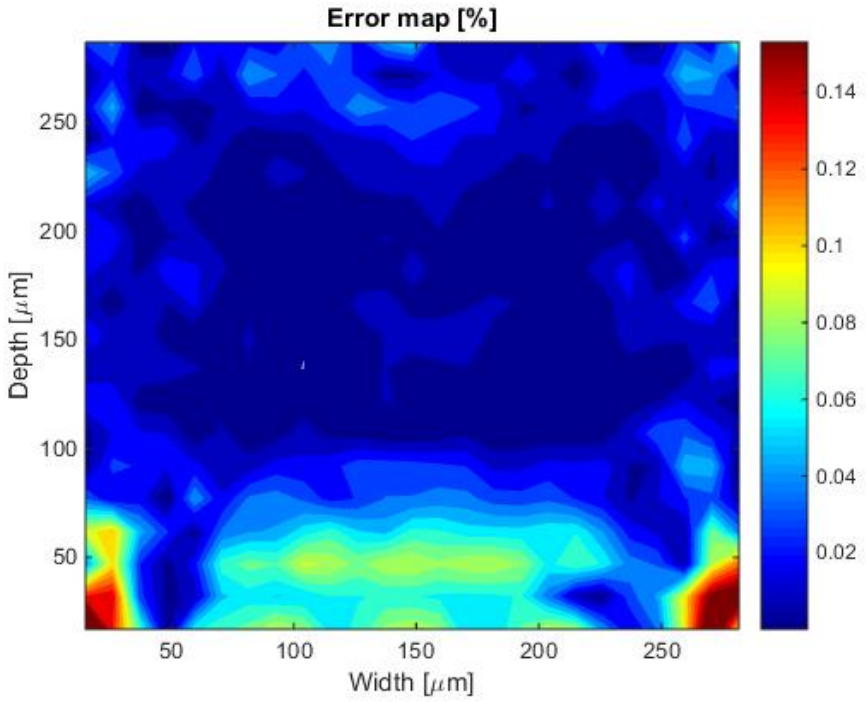

Figure 2.20: Error map obtained from the comparison between experimental velocity points and ones obtained with a numerical simulation in which a trapezoidal shape with Φ angles of 88° is assumed as the geometry of the microchannel cross-section.

The error map, that is created through a careful comparison of the velocity expressed by each experimental single points with the related numerical prediction, underlines as the largest errors are concentrated close to the bottom corners of the cross-section by reaching local values beyond 14 %.

2.5.2 SEM analysis on straight channel

In order to confirm the predictions made through the inverse use of the μPIV technique, a destructive analysis with Scanning Electron Microscopy has been conducted on this microchannel. The microchannel was firstly cut into different slices by a *LKB 7800 knife maker*, then, since the microchannel substrate is in fused silica, the samples are coated by thin deposition of gold. Afterward, the gold-coated slices were analyzed with a *Zeiss EVO 50EP* SEM Microscope. The SEM image of the real cross-section of the microchannel is shown in fig. 2.21. From this image, in which a picture of the inner geometry is taken with a magnification of 800 ×, is clearly visible as the shape is slightly trapezoidal and the lower corners of the channel present a rounded curvature.

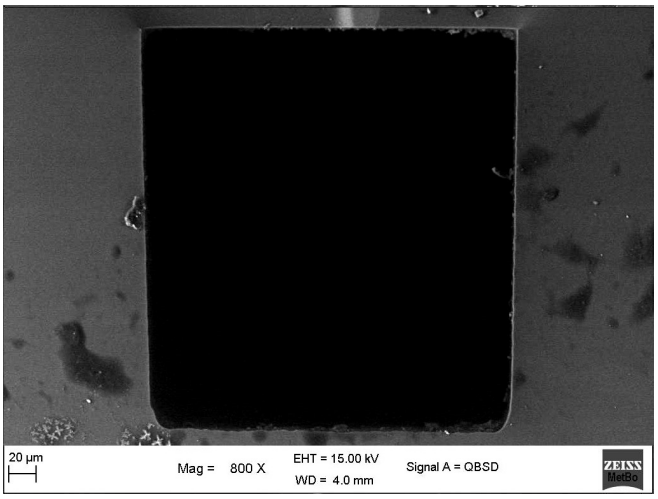

Figure 2.21: SEM image with a magnification of 800 ×.

In fig. 2.22 the discrepancy between the squared geometry declared by the manufacturer of the channel and the trapezoidal shape with $\Phi = 88°$ indicated as best geometry from the μPIV measurements, is highlighted by yellow lines, with a zoomed view of the rounded corners of the channel. From a quantitative analysis of the SEM images, the angle Φ_1 is found to be equal to 88.1° and Φ_2 equal to 88.3°. Moreover, concerning the depth of the channel, the value found through the experimental procedure described previously was in agreement with the nominal value of 300 μm declared by the manufacturer and this value is also confirmed from the SEM analysis. In addition, the cross-section area used for the numerical comparison following the experimental predictions is equal to 86850 μm^2, while the area evaluated by using the SEM images considering the rounded angles is equal to 85980 μm^2 with a relative difference of around 1 %. The difference in terms of area increases if the squared cross-section declared by the manufacturer is considered (4.5 %). The results shown in this thesis demonstrate in addition that the inverse use of μPIV allows the identification of the presence of local singularities around the perimeter of the channel.

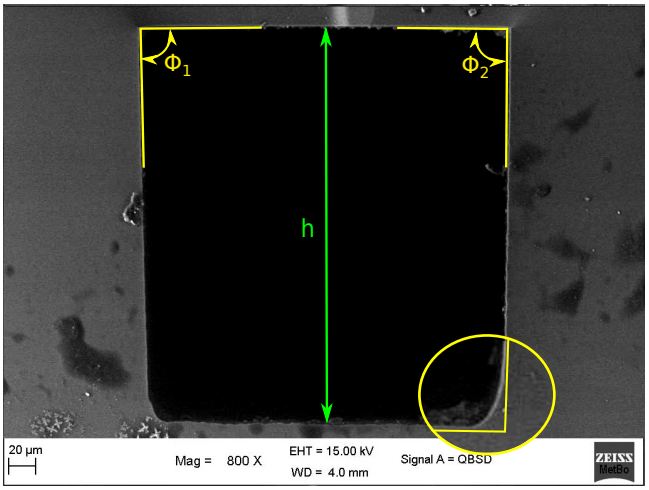

Figure 2.22: SEM image with references.

This data are also reported in Table 2.8, in which the nominal cross-section is also reported for comparison.

Table 2.8: Comparison between nominal, predicted and real values of the microchannel cross-section.

	Φ_1 (°)	Φ_2 (°)	Depth, h (µm)	Area (µm^2)
Nominal	90.0	90.0	300	90000
Predicted	88.0	88.0	300	86850
Real	88.1	88.3	300	86080

In conclusion, it can be stated that the good agreement between the SEM analysis and the prediction made by using as an inverse method the µPIV velocity measurement for a laminar steady state flow of water through a microchannel, demonstrates the reliability of the methodology proposed for a non-destructive check of the real geometry of a microdevice. Therefore, the inverse use of the µPIV technique can be a useful methodology for finding in a non-destructive way the real shape of a microchannel having an optical access.

2.5.3 µPIV measurement for a micro T-junction

In order to extend the analysis carried on the straight channel described before to more complex geometries, a micro T-junction has been investigated with the µPIV technique. The micro T-junction is made through a fabrication process very similar to that used for the channel analyzed in the previous sections. The manufacturer declares that the channels of the T-junction are squared with a side of 300 µm. The material of the substrate is the same of the previous channel (*i.e.* fused silica) and also the material used for the thermal bonding of the channel is the same. To verify if the real cross-section corresponds to the declared one, the methodology reported in Section 2.4 is repeated for the long straight branch of the device. As happened for the straight channel, the comparisons between the experimental µPIV measurements and numerical data by assuming the nominal cross-section give a bad matching. This indicate that also for the micro T-junction, the real cross-section is different from the one declared by the manufacturer and therefore a detection of its actual shape and dimensions is required. In particular, similarly to the previous case, a slightly trapezoidal shape of the cross-section was found. In addition, as concerns the channel depth, the analysis carried out in order to individuate the position of the bottom and upper walls performed using the particles stuck to the bottom wall and to the upper wall, have revealed a reduced depth of the microchannel (*i.e.* 265 µm) compared to the nominal one of 300 µm.

However, in this case, due to the complexity of the device, SEM analysis is not possible, therefore, the micro T-junction geometry has been analyzed by means of confocal fluorescence microscopy. With this method the microchannel is filled with a fluorescent liquid (Rhodamine beta in deionized water) and illuminated. Then, the light emitted by the fluorescent fluid is recorded. Since the fluorescent fluid fills completely the microchannel, the cross-section shape of the microchannel can be reconstructed plane by plane by moving the focal plane from the bottom to the upper wall.

The measurements via a confocal fluorescence microscopy were carried out in the Laboratory of Life Science at the University of Bologna under the supervision of Prof. Laura Calzà and the cooperation of Dr. Chiara Mangano and Dr. Luisa Stella Dolci. The sample under investigation has been analyzed through a microscope *Nikon Eclipse Ti A1R* for confocal fluorescence microscopy that is equipped with a *Plan Apo* objective lens having a magnitude of 20 × and NA of 0.75. The working distance of the lens (WD = 1.0 mm) and the cover glass thickness (CG = 0.17 mm) enable the complete scanning of the channel down to its bottom wall. Due to the property of absorption and emission of the Rhodamine beta, a laser with a wavelength of 561.4 nm has been chosen as illuminating source. As it is visible form fig. 2.23 the analysis is carried out both along the long straight branch of the T-junction and in correspondence of the junction.

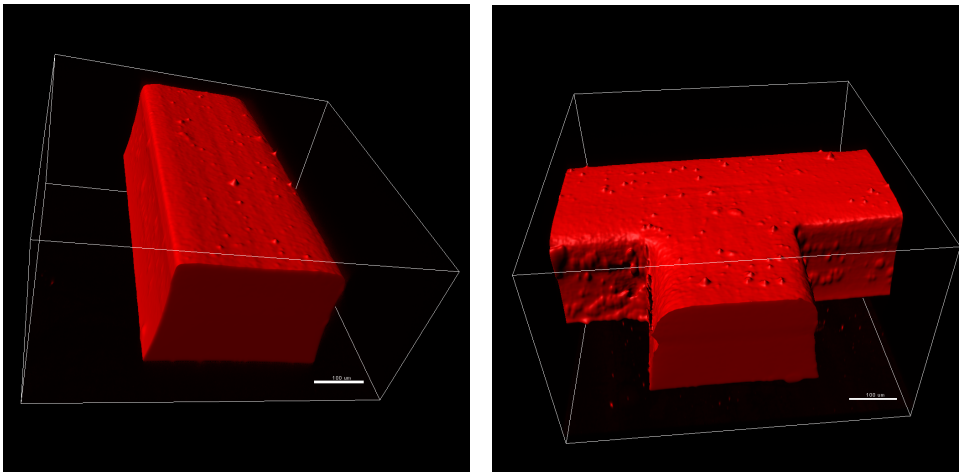

Figure 2.23: Reconstruction of the three-dimensional shape of the fluorescent fluid.

For what concerns the analysis of the images and results two main things have to be kept in mind:

1. The inner medium is a liquid (substantially the mixture is deionized water). Thus, similarly for the PIV measurements, it entails a different refractive index between the external medium and the inner one. Consequently, the references for the z-axis (the vertical one) have to be multiplied for 1.333 (*i.e.* water refractive index). For this reason in the pictures reported in fig. 2.23 and fig. 2.24, the cross-section appears to be more flattened than in reality.

2. Due to the properties related to the fluorescent seeding, the quality of the measurements is lower in correspondence to the lateral edges while is higher in correspondence to the sharp corners. This effect is easily visible in fig. 2.23 and fig. 2.24 where in correspondence to the lateral boundaries the image shows a fictitious inner concavity.

For this reasons the reference points for the measurements are taken in correspondence of the sharp edges as it is depicted in fig. 2.24. The supposed uncertainty was in the order of 5 %.

In order to evaluate the dimensions of the inner geometry of the microchannel (depth, width and angles), the measurements of the side lengths are taken in several position. In particular, since the shape of the cross-section is clearly trapezoidal, the length of the higher base L (position I in fig. 2.24) and the length of the lower base l (position II in fig. 2.24) are taken for three different positions along the streamwise direction. The depth of the cross-section d is evaluated as the distance between the two sharp edges in correspondence to the higher and the lower basis. The results for the straight branch are reported in Table 2.9.

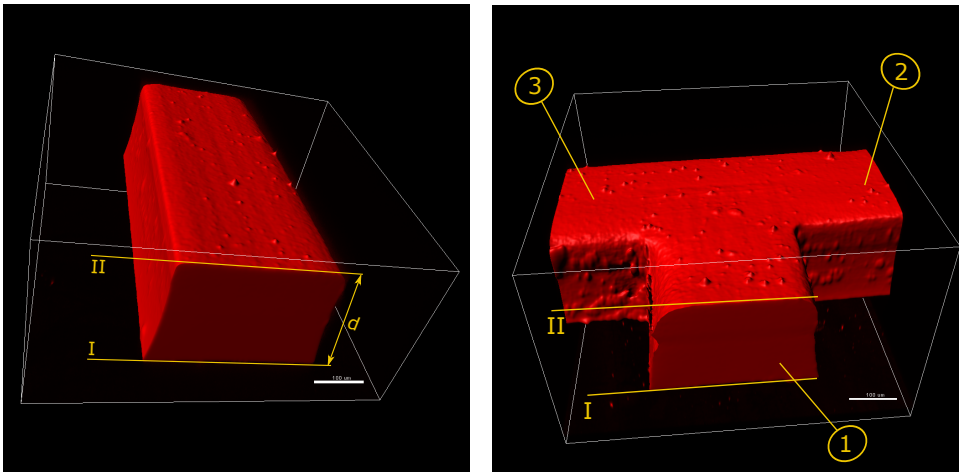

Figure 2.24: Reconstruction of the three-dimensional shape of the fluorescent fluid with references

Table 2.9: Results for the straight branch of the micro T-junction.

	h_2 (µm)	w (µm)	$\bar{w}$ (µm)
L	0	287/288/289	288
l	266	269/271/269	270

where h_2 is the z coordinate of the bottom and upper walls, w is the measured width for three different positions along the streamwise direction and $\bar{w}$ is the mean of the w values.

Similar measurements are done for the junction. In particular, for the junction the measurements are repeated for all the three branches that compose the T-junction, depicted in fig. 2.24 with numbers 1, 2, 3. Here, the evaluation of the depth is made through two different measurements for each branch, as reported in Tab. 2.10, while width measurements are taken for two planes common to every branch: one is located in correspondence to the bottom wall (h_2=0) and one close to the upper wall, see Table 2.11.

Table 2.10: Measurements of the actual depth of the three branches at the junction.

branch	d_2 (µm)
(1)	263/260
(2)	256/263
(3)	261/253

Table 2.11: Results for the three branches of the micro T-junction.

Branch	h_2 (µm)	w (µm)
(1)	0	290
	246	273
(2)	0	288
	246	266
(3)	0	287
	246	269

The depth of the microchannel found via the confocal fluorescence microscopy is of 266 µm along the straight branch and around 260 µm for the three branches close to the junction, the same depth is found looking the the fluorescent particles stuck to the horizontal walls during the µPIV measurements. Also the presence of rounded corners appears distinctly in the images depicted in fig. 2.23. As the last step the Φ value assumed by the acute angle Φ are calculated from the measurements reported in Tab. 2.9 - 2.11.

Under the assumption of symmetric cross-section and considering the sloping sides as straight without any inner curvature the Φ angles can be calculated as follows:

$$\Phi = tan^{-1}\left(\frac{h}{\delta_l}\right) \qquad \text{where} \qquad \delta_l = \frac{L-l}{2} \tag{2.21}$$

where L and l are respectively the higher base and the lower base of the trapezoidal cross-section and h is the height of the channel, as shown in the sketch illustrated in fig. 2.25.

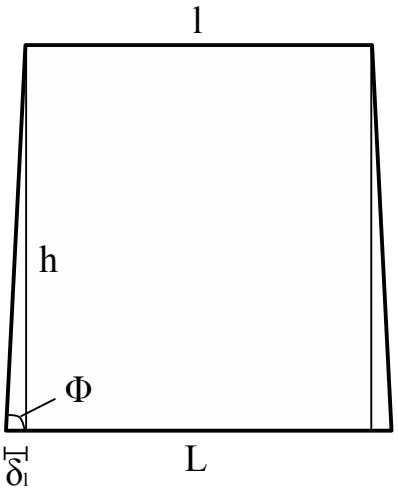

Figure 2.25: Sketch of the trapezoidal section with references.

The results obtained by using Eq. (2.21) are reported in Tables 2.12 and 2.13:

Table 2.12: Calculation of the Φ angles of the straight branch.

L (μm)	l (μm)	δ_l (μm)	h (μm)	Φ (°)
288	270	9	266	88.0

Table 2.13: Calculation of the Φ angles of the branches close to the junction.

Branch	L (μm)	l (μm)	δ_l (μm)	h (μm)	Φ (°)
(1)	290	273	8.5	246	88.0
(2)	288	266	11.0	246	87.4
(3)	287	269	9.0	246	87.9

An experimental evaluation of the mixing and splitting of water flows inside the T-junction is carried out for different configurations and the results are compared with numerical simulations. In particular the following configurations of the T-junction have been investigated: mixing of two liquid inlets in which both of them are perpendicular to the outlet (case 1 in fig. 2.26 and fig. 2.27), mixing of two liquid flows in which only one of them (secondary flow) is perpendicular to the outlet (case 2 in fig. 2.26 and fig. 2.28) and splitting of a water flow into two flows (case 3 in fig. 2.26).

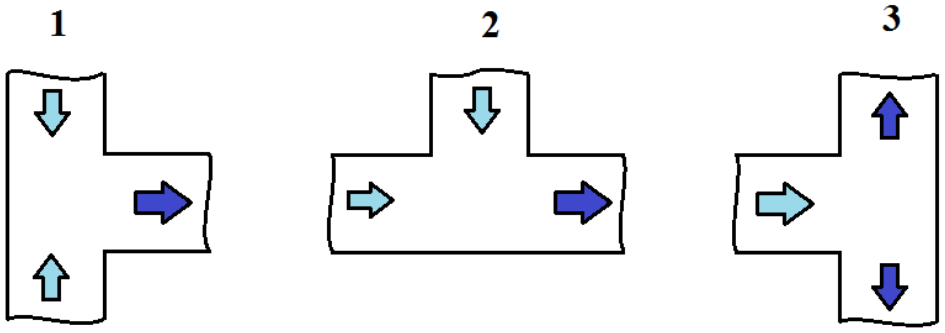

Figure 2.26: Different configurations utilized for the μPIV measurements inside the micro T-junction.

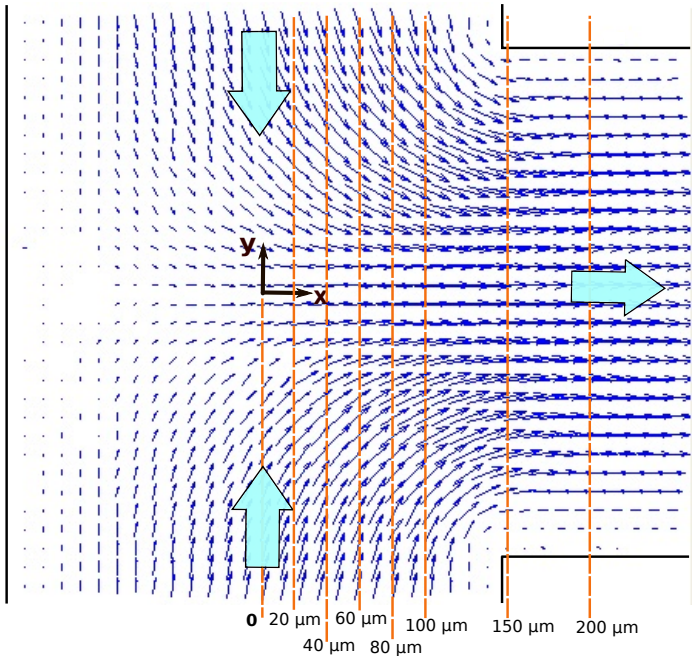

Figure 2.27: Vector map of the experimental velocity distribution for the configuration 1 with references.

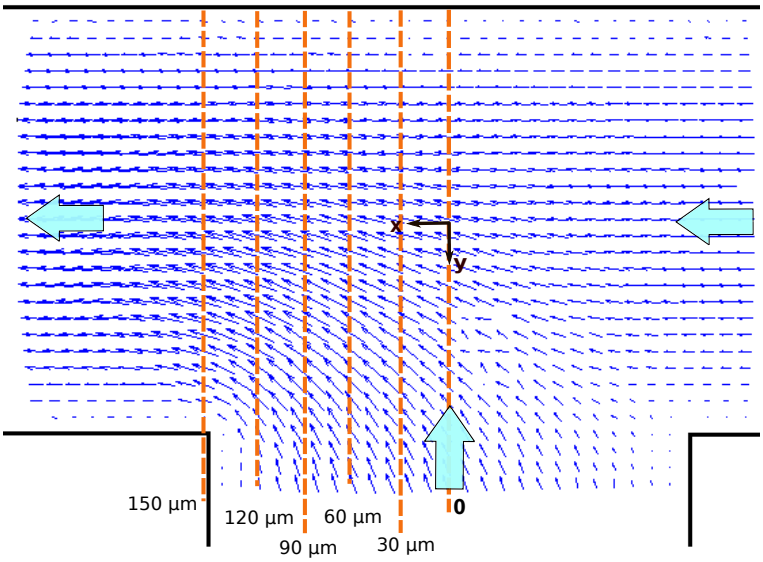

Figure 2.28: Vector map of the experimental velocity distribution for the configuration 2 with references.

In these cases, however, the comparisons have not been made along the depth of the microchannel, but the development of the velocity profiles is analyzed along

the streamwise direction only on the central plane of the T-junction. Nevertheless, the quality of the velocity measurements obtained by using µPIV is highlighted by the good agreement with the predictions of the numerical simulations made with the commercial software Comsol Multiphysics®. In this case, the geometry of the cross-section is known with a good accuracy thanks to the confocal fluorescence microscopy. For the configuration 1, the comparison between experimental measurements and numerical velocity profiles, for different positions along the streamwise direction, gives a NRMS error that ranges between 1.2 % and 5.8 %. For example in fig. 2.29 is shown the comparison between experimental and numerical data obtained by imposing an equal value of the volumetric flow rate (4 ml/h) for both the two inlet branches. The comparisons are depicted for different positions along the outlet direction starting from a condition in which the two flows are almost completely separated (x = 0) up to the condition close to the fully developed laminar flow (x = 200 µm). The position within the T-junction investigated can be seen in figure 2.27. As it is visible from fig. 2.29, the experimental velocity profiles are in excellent agreement with the numerical data for all the planes.

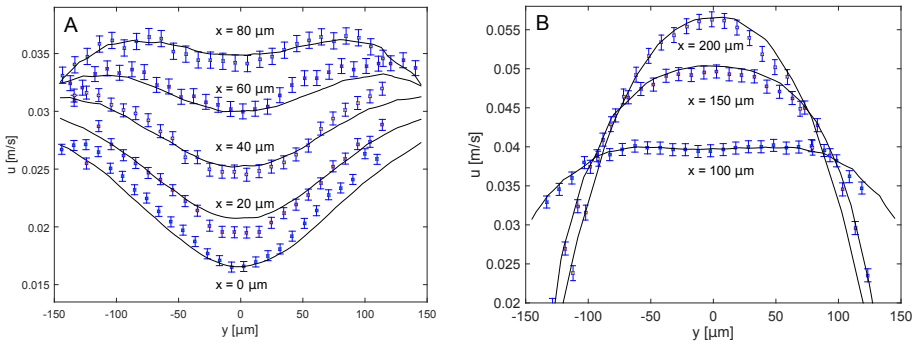

Figure 2.29: Comparison between experimental and numerical data for the configuration 1. The different positions refer to the image depicted in fig. 2.27.

Similar results are achieved for the configuration 2, in which, also for this case, the comparisons between experimental velocity profiles and numerical data are carried out for several position along the streamwise direction of the main stream. The position of the planes used for the comparison is given in fig. 2.28. As an example, in fig. 2.30 is reported the comparison between experimental and numerical velocity profiles obtained for different positions, starting from the central position (x = 0) up to the exit of the T-junction, with a step of 30 µm. In order to give comparable results with the previous case, also in this configuration a volumetric flow rate of 4 ml/h is imposed for the two inlet flows. As expected, the comparisons between experiments and numerical data are in good agreement also for this configuration; the NRMS error between experimental and numerical local velocity is in general lower than 5 % and in the most cases lower than 4 %.

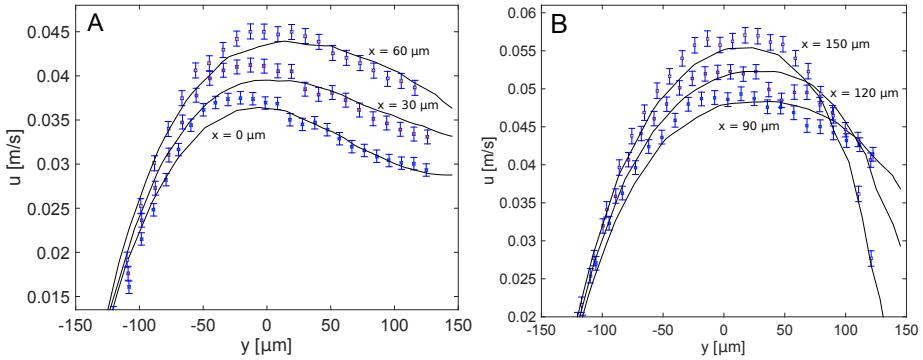

Figure 2.30: Comparison between experimental and numerical data for the configuration 2. The different positions refer to the image depicted in fig. 2.28.

Finally, it is worth to mention that, differently from what made for the straight channel, for the evaluations concerning the micro T-junction, the vector map (see fig. 2.27 and fig. 2.28) does not contained equals row vectors since the flow is not in a fully developed condition close to the center of the T-junction but changes along the streamwise direction. Therefore the process of cross-correlation led to higher uncertainty in the association of the velocity vectors to the cross-section cells. From this reason it can be explained the higher NRMS errors found for the measurements carried for the T-junction, with respect to NRMS values carried out for the straight channel.

2.6 Conclusions

In this chapter has been demonstrated how the μPIV technique can be applied in order to reconstruct the real shape of the inner geometry of a commercial microchannel having an optical access. For this aim two microchannels, one straight and one T-junction, are analyzed and the results for both have been reported. Both the microdevices have a cross-section that differs from the nominal one. In particular the real shape of the cross-section of both microchannels is slightly trapezoidal with acute angles of 88°. The procedure based on μPIV uses the systematic comparison between the experimental data and numerical velocity values carried out for different shapes of the microchannel cross-section in order to minimize the difference between experimental and numerical velocity values. The cross-section geometry which is characterized by the minimum value of the average NRMS error is then taken as the real geometry of the microchannel. SEM analyses on the straight microchannel have confirmed the predictions made via the inverse usage of the μPIV technique. Therefore, the results obtained in this thesis show that this technique can be used for a preliminary investigation of the geometry of a channel. For this reason the methodology proposed in this dissertation, can be successfully used for the estimation of the actual geometry of commercial microchannels. In addition, the proposed methodology has the great advantage to be non-destructive and with particular care is able to detect also significant local singularities of the cross-section geometry. Other microscopy techniques for direct optical observations of the cross-section geometry of a microchannel with an optical access, like the confocal fluorescence microscopy, can be employed instead of the inverse method based on the μPIV measurements shown in this dissertation. However, even if these techniques do not require a numerical solution of the velocity field, they are anyway expensive and require specialist equipments which are not always available in all laboratories devoted to experimental investigations in microfluidics.

2.7 Perspectives

In the future, work must be done in order to obtain the method proposed in this dissertation as automatic. With an automated developed routine it will be possible to evaluate different kinds of cross-section of the microchannel and manage different types of parameters, such as for example different "right" and "left" angles of trapezoidal geometries. In addition, it will be possible to take into account all the common features deriving from the process of manufacturing of the microchannel, like the rounded angles. This will create a very refined methodology and will be suitable also in the situations in which the geometry of the channel is not known in advance.

Chapter 3

Non-encapsulated Thermochromic Liquid Crystals

3.1 Introduction

The measurement of local temperature for a flow inside a microchannels is a difficult task. A review of the experimental techniques proposed for the measurement of temperature in microchannels is given in Chapter 1. All the techniques proposed up to now still present some lacks due to the limitations of these methods in terms of accuracy, applicability and scalability. For this reason, different techniques and methods continue to be under development. One way to perform local temperature measurements in a flow inside a microchannel is given by the thermography through a dispersion of Thermochromic Liquid Crystals (TLCs). TLCs are cholesteric or chiral-nematic liquid crystals that shine different colors when their temperature changes (Lagerwall and Scalia, 2012). The peculiarity of TLCs is that they have properties both of isotropic liquid state (mobility) and solid crystal state (anisotropy, birefringence). When illuminated by a white light circularly polarized, they reflect different light wavelengths in a narrow band, giving back colors ranging from violet/blue in correspondence of the upper limit of their working temperature, to red (lower limit of their working temperature), passing through the intermediary wavelengths by means of a reversible process (Fergason, 1968; Sage, 2011).

The great advantage achieved by using TLC particles, is that, since in this

This chapter is based on the publications:
Puccetti G., Rossi M., Morini G.L. and Kähler C.J., 2016, Sensitivity to shear stress of non-encapsulated thermochromic liquid crystal (TLC) particles for microfluidic applications, *Microfluidics and Nanofluidics*, **20**(1):1-7. http://dx.doi.org/10.1007/s10404-015-1694-x.

Puccetti G., Rossi M., Kähler C.J. and Morini G.L., 2015, Non-encapsulated thermoliquid crystal particles: a way for temperature measurements inside microchannels, *33rd UIT Heat Transfer Conference*, L'Aquila, 22-24 June 2015.

case the thermography is based on hues of the particles and not on fluorescence, point-wise measurements can be made without any volumetric integration. For this reason the thermography via these particles ensures a higher spatial resolution compared to the employment of fluorescent dyes or luminophores. In addition, the motion of TLC particles can be also tracked either through an Eulerian scheme, such as with the PIV technique (Park et al., 2001; Stasiek and Kowalewski, 2002; Pottebaum and Gharib, 2006), or a Lagrangian scheme, such as by means of APTV technique (Segura et al., 2015). In this way, by using a single type of tracer is possible to perform, at the same time, local measurements on both temperature and velocity.

Pure TLC material, has been used as film depositions by many researchers (Buffone and Sefiane, 2005; Muwanga and Hassan, 2006; Wagner and Stephan, 2006) for surface temperature measurements, while for applications in which the crystals were involved as fluid tracers, the bulk material was so far coated with a polymeric shell in the form of encapsulated beads (Chaudhari et al., 1998; Park et al., 2001; Basson and Pottebaum, 2012).

Encapsulated TLCs with diameters of the order of 10 - 20 µm (*R-30 Japan Capsular Product Inc, Tokyo*) were successfully employed by Ozawa et al. (1992) as flow tracer to determine the temperature and bidimensional velocity distribution in Hele-Shaw cells through a color-image-processing approach. The encapsulated TLCs were dispersed into two silicon oils with a kinematic viscosity of 3 cSt and 20 cSt respectively, with a concentration of TLCs in oil of the order of 0.1% in weight. The authors demonstrated that this technique allows a temperature measurement affected by a resolution of 0.3 K over a range of about 2 K (from 28.1 °C to 29.9 °C).

In microchannels, temperature measurements using the encapsulated TLCs as seeding particles in a deionized water flow, were carried out by Basson and Pottebaum (2012). The microchannel employed had a squared cross-section with a side of 100 µm and it was realized in fused silica; the encapsulated TLCs had a diameter in the range of 10 - 15 µm. Particular care was used in order to detect correctly the color reflected by the encapsulated crystals. First of all, they adopted a filtering system in order to avoid the background bright noise and to improve the quality of the signal given by the particles, then they used a Hue Saturation Intensity scheme (HSI) in order to correlate the colors shined from the particles with their temperature. With the adopted method Basson and Pottebaum (2012) were able to measure the local flow temperature with an accuracy of 0.4 K - 2.4 K over a temperature range of 7.4 K (36.3 °C - 43.7 °C).

Nevertheless, the encapsulation process is not the best solutions for the detection of the color reflected from the liquid crystals, since the polymeric shell around the particles strongly decreases the quality of the signal. In fact, the external shell introduces additional light reflections that are not related to the core of the liquid crystal (Segura et al., 2013); as a consequence, the color shined by the TLC particles is affected from the external coating, entailing an additional bias error on the temperature measurements. For this reason, when

encapsulated particles are used, accurate temperature measurement cannot be carried out using a single TLC particle and only average temperature data can be retrieved (Basson and Pottebaum, 2012). On the other hand, the encapsulation process prevents possible mechanical corruptions of the core structure of the liquid crystals, therefore the improvement of temperature measurements via individual TLC particles passes through the development of stable suspensions of non-encapsulated TLCs.

An example of suspended non-encapsulated TLCs used in order to evaluate the temperature and velocity distribution of glycerol in Rayleigh-Bénard convection cells can be found in the work of Ciofalo et al. (2003). In this work the authors used droplets of suspended TLCs with diameters of the order of 100 µm (*Hallcrest BN/R20C12 W*) in a glycerol layer (ρ = 1261 kg m^{-3}, μ = 1.5 Pa s). The involved TLCs were suitable for temperature measurements in the range between 20 °C and 32 °C. A PIV approach was used in order to obtain data on the velocity field while the temperature measurements were carried out through a HSI correlation. Average uncertainties of the order of ± 10 % were reported from Ciofalo et al. (2003) for both temperature and velocity distributions. However, the authors demonstrated that stable suspensions of pure TLCs can be obtained and proficiently used only when the droplets of liquid crystals are dispersed inside solutions in which they are immiscible. On the contrary, the dispersion in water of the non-encapsulated TLC proposed by the authors is not eligible.

At the best knowledge of the author, a stable suspension of non-encapsulated TLC particles in water solutions was only recently proposed by Segura et al. (2015) with the aim to use this particles for three-dimensional velocity and the temperature measurements. The authors have utilized unsealed TLCs particles having diameters of the order of 13 µm, produced from a membrane emulsification process in which the liquid crystal bulk material (*Hallcrest UN R20C1W*) was dispersed inside an aqueous solution of poloxamer 188 and thiomersal (Segura et al., 2013; Segura, 2014). Segura et al. (2015) used a POD correlation between the temperature of the particles and their color in order to determine the water temperature distribution and the APTV method in order to track the particles motion inside the water droplet. Experimental uncertainties of ± 0.1 K over a range of 1.5 K (6.7 %) were reported from the authors. However, no further studies about the stability of this kind of non-encapsulated particles were reported up to now.

3.2 Aim of the work

In this thesis a series of experimental tests are conducted with the aim to check if non-encapsulated TLC particles can be proficiently used in microchannels with water flows without to put in evidence an alteration of the particles' color linked to the presence in the flow of a shear stress. More precisely, the tests are addressed to show if the effect of the shear rate on the particles induces or not a modification of their crystal structure by modifying the reflected light from particles at a fixed local temperature. Furthermore, the experimental measurements have been oriented to the detection of the maximum value of the shear rate in correspondence of which the TLC particles start to collapse.

The experimental part of this work was realized in the laboratory of the Microfluidic Research Group at the Institute of Fluid Mechanics and Aerodynamics (LRT 7) of Universität der Bundeswehr München.

First of all, the mechanical and optical stability of the non-encapsulated TLC particles have been tested in a series of experiments in which different values of shear rates were applied on the particles' surface (Section 3.5). The study was conducted on TLC particles stuck to the bottom surface of a microchannel in which the working fluid was forced to flow by means of a syringe pump. The microchannel was carved from a copper substrate then sealed with a typical microscope glass slide. In this way three walls of the microchannel were kept at a constant temperature while the bottom one, the transparent wall where the particles were stuck, resulted to be nearly adiabatic. The shear rates applied to the particles' surface was regulated through the syringe pump by imposing a constant flow rate of water.

An experimental investigation of the 3D velocity field and temperature distribution via APTV for a laminar water flow in a microchannel was later performed (Section 3.7). This experimental test was made using the same microchannel used during the tests described in Section 3.5. As for previous experiments, the Peltier device imposed a fixed temperature to the walls of the microchannel. However, due to the color camera sensitivity and to the low power of the illumination source, the maximum flow rate that could be properly investigated is limited to 0.05 ml/h. This means that for those flow rates, the fluid bulk temperature was equal to the imposed temperature at the walls after an entrance length of 50 μm, therefore the temperature of the fluid was uniform on the whole cross-section and along the axial direction. The experimental test on the stability of the non-encapsulated TLC have been conducted under quasi-isothermal conditions. In order to test the TLC particles under a significant axial temperature gradient along the microchannel a specific test rig has been designed and manufactured by IMTV-KIT (Germany). The description of the test rig for non-isothermal tests is given in Section 3.8. Unfortunately, no experimental tests have been concluded before the closure of this thesis. However, the planned tests will be conducted in Munich in next future, beyond the deadline of this Ph.D. thesis.

3.3 Fundamentals of thermochromic liquid crystals

The "liquid crystals" term is referred to those materials existing in a mesomorphic phase (see fig. 3.1) in which they exhibit characteristic long range order interactions, such as optical properties of anisotropy and birefringence typical of a crystalline solid, maintaining the dynamical macroscopic behavior of a liquid.

Early works concerning the liquid crystals have to be attributed to Reinitzer (1888) and Lehmann (1889). In his work, Reinitzer observed that the chemical compound of cholesteric benzoate had a double melting point: at 145.5 °C the solid crystal melted into an opaque and cloudy liquid (Melting point in fig. 3.1), whereas the turbidity suddenly disappeared if the cholesteric benzoate was heated beyond its second melting point at 178.5 °C (Clearing point in fig. 3.1) giving to the liquid a clear appearance. One year later, Lehmann (1889) cited the compound found by Reinitzer as a "flowing crystals", later defined by himself with the currently used name of "liquid crystals". At the end of his work, Lehmann has outlined this discovery as the first time in which a liquid with birefringence property was observed.

Nowadays, the accepted classification system of the thermochromic liquid crystals' phases (graphically represented in fig. 3.1), is based on the work of Friedel (1922).

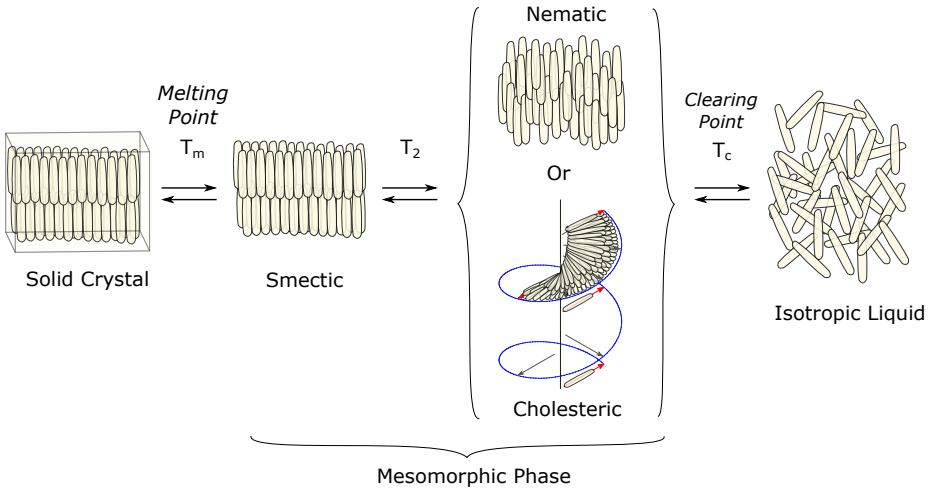

Figure 3.1: Schematic representation of phase transitions typical of thermochromic liquid crystals (Image adapted from Hallcrest LCR (2014)).

Friedel, defined the reversible transition region between the solid crystalline state and the isotropic liquid state, as a mesomorphic phase in which two distinct different phases may be present together: the smectic phase (fig. 3.2) and the nematic phase (fig. 3.3).

In the smectic mesophase, the liquid crystal is characterized by proper-

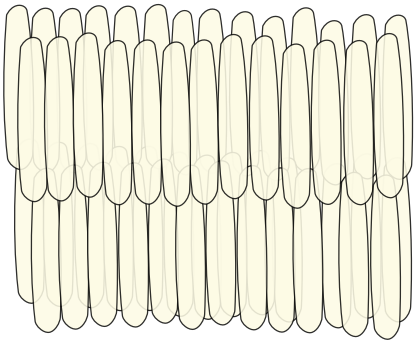

Figure 3.2: TLC in a smectic phase.

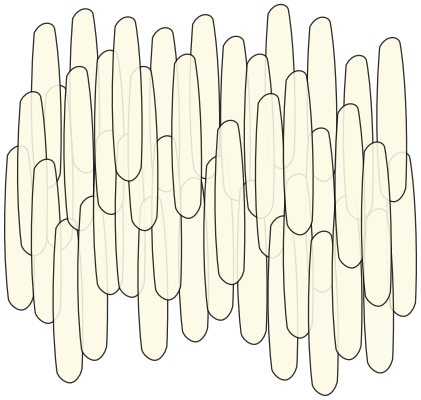

Figure 3.3: TLC in the nematic phase.

ties similar to those of soaps at ordinary temperatures (Friedel, 1922). In this mesophase the rod-shaped molecules that composes the liquid crystal structure, are organized into layers in which the molecules are parallel to each other (see fig. 3.2). Moreover, the smectic mesophase can have further long-range orders within each layer, entailing consequently the development of different smectic structures (see works of Brostow (1990) and de Gennes and Prost (1993)). In the nematic mesophase (fig. 3.3) the structural order of the liquid crystal is reduced. This is the simplest phase in which the liquid crystal can exist in the mesomorphic state. In the nematic phase the molecules remain substantially oriented in the same way, but there is no further positional orders or layered structures (Brostow, 1990; Lagerwall and Scalia, 2012).

If chiral molecules are added to the liquid crystals, the compound shows an additional chiral behavior, generating the so called chiral-nematic or cholesteric mesophase, the most striking and studied phase among the thermochromic liquid crystals' mesophases (Lagerwall and Scalia, 2012). As outlined in the *Handbook of Thermochromic Liquid Crystal Technology* provided by Hallcrest LCR (2014), cholesteric (Ch) liquid crystals and chiral-nematic (N*) liquid crystals differ themselves for their chemical composition: ChLC are compounds characterized by the presence of cholesterol and/or other sterol derived chemicals, while N*LC are compounds made up without the employment of sterol based chemicals. In works where the TLCs are used for thermometric purposes, they refer to liquid crystals in their Ch or N* mesophase. As for the smectic and nematic mesophases, each single molecule that composes the TLC's Ch or N* mesophase is "rod-shaped". It becomes possible to define a molecular versor along the longitudinal axis of each rod-shaped molecule, called molecular director (see fig. 3.4). Furthermore, the cholesteric mesophase shows a continuous self-assembled twisted structure along the direction normal to each molecular versor. For this reason, the overall structure of the liquid crystal is an helicoidal structure having

a defined helical pitch p (de Vries, 1951; Sage, 2011; Lagerwall and Scalia, 2012).

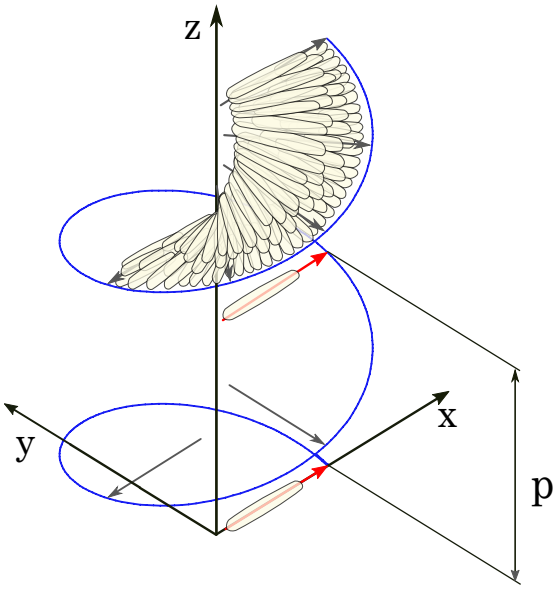

Figure 3.4: Thermochromic liquid crystal structure in the cholesteric phase. p is the pitch of the helical path.

The structural anisotropy of TLCs in the Ch or N* mesophase, causes their optical anisotropy; which means that the refractive index parallel to the molecular long axis (n_e) is different from the refractive index orthogonal to the molecular long axis (n_0). In particular the Ch or N* structures are uniaxial with an optical axis directed along the helical path. Consequently, the refractive index perpendicular to the molecular long axis is generally greater than the parallel one. The TLCs' birefringence can be expressed by means of the difference of refractive indexes: $\Delta n = n_e - n_0$ (Fergason, 1966; Sage, 2011; Lagerwall and Scalia, 2012).

Therefore, circularly polarized light with an handedness that matches the twist of the cholesteric liquid crystal's structure, is reflected by the twisted structure of the liquid crystal, in an analogous way to Bragg reflection from a layered structure (Sage, 2011), within a narrow band of wavelength $\Delta\lambda$ without a change of its polarization sense. The value of $\Delta\lambda$ can be linked to the refractive indexes by means of the following relationship:

$$\Delta\lambda = 2\lambda \cdot \frac{(n_e - n_0)}{(n_e + n_0)} = p \cdot (n_e - n_0) = p\Delta n \tag{3.1}$$

The light reflection is centered at a wavelength λ which is directly proportional to the helical pitch p of the twisted rod-shaped molecules (Dreher and Meier, 1973; Ha et al., 2008; Sage, 2011; Noh et al., 2014):

$$\lambda = p \cdot (n_e + n_0)/2 \tag{3.2}$$

A huge effort has been made from researchers in order to describe accurately the structure of thermochromic liquid crystals and quantify their related optical properties; for a further and deeper reading about this, the readers are invited to refer to the following works: Oseen (1933); de Vries (1951); Fergason (1966, 1968); Adams et al. (1969); Berreman and Scheffer (1970a,b); Melamed and Rubin (1971); Dreher and Meier (1973); Belyakov et al. (1979); Brostow (1990); de Gennes and Prost (1993); Abbate et al. (2007); Sage (2011); Lagerwall and Scalia (2012); Chen and Yeh (2012) and Noh et al. (2014).

Since the pitch p of the helical path varies in relation to the crystal's temperature, TLCs can be used as temperature sensors. Two different mechanisms are in competition when the temperature of the TLCs increases: an increase of the temperature determines an increase of the intermolecular distances between the rod-shape molecules and in the same time a more pronounced twist of the TLCs' structure. The consequence of the first mechanism is a more elongated helical path (a longer pitch p) and consequently in a longer wavelength of the reflected light, while the second one acts in the opposite way resulting in a decrease of the helical pitch p length and associated reflected wavelength (Hallcrest LCR, 2014). For the majority of commercial TLCs proposed for temperature measurements, the second mechanism dominates over the first one and the color shined by TLC particles changes from red to blue passing through the green as the temperature of the TLCs increases. For example in fig. 3.5 is reported the color trend of non-encapsulated TLC particles within a temperature range of 10 K. As it is visible from the figure the particles start to shine a red color at 20 °C and reaches the blue coloration at 30 °C, passing through the green color and related shades between the red, green and blue color.

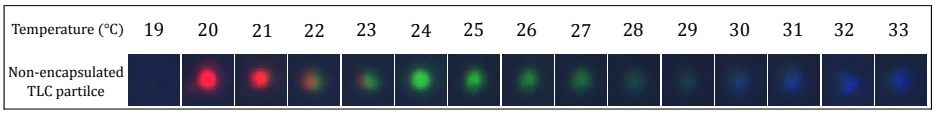

Figure 3.5: Example of the color play shined from non-encapsulated TLCs particles (made with Hallcrest bulk material "R20C10W").

The color play of TLCs, *i.e.* the temperature difference between the "blue" temperature and the "red" temperature, can be selected during the production phase. Several TLC mixtures are currently commercially available for different working temperature ranges starting from - 30°C up to 115°C as it is shown in the *"Handbook of thermochromic liquid crystal technology"* provided by the Hallcrest LCR (2014).

3.3.1 TLC colorimetry

In the previous paragraph how the TLCs reflect selectively colors in relation to the their temperature have been described. From an experimental point of view, the accuracy of the temperature measurement is related to the ability of capturing correctly the colors shined from these particles and to their correct interpretation. In microfluidics, the light reflected from TLCs can be recorded by a charged-coupled device (CCD) array sensor, coupled to the optics of an inverted microscope. However, since the CCD array sensor is generally monochromatic, a filter system must be involved in order to selectively detect the light wavelengths reflected by the TLCs. As also reported in the PhD dissertation of Segura (2014), there are two main ways to realize this filtering system:

- The first one is the so called *Bayer Mosaic sensor* or *Bayer filter mosaic* which consists in arranging a filter composed by several filters of single pixels sensible to red, green and blue wavelengths on the squared grid of the CCD sensor. In this system each surrounding pixel detects a different color with respect to the central one, while globally the filter reconstructs the color pattern associated to the image recorded. This filter system is involved when a single CCD sensor is employed.
- The second system is based on a prism placed along the light path and it is used in combination with 3 CCD sensors. The prism filter is able to split the red, green and blue wavelengths which are recognized by the three CCD sensors. This filtering system guarantees a better resolution compared to the first one since all the pixels of each single CCD sensor carry out the desired information.

In this work, a 8 bit 3CCD color camera (second system) is employed as acquiring system. In this way, 3 different matrices, one for each CCD sensor, which respectively contain the information of monochromatic intensity of the red, green and blue wavelengths, were generated for every recorded image of TLC particles.

The simplest way to analyse the colors recorded and consequently the temperature of TLCs, is to use directly the intensity data linked to red, green and blue (RGB, see equations 3.3) hue of the particles acquired by the 3CCD color camera, creating therefore a calibration curve (Vejrazka and Marty, 2007; Dabiri, 2009).

If P_λ is the spectral power of the light source and $\bar{r}(\lambda)$, $\bar{g}(\lambda)$, $\bar{r}(\lambda)$ are the tristimulus spectral color-matching average functions (Dabiri, 2009), it is possible to obtain RGB data by the following equations:

$$\begin{aligned} R &= \int P_\lambda \bar{r}(\lambda) d\lambda \\ G &= \int P_\lambda \bar{g}(\lambda) d\lambda \\ B &= \int P_\lambda \bar{b}(\lambda) d\lambda \end{aligned} \tag{3.3}$$

By knowing the value assumed by the R, G, B components, the color of the particles is univocally determined by using the colorimetric rules established by the Commission Internationale de l'Eclairage (CIE) in 1931. Therefore, it is possible to build a calibration curve directly starting from the RGB data. It is possible to demonstrate that the RGB color space based only on the hue values of the acquired images is not the optimal space to make a robust correlation between the detected colors and the temperature of the particles. In fact, a calibration made directly on the RGB color space is based only on the relationship between the particles' hue and their temperature while information about the intensity and saturation of recorded colors are not used. These variables are taken into account in the HSI (Hue - Saturation - Intensity) color space which represents the improvement of the RGB color space. The definition of the Intensity (I), Saturation (S) and Hue (H) based on the values of R, G, B are recalled here:

$$\begin{aligned} I &= max(R,G,B) \\ S &= (I - min(R,G,B))/I \\ H &= \frac{1}{6}\begin{cases} (G-B)1/S & if \quad R > B,G \\ 2+(B-R)1/S & if \quad G > R,B \\ 4+(R-G)1/S & if \quad B > R,G \end{cases} \end{aligned} \tag{3.4}$$

The (3.4) is not the unique way to transform the RGB color space into the HSI color space. Other and more complicated transformations could be found in the works of Hay and Hollingsworth (1996, 1998); Fujisawa and Funatani (2000); Pratt (2001); Russ (2002) and Roesgen and Totaro (2002). The transformation described by (3.4) is implemented by the function `rgb2hsv`of Matlab.

A further step in the calibration approach is performed by the statistical calibration approach in which the proper orthogonal decomposition (POD) is applied to the RGB color space in order to transform the raw digital image data into a compressed space of uncorrelated variables. This approach was proposed by Roesgen and Totaro (2002).

First of all, a set of N discrete R,G,B calibration triplets is used to build a set of N normalized RGB values by using the following relationships:

$$\begin{aligned} r &= R/(R+G+B) \\ g &= G/(R+G+B) \\ b &= B/(R+G+B) \end{aligned} \tag{3.5}$$

Now it is possible to calculate the covariance matrix **C** defined as follows:

$$\begin{aligned}\mathbf{C} &= Cov(r,g,b) \\ &= \begin{pmatrix} \overline{(r-\bar{r})^2} & \overline{(r-\bar{r})(g-\bar{g})} & \overline{(r-\bar{r})(b-\bar{b})} \\ \overline{(r-\bar{r})(g-\bar{g})} & \overline{(g-\bar{g})^2} & \overline{(g-\bar{g})(b-\bar{b})} \\ \overline{(r-\bar{r})(b-\bar{b})} & \overline{(g-\bar{g})(b-\bar{b})} & \overline{(b-\bar{b})^2} \end{pmatrix}\end{aligned} \tag{3.6}$$

where the mean values $\bar{c}$ are calculated as $\bar{c} = \frac{1}{N}\sum_{1}^{N} c_n$.

Then the POD or Karhunen-Loève transform is expressed by the linear transformation:

$$\begin{bmatrix} x_1 \\ x_2 \\ x_3 \end{bmatrix} = \mathbf{T} \begin{bmatrix} (r-\bar{r}) \\ (g-\bar{g}) \\ (b-\bar{b}) \end{bmatrix} \tag{3.7}$$

where **T** is a rotation matrix in which the eigenvectors $\mathbf{t}_1$, $\mathbf{t}_2$ and $\mathbf{t}_3$ are disposed in rows such that $\mathbf{T}^{-1} = \mathbf{T}^t$. The coefficients $\mathrm{T}_{i,j}$ are given by the condition that the new covariance matrix must be diagonal (Roesgen and Totaro, 2002):

$$Cov(x_1,x_2,x_3) = \begin{bmatrix} \lambda_1 & 0 & 0 \\ 0 & \lambda_2 & 0 \\ 0 & 0 & \lambda_3 \end{bmatrix} \tag{3.8}$$

This leads to the establishment of an eigenvalue problem where the eigenvectors **t** are determined by solving the following equation:

$$\mathbf{Ct} = \lambda\mathbf{t} \tag{3.9}$$

The final results is that only the first two components x_1 and x_2, which are respectively related with the direction of the eigenvalues λ_1 and λ_2, carry all the relevant information of the color while the component x_3 is null since the eigenvalue λ_3 always vanishes due to the data normalization. In this way an optimal data compression is provided without losing any original information. The issue of the temperature calibration of the TLC particles based on their color has been the subject of the work of many researchers over the last twenty years as demonstrated in the works of Dabiri and Gharib (1991); Behle et al. (1996); Smith et al. (2001); Rao and Zang (2010); Cukurel et al. (2012) and reported in the reviews of Dabiri (2009) and Abdullah et al. (2010).

These three mentioned methods were used by Segura et al. (2013) in their study on the temperature calibration of the non-encapsulated TLCs. In addition, Segura in his PhD dissertation has performed a study on the same non-

encapsulated TLC particles used in the present PhD dissertation, in which the three different calibration methods presented above were compared in order to find the best way to correlate the color reflected from the TLCs with their temperature. As conclusion of his study, Segura stated that the temperature calibration performed with the POD variable space resulted to be more robust than the calibrations performed with the RGB or HSI color spaces. In particular, in comparison with the RGB color space, the calibration based on the POD of the RGB data uses only two uncorrelated variables instead of the three used by the RGB color space, resulting to be best suited for a reversible correlation between the temperature and hue of the TLC particles. For what concerns the calibration by using the HSI variable space, the author found that it yields higher errors in comparison with the calibration based on the POD variable space, in particular for the higher temperature (blue coloration of the particles). His studies were carried out on four different kinds of non-encapsulated TLC particles that differ for their temperature range (ΔT = 1K, 5K, 10K and 20 K) while all the particles had the same temperature starting point equal to 20°C. The three kinds of particles with ΔT = 5K, 10K and 20K showed a standard deviation from the average measured temperature in the range of 2 - 5 % for all the temperature range with the temperature calibration realized using the POD variable space. On the contrary, the particles with ΔT = 1K exhibit higher uncertainties (2 - 8 %). These uncertainty values are related to the use of a lens with a magnification of 20×, while with a lens with a magnification of 10× the standard deviation from the average measured temperature resulted to be higher and in many cases was over the 6 % (Segura, 2014). In addition for the studied particles, Segura did not find any substantial effect of hysteresis nor bleaching of the material, concluding that the non-encapsulated TLC particles were a viable solution for the measurement of local temperature in microflows.

As concerns the studies and results reported in this dissertation, both the HSI (Eq. (3.4)) and the POD variable spaces (Eqs. (3.5) - (3.9)) have been used and finally the POD variable space was chosen as the best calibration method for coupling the colors shined from the TLC particles with their temperature.

3.3.2 Non-encapsulated TLC particles

The non-encapsulated TLC particles analyzed in this work are produced at the Institute of Pharmaceutical Technology of the Braunschweig University of Technology. These non-encapsulated particles are suitable to be dispersed inside aqueous solutions and have three different temperature working ranges: ΔT = 1 K, 5 K and 10 K. All the three kind of particles start to reflect red wavelengths at 20 °C, hence the blue coloration and intermediate shades are shined from the TLCs depending to their own temperature range. In order to provide an aqueous stable dispersion of unsealed TLCs, the particles were produced by means of an emulsification process via a Shirasu Porous Glass (SPG) membrane (Joseph and Bunjes, 2014) having pores with a size of the order of 5.5 µm, in which the

poloxamer 188 was employed as emulsifier and the thiomersal as preservative. The bulk material was provided by the *Hallcrest LCR* and in the specific case *R20C1W* was used for the particles with a $\Delta T = 1$ K, *R20C5W* for the particles with a $\Delta T = 5$ K and *R20C10W* for the particles having a $\Delta T = 10$ K. After the emulsification process, the non-encapsulated TLC particles were cooled below their melting point, *i.e.* 20 °C, and stored at this temperature inside an aqueous solution. For the subsequent employment as suspended tracers, the mixture containing the non-encapsulated TLC particles was further diluted inside the working fluid (deionized water) with the addition of pure sodium iodide in order to balance the density of the bulk TLCs mixture with the density of the deionized water. The full description of the emulsification process can be found in Segura et al. (2013) and Segura (2014).

An image in which the non-encapsulated TLC particles are observed through a magnification of 20 × and a filtering system is reported in fig. 3.6.

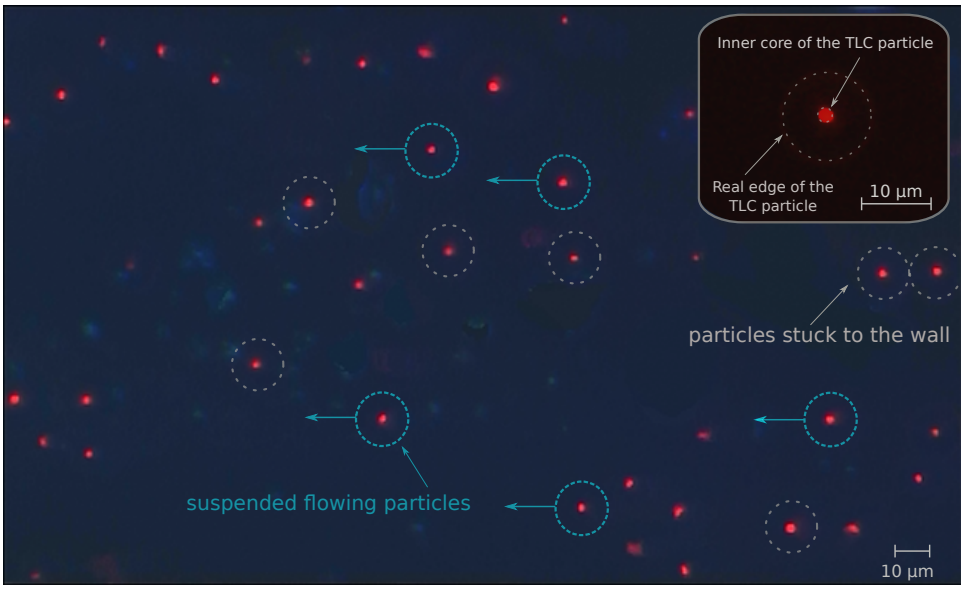

Figure 3.6: Non-encapsulated TLC particles at a fixed temperature (20.2 °C) inside a microchannel: the suspended flowing particles are marked by the circles with an arrow while stuck particles are marked from the gray dotted circles. The top right box shows a zoom of a TLC particle in which both the real edge of the particle and its central core are visible. As it is shown from the inset, only the central core of the particle reflects light depending on its temperature, while the peripheral area is almost transparent.

In the previous image, all the TLCs are kept at a fixed temperature (20.2°C) and both the suspended non-encapsulated TLC particles and the stuck particles to the transparent wall of a microchannel are visible. Suspended non-encapsulated TLC particles are marked by a light blue circle with an arrow while the particles stuck are marked by a dotted gray circle. As it is visible from fig. 3.6 there is no

a marked visible difference between the stuck particles and the moving ones. However, as it is appreciable from the inset in top right of fig. 3.6, only the central core of the unsealed TLC particle (diameter in the order of 13 μm) shines of a visible color. This puts a lower limit to the required minimum magnification of the particles in order to perform reliable observations, entailing consequently a reduced area of the total field of view of the acquired images. For instance, as highlighted by Segura (2014), objective lenses with a magnification of 10 × cannot be used in order to gain reliable observations from these particles and only magnifications of 20 × or higher have to be employed.

3.4 Experimental Apparatus

The experiments on the non-encapsulated TLCs were performed in the laboratory of the Institute of Fluid Mechanics and Aerodynamics (LRT-7) of the Universität der Bundeswehr München (Neubiberg, Germany). A simple sketch of the complete experimental test rig is presented in fig. 3.7.

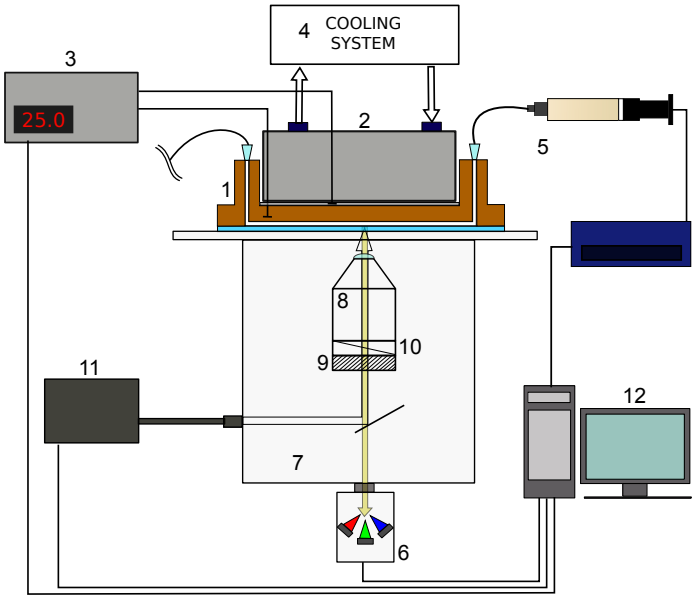

Figure 3.7: Experimental test rig layout. *(dimensions not in scale)*

The main components of the test rig are the followings: 1) Copper microchannel 2) Heating device 3) Thermal control unit 4) Cooling system of the heating device 5) Syringe pump 6) RGB color camera 7) Inverted Microscope 8) Objective lens 9) Filter: linear polarizer 10) Filter: achromatic quarter wave plate 11) White light source 12) Acquisition software.

3.4.1 Microchannel, heating system and injection

The microchannel (1 in fig. 3.7) in which the particles are analyzed is manufactured through a milling process on a copper substrate and have a rectangular cross-section with sides of 500 µm and 200 µm (width and depth). The optical access is assured by a microscope glass slide (1 mm in thickness) bonded to the copper substrate in which the microchannel has been carved (fig. 3.8). In this way the microscope slide acted also as the bottom microchannel wall on which the TLC particles are let to deposit. A Peltier cell (2) is used in order to fix the wall temperature on the copper side of the microchannel. The control of the Peltier cell is executed automatically through a customized unit (Peltier-Controller TC2812 *CoolTronic GmbH*, 3) directly connected to the in-house software developed in

the Matlab environment for the acquisition of the images. The temperature of the microchannel wall is measured by a mini Pt1000 RTD sensor directly enclosed in the copper substrate through a specific carved hole (fig. 3.8 (B)). Hence, since the Peltier cell is in direct contact with the whole outer surface of the microfluidic device, due to the high thermal conductivity of the copper substrate ($k_{Cu} \sim 400$ W/mK), a constant temperature as boundary condition for all the copper walls can be assumed, while the glass slide ($k_g = 1.4$ W/mK) can be considered as a nearly adiabatic wall. A custom cooling system (4) is coupled with the Peltier cell in order to guarantee the right operation of the device.

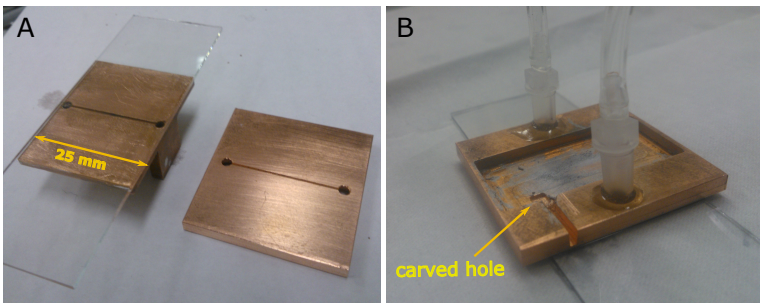

Figure 3.8: Bottom view (A) and top view (B) of the microchannel carved into the copper substrate and sealed to a microscope slide. In the picture B is visible the hole carved into the copper substrate for housing the mini Pt1000.

A servo driven high precision syringe pump (*Cetoni neMESYS*, 5) is used for injecting the working fluid with suspended particles inside the microchannel. A Hagen – Poiseuille flow is established inside the microchannel, hence for a given flow rate the flow velocity distribution can be analytically calculated. All the connecting tubes are polymeric minichannels with an inner diameter of 0.762 mm (0.03 inch).

3.4.2 Image acquisition system

The microchannel is placed upon an inverted microscope (*Zeiss Observer Z.1*, 7) and observed through an objective lens with a magnification of 20 x (*LD Plan-NEO-FLUAR*, M=20x and NA=0.4, 8). Hence, the images are recorded by means of an RGB color camera (6) *JAI AT-200 GE*, with 3 Progressive Scan CCDs having 8 bit each, directly connected to the inverted microscope. In order to enhance the quality of the images acquired, a polarizing filter is placed just below the objective lens. Specifically, the filter is composed by a linear glass polarizer (*Edmund Optics NT47-216*, 9) with its axis aligned at 45° from the fast axis of an achromatic quarter wave plate (*Melles Griot ACWP 400-700-06-4*, 10). In this way the light that is transmitted to the TLC particles results to be circularly polarized. Therefore, the circularly polarized light that matches in a narrow-band of wavelengths the twisting of the TLC molecules is reflected from them. Moreover, since the TLCs does not invert the handedness of the reflected light, the wavelengths reflected

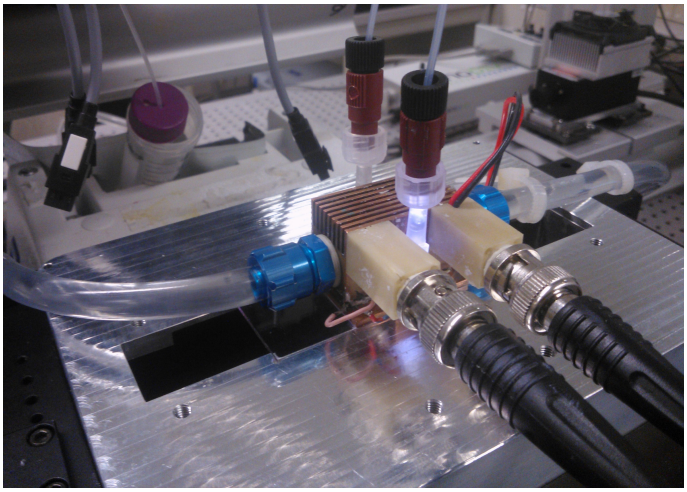

Figure 3.9: Picture of the coupling between the microchannel and the Peltier heating device.

from the TLCs travel back through the filter and reach the RGB color camera. On the contrary, the other surfaces like the metal boundaries, invert the sense of the circularly polarized light, preventing consequently to reflected light by them to pass through the filter. The final result is that only the light reflected by the TLCs is able to travel back through the filter while other unwanted reflections are blocked (Basson and Pottebaum, 2012; Segura et al., 2015).

The illumination source is chosen in order to prevent the saturation of the RGB components of the light reflected by the TLCs. For this reason, a white light engine (*Lumencor Spectra X*, 11) which produces a tunable set of the emitted light wavelengths across the visible spectrum, starting from six solid-state light sources, is selected as the proper way to illuminate the non-encapsulated TLC particles (Segura, 2014). The light provided by the light engine is sent to the rear aperture of the microscope through an optical fiber and redirected to the filtering system via a bright-field filter cube, mounted inside the inverted microscope. All the setup is placed on a damped optical table in order to avoid any effect due to vibrations. The post-processing of the images, such as the color detection and temperature calibration, is performed through a code written in Matlab (12). A picture of the experimental test rig is showed in fig. 3.10 and fig. 3.11. More picture of the experimental test rig are reported in the Appendix A.

Figure 3.12 and fig. 3.13, show two images of the non-encapsulated TLC particles, taken by the RGB color camera, with the employment of the described experimental test rig. Both images refer to the TLC particles having a temperature range $\Delta T = 5$ K (*Hallcrest UNR25C5W*). In particular in fig. 3.12 the temperature of the Peltier device is set to 20.6 °C and the particles appear as red dots, while in fig. 3.13, the temperature of the Peltier device was set to 22.2 °C and the particles appear as green dots.

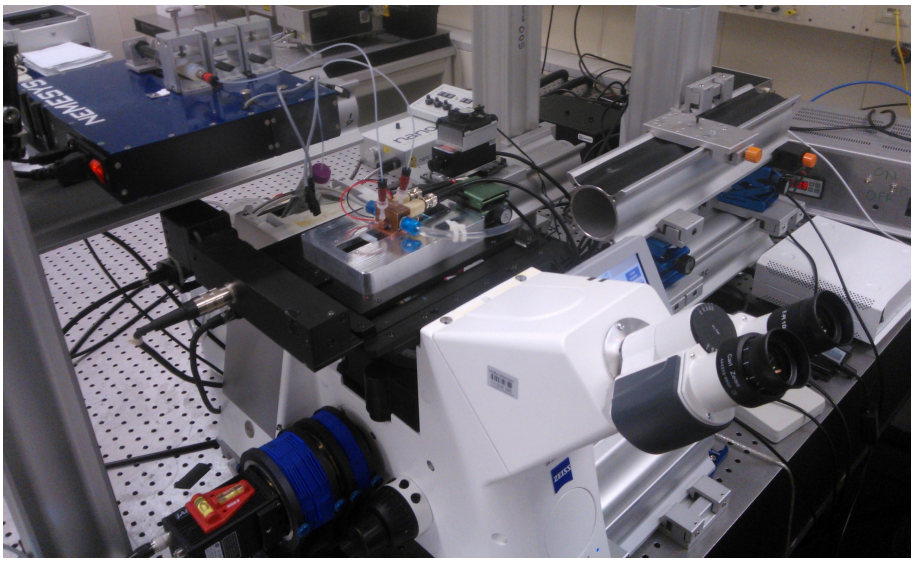

Figure 3.10: Front picture of the experimental apparatus.

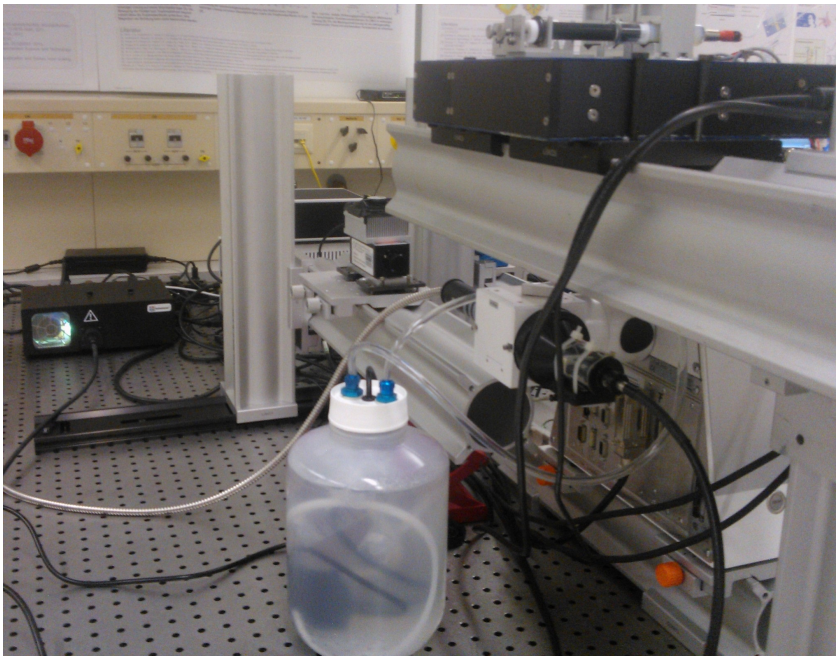

Figure 3.11: Rear picture of the experimental apparatus.

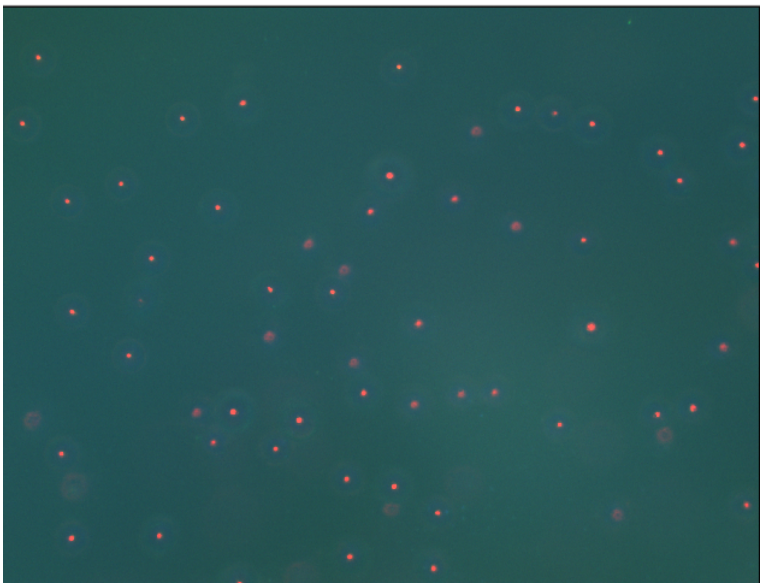

Figure 3.12: Non-encapsulated TLC particles (*Hallcrest UNR25C5W*) at 20.6 °C.

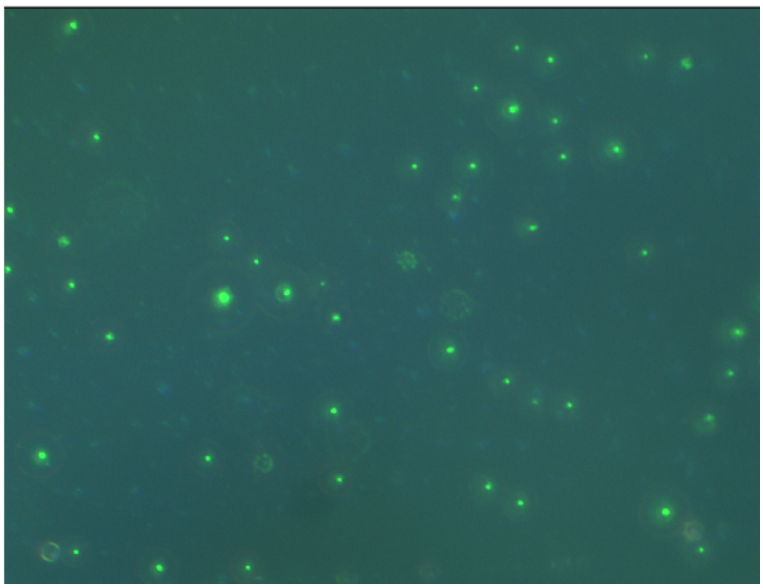

Figure 3.13: Non-encapsulated TLC particles (*Hallcrest UNR25C5W*) at 22.2 °C.

A summary of the main characteristics of the instruments used in the described test rig is reported in Table 3.1.

Table 3.1: Summary table of the principal components of the experimental setup.

Ref.	Component	Description
1	Microchannel	Milling in a Copper substrate, Glass bottom wall k_{Cu} = ~400 W/mK, k_g = 1.4 W/mK Width = 500 µm, Depth = 200 µm, Length = ~25mm
3	Peltier Controller	TC2812 Peltier-Controller *CoolTronic GmbH* with a mini Pt1000 thermocouple PID-Controller, Parameters programmable Reading- and Control range: -50.0 to +150.0°C nominal monitoring –75.0 to +175.0°C Reading resolution: 0.1 K
5	Syringe Pump	Cetoni neMESYS GmbH Low Pressure Syringe Pump servo drive Position & velocity: closed loop PID control Syringe: Hamilton Gastight 10.0 ml with 14:1 gear box: · min flow rate: 0.012 µl/min (Qmixelements) · min flow rate: 0.8 µl/min (user interface) · min flow rate pulsation free: 10.42 µl/min · max flow rate: 63.29 ml/min with 29:1 gear box: · min flow rate: 0.004 µl/min (Qmixelements) · min flow rate: 0.8 µl/min (user interface) · min flow rate pulsation free: 5.02 µl/min · max flow rate: 30.52 ml/min
6	RGB Color Camera	*JAI AT-200 GE* 3CCD Progressive Scan RGB Color Camera 1624 x 1236 pixels for each CCD Compact RGB prism for C-mount lenses 15.4 frames per second with full resolution 24-bit RGB (8-bit per sensor),
7	Inverted Microscope	Axio Observer Z1 (*Carl Zeiss AG*)
8	Objective Lens	LD Plan-NEOFLUAR Corr Ph2 M27 (*Carl Zeiss AG*) Magnification = 20×, Numerical Aperture = 0.4
9	Linear Glass Polarizer	Edmund Optics NT47-216 Wavelength Range = 400 - 700 nm Extinction Ratio = 10000:1
10	Achromatic Quarter Wave Plate	CVI/Melles Griot, ACWP 400-700-06-4
11	Light Source	Lumencor SPECTRA X Light Engine

3.5 Methodology

3.5.1 Experimental approach

The analysis of the sensitivity of non-encapsulated TLC particles to shear stresses when these particles are used as seeding in a laminar flow has been carried out by means of a series of observations made on particles stuck to the bottom wall of a microchannel in which a pressure driven flow is established. In general, for particles dispersed into a fluid in motion, the flow exerts on the particles' surface a shear stress that depends on the relative velocity field $\mathbf{u}_r(\mathbf{x})$ between the particle and the fluid.

Let's consider the situation in which a spherical tracer particle is free to move in a shear flow, as depicted in fig. 3.14 (A). If the particle has the same density of the working fluid, the drag force between the particle and fluid can be considered negligible. Hence, if the particle rotation is neglected, the relative velocity can be simply expressed as: $\mathbf{u}_r(\mathbf{x}) = \mathbf{u}_f(\mathbf{x}) - \mathbf{u}_p$, where $\mathbf{u}_f(\mathbf{x})$ is the flow velocity distribution and $\mathbf{u}_p$ is the particle velocity. Therefore, the shear stress exerted by the fluid on the particle surface will be proportional to the local shear rate $\dot{\gamma}_c$, which becomes maximum ($\tau_{\max}$) in correspondence of the outer limits of the particle. If the particle's rotation is present due to the shear rate applied on the outer part of the particle, the maximum shear stress $\tau_{\max,\mathrm{r}}$ on the particle surface will be consequently reduced.

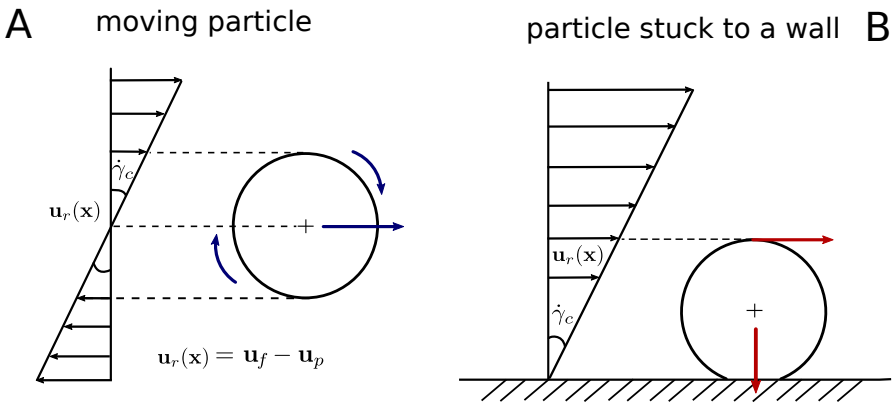

Figure 3.14: Relative velocity between a spherical particle and an unperturbed shear flow, (A) for a particle that follows faithfully the flow and (B) for a particle stuck to a surface.

The situation of a particle is stuck to a surface and immersed in a fluid flow, as illustrated in fig. 3.14 (B) is different. In such case, the shear stress linked to the velocity distribution close to the wall, is higher than the shear stress exerted on the same particle suspended in the flow.

For a microchannel having a rectangular cross-section (width = 500 μm and depth = 200 μm) and exposed to a pressure driven flow, the shear rate $\dot{\gamma}_c$ linked to the laminar velocity distribution can be calculated analytically. The analytical expression of the dimensionless velocity distribution $V(y^*, z^*)$ for a Poiseuille flow through a rectangular microchannel is given in Chapter 2 by Eq. (2.15) and (2.16). By indicating with $u(y,z)$ the dimensional local velocity, with W the average velocity on the microchannel cross-section having an area A, with y^* and z^* dimensionless length defined as $y^* = y/a$ $(0 < y < 1)$ and $z^* = z/a$ $(0 < y < \beta)$ where a is the the longer side of the rectangular cross-section and β is the aspect ratio of the cross-section (ratio between short and long side of the rectangular cross-section) it is possible to calculate the local value of the shear rate $\dot{\gamma}_{y,z}$ as follows:

$$\begin{aligned} \dot{\gamma}_{\mathrm{y,z}} &= \frac{\partial u(y,z)}{\partial z} = \frac{W}{a}\frac{\partial V(y^*,z^*)}{\partial z^*} \\ &= \frac{W}{a}\sum_{n=1,odd}^{\infty}\sum_{m=1,odd}^{\infty} v_{n,m}\frac{m\pi}{\beta} sin\left(n\pi y^*\right) cos\left(\frac{m\pi}{\beta}z^*\right) \end{aligned} \tag{3.10}$$

where the coefficients $v_{n,m}$ are indicated in Eq. 2.16. Then, the local value of the shear stress can be calculated as:

$$\tau_{\mathrm{y,z}} = \mu\,\dot{\gamma}_{\mathrm{y,z}} \tag{3.11}$$

where μ is the dynamic viscosity of the fluid. From Eq. (3.10) and (3.11) it is evident that the maximum value of the shear rate and of the shear stress is always in correspondence of the fixed solid wall where the velocity gradient assumes its maximum value.

The observation of the effects of shear stresses on TLC particles stuck to the solid wall of a microchannel allows to obtain these advantages:

1. The flow field in the neighborhood of the particles is the same.

2. For a given imposed flow rate, the shear stress exerted on the stuck particles surface is the maximum possible.

3. No effect of the particles' rotation is present.

Finally, since the outward aspect of the TLC particles and the shined colors are not affected from the adhesion mechanism that keeps stuck the particles to the bottom wall of the channel, the considerations made in these tests for the attached particles can be extended also to the suspended ones.

3.5.2 Experimental Procedure

A series of measurements have been carried out on non-encapsulated TLC particles stuck to the bottom wall of the copper rectangular microchannel. The region of the glass side of the channel where the stuck TLC particles are observed, is the central one, in which the shear rate assumes an uniform value close to its maximum (± 3 % with respect to the average value) due to the small aspect ratio of the channel (*i.e.* β = 0.4) (see Fig. 3.15).

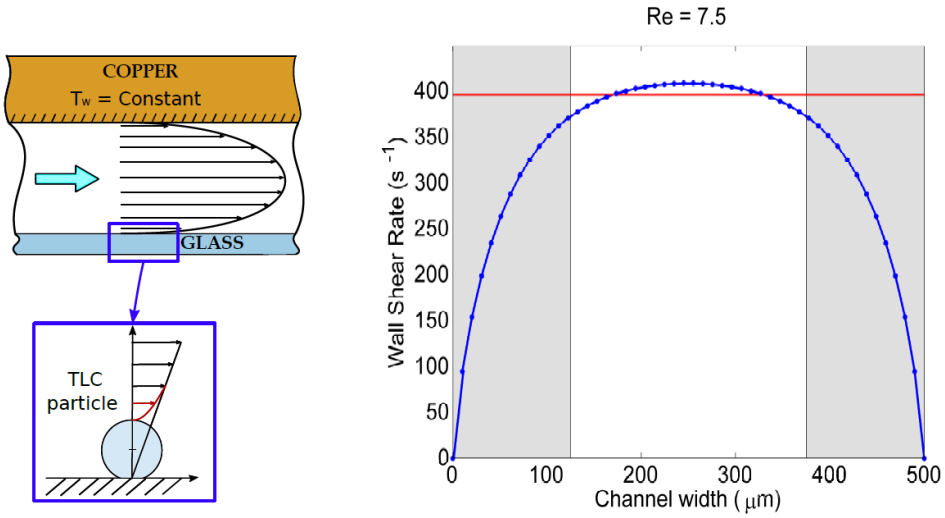

Figure 3.15: *On the left*: Sketch of a longitudinal section of the microchannel. In the blue box a sketch of a TLC particle stuck to the bottom wall exposed to the flow. *On the right*: Distribution of shear rate at the bottom wall for an unperturbed flow at Re=7.5.

The reconstruction of the distribution of the shear rate close to the solid wall has been made by using Eq. (3.10) with $z^* = 0$. The measurement zone is set in the middle zone of the channel sufficiently distant from its inlet and outlet sections, in order to obtain a constant temperature distribution in the fluid and a fully developed flow for all the flow rates taken into account. (Morini, 2008a). Then, for all the three TLC particles under investigation, a calibration curve is realized through the acquisition of the color reflected from the TLCs stuck to the bottom wall of the microchannel at different imposed temperatures in the condition of no flow imposed. As an example, in fig. 3.16 the images of a single non-encapsulated TLC particle exposed to different values of temperature and without any shear rate imposed on its surface are reported. In particular, in fig. 3.16 A is reported the correspondence color-temperature for a TLC particle having a color play of 5 K, while in fig. 3.16 B the same correspondence is given for a TLC particle having a color play of 10 K. As it is visible from the figure, both particles have the red starting point at 20°C.

For what concerns the calibration, RGB (Eqs. 3.3) and HSI (Eqs. 3.4) color

spaces and proper orthogonal decomposition (POD) of RGB color space (Eqs. 3.7) have been used and a calibration based on POD variable space data has been finally chosen to evaluate the color response shined by the crystals as a function of the local temperature.

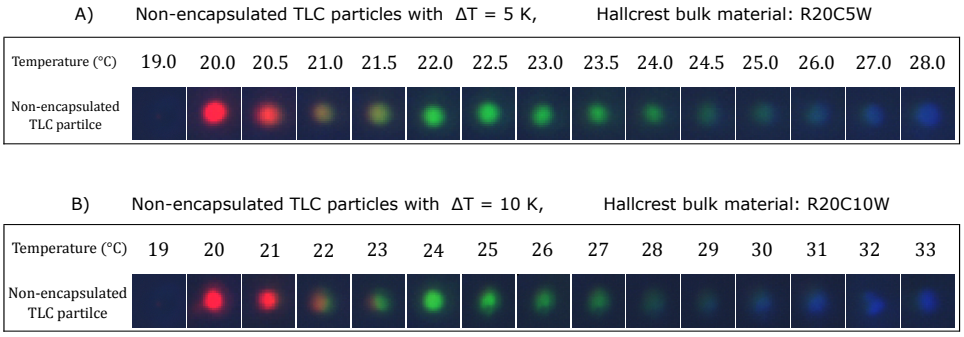

Figure 3.16: Color shined by non-encapsulated TLC particles at different temperature when no shear flow is imposed on them. In the row A) particles with a color range of 5 K (*Hallcrest R20C5W*) while in row B) particles with a color range of 10 K (*Hallcrest R20C10W*).

Then, the experimental run is managed as follows:

i Since the aim of the experiments is to evaluate the influence of shear stresses on the colors reflected from the particles, a mixture in which the density of the working fluid is slightly lower than the density of particles is created. In this way the non-encapsulated TLC particles naturally tend to deposit on the bottom wall in absence of imposed flows. For this reason, after filling the microchannel with the mixture containing the suspended particles, a waiting time is observed in order to leave the particles to accumulate on the bottom glass wall of the microchannel. In average, the total amount of non-encapsulated TLCs stuck to the glass wall is close to 50.

ii The desired temperature is imposed to the copper walls of the microchannel through the Peltier device and a constant flow rate is imposed by means of the syringe pump.

iii The images of the particles are acquired for 20 seconds at a frame rate of 15 fps for a total amount of 300 images for each set of imposed temperature and flow rate.

iv The experiments are repeated keeping fixed the wall temperature and increasing step by step the flow rate from a minimum value of the Reynolds number of 0.1 up to a Reynolds number of 7.5, which correspond to a wall shear rate in the range of 4 - 400 s^{-1} (shear stress at the wall in the range of $3 \cdot 10^{-3}$ - 0.4 Pa.

3.6 Results and discussion

In fig. 3.17, are reported the zoomed images of the colored central core of a single particle (ΔT=10 K) attached to the wall when exposed to different shear rate conditions. In fig. 3.17, the color shined from the non-encapsulated TLC particle exposed to different shear rates, is shown for three different values of temperature corresponding to the red (21.2 °C), green (23.3 °C) and blue color (29.8 °C). From a qualitative observation of the pictures, the shear rate exerted on the particle's surface does not affect the color shined by TLCs. This means that if some modification occurs on the color reflected from the TLCs due to the imposed shear rate on their surface, this is not visible from a naked eye vision. The values of shear shown in fig. 3.17 - 3.18 are calculated by approximating the shear rate acting on the particles with the value at the wall calculated for the imposed flow rate and for the rectangular geometry of the channel by means of Eq. (3.10). Then, the shear stress that acts on the stuck TLC can be estimated by multiplying the shear rate at the wall with the dynamic viscosity of the fluid, as indicated by Eq. (3.11). In general the dynamic viscosity of the working fluid (solution of deionized water with pure sodium iodide with a concentration of 7 ‰) ranges from 1.015 mPa·s at 20 °C up to 0.809 mPa·s at 30 °C depending on the temperature of the fluid.

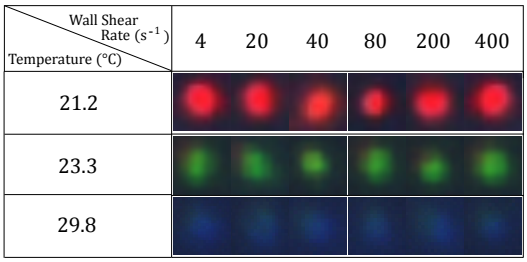

Figure 3.17: Image of a single non-encapsulated TLC particle (ΔT=10K) exposed to different wall shear rate for different values of imposed temperature.

In order to conclude that the color shined from the non-encapsulated TLC particles is not affected by the shear rate imposed to their surface, a more quantitative analysis is required. Therefore, a quantitative analysis is performed through the direct comparison of the individual temperature values obtained from each particle after a pre-processing of the images and the application of the color-temperature calibration procedure described by Eq. (3.5) - (3.9). The results obtained for all the three kinds of TLC particles used (ΔT = 10 K, 5 K and 1 K) are presented in Fig. 3.18.

In particular, the results reported in fig. 3.18 are obtained from the analysis of 300 consecutive images for 10 particles stuck to the bottom transparent wall of the microchannel. The continuous line in each graph represents the temperature measured by the Pt1000 sensor and imposed by the Peltier device, affected by an uncertainty shown by dashed lines (*i.e.* 0.1 K). Three different temperature values

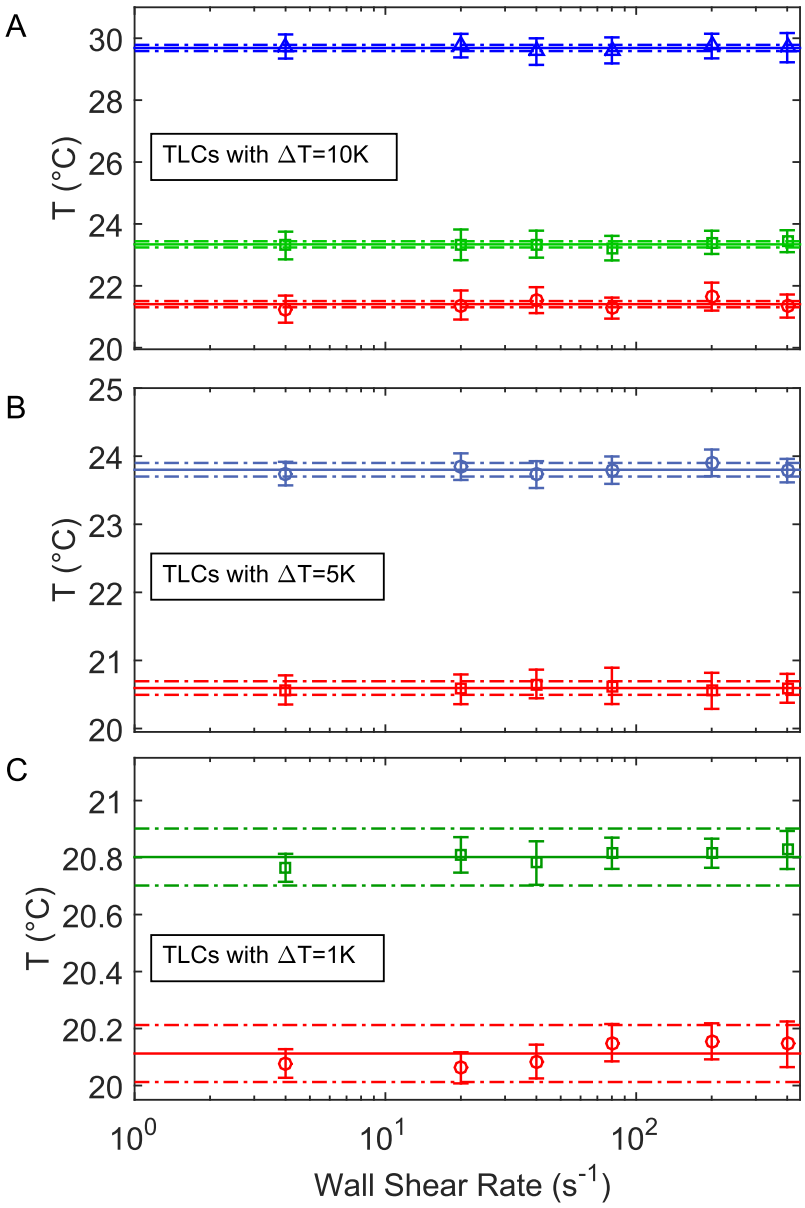

Figure 3.18: Temperature response as a function of the average wall shear rate for TLCs with ΔT = 10 K (A), ΔT=5K (B) and ΔT=1K (C). The continuous line represent the average temperature imposed by the Peltier element and the dashed lines represent the uncertainty of the thermal control.

are analyzed for TLC particles with ΔT = 10 K (fig. 3.18 A): 29.8 °C (blue line), 23.3 °C (green line), and 21.2 °C (red line). For all the three cases, the temperature measured by the non-encapsulated TLCs have an average standard deviation

from the mean value less than 4.6% (the value is normalized on the working temperature range of 10 K). This value is in agreement with the uncertainty evidenced for the same particles by Segura et al. (2013) (*i.e.* 4.9 %). It is also evident that no particular bias errors can be identified as the shear rate at the wall is increased. Similar results for the non-encapsulated TLCs having $\Delta T = 5$ K, which are plotted in fig. 3.18 B for temperature values of 20.6 °C (red line) and 23.8 °C (light blue line), are achieved, while for TLCs with $\Delta T = 1$ K, plotted in fig. 3.18 C for temperature values of 20.1 °C (red line) and 20.8 °C (green line), slightly higher uncertainties have been found (the average standard deviation normalized on the working temperature range of 1 K is equal to 6 %). Also in this case this value is in agreement with the average standard deviation obtained by Segura (2014) for the same particles. The higher uncertainties found for the non-encapsulated TLCs having $\Delta T = 1$ K are due to the higher sensitivity (reduced working range) of these particles compared to the particles with a wider temperature working range, combined with a larger relative instability introduced by the temperature control system when the imposed temperature changes of some 0.1 K. This explains also the fluctuations found for these particles. In order to clarify this aspect, in fig. 3.19 - 3.21 the deviation between the mean measured temperatures using the TLCs and the temperature imposed by the Peltier device and measured by the Pt1000 sensor is shown for the three TLC particles tested.

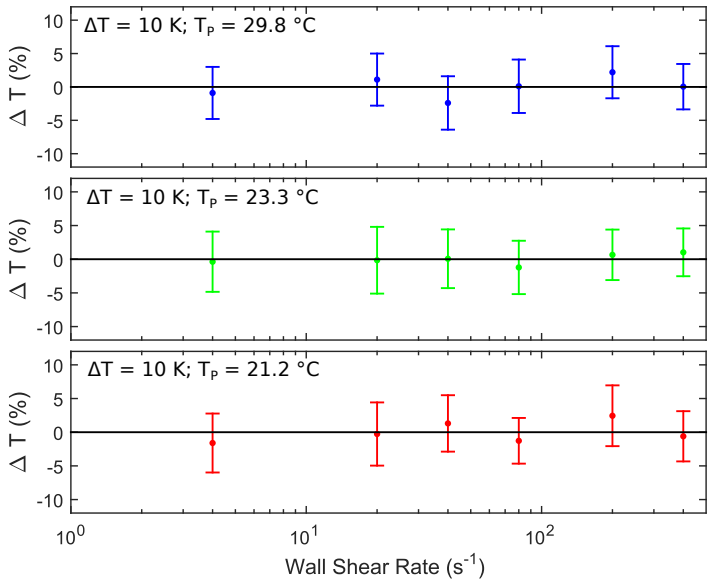

Figure 3.19: Difference between the mean measured temperatures (dots) and the temperature imposed by the Peltier device normalized with the temperature working range of 10 K.

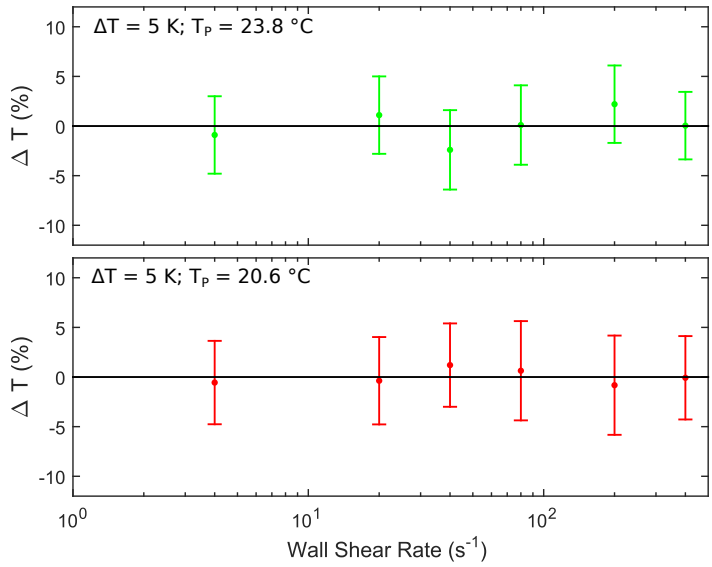

Figure 3.20: Difference between the mean measured temperatures (dots) and the temperature imposed by the Peltier device normalized with the temperature working range of 5 K.

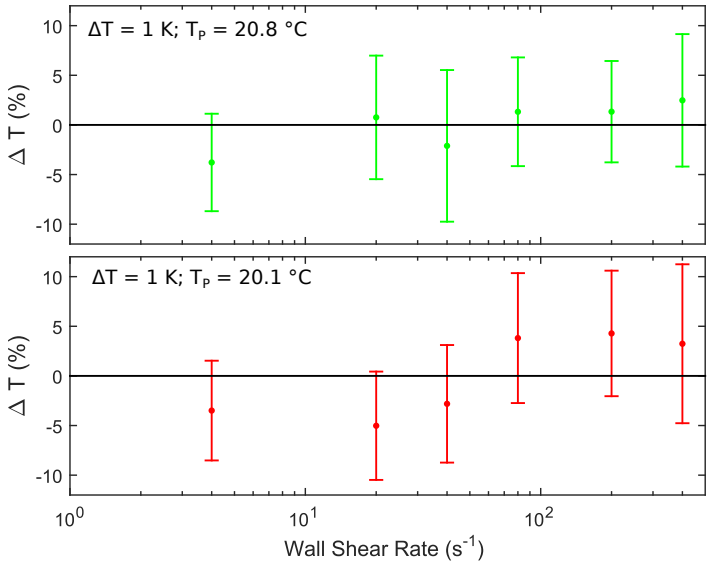

Figure 3.21: Difference between the mean measured temperatures (dots) and the temperature imposed by the Peltier device normalized with the temperature working range of 1 K.

In order to enable the comparison between fig. 3.19 - 3.21, the temperature difference has been normalized with the temperature working range of the TLC particles, that is respectively 10 K, 5 K and 1 K. The error bars represent the temperature standard deviation from the mean measured temperature.

Hence, it can be concluded that the color reflected from the non-encapsulated TLC particles is not affected by the shear stress exerted on the particles' surface for shear rate values up to 400 s^{-1} which correspond to shear stresses up to 0.4 Pa depending on the temperature of the fluid. For this reason, up to these shear stress values, the color reflected from the TLCs depends exclusively from the temperature of the particles, meaning that the non-encapsulated particles can be used safely for measuring the local temperature of laminar flows in microchannels.

Even if previous experiments show that no influence on the color of the particles is given by the shear stress exerted on particles' surface, it has been observed that when the shear rate increases some TLC particles start to collapse releasing the material on the bottom transparent wall of the microchannel. This phenomena is shown in fig. 3.22 where the flow rate of the working fluid in the picture B is higher with respect to picture A. In fig. 3.22 both the intact particles and the broken one are distinguishable. The broken particles are visible inasmuch they have lost their peculiar aspect, in which the core shines of a pure, uniform and brilliant color while the outer zone is nearly transparent. In particular the difference between an intact and a broken particle is clearly shown by comparing the pattern of the particle marked by a yellow circle in fig. 3.22.A and fig. 3.22.B. Hence, since the color shined by the broken particles is no more uniform and presents different shades, reliable temperature measurements cannot be consequently performed on broken particles. Then, since the working fluid continues to flow inside the microchannel the TLC bulk material is spread on the glass surface. The spreading of the TLC material on the bottom glass surface is highlighted in fig. 3.22 by red arrows. As it is visible, as the TLC material is spread on the transparent wall of the microchannel the dependence between the crystal color and its temperature is completely lost since a blue coloration starts to be shined as the working fluid continues to flow.

An additional effect related to the increase of the flow rate of the working fluid is the detachment of some particles stuck to the wall. This effect does not entail any corruption of the particles, but nonetheless decreases the number of valid particles that can be evaluated. This effect is obviously intensified increasing the flow rate. The detachment of the particles is visible comparing the particles inside the green box of fig. 3.22.A and fig. 3.22.B. The destructive effect of different values of the shear stress exerted on the particles' surface is depicted in fig. 3.23 in which the ratio between the destroyed particles over the total amount of the particles stuck to the wall is reported as a function of the wall shear rate. The data reported in figure 3.23 have been obtained through the analysis of the particles behavior during 1 minute after the imposition of the flow rate. However, it is worth to clarify that, for each imposed value of the flow rate, the effect of the particles' destruction starts immediately after the flow rate imposition and

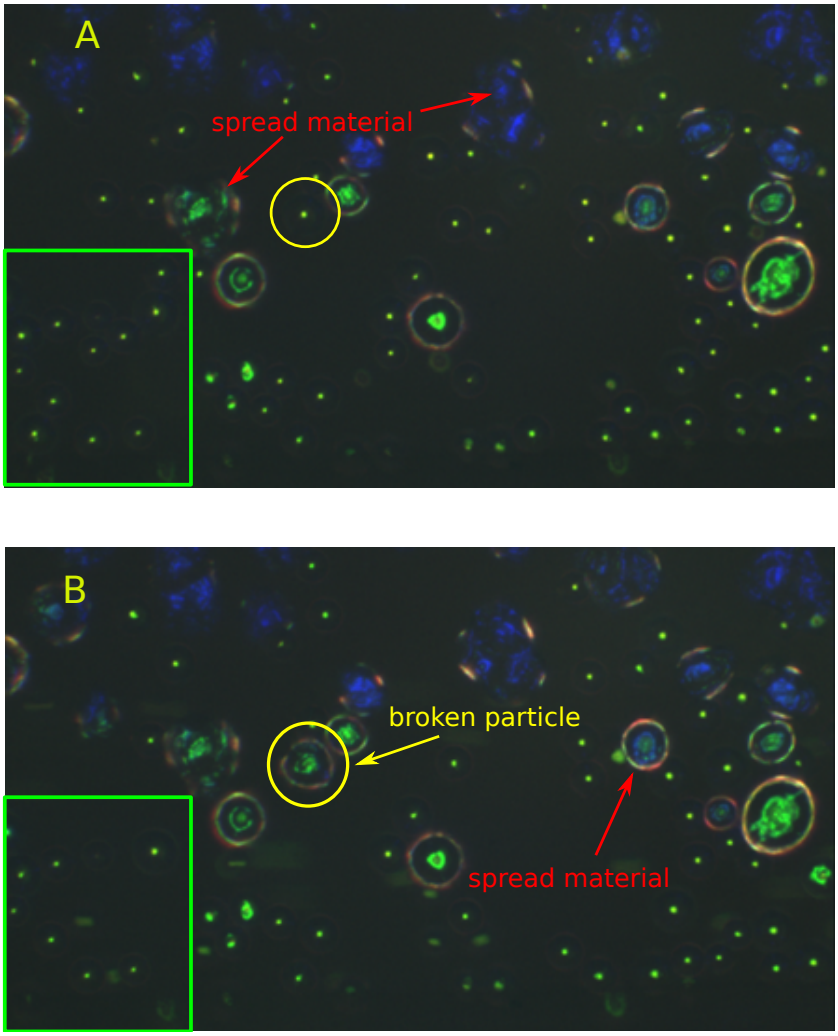

Figure 3.22: Pictures of particles stuck to the glass bottom wall of the microchannel under different flow rate conditions of the working fluid: specifically, in the picture B the flow rate is higher than in picture A. In the figure are shown all the effects related to the flowing of the working fluid on the particles stuck to the wall. The destruction of a particle is highlighted inside the yellow circle, while the red arrow marks the spreading of the TLC material on the glass wall. In the green box is possible to see the particles' detachment when the flow rate of the working fluid is increased.

only few particles collapse some seconds later. After one minute no additional destruction rates have been observed. This fact suggests that the mechanical stability of non-encapsulated TLCs changes from particle to particle. Concerning the amount of particles destroyed, as it is visible from fig. 3.23, the effect of the particles destruction is visible only for shear rate higher than 80 s^{-1} (shear stresses in the order of $8 \cdot 10^{-2}$ Pa), below this value the particles remain almost intact.

For higher shear rates ($\dot{\gamma}_c > 80$ s^{-1}), the amount of particles destroyed increases with the increasing of the shear rate until reaching shear rates of 4000 s^{-1} (shear stresses in the order of 4 Pa) for which the particles are almost all destroyed.

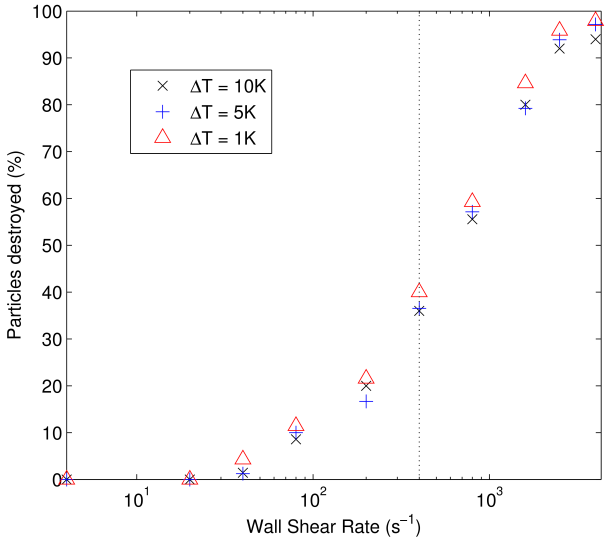

Figure 3.23: Destroyed non-encapsulated TLC particles (%) depending on the wall shear rate. The dotted line corresponds to wall shear rate of 400 s^{-1}.

The mechanical stability of the non-encapsulated TLC particles and the reason behind their destruction under certain level of shear rates, is out of the purposes of this dissertation which aims only to analyze the reliability of the temperature detection performed through the non-encapsulated TLC particles when exposed to different levels of shear stress. From this viewpoint, the process that brings to the collapse of the non-encapsulated TLC particles does not alter the reliability of temperature measurements performed with them, since no deviation in their color response is observed before their destruction.

From the above presented analysis on the sensitivity of the non-encapsulated TLC particles to shear rates, it can be concluded that no modification of the color shined by the core of the TLCs takes place due to the shear stress induced by the Poiseuille flow on the particles' surface for shear rates lower than 400 s^{-1} ($\tau_{\max}$ ~ 0.4 Pa). Up to 400 s^{-1} the reliability of the temperature indication given by the non-encapsulated TLC particles still remains unaffected from the shear rate exerted on their surface. Nevertheless, when the shear rate increases the particles tend to be destroyed. The particles destruction starts for shear rates close to the wall larger than 80 s^{-1} ($\tau_{\max} \sim 8 \cdot 10^{-2}$ Pa), but this effect has a limited relevance for shear rates up to 400 s^{-1}, for which, the ratio between the destroyed particles and the intact ones is around the 35 %. In addition, suspended TLC particles will be subjected to lower shear stress values if compared to the particles attached to the wall; therefore, it is possible to conclude that the non-encapsulated TLC

particles can be safely used as temperature-sensitive tracers for water flow inside a microchannel for typical flow rate values encountered in microfluidics (*i.e.* Re < 10).

3.7 Preliminary results on temperature measurements

The study performed in the previous section shows that the color shined by the non-encapsulated TLC particles is only related to the temperature felt by the particles and that the shear stress exerted on their surface has the only consequence to determine the particles' collapse under certain shear stress values. It has been demonstrated that for Re < 10 the non-encapsulated TLC particles can be safely used for measuring the temperature of a fluid in motion.

In this section, a study in which the TLC particles are employed in order to detect the three-dimensional velocity field and temperature distribution for a flow in a microchannel is presented. For a preliminary test case, the TLC particles are utilized for measuring the temperature distribution for a Poiseuille flow in a microchannel subjected to a constant wall temperature. The achieved results, as well as the critical issues encountered during the experiments are summarized in the following sections.

3.7.1 Experimental Apparatus

The experimental apparatus utilized for the simultaneous measurement of the three-dimensional velocity field and temperature distribution inside a microchannel, is basically the same reported in Section 3.5 except for the addition of a cylindrical lens along the light path just before the RGB color camera (see fig. 3.24).

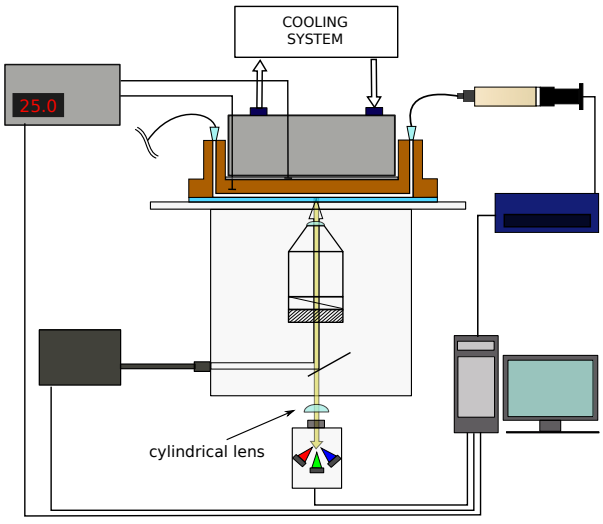

Figure 3.24: Layout of the experimental apparatus for the TLC temperature measurements with the addition of the cylindrical lens.

The cylindrical lens has a focal length of 500 mm (f_{cyl}) and it is placed in front of the RGB camera sensor to induce an astigmatic aberration to the particle images. This lens is the base for the Astigmatism Particle Tracking Velocimetry (APTV), a single-camera 3D particle tracking method able to determine the position and velocity of the TLC particles in the flow. The APTV technique was first developed by Cierpka et al. (2010, 2011) for the determination of the three components of the velocity field in a micro volume and then optimized some years later by Rossi and Kähler (2014). With the simply employment of a spherical lens (fig. 3.25 A), the spherical particles are projected on the bi-dimensional sensor of the camera as circular images in which the diameter of the particles increases with the increasing of distance of the particles from the focal plane. Differently from the spherical lens, a cylindrical lens has a curvature in only one direction. For example with referring to the fig. 3.25 B, only the y-axis of the lens has a curvature while along the x-axis, the lens is flat. Hence, through the introduction of a cylindrical lens along the light path, a new focal plane is introduced inside the volume of fluid under investigation, namely with referring to fig. 3.25 B, the

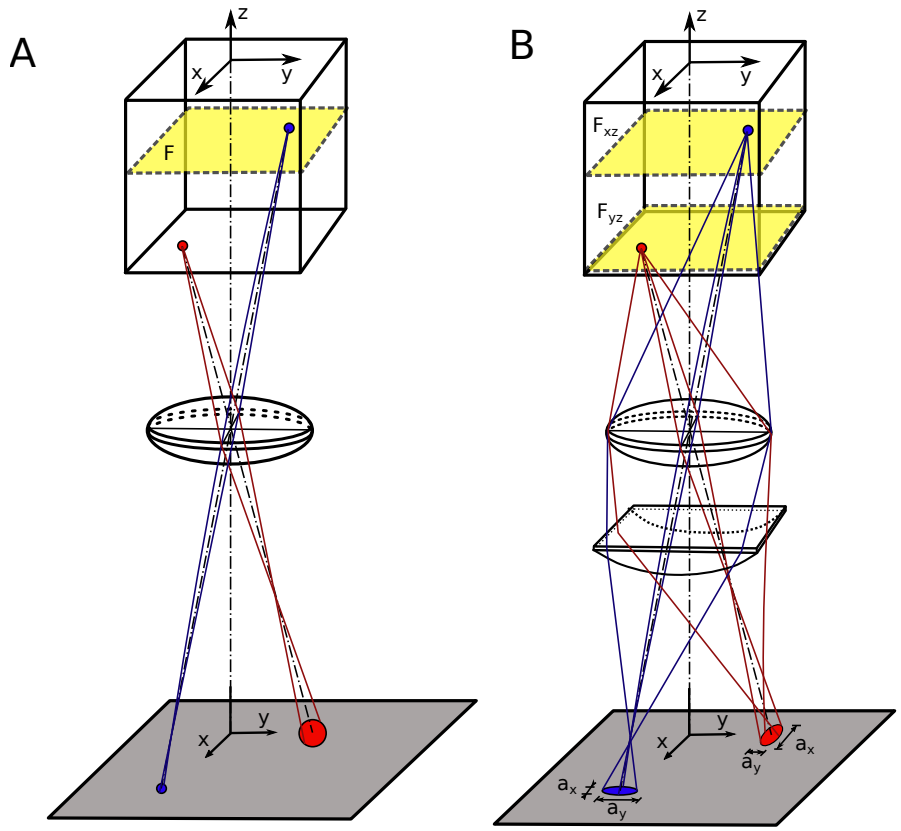

Figure 3.25: Schematic sketch of the working principle of particles' defocusing in the APTV method. Image adapted from Segura (2014).

plane F_{yz}. Since the cylindrical lens does not affect the dimensions of the images along the x-axis, the F_{xz} plane still remains on the same position of the focal plane F introduced by the spherical lens without the further introduction of the cylindrical one. Hence, the final result is that the images of the spherical particles are projected as an ellipses instead of being circular images. In particular the a_x dimension of the ellipsis is determined by the distance from the F_{xz} plane while the a_y dimension of the ellipsis is determined by the distance from the F_{yz} plane, as it is visible from the figure 3.25 B. Therefore, through a precise calibration of the obtained ellipsoidal images it is possible to define the particle position along the z-axis (Cierpka et al., 2011). As demonstrated by Segura et al. (2015) the APTV method can be proficiently coupled with non-encapsulated TLC particles in order to study simultaneously the three dimensional velocity field and the local temperature distribution in microfluidics applications. In particular the authors applied the APTV method coupled with the TLCs thermography in order to study the rising flow in a small region of a warm water droplet.

3.7.2 Methodology

The simultaneous reconstruction of the three-dimensional velocity field and temperature distribution, has been performed in co-operation with Dr. Massimiliano Rossi in the laboratory of the microfluidic group, at the Universität der Bundeswehr of Munich. First of all, the calibration of the TLC particles was performed. The relationship between the color shined from the particles and their temperature has been made by following a calibration procedure similar to that described for the analysis on shear stresses. The calibration of the APTV system, instead, is performed following the approach described in the work of Rossi and Kähler (2014). Specifically, the calibration curves are obtained experimentally looking at stationary TLC particles resting at the bottom of the channel and moving the microscope focal plane gradually, step-by-step, away from the wall. Each step consists in a displacement of the focal plane equal to 1 µm and covers a span of 30 µm (*i.e.* ± 15 µm from the central position). In this way all the different shapes of the defocused particle are detected until their complete vanishing.

An example of astigmatic images of non-encapsulated TLC particles used for the simultaneous measurement of 3D temperature and velocity field in the microchannel is reported in fig. 3.26.

One limitation of the current experimental setup is given by the relatively low light intensity provided by the white light engine with respect to the sensitivity of the RGB camera. In particular, a minimum exposure time of 25 ms is required to obtain particle images with a sufficiently large signal-to-noise ratio. This put a limit on the maximum flow rate that can be utilized, since, if particles move too fast, they can start to give blurred images that cannot be used for the analysis. Consequently, a flow rate of 0.05 ml/h which corresponds to a nominal maximum velocity of 267 µm/s (Re = 0.04) has been chosen. At this flow rate, for

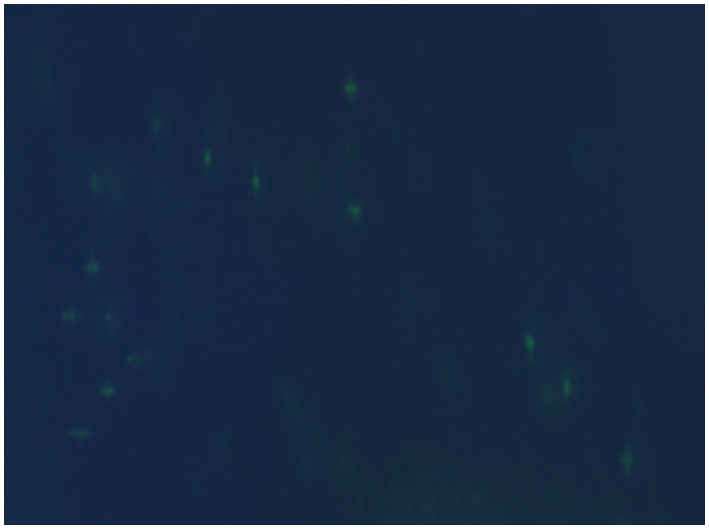

Figure 3.26: Astigmatic images of the non-encapsulated TLC particles used for the simultaneous measurement of 3D temperature and velocity field in the microchannel.

the involved magnification of 20 ×, the blurring effect is negligible. The involved microchannel (the same of the previous analysis) has a rectangular cross-section (500 µm in width and 200 µm in depth, *i.e.* β = 0.4) and it is carved into a copper substrate (k_{Cu} ~ 400 W/mK) and sealed with a microscope glass slide (k_g = 1.4 W/mK) to guarantee the optical access. The heating of the microchannel is provided by a Peltier cell which is in direct contact with the copper surface of the microchannel and it is used in order to fix the wall temperature of the copper side of the microchannel. In this way a boundary condition of constant temperature can be assumed for the three copper walls while the bottom glass wall can be treated as a nearly adiabatic surface. Therefore, given the mass flow rate, the channel geometry and temperature condition at the inlet, the trend of the bulk temperature $T_b(x)$ along the flow axis, for a channel with three walls heated at a fixed temperature (T_w), can be calculated by using the following equation (Incropera et al., 2006):

$$T_b(x) = T_w - (T_w - T_{b,0})e^{-\frac{hP}{\dot{m}c_p}x} \tag{3.12}$$

where

$$T_{b,0} = T_b(x=0) \qquad \text{and} \qquad h = \frac{Nu \cdot k}{D_h}$$

In Eq. (3.12) $T_{b,0}$ is the fluid bulk temperature at the inlet section of the microchannel and in this case it is equal to the room temperature (20 °C), h is the convective heat transfer coefficient and can be calculated as the product of the

Nusselt number Nu (2.603 for rectangular channel having an aspect ratio of 0.4 with three walls heated at fixed temperature (Shah and London, 1978)) and thermal conductivity k (0.6 W/mK for water) divided by the hydraulic diameter D_h, P is the heated channel perimeter, $\dot{m}$ is the mass flow rate and c_p is the specific heat (4186 J/kgK for the water).

The trend of the bulk temperature $T_b(x)$ along the streamwise direction, calculated with Eq. (3.12), is plotted in fig. 3.27 for a fixed wall temperature T_w of 25°C. As it is visible from fig. 3.27, the bulk temperature of the fluid reaches the value of the wall temperature after 50 µm. This means that the temperature of the fluid is equal to the temperature imposed to the walls by the Peltier device, already inside the inlet connection. Consequently, the fluid temperature can be considered uniform along the entire length of the microchannel and the axial temperature gradient inside the fluid is negligible.

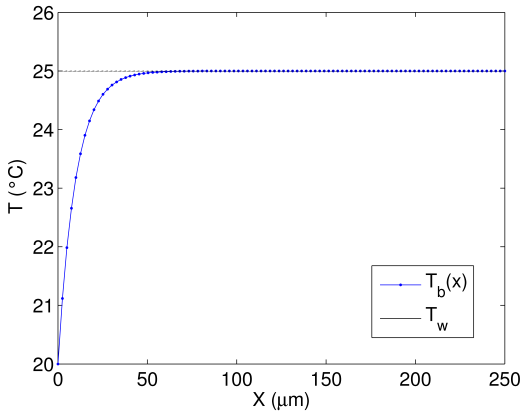

Figure 3.27: Trend of the bulk temperature $T_b(x)$ in the streamwise direction for a microchannel with three wall heated at a constant temperature.

3.7.3 Results and discussion

The result of a simultaneous measurement of temperature, via TLC particles' thermometry, and three-dimensional velocity, via the APTV method, for a flow in a microchannel with three walls heated at a constant temperature, is shown in fig. 3.28.

The measurements are performed on 16 different planes (12.5 µm of spacing between each others) along the depth of the microchannel. An additional measurement plane is taken in correspondence of the central plane of the microchannel in order to perform in-plane velocity measurements for the higher velocities. For each plane 200 images acquired with a frame rate of 15 fps have been analyzed. Due to the symmetry of the problem, the measurements are performed only in one half of the microchannel. In particular, the xz-plane at y = 0 is the symmetry plane in the center of the microchannel while the xz-plane at y = 250 µm corresponds to the lateral wall. Each data point in the graph corresponds to the streamwise velocity component of a TLC particle as a function of its z- and

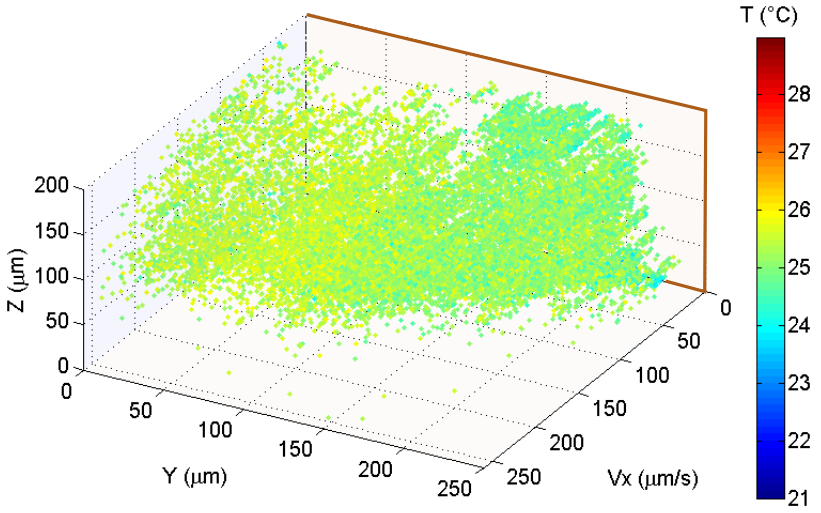

Figure 3.28: Simultaneous three-dimensional measurement of the temperature and velocity field for a flow in microchannel with a three walls heated at a constant temperature.

y-coordinate. The color of each point gives corresponding temperature of the particle and the related value is readable from the scale bar on the right of the picture.

The velocity measurements show the typical velocity profile expected for a Poiseuille flow in a rectangular duct. The corresponding measurement uncertainty is evaluated as the standard deviation of the velocity along the y- and z-axis, where the velocity is zero for a Poiseuille flow. The obtained uncertainty values are ± 5 µm/s (2 % with respect to the maximum velocity) for the in-plane velocity and ± 29 µm/s (11.7 % with respect to the maximum velocity) for the out-of-plane velocity. The maximum velocity obtained from the experiment is 250 µm/s, 6.4 % lower with respect to the theoretical one (*i.e.* 267 µm/s). This mismatching is most likely due to discrepancies between the nominal dimensions of the microchannel, used in the analytical calculations (Eq. (2.15)), and the real dimensions. As reported in Section 3.4, the microchannel has been realized through a handcrafted milling in a copper substrate and sealed to a microscope slide with UV glue. Therefore the actual dimension of the microchannel cross-section could not match perfectly the theoretical one, and in addition, there was not a precise control on the roughness of the microchannel walls.

The temperature measurement shows a uniform temperature field with an average temperature of 25.2 °C. For this measurement, the non-encapsulated TLC particles *Hallcrest UNR20C5W* were employed. The temperature fluctuations are within the estimated uncertainty of ± 0.5 K over a temperature response range of about 7.5 K. The uncertainties reported here are higher with respect to the

one in which the thermometry via TLC particles and the determination of the 3D velocity profile through the APTV method are performed separately.

In fact, as stated by Segura et al. (2015), the APTV method is optimized and best suited for the usage of a fluorescent seeding coupled with high power illumination sources like lasers. In addition, since no color of the fluorescent seeding have to be detected, a camera with higher sensitivity can be employed instead of the RGB color camera. Therefore the application of the APTV method to particles with lower brightness and detected by camera with lower sensitivity corresponds to higher uncertainties in terms of detection of particles' position.

A more powerful illumination system and a more sensitive camera gives also advantages in terms of temperature detection: brighter particles coupled with an acquisition system with higher accuracy, means a more robust and precise calibration curve and consequently temperature measurements with lower uncertainties.

Anyway, here is demonstrated that a simultaneous measurement of the 3D velocity field and temperature distribution of a flow inside a microchannel, is already available with the current technology for situations in compliance with the limitations above described ($\mathrm{Re} \leq 0.04$ and $\dot{\gamma} \leq 400\ \mathrm{s}^{-1}$) if non-encapsulated TLC particles are involved.

Even if an improvement of the experimental equipments is required to extend the range of application of the TLC thermometry to faster flows, it would be advisable an investigation in which the TLC particles will be dispersed in flows in which a temperature gradient is established. In this way it would be possible to carry out a more deepened study on the resolution and sensitivity of the present measurement approach. The manufacture of a microchannel in which a temperature gradient is established in flows with low flow rates, is not a trivial task. Therefore, the aim of the next section, is to show the design, of a device able to generate steady-state temperature gradients, along the flow direction, independently to the used flow rate of the working fluid.

3.8 Device design for investigations on temperature gradients

The limitations of the power of the white light source and the low sensitivity of the RGB color camera used in these tests, give a limitation to the maximum flow rate of the working fluid that can be utilized in order to acquire correctly the images. A restriction in terms of maximum flow rate, means that, the flow rate of the working fluid cannot be increased as desired in order to create an axial temperature gradient. The aim of this section is to show in which way the design of a test section able to provide a temperature gradient along the channel independent on the flow rate, can be obtained by imposing an heat flux on the channel surface. This can be achieved coupling a microchannel made by a substrate with a low thermal conductivity to a constant heat flux heater. To perform this task, the device will be heated by means of a flexible electrical heater coupled to the external surface of the device (heating zone in fig. 3.29).

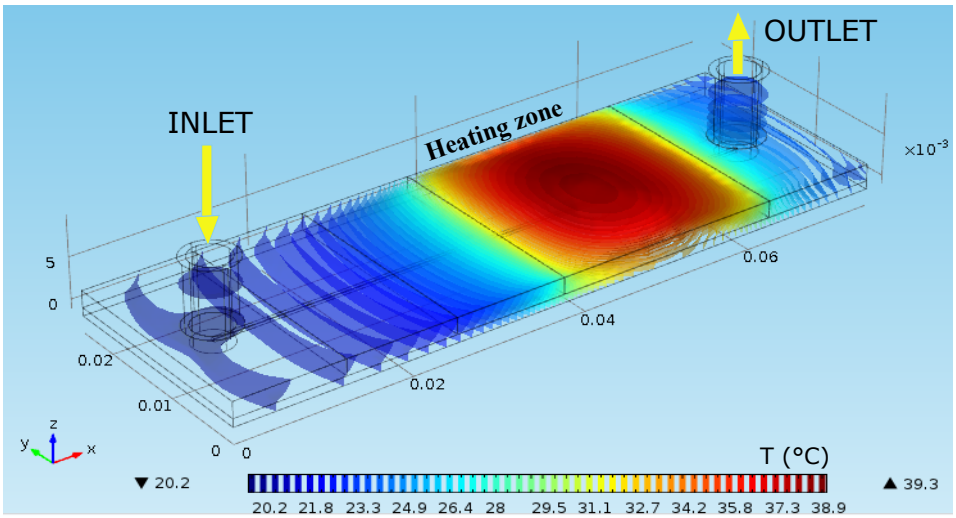

Figure 3.29: Picture of the new channel under study: the heating zone represents the zone where the flexible heater will be placed (Puccetti et al., 2015).

Different kinds of materials, dimensions, powers and positions of the heating source and different sizes of the connectors, have been tested numerically to find the optimal set that can provide a temperature variation in the fluid compatible with the working range of the TLC particles. The problem of the conjugate heat transfer between fluid and solid walls is then analyzed numerically using the software COMSOL Multiphysics®.

The conjugate thermal problem can be described by the following governing equations:

$$\begin{cases} \nabla \cdot (\rho_f \bar{u}) = 0 & (3.13) \\ \rho_f (\bar{u} \cdot \nabla) \bar{u} = \nabla \left[-p\bar{I} + \mu_f (\nabla \bar{u} + (\nabla \bar{u})^T) \right] & (3.14) \\ \text{Solid:} \quad \rho_s c_{p,s} \dfrac{\delta T_s}{\delta t} = \nabla \cdot (k_s \nabla T_s) & (3.15) \\ \text{Liquid:} \quad \rho_f c_{p,f} \dfrac{\delta T_f}{\delta t} + \rho_f c_{p,f} \bar{u} \cdot \nabla T_f = \nabla \cdot (k_f \nabla T_f) & (3.16) \end{cases}$$

where equation (3.13) and (3.14) represent the continuity and momentum equation for the determination of the water velocity field within the channel (the velocity is assumed in steady-state conditions). The time-dependent field of temperature both for solid and water is determined by solving the Fourier equation in the solid region (equation (3.15)) and the energy equation for convective flows in the liquid region (equation (3.16)).
This system of equation is completed by the following boundary conditions:

$$\begin{cases} \bar{u} = 0 \qquad \text{at walls} & (3.17) \\ M_v = -\displaystyle\int_{\delta\Omega} \rho (\bar{u} \cdot \bar{n}) dS \qquad \text{with } M_v \text{ constant} & (3.18) \end{cases}$$

$$\begin{cases} \text{For the heated area:} \quad -\bar{n} \cdot (-k_s \nabla T) = q_0 \quad \text{where} \quad q_0 = Q/A_H & (3.19) \\ \text{For the other surfaces:} \quad -\bar{n} \cdot (-k_s \nabla T) = h(T_{ext} - T_s) & (3.20) \\ \text{At the inlet surface:} \quad T_{in} = 20^\circ C & (3.21) \end{cases}$$

No slip at the walls (Eq. (3.17)) and constant value of mass flow rate at the inlet section (Eq. (3.18)) are set as boundary conditions for the continuity equation and momentum equation. In all the simulations, a microscope slide in fused silica (k_g = 1.4 W/mK) is considered as the bottom wall of the device. Equations (3.19)-(3.21) show the boundary conditions set for the heat. The boundary condition (3.19) is set for the heated zone (fig. 3.29), where Q represents the constant heat power released by the flexible electrical heater and A_H is total heated area. On the other surfaces a third kind thermal boundary condition is imposed by considering the heat exchange for natural convection with the room air (Eq. (3.20)). Different values of the convective heat transfer coefficient h, are taken into account in equation (3.20) to best simulate the laboratory conditions. T_{ext} is the external temperature and here it is equal to the room temperature (20 °C) while T_s is the superficial temperature of the device. A fixed temperature of 20 °C is set at the inlet fluid surface as inlet boundary condition (3.21) for the energy equation written for the liquid region. The set of the boundary conditions is completed by

imposing the temperature continuity between fluid and solid boundary interface. An equilibrium initial value of temperature equal to the room temperature (20 °C) is set for all the surfaces. The numerical model of the device allows to investigate the sensitivity of the system to the heat transfer linked to the natural convection established between the room air and the external surface of the test rig (Eq. (3.20)). The heat transfer due to natural convection on the external surface of the device is taken into account through two different approaches:

- The convective heat transfer coefficient h of Eq. (3.21) is imposed to be constant on the whole external surface assuming values between 2 W/m^{2}K and 10 W/m^{2}K as a function of the room conditions (uniform convective heat transfer coefficient).
- The convective heat transfer coefficient h of Eq. (3.21) is calculated as a function of the geometry of the different regions of the external surface of the device by using the correlation of Churchill and Chu (1975) and correlations reported in Incropera et al. (2006) (see eqs. (3.22) - (3.28)). In this way the convective heat transfer coefficient changes point by point on the external surface of the test rig (non-uniform convective heat transfer coefficient).

  For vertical and inclined plates the convective heat transfer coefficient h for natural convection is calculated according to the correlation of Churchill and Chu (1975):

$$h = \begin{cases} \dfrac{k}{L}\left(0.68 + \dfrac{0.67\,(cos(\theta)Ra_L)^{1/4}}{\left(1+\left(\frac{0.492}{Pr}\right)^{9/16}\right)^{4/9}}\right) & \text{if } Ra_L \le 10^9 \qquad (3.22) \\ \dfrac{k}{L}\left(0.825 + \dfrac{0.387\,(cos(\theta)Ra_L)^{1/6}}{\left(1+\left(\frac{0.492}{Pr}\right)^{9/16}\right)^{8/27}}\right)^2 & \text{if } Ra_L \ge 10^9 \qquad (3.23) \end{cases}$$

  where Ra_L (Rayleigh number) is the dimensionless number associated with the natural convection and it is defined as:

$$Ra_L = \frac{g\beta(T_s - T_{ext})L^3}{\nu\alpha} \qquad (3.24)$$

  in which g is the gravitational acceleration (9.81 m/s^2), β is the thermal expansion coefficient, T_s is the temperature of the device surface, T_{ext} is the room temperature and L is the length of the wall. ν is the kinematic viscosity of air while α is the thermal diffusivity ($k/(\rho C_p)$).

  Pr is the Prandtl number of air and it is defined as:

$$Pr = \frac{\nu}{\alpha} = \frac{\mu C_p}{k} \tag{3.25}$$

In eqs. (3.22) - (3.23), θ is the angle between the plate and the vertical direction (for a vertical plate $\theta = 0$) and can be in the range of $0 \leq |\theta| \leq 60°$ in order to have valid correlations (Incropera et al., 2006).

For horizontal plates, the convective heat transfer coefficient h is calculated according to the correlations reported in Incropera et al. (2006) (eqs. (3.26) - (3.28)).

For upper surface of hot plate or lower surface of cold plate:

$$h = \begin{cases} \frac{k}{L} 0.54 Ra_L^{1/4} & \text{if } 10^4 \leq Ra_L \geq 10^7 \quad (3.26) \\ \frac{k}{L} 0.15 Ra_L^{1/3} & \text{if } 10^7 \leq Ra_L \geq 10^{11} \quad (3.27) \end{cases}$$

For lower surface of hot plate or upper surface of cold plate:

$$\frac{k}{L} 0.27 Ra_L^{1/4} \qquad \text{if } 10^5 \leq Ra_L \geq 10^{10} \tag{3.28}$$

With the adopted model is possible to calculate the temperature distribution within the fluid along the streamwise direction. Therefore, the numerical model is employed to test the influence of the substrate material in which the microchannel is realized, on the axial temperature distribution along the development of the microchannel. The restriction to low flow rates due to the use of white light, limits the typologies of materials that can be utilized for the device. In fact, materials with high values of thermal conductivity like aluminum (k_{Al} = 238 W/mK) and copper (k_{Cu} = 400 W/mK), cannot be employed in order to create a variation of the fluid bulk temperature along the flow direction. Indeed, in this case, the conduction in the solid becomes predominant with respect to the heat removal from the convection in the fluid. Hence, the fluid experiences a strong axial temperature gradient concentrated close to the inlet of the channel with a slight increase along the heated region of the microchannel. Figure 3.30 shows an example of the axial temperature trend in the central point of the channel cross-section, along the development in the flow direction from the inlet to the outlet of the microchannel, for devices realized in aluminum and copper. In such examples the microchannel has a square cross-section with a side of 400 µm, the flow rate is equal to 0.05 ml/h and the flexible electric heater imposes a thermal power of 0.18 W. The two red vertical lines in fig. 3.30 and fig. 3.31 are the initial and final points of the heating zone of the microchannel.

By observing fig. 3.30, it is clear that in presence of highly conductive solid walls, the pre-heating effect becomes very strong and the liquid starts to increase

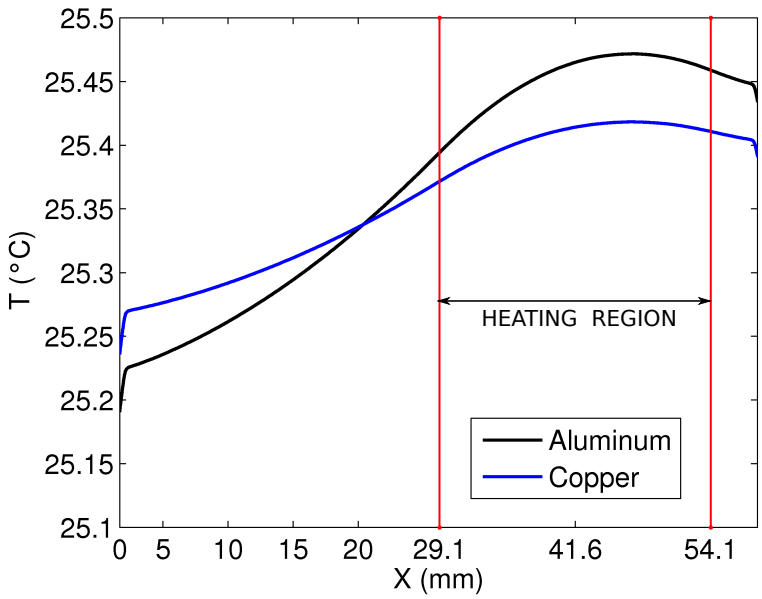

Figure 3.30: Trend of the temperature in the central point of the channel cross-section, for devices realized in aluminum and copper, in steady state conditions.

its temperature before entering the heating region. In the heating region, a variation of 0.1-0.2 K is obtained using copper or aluminum that would be too small to observe a significant color change of TLC particles along the channel. In fig. 3.31 the same axial temperature distribution is reported for a device made by PMMA (k_{PMMA} = 0.19 W/mK) by imposing, for the same water flow rate (0.05 ml/h), different values of heat flux at the walls between 0.02 W and 0.18 W. Both the results depicted in fig. 3.30 and fig. 3.31 are obtained by considering a non-uniform distribution of the convective heat transfer coefficient on the external surface of the device according to the correlation of Churchill and Chu (1975) and correlations reported in Incropera et al. (2006), (Eqs. (3.22) - (3.28)).

It is evident that in this case, due to the low value of the thermal conductivity of the PMMA, the water temperature rises gradually in the initial part of the microchannel and grows more rapidly when the fluid approaches the heating zone, reaching its maximum temperature value in the central part of the heating zone.

As it is visible from fig. 3.31, for a microchannel made by PMMA, a variation from 0.02 W up to 0.18 W of the thermal power given by the flexible heater corresponds to a variation of the fluid maximum temperature in the central part of the microchannel cross-section from 22°C up to 37 °C. The possibility to vary the maximum temperature of the fluid, keeping fixed the minimum fluid temperature at almost 20 °C, enables to use this device in order to test different kinds of TLC particles with different temperature working ranges (*e.g.* with a nominal tem-

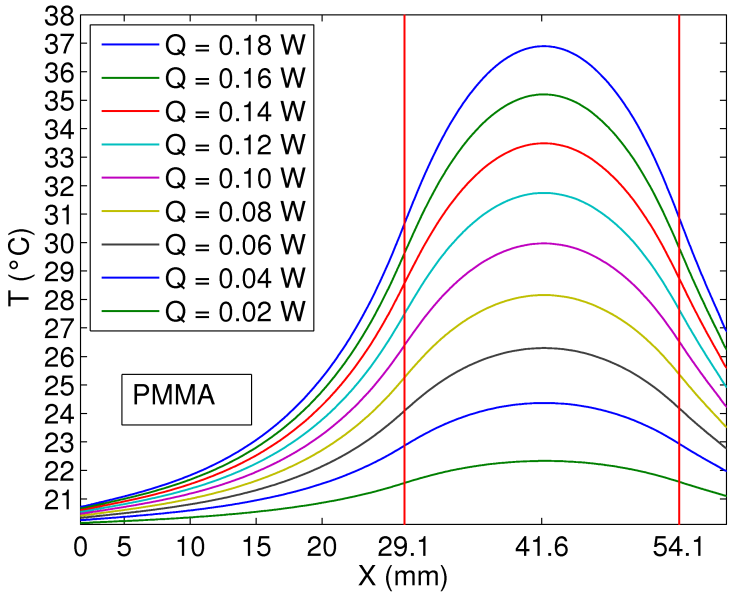

Figure 3.31: Trend of the temperature in the central point of the channel cross-section, for a device realized PMMA, for different values of flexible heater power, in steady state condition.

perature working range of 1K, 5K or 10K). This result demonstrates that PMMA can be considered a good material for the device. In Table 3.2 are reported the main physical properties of the PMMA like density (ρ), specific heat (C_p), thermal conductivity (k), the coefficient of thermal expansion (β) and the refractive index of the transparent material (n). As it is visible from Table3.2, the refractive index of the PMMA is similar to the one of the glass used for microscope slides (n = 1.51 - 1.52), therefore, if for technical reasons is required that also the optical access has to be made in PMMA, this does not entail any change on the objective lens as regards the correction adopted about the cover glass thickness.

Table 3.2: Main properties of the PMMA used during the simulations.

	ρ (kg/m^3)	C_p (J/kgK)	k (W/mK)	β (1/K)	n (-)
PMMA	1190	1420	0.19	70 e^{-6}	1.49

In Table 3.3 the effect of the convective heat transfer coefficient on the numerical results is shown. Indeed, in the table is reported the maximum value of temperature in the central point of the channel cross-section, reached in the heating region. The results are obtained by varying the heat flux imposed at the walls in the range of 0.02 W and 0.18 W, for different values of the convective heat

transfer coefficient. In particular, a variable convective heat transfer coefficient on the external surface of the device due to natural convection and two different uniform values (5 W/m^{2}K and 8 W/m^{2}K) of the convective heat transfer coefficient on the external surface of the device are compared in Tab. 3.3. From the comparison of the results reported in Table 3.3, it is evident that the correlations used by COMSOL (see equations (3.22) - (3.28)) for the estimation of the local value of h suggested an h value on the external surface of the device included between 5 W/m^{2}K and 8 W/m^{2}K. Hence, the sensitivity of the results to the natural convection heat transfer on the external surfaces of the device, suggests to keep under control the laboratory ambient conditions during the whole duration of the experimental runs, in order to obtain the desired variation of temperature along the channel, and consequently to be able to make a quantitative comparison between experimental results and numerical data.

Table 3.3: Maximum Temperature of fluid flow as function of different values of the imposed heat flux Q at the wall both for a non-uniform distribution and for uniform distributions of the convective heat transfer coefficient h on the external surface of the device.

		Q(W)								
		0.02	0.04	0.06	0.08	0.10	0.12	0.14	0.16	0.18
h (W/m^{2}K)	5	22.5	25.0	27.6	30.2	32.7	35.2	37.8	40.3	24.8
	non-unif.	22.3	24.5	26.5	28.0	30.0	32.0	33.5	35.1	37.0
	8	21.9	23.8	25.6	27.5	29.4	31.3	33.2	35.0	36.9

Finally, it is possible to evaluate the time lapse required to reach the steady state condition in terms of temperature distribution. For this purpose, fig. 3.32 shows the evolution in time of the temperature in the central point of the channel cross-section, for a device realized PMMA with an imposed heat flux at the walls equal to 0.08 W and a non-uniform convective heat transfer coefficient on the external surface of the device. As it is visible from fig. 3.32, a time lapse of 22- 25 minutes is required to reach the steady state condition; this time lapse is compatible with the use of the device in an experimental campaign on the characterization of the TLC particles.

It can be concluded that a device made in PMMA can be considered a good option for testing TLC particles. The last remark concerns the enhancing of the quality of the image recorded by the RGB color camera: if the upper wall of the microchannel is painted with an opaque dark paint, the background reflections can be minimized and the color of the TLCs becomes more defined. More defined colors means a more reliable image analysis and, consequently, more accurate results.

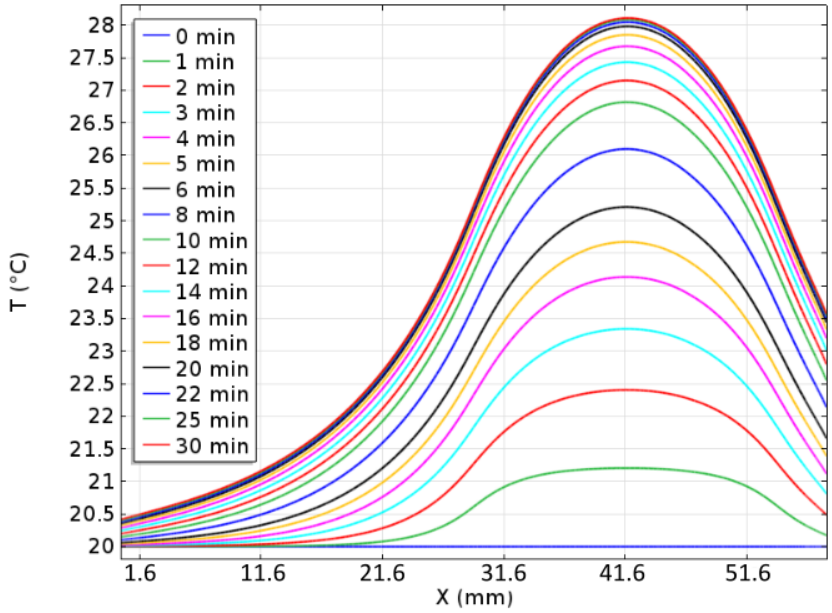

Figure 3.32: Trend of the temperature in the central point of the channel cross-section as function of time, for a device realized PMMA and a thermal power of the flexible heater equal to 0.08 W.

3.8.1 The heating of the device

The establishment of a temperature gradient in the fluid along the streamwise direction is achieved by heating the device with a constant heat flux. This kind of heating can be obtained by means of an electrical heater placed upon the external surface of the device. The electrical heater selected in this work is a squared electrical flexible heater (*HK5163R157L12A*) with a side of 1 inch, made in a polyimide substrate and produced by *MINCO* (fig. 3.33). The heater has a resistance of 157 ± 0.5 ohm and is suitable for the production of the desired heating power depending to the surrounding thermal resistances, in a range of 1-10 V. Therefore, through a precise calibration of the heating device it is possible to control accurately the heating power released by the flexible heater to the PMMA substrate.

One of the remarks resulting from the numerical study illustrated in the previous section, is that the temperature reached by the fluid inside the microchannel is influenced by the heat transfer coefficient on the external surface of the device. Therefore, in order to perform a comparative analysis between the experimental test and the numerical study, the heat transfer coefficient h has to be evaluated during all the experimental run. The heat transfer coefficient can be experimentally evaluated from the comparison between the temperature reached by the surface of the device coupled with the electrical heater and the room temperature close to the device. If the heat flux imposed by the flexible heater is constant,

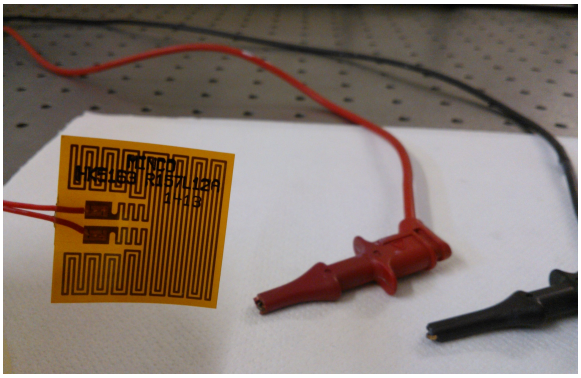

Figure 3.33: Flexible electrical heater.

the difference of these two temperature (ΔT_f, Eq. (3.29)) depends from the total thermal resistance of the system.

$$\Delta T_f = T_{heat} - T_{room} \tag{3.29}$$

Now, if the composition of the device (dimensions, materials, insulation, etc...) does not change, a change of the temperature ΔT_f is related to a variation of the heat transfer coefficient due to the natural convection. Then, from a continuous evaluation of the thermal heat flux released by the flexible electrical heater, coupled with the measurements of the temperature of the device close to the heater and the room temperature, is possible to evaluate the actual heat transfer coefficient on the external surface of the device and adjust the one used in the numerical simulation. Hence, in order to perform correct experimental measurements a thermocouple must be placed between the PMMA device and the electrical heater and another thermocouple has to to be placed close to the device for measuring the room temperature.

It is easy to realize that for a reliable measure the two thermocouples have to measure the temperature the more accurately as possible. For this work, the two thermocouples were calibrated using a calibration bath (*Heto*) and employing the temperature measured by a platinum resistance thermometer as temperature reference (*Fluke Hart scientific 5626*) having a declared accuracy of ± 0.006 °C at 0 °C and ± 0.015 at 420 °C. With the adopted calibration, the estimated uncertainty related to the temperature measurement performed by the two thermocouples is always lower than 0.1 K for all the temperature range involved during experiments. A picture of the apparatus for the calibration of the thermocouples is reported in fig. A.5

The designed test rig is currently under fabrication at IMTV-KIT (Germany) and it has been subjected to some modification in order to ensure its proper functionality. Therefore, unfortunately it has not been possible to use the designed device in order to carry out the desired experimental tests before the closure of this thesis. However, the planned tests will be conducted in Munich in next future, beyond the deadline of this Ph.D. thesis.

3.9 Conclusions

In this chapter the experimental methodology for measuring the temperature of a fluid flow inside a microchannel through the usage of non-encapsulated thermochromic liquid crystals (TLCs) as seeding particles has been presented. As explained in Section 3.3, the TLCs are special substances that shine of different hues depending on their temperature. Segura et al. (2015) demonstrated that TLCs can be used as tracer particles in the unsealed form for temperature measurements with a higher accuracy level compared to the usage of encapsulated TLCs. However, the major doubt about their safe use concerns the behavior of non-encapsulated TLC particles if in presence of a significant shear stress. Therefore, in order to clarify this point in Section 3.5 an experimental investigation on the shear stress sensitivity of TLC particles has been carried out. The TLC particles inside the microchannels are stuck to the glass bottom wall of the device in such way to be able to monitor the effect of the increasing shear rate levels on those particles. The condition of stable and constant temperature is supplied by a Peltier device directly coupled on the top of the microfluidic device. The mixture containing the TLC particles is injected inside the microchannel using a syringe pump through which it is possible to set a precise flow rate to the mixture. In this way the generated Poiseuille flow exerts on stuck particles a different value of the shear rate and therefore a different value of the shear stress. The safe and proper usage of the non-encapsulated TLC particles for microfluidic applications has been later demonstrated both qualitatively and quantitatively in Section 3.6. For all the three kinds of TLC particles tested (which differ themselves for the working temperature range, (*i.e.* ΔT = 1 K, ΔT = 5 K and ΔT = 10 K) it has been demonstrated that the temperature measurements remain reliable for shear rates up to 400 s^{-1} that corresponds to shear stresses of around 0.3 - 0.4 Pa depending on the temperature of the working fluid. As the shear stress exerted on the TLCs becomes more and more stronger, the particles begin to smash losing their original compact structure. This led to the spreading of the TLC material inside the working fluid and upon the transparent wall. In order to give an estimation of this phenomenon, an empirical test has been conducted with the aim to evaluate the percentage of the TLC particles destroyed as a function of the shear rate. It has been demonstrated that for low values of the shear rate, the TLCs are not affected by this destructive phenomenon that raises for shear rate up to 200 s^{-1} and results into the complete destruction of almost all the particles for shear rates higher to 4000 s^{-1}, that correspond to shear stresses in the range of around 3 - 4 Pa depending to the temperature of the particles. However, this effect has a limited relevance for shear rate up to 400 s^{-1} at which the ratio between the destroyed particles and the intact ones is around the 35 %. In addition, since for non-encapsulated TLC particles used as tracer particles in aqueous flows the shear stresses are lower than those on stuck TLC particles at the wall of a microchannel, these results demonstrate that the non-encapsulated TLC particles can be safely used in order to measure the fluid temperature for common

applications in microfluidics (Re < 10).

Finally, a preliminary combined temperature-velocity measurement for an isothermal flow in a microchannel has been shown using unsealed TLC particles as tracer for APTV and temperature sensors.

3.10 Perspectives

A substantial improvement on the accuracy of the results obtained through the usage of TLC as tracer particles can be achieved increasing the power of the white light source and increasing the resolution of the RGB color camera. With these two improvements the quality of the images acquired will be enhanced, this means a more robust and precise calibration curve and consequently temperature measurements with lower uncertainties. In addition, as concerns the three-dimensional astigmatic velocity measurements, a brighter image of the TLC particles gives a signal with higher strength, hence the uncertainty associated to the displacement of the in-focus and out-focus particles will be reduced. Moreover, in order to make the non-encapsulated TLC particles more stable and enlarge their availability for the measurements of the temperature in flows in which the shear stresses exerted on the particles are over 1 Pa, further developments in the production of the unsealed TLCs are required.

On the other hand, from an experimental point of view, the understanding of the behavior of those TLC particles in flows in which temperature gradients are established is interesting. For this reason, the design of a device in which a stable and well known temperature gradient inside a fluid flow is established has been described. Particular care on the choice of the material for this device must be observed. Basically, in this case, the device must provide a temperature gradient of almost 15 K (maximum working temperature range of the TLC particles) keeping fixed the inlet temperature equal to the laboratory temperature. It has been demonstrated that all the materials with high thermal conductivity, such as copper or aluminum, cannot be employed for this device; PMMA has been selected as the best material for the realization of the microfluidic device. With PMMA as substrate material, temperature gradients of around 15 K along the streamwise direction can be achieved along the overall length of the device (70-80 mm) and without affect substantially the inlet temperature of the fluid. Finally, the numerical simulation of the test temperature distribution on the device has demonstrated that particular attention must be taken in order to keep under control the effect of natural convection on the external surface of the device.

Chapter 4

Optical detection of air and water mixtures in microchannels

4.1 Introduction

The experimental techniques for the optical investigation in microfluidics become fundamental when two-phase flow mixtures are involved. Two-phase flow systems can be found in a wide range of technological applications such as drug delivery, chemical technologies, heat exchange systems and so on (Tabeling, 2005; Zhao, 2013). Therefore, an accurate understanding of the parameters that control the physics of these systems is very important. Even if for macro devices the main aspects are nowadays deeply studied and reported in open literature (Carey, 1992), these data are not sufficient in order to predict the flow pattern for two-phase flows in microfluidics (Serizawa et al., 2002; Shao et al., 2009). Due to the increased surface-to-volume ratio in micro systems, the importance of superficial forces increases with respect to the volumetric forces in microdevices (Tabeling, 2005; Bruus, 2008; Colin, 2010). For this reason, the evolution of the flow patterns in microchannels can change significantly due to the different importance assumed by capillarity and inertial forces. It has been demonstrated that the two-phase flows are sensible to the geometry of the channel as well as to the superficial treatments of the solid surfaces (Hassan et al., 2005; Shao et al., 2009; Zhao and Middelberg, 2011). As a consequence, as outlined also by Shao et al. (2009), systematic studies that cover all the typologies of microchannels are needed in order to be able to predict the evolution of two-phase flow patterns in microfluidic devices. Among all the possible two-phase mixtures, air and water mixtures probably represent the most widely used and investigated.

This chapter is based on the publication:
Puccetti G., Tosi M., Pulvirenti B. and Morini G.L., 2015, Flow patterns of an air–water mixture at the exit of a micro T-junction, *Experimental Thermal and Fluid Science*, **67**:62-29. http://dx.doi.org/10.1016/j.expthermflusci.2015.01.010

Works concerning air and water mixture are reported in the review of Shao et al. (2009) in which the main studies on this field are summarized both for mini and microchannels, from 1964 up to 2008. Kawahara et al. (2002) published a work in which a mixture of co-current flows of water and nitrogen was initially premixed in a crossed junction and then observed in a straight circular channel of fused silica with an inner diameter of 100 µm. The flow patterns reported from the authors were observed for a gas superficial velocity ranging from 0.1 m/s up to 100 m/s and a liquid superficial velocity from 0.04 m/s up to 5 m/s. Different regimes from intermittent to semi-annular flow were observed. Cubaud and Ho (2004) studied an air-water mixture inside two different microchannels made by glass and silicon and having a squared cross-section with a nominal side of 200 µm and 525 µm. Air and water flows were previously mixed in a mixing chamber composed by cross squared microchannels with a nominal side of 50 µm. For both the test sections, the authors observed flow patterns from bubbling to dry passing through wedging, slugs and annular regimes. The superficial velocities of gas and liquid ranged from 0.001 m/s up to 10 m/s for air and from 0.001 m/s up to 2 m/s for water. Chung and Kawaji (2004) published a work in which the effect of the inner diameter of the microchannel on flow patterns for a mixture of nitrogen and water were analyzed. Four different circular channels with inner diameters of 530 µm, 250 µm, 100 µm and 50 µm were investigated. All the microchannel were realized in a substrate of fused silica coated with standard polyimide. The microchannels with an inner diameter larger than 250 µm exhibit the same flow patterns obtained with minichannels: from bubbly to annular flow passing through slug, churn and slug-annular regimes. On the contrary, for the two smaller geometries only the presence of a slug flow pattern was observed for the whole range of the superficial velocities investigated. Haverkamp et al. (2006) made a study on the effect of different mixing geometries for the generation of two-phase flows based on nitrogen and water and isopropanol and water. In particular, for the establishment of the two-phase flows, the authors used a cross shaped mixer and a smooth shaped mixer. Both devices were realized in borosilicate glass and with microchannels having a rectangular cross-section (400 µm x 50 µm) for the inlet of the mixing chamber, which had smaller dimensions with respect to the inlet branches. Slug and annular regimes were detected for the mixture of nitrogen and water while a bubbly flow pattern appeared for the mixture of isopropanol and water. In both cases the superficial velocity of the water ranged from almost 0.01 m/s up to 0.1 m/s while the gas flow ranged from 0.04 m/s up to 30 m/s Saisorn and Wongwises (2010), published a work in which an air-water mixture was established by injecting the liquid flow through an angle of 30° with respect to the main gas stream. The obtained mixture was later driven into circular microchannels made in fused silica with an inner diameter of 530 µm, 220 µm and 150 µm. For each microchannels the authors reported a flow pattern map realized by changing the superficial liquid velocity from 0.005 m/s up to 3 m/s and the gas superficial velocity from 0.37 m/s up to 42 m/s. For the microchannel with the larger diameter the authors found flow patterns from

slug to annular, while for the medium one different types of annular flow were observed. For the smallest diameter, unstable conditions were found in which liquid flow pattern and annular flow were alternatively observed. Santos and Kawaji (2010), used a micro T-junction in order to mix deionized water with air. The micro T-junction had a rectangular cross-section with sides of the order of 110 µm - 120 µm, the flow of water was injected in the same direction of the outlet while the gaseous inlet was orthogonal to the water direction. The superficial velocity of the water ranged between 0.042 m/s up to 0.757 m/s while air ranged between 0.04 m/s up to = 0.791 m/s. Within these ranges a flow pattern map was obtained through 27 different combinations of liquid and gas flow rate. In particular, several types of slug flows and annular flow were found. In addition, the authors compared the observed flow patterns with numerical simulations. Good agreement were found by the authors between experimental and numerical results for short slugs (length shorter than 400 µm), while some discrepancies were found in this comparison for the largest bubbles. The review summarized here is an example of the effort made during the last decade for the analysis of gas-liquid mixtures in microdevices and for the creation of validated flow pattern map able to predict the most important regimes originated in microchannels. Other works obtained by considering different configurations of superficial velocities of the liquid and gaseous phase are due to Serizawa et al. (2002); Hassan et al. (2005); Cubaud et al. (2006); Fu et al. (2010); Yamamoto and Ogata (2013) and Arias and González-Cinca (2013). In order to summarize the main results obtained for air-water mixtures it is possible to conclude that, six main two-phase flow patterns can be observed depending on the superficial velocity of gas and liquid phase in microchannels, as reported in the flow pattern map shown in fig. 4.1.

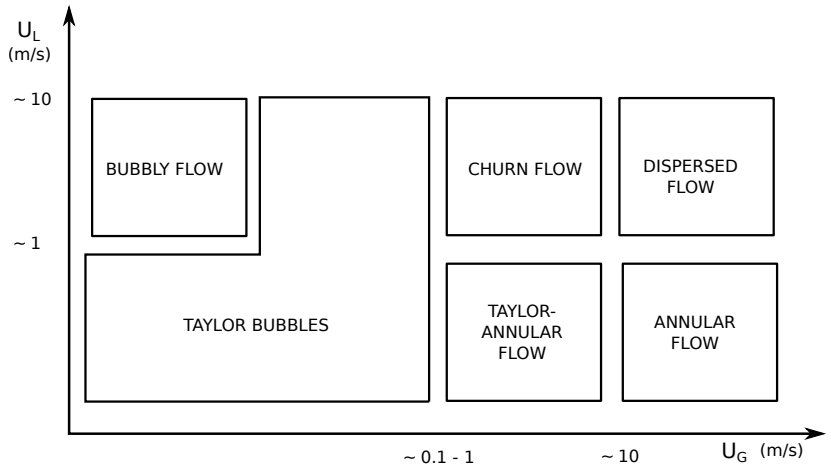

Figure 4.1: Classification of typical two-phase flow patterns observed in microchannels. The image is adapted from (Shao et al., 2009).

Bubbly flow and Taylor bubbles appear at low superficial velocity of gas flow when the surface tension forces dominate over inertial forces. On the contrary, when inertial forces dominate over the surface tension forces, dispersed and annular flow are visualized (which happens for high superficial velocity of gas flow). The transitional region linked to values of gas superficial velocity between 1 and 10 m/s, is characterized by churn and Taylor-annular flow-patterns (Shao et al., 2009). The values of superficial velocities at which the transitions between the different flow patterns occur are however dependent either on the nature of the fluids, than from the size of the microdevice (inner diameter and length). Therefore, the values of the superficial velocities shown in fig. 4.1 have to be regarded only as an indication at which the transitions of the flow patterns are usually observed.

4.2 Aim of the work

A specific test rig has been designed in order to be able to detect air bubbles inside a liquid flow in a microchannel, with the aim to build a flow pattern map by means of which the flow configuration of air/water mixtures can be reconstructed as a function of the superficial velocities of gas and liquid phases. The development of an experimental technique able to give accurate measurements about the physical aspects of a two-phase flow inside a microchannel has a remarkable importance since it provides suitable data for the validation of numerical codes for the modeling of two-phase mixtures, that is one of the most complex issues for the fluid dynamic simulations in micro systems.

For this work a micro T-junction made in fused silica was used as mixer for the air-water flow. The geometry of the micro T-junction was previously analyzed in detail through the inverse use of the μPIV technique and the real inner geometry of the device is known. As reported in Section 2.5.3, the prediction made via the μPIV technique (and later confirmed from an analysis through the confocal fluorescence microscopy) revealed a slightly trapezoidal cross-section with a higher base of 300 μm, a depth around 265 μm and acute angles of 88°. In order to build a flow pattern map, 256 different experimental runs were carried out for different conditions of superficial velocity of water and air. In particular, both the superficial velocity of water and air ranged from 0.005 m/s up to 0.15 m/s; the investigation region covered in this thesis is depicted in fig. 4.2 by the dashed area.

In the present work, this specific area has been selected as the investigation region of the air-water flow patterns, since, to the best knowledge of the author, up to now the flow patterns for air/water mixture in micro T-junctions are extensively reported only for superficial velocities of both the inlet fluids larger than 0.1 m/s. Below these superficial velocity values only few data are present in literature. For example Santos and Kawaji (2010) have reported a flow pattern map of an air - water mixture in a micro T-junction similar to the map used in this work, in which,

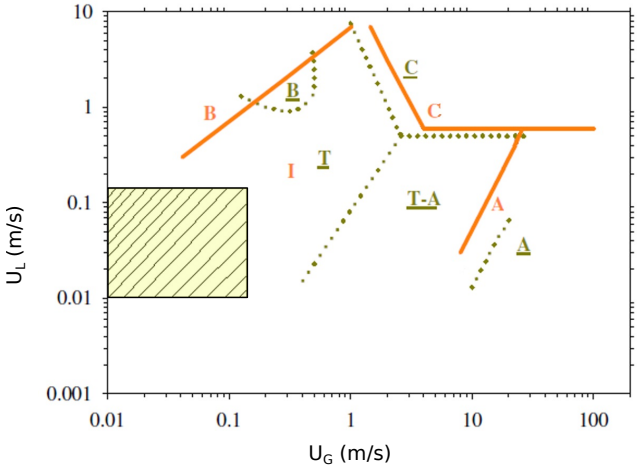

Figure 4.2: Example of air/water flow patterns observed in literature for an air-water mixture inside a micro mixer: in orange are drawn the flow pattern transitions found by Hassan et al. (2005), with dotted green lines the transitions observed by Chung and Kawaji (2004). The highlighted area represents the region under investigation in this work. The image is adapted from Shao et al. (2009).

from all the whole set of observations made by the authors, only six of them was within the region investigated by the dashed area of fig. 4.2. In particular, no one observation on flow pattern has been reported by the authors for superficial velocities of air and water lower than 0.04 m/s. For this reason it is possible to conclude that the results reported in this chapter extend and complete the set of available data for an air-water mixture inside a micro T-junction to the region characterized by low gas and liquid superficial velocity values.

4.3 Experimental Apparatus

A simple sketch of the experimental setup is presented in fig. 4.3.

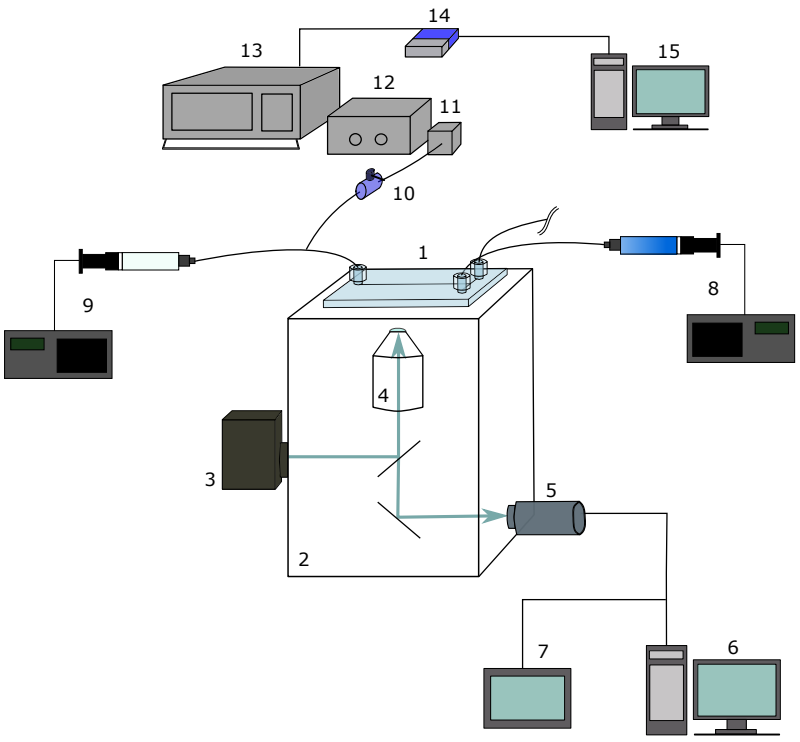

Figure 4.3: Layout of the experimental apparatus: 1) Microchannel 2) Inverted microscope 3) Mercury lamp 4) Objective lens 5) High-speed Camera 6) Software unit 7) Supplementary LCD monitor 8) Water system supply 9) Air system supply 10) Shut-off valve 11) Differential gauge pressure 12) Signal amplifier 13) Multimeter 14) Analog Input Module 15) Software unit. *(dimensions not in scale)*

A commercial micro T-junction (1 in fig. 4.3) made in fused silica (*Translume* TUC-300300-L-1-170) is employed in order to generate the air/water mixture. The geometry of the T-junction used in these tests has been shown in Chapter 2 by using the confocal microscopy. The geometry of the mixer is well known: the confocal fluorescence microscopy confirmed that the microchannels of the T-junction are characterized by a slightly trapezoidal shape with acute angles of 88° and a hydraulic diameter of around 280 µm. The micro T-junction is arranged upon an inverted microscope (2, *Nikon Eclipse TE 2000-U*) equipped with an objective lens (4, *Nikon CFI 10X*) with magnification M = 10 × and numerical aperture NA = 0.25.

The water flow enters the micro T-junction in the same direction of the outlet streamflow while the air flow is mixed to the water flow orthogonally to it (fig. 4.4).

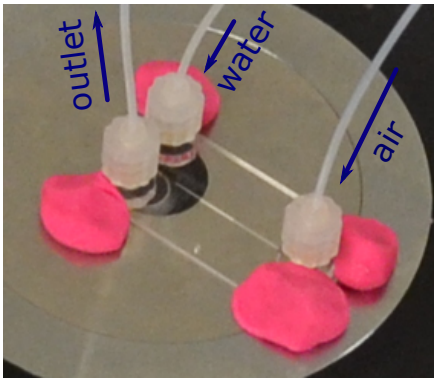

Figure 4.4: Picture of the microchannel mounted on the inverted microscope. In the picture are reported the inlet flows of water and air, as well as, the outlet branch.

The illumination is delivered by a mercury lamp (3, *Nikon* HMX-4B) directly installed in the rear access of the inverted microscope. The mercury lamp is powered by a current generator (*Nikon* C-SHG1) that provides a power of 100 W. The light delivered by the mercury lamp reaches the microchannel through the objective lens and the images are acquired by a high speed camera (5, *Olympus i-SPEED 2*). The high speed camera acquires the images with frame rate of 1500 fps, which corresponds to a time delay of 667 µs between two subsequent frames. The selected frame rate gives images with a resolution of 672 × 504 pixels and an additional zoom ratio of 1.19. A supplementary controller display unit (7, 8.4" LCD monitor) is additionally connected to the high speed camera. In this way it is possible to monitor constantly the evolution of the flow pattern and perform the acquisitions in the proper way. Indeed, the images are acquired both at the junction, where the two flows are joined together, and along the outlet stream flow, where the two-phase flow pattern is established. The two fluids are stored inside gas-tight glass syringes with a volume of 10 ml (*Hamilton Gastight #1010*) and the flow rates of both fluids are supplied by means of two independent syringe pumps (8, *Harvard Apparatus PHD 4400* and 9, *Cole-Parmer Hills*). By means of the syringe pumps the volumetric flow rates of air (Q_a) and water (Q_w) can be imposed and, by means of these quantities and the area of the microchannel cross-section (A), the superficial velocities linked to the flows ca be calculated as follows:

$$U_A = \frac{Q_a}{A} \qquad U_W = \frac{Q_w}{A} \tag{4.1}$$

The flow rates imposed to the water flow and to the air flow are varied in order to have an imposed superficial velocity of air and water (U_A and U_W, defined as reported in Eq. (4.1)) ranging between 0.005 m/s up to 0.15 m/s.

Particular care has been devoted to the gaseous inlet branch. Indeed, since air is a compressible fluid, its pressure value tends to increase during the action of the pump until the reaching of a steady state condition. Therefore, the pressure of air inlet flow was an important value to be checked because a constant pressure

value is the signal of the establishing of a steady state flow condition in the system. In order to evaluate the pressure of the air inlet branch, a differential pressure gauge (11, *Validyne DP15*) is installed along a derivation of the incoming air branch through a shut-off valve. The shut-off valve (10) allows to disconnect the whole system of pressure measurement, preventing to the liquid flow to reach the differential pressure gauge during the phases of charging or cleaning of the device. The differential pressure gauge is a capacitive sensor in which the full scale can be changed by means of the use of different membranes. In these experiments a full scale value of 860 kPa has been fixed for the sensor. The pressure signal is converted in a differential electrical potential signal which is amplified by means of a demodulator (12, *Validyne CD15 Sine Wave Carrier Demodulator*) which is, in turn, connected to a multimeter (13, *Agilent 34401A*). The multimeter allows to directly measure the voltage value associated to the air pressure. By means of an USB connector (14, *NI USB-9219*) the signals are transferred to a PC. The management of the acquisition data system is driven by a LabView® code.

In order to avoid the bouncing effect of the pressure caused by the alternative exit of water droplets and air bubbles, the outlet branch was immersed inside a water reservoir at a depth of 2 cm. All the experimental apparatus is installed on a dumped table. The two inlet branches of the fluids, as well as the differential pressure gauge, the shut-off valve and the outlet reservoir are shown in fig. 4.5. Pictures of the experimental apparatus are reported in fig. 4.6 and fig. 4.7. In particular in fig. 4.6 is possible to see the system used for measuring the pressure of the air inlet branch while in fig. 4.7 a view of the instrumentation connected to the inverted optical microscope is shown.

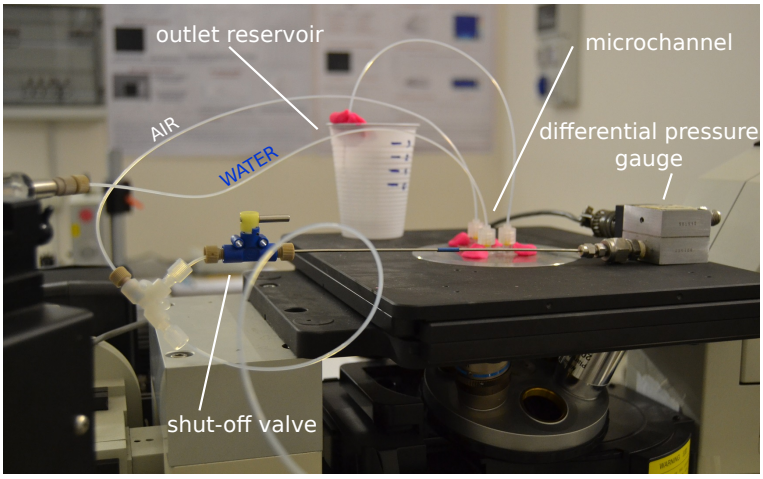

Figure 4.5: Picture of the differential pressure gauge connected to the air inlet branch. In the picture are also highlighted the shut-off valve connected to the pressure measurement system and the outlet reservoir.

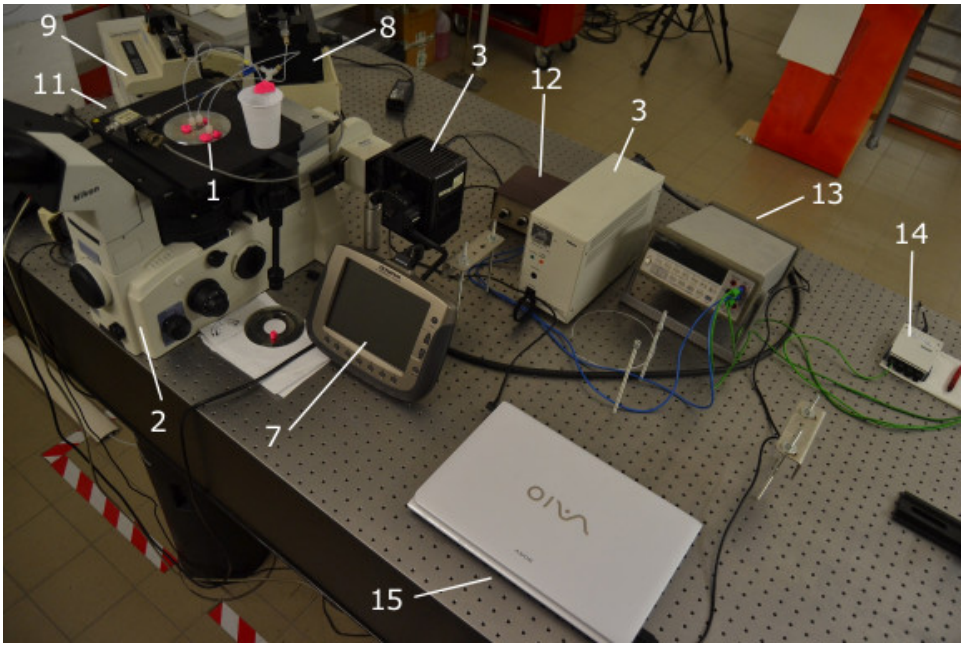

Figure 4.6: Picture of the entire experimental apparatus.

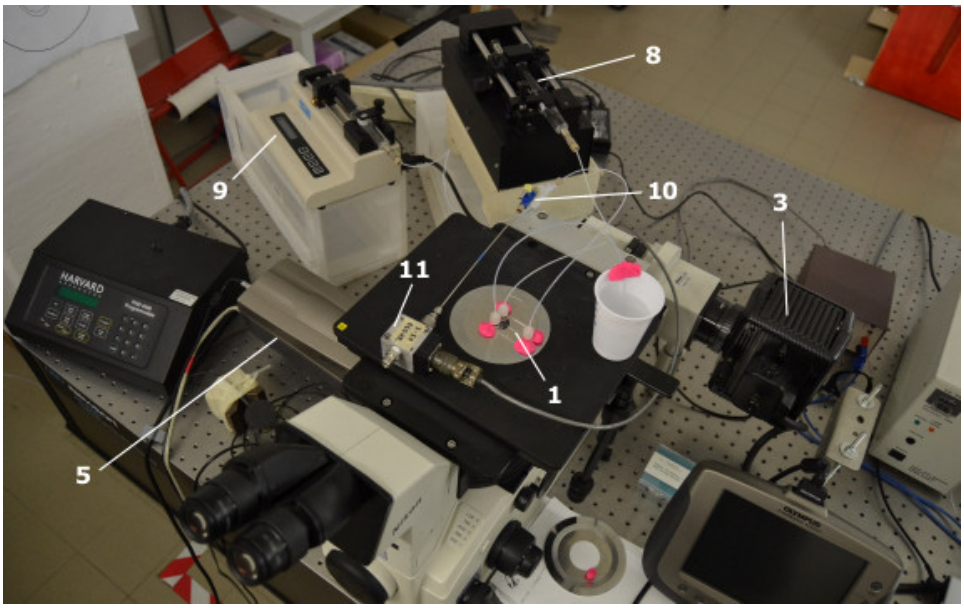

Figure 4.7: Detailed view of the experimental apparatus.

In Table 4.1 the main technical features of the devices involved in the test rig described above are summarized.

Table 4.1: Summary table of the principal components of the experimental setup.

Ref.	Component	Description
1	Microchannel	T-junction made in Fused Silica Glass Nominal: squared with a side of 300 µm Effective: trapezoidal with acute angles of 88° (see section 2.5.3)
2	Inverted Microscope	Eclipse TE 2000-U (*Nikon*)
3	Mercury Lamp	*Nikon* HMX-4B *Nikon* C-SHG1 Power: 100 W
4	Objective lens	*Nikon CFI 10X* Magnification = 10 × Numerical Aperture = 0.25 W.D.: 6.1 mm, C.G.: 0.17mm
5	High speed camera	*Olympus i-SPEED 2* CMOS sensor resolution 800 × 600 pix Electronic shutter to 5 µs @ 1500 fps: resolution 672 × 504 pix, zoom ratio 1.19
7	*Olympus i-SPEED 2*	Controller display unit 8.4" LCD daylight viewing
8	Water System Supply	Syringe: *Hamilton Gastight #1010* Syringe pump: *Harvard Apparatus* PHD 4400 Programmable Minimum flow rate = 0.0001 µl h^{-1} Maximum flow rate = 220.82 ml min^{-1} Uncertainty ± 0.35%
9	Air System Supply	Syringe: *Hamilton Gastight #1010* Syringe pump: *Cole-Parmer Hills* For a syringe of 10 ml: Minimum flow rate = 0.1 ml h^{-1} Maximum flow rate = 125 ml h^{-1} Uncertainty ± 0.5%
10	Shut-off valve	*Upchurch* Tefzel®(ETFE) with 1/16" Fittings
11	Differential pressure gauge	*Validyne DP15* Membrane full scale: 860 kPa
12	Signal amplifier	*Validyne CD15 Sine Wave Carrier Demodulator*
13	Mulitmeter	*Agilent 34401A*
14	Analog Input Module	*NI USB-9219* 4-Channel Universal Analog Input Module

4.4 Methodology

First of all, before to start each experiment, the micro T-junction is dried out in order to eliminate the residual presence of water droplets inside the inlet air branch. In fact, the presence of water droplets could threaten the correct charging of the air flow during the preliminary steps of each experimental runs, delaying consequently the establishment of the pressure steady state conditions. Then, once dried out the channel, the air supply system is activated in the continuous pumping mode while the syringe pump which controls the inlet of water is periodically stopped until the establishment of the equilibrium pressure. This operation requires a time between 200 s and 800 s depending on the flow rates imposed. The establishment of the equilibrium pressure is highlighted from a stable and constant value of the inlet air pressure. More precisely, during the phase of the air charge, the pressure of the gas increases monotonically until a steady state condition is reached; from this measurement the air pressure remains fixed to the equilibrium value (see fig 4.8). At the equilibrium condition, the characteristic flow pattern is established and both the syringe pumps are set in a continuous pumping mode.

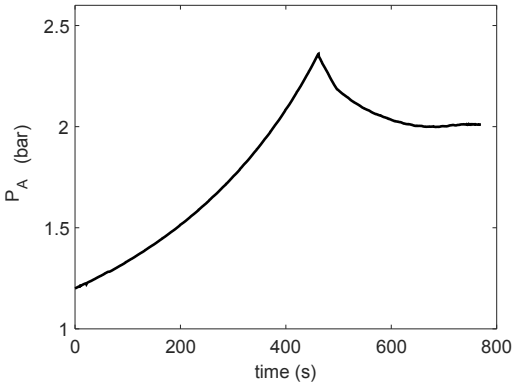

Figure 4.8: Pressure trend during the phase of air charge for U_W = 0.13 m/s and U_A = 0.12 m/s.

Afterwards, the images of two-phase flow are acquired for 8 s at 1500 fps along the outlet branch. Additional images with the same frame rate acquisition, are also recorded at the junction in order to understand the mechanism of the bubbles' formation. Since the Capillary number (Ca, see Eq. (4.2)) is always lower than 0.002 for all the water flow rates investigated, no droplets with dimensions smaller than the microchannel cross-section are expected. In fact, as remarked by Garstecki et al. (2006), for Ca < 0.01 the dispersed phase fills completely the outlet branch of the T-junction since the shear stress exerted on the interface of the developing droplet is not sufficient to deform it, therefore the bubbles are formed from the squeezing of the neck of the dispersed phase against the edge of the junction. The definition of the Capillary number is reported here:

$$Ca = \frac{U_W \mu_W}{\sigma} \tag{4.2}$$

where μ_W is the dynamic viscosity of the continuous phase and σ is the surface tension between the continuous phase and the dispersed phase (*i.e.* for air-water mixture a value of 0.073 N/m can be considered). An example of the mechanism of the bubble's detachment is shown in figure 4.9. In figure 4.9 six different images at a different time are shown. In particular, the time delay depicted in fig. 4.9 is calculated starting from the top left image, that is set as the frame # 0.

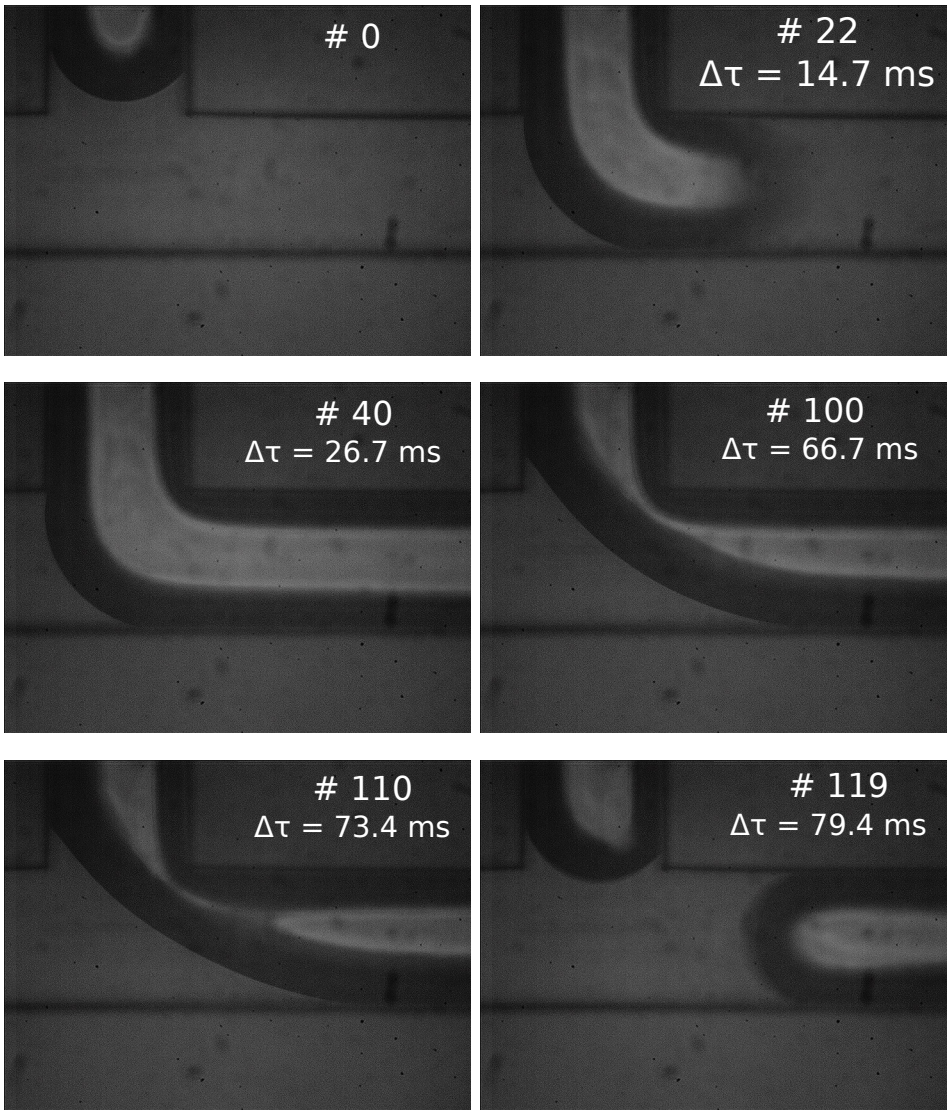

Figure 4.9: Mixing zone of the T-junction at different frames: the air flow (white flow) enters from the top vertical branch while the water flow enters from the left horizontal branch (water flow is transparent). The right branch is the branch of the outlet flow.

In the reported example (U_W = 0.02 m/s and U_A = 0.13 m/s) the air flow, entering from the top vertical branch, is pushed by the water flow to the outlet branch, in around 15 ms. Then, for almost 60 - 70 ms the air fills the outlet branch and after around 75 ms from the frame # 0 the detachment phase starts. The detachment is determined by the progressive reduction of the thickness of the bubble squeezed against the T corner. When the bubble fills the T region the water flow is strongly reduced. Water pushes the bubble against the outlet corner and a squeezing of the bubble occurs. Finally, after a time delay of almost 80 ms squeezing is completed and the bubble is formed. Several bubbles are formed during the 8 s of recording time while the time of formation of the bubble and the length of the same change in each experimental test depending to the imposed superficial velocities of air and water. The described procedure is repeated for all the experimental runs. In order to fill the flow pattern map, several experimental runs are carried out changing the flow rates imposed to the two inlet fluids and consequently the superficial velocities of the two phases, for each different experimental run. The superficial velocities of both fluids are ranged from 0.005 m/s up to 0.15 m/s, obtaining 256 different couples of superficial velocities of air and water. However not for all the combinations of the superficial velocity of water and air was possible to obtain a stable and repeatable flow pattern. In particular, for the slower air and water superficial velocities, unstable conditions with a no repeatable flow pattern are observed and therefore for these conditions the images are not post-processed and the flow regime not inserted in the flow pattern map. The reason behind this behavior is mainly due to the reduced volumetric capacity of the air syringe pump which is for these regimes not sufficiently large in order to reach the stable pressure of the inlet air flow. In addition, when Ca is below 0.0005 (*i.e.* $U_W < 0.04$ m/s) bubbles with a high non-uniformity of their length are produced. Hence, as it will be shown in the following (Section 4.5), the obtained flow pattern map is composed by 195 flow regimes experimentally observed with superficial velocities of air and water ranging between 0.010 m/s up to 0.15 m/s.

For the construction of the flow pattern map, the experimental analyses and the acquisition of the images are carried out along the outlet branch where the two-phase flow mixture is already developed. The acquisition are taken by means of the positioning of the focal plane of the optical microscope in the central plane of the channel. Due to the dimension of the hydraulic diameter of the microchannel coupled with the superficial velocities imposed to the air flow and to the water flow, only the Taylor-Annular regime and different types of Taylor bubbles are detected. Therefore, the post-processing analysis is focused on the proper reconstruction of the shape of the bubble in order to evaluate correctly the length and velocity of the single bubble and the related quantities, like the void fraction of the mixture. Two different conditions depending on the imposed superficial velocities of the two flows are observed. For the longer bubbles, the bubble can be detected through several frames. In fact, in these cases the back side of the bubble appeared various frames later with respect to the front side

of the bubble as it is visible from fig. 4.10. On the contrary, for high superficial velocities of the two fluids, the bubbles are shorter and they can be detected entirely in a single frame as it is depicted in fig. 4.11. The images were initially acquired with the software *Olympus I Speed 2* and pre-processed with a pixel smoothing filter in order to increase the quality of recorded images (fig. 4.10 and fig. 4.11). However, the image acquired by the high speed camera were difficult to handle in order to produce quantitative results due to the shaded peripheral area of the bubble which made very difficult to detect the proper contour. Hence, the images are treated through a customized post-processing method developed in the Matlab environment.

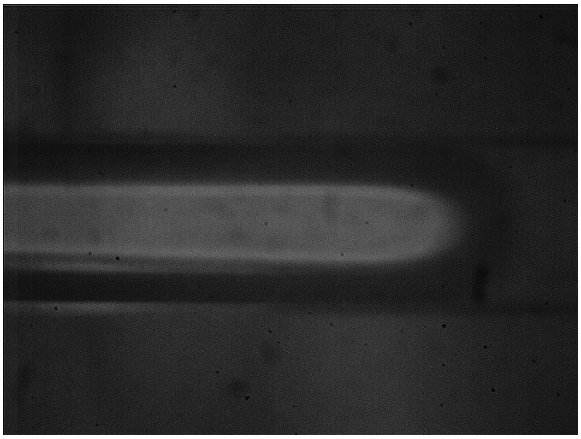

Figure 4.10: Bubble along the outlet branch detected in more than one frame.

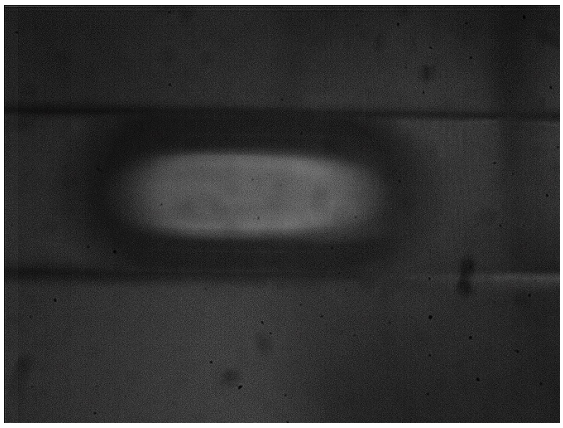

Figure 4.11: Bubble along the outlet branch detected in one frame.

For a long air bubble the post-processing treatments are divided into three main steps and are applied to all the frames between the front and back sides of the bubble (fig. 4.12):

1. First of all, the channel boundaries are detected and two lines drawn in correspondence to them. An additional line in the middle of them is hereafter traced (see the final image shown in fig. 4.14). This line represents the

bubbles' axis for all the subsequent evaluations since all the bubbles are assumed to be axisymmetric with respect to the axis of the microchannel.

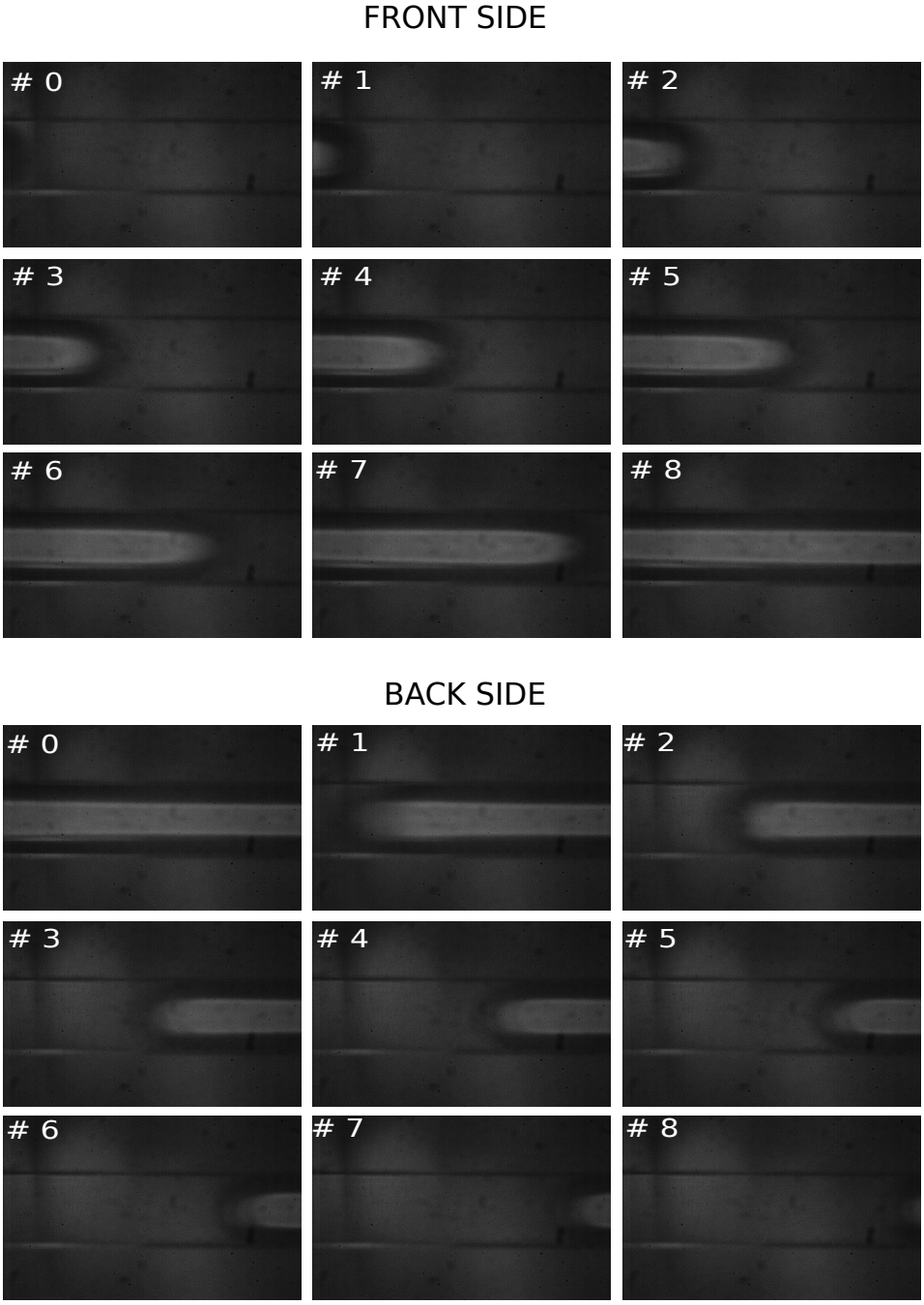

Figure 4.12: Raw images of the detected front and back sides of a bubble belonging to the "Middle Taylor" flow pattern.

2. In order to detect correctly the bubbles' contours, the contrast between the bubbles and the background has been enhanced by multiplying each image containing a bubble for a fixed factor (1.1 - 1.2 depending on the images) and subsequently subtracting all of them with an image in which the microchannel is completely filled with water. In order to define this factor the Matlab function `graytresh`, which is based on the Otsu's method (Otsu, 1979), has been utilized. Black holes, given by the dust inclusions on the objective lens of the microscope or on the outer side of the microchannel, are filled using the Matlab function `imfill` and then converted into gray regions in order to not being confused with the black pixels of the bubble's edges. Then, the images are converted from the grayscale to black and white binary images (see fig. 4.13 A). For making this, a high-pass filter coupled with a low-pass filter has been applied to the original gray images in order to convert each pixel having an intensity lower than the threshold value (t = 0.24 - 0.29 depending on the images) into a white pixel (1) while the other ones are converted into black pixels (0). The Matlab functions `imadjust` and `imcontrast` are utilized in order to handle the gray images and choose the proper level of the threshold value while the function `im2bw` is used in order to convert the gray pixels into a black or white ones. The result of the conversion is a segmented image in which the core of the bubble, that has to be completely white, still presents some areas of black pixels. For this reason the command `imfill`, has been applied to each image in order to produce an image in which the core of the bubble is completely detected through a white area (fig. 4.13 B).

3. The last step of the post-processing of the images enables to trace the line in correspondence of the edges of the bubbles. Firstly, the line corresponding to the inner core of the bubble is drawn, this line is the red line shown in fig. 4.14. Then, the peripheral part of the bubble is added to the core to detect the actual edges of the bubble. This procedure is supplied by an in-house developed routine that evaluates the gray-gradient of the peripheral part of the bubble and adds the shaded outer layer to the central core of the same. The whole bubble contour is at the end enclosed from the yellow curve depicted in fig. 4.14. The drawn lines are later used in order to detect the displacement of the front side and back side of the bubbles.

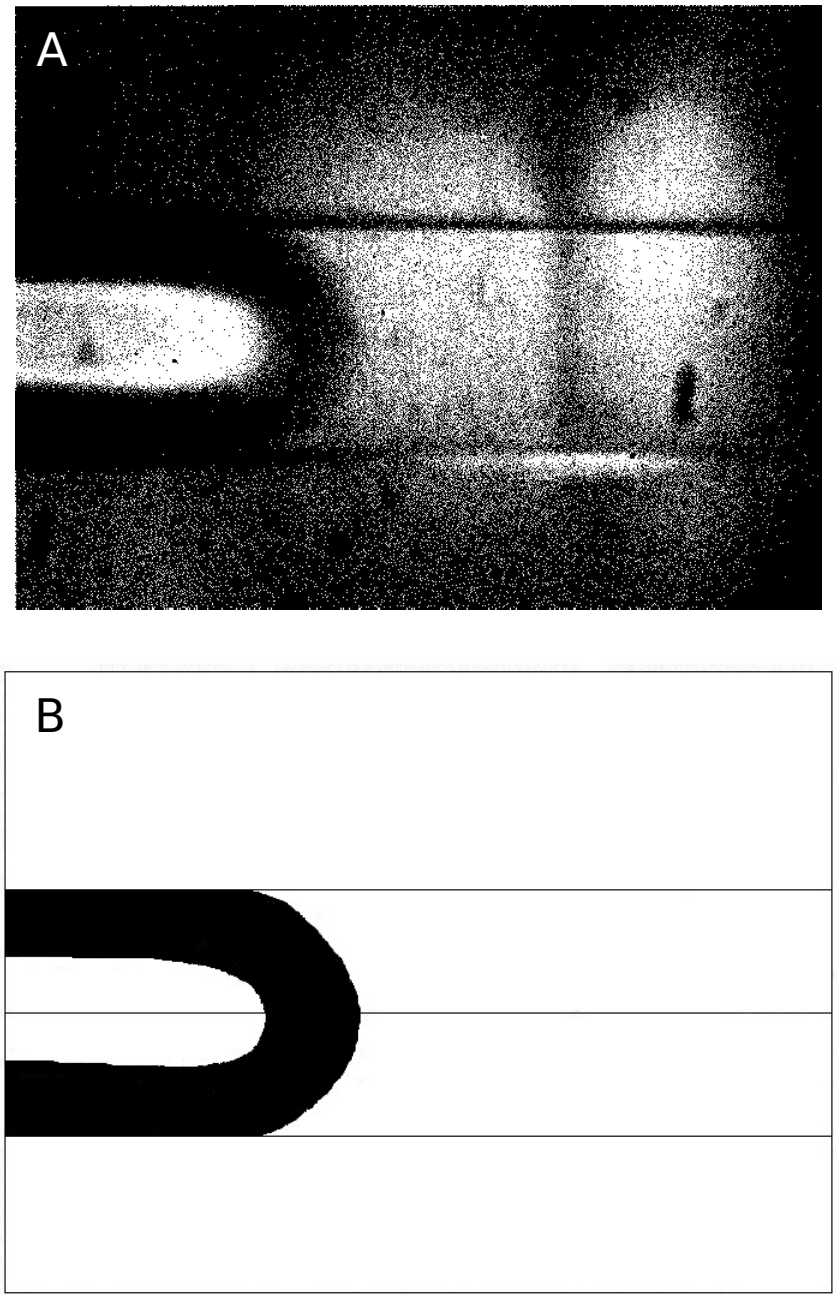

Figure 4.13: Conversion of the images from a grayscale into a black and white images. A) A threshold filter was applied in order to convert light gray pixels into white pixels and dark gray pixels into black pixels. B) A segmentation filter was later applied in order to fill the white area through the conversion of the black pixels into white pixels.

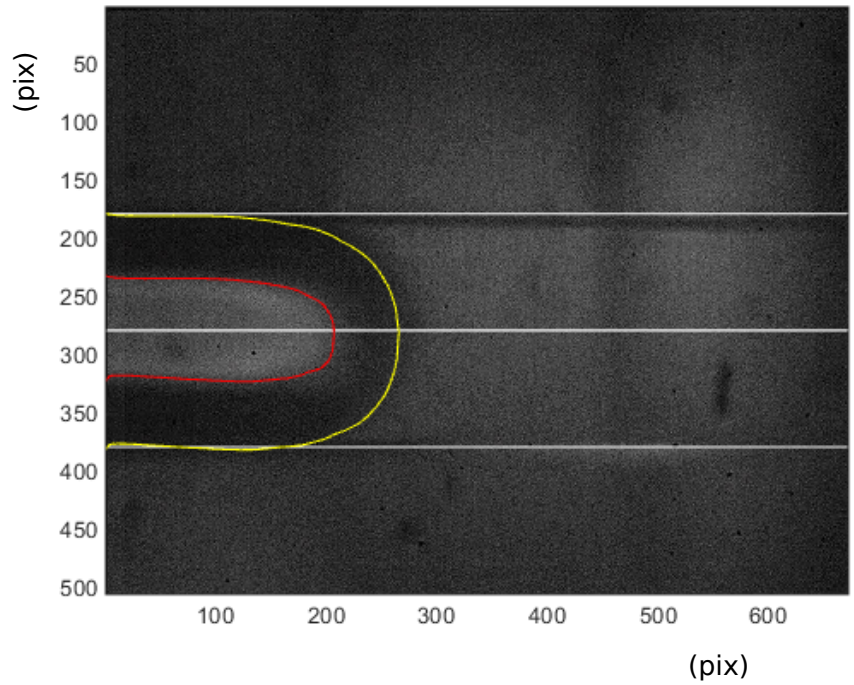

Figure 4.14: Final image of a bubble with lines drawn in correspondence of its contours: in red is detected the inner core of the bubble, while in yellow the outer shape.

4.4.1 Experimental determination of the velocity and length of the bubbles

The experimental evaluation of the bubbles' velocity (W_{Bi}) is basically obtained by dividing the displacement of the front side and back side of the bubbles for the unit time since all the series of images are acquired with a constant time delay of around 667 µs. More precisely the velocity of each single bubble i-th (W_{Bi}) is estimated by averaging the displacement per unit time of the front side of the bubble (W_{fi}) with the displacement per unit time of the back side of the bubble (W_{ci}):

$$W_{Bi} = \frac{\frac{1}{F}\left(\sum_{f=1}^{F} W_{fi}\right) + \frac{1}{C}\left(\sum_{c=1}^{C} W_{ci}\right)}{2} \tag{4.3}$$

where F and C are respectively the total number of the displacements per unit time of the front side and back side of each bubble i-th.

Then, the corresponding velocity of the bubbles associated to each couple of superficial velocity of air and water is obtained by averaging the velocity obtained by Eq. (4.3) for all the bubbles contained in the recorded images:

$$W_B = \frac{1}{I}\left(\sum_{i=1}^{I} W_{bi}\right) \tag{4.4}$$

Same procedure is followed in order to evaluate the velocity of the liquid slug between two subsequent bubbles. In this case the front of the liquid slug corresponds to the back side of the previous bubble while the back side of the liquid slug is the front side of the following bubble.

Once calculated the average velocity of each bubble it is possible to estimate directly their length using a reference line and counting the number of time n_{Bi} that the bubble crosses the line starting from the first crossing of the front side until the last one of the back side. This number is then multiplied by the average displacement of the bubble ($W_{Bi}\Delta\tau$). The length of the bubbles associated to each couple of superficial velocity of water and air is finally calculated as the average of the lengths of each single bubble of the set of imposed flow rates:

$$L_B = \frac{1}{N_B}\left(\sum_{i=1}^{N_B} W_{Bi} n_{Bi} \Delta\tau\right) \tag{4.5}$$

$$L_L = \frac{1}{N_L}\left(\sum_{i=1}^{N_L} W_{Li} n_{Li} \Delta\tau\right) \tag{4.6}$$

Same procedure is followed in order to evaluate the length of the liquid slug L_L between two subsequent bubbles. Also in this case the front of the liquid slug is taken in correspondence to the back side of the preceding bubble and the back side of the liquid slug coincides with the front side of the consecutive bubble. In order to test the repeatability of the results several bubbles (at least 7) for each couple of the imposed flow rates have been evaluated. With the adopted methodology, the error associated to the estimation of the length of bubbles and liquid slugs, gives in the worst case an overestimation of the length measurement by a quantity equal to the value of a single displacement ($W_{Xi}\Delta\tau$ with $X = B, L$). Obviously this overestimation is negligible for the flow regimes characterized by a low superficial velocity of the water ("Taylor - Annular" and "Long Taylor"), in which the bubble length is in the order of some millimeters and consequently the overestimation associated is for the worst case below the 2 %. However, as the liquid superficial velocity increases and consequently the length of the bubbles is reduced, this overestimation becomes more and more

important and reached an average relative error of around 6 % for the flow regime named as "Middle Taylor" and around 18 % for the flow regime named "Short Taylor", where, the higher number of bubbles analyzed decreases the weight of the maximum overestimation over the evaluation of the bubbles' length. Finally from the knowledge of the length of the bubbles and of the liquid slugs between the bubbles, it is possible to calculate the time-averaged void fraction of the mixture (α), defined as the ratio between the air volume over the total volume of the mixture, for each flow pattern observed:

$$\alpha = \frac{V_{\mathrm{B}}}{V_{\mathrm{B}} + V_{\mathrm{L}}} \tag{4.7}$$

4.5 Results and discussion

All the experimental observations have been collected in a map that summarizes the flow patterns observed during the tests; this map is depicted in fig. 4.15. As previously mentioned, two kinds of flow pattern are observed: Taylor slugs and Taylor-Annular flow. This results are not surprising considering the hydraulic diameter of the channel and the flow rates imposed. In fact, the results achieved are in agreement with the predictions of the previous flow pattern maps for low superficial velocity values reported in literature for similar conditions.

However, the performed research has been conducted by designing the experiment in order to be able to obtain not only the flow pattern but also a series of physical quantities (void fraction, length of the bubbles, neck configuration, bubble velocity, slug length and so on) which enable the deeper understanding of the physics linked to the air/water mixtures in microchannels. From the evaluation of the trend of the mentioned physical quantities, it is possible to subdivide the Taylor slug regime into three different regimes named "Long Taylor", "Middle Taylor" and "Short Taylor". In fact, the bubbles in Taylor slug regime can be characterized by a large range of length values. The bubbles belonging to the "Short Taylor" flow pattern are extremely short, most of them detected in a single frame (see fig. 4.11), while, as the flow patterns switched into "Middle Taylor" and "Long Taylor" the bubbles becomes more and more longer and several frames are necessary in order to detect completely the bubbles. It is proposed in this thesis to divide the Taylor bubbles in four categories by using the non dimensional number l defined as the ratio between the length of the bubbles L_B and the hydraulic diameter of the channel D_{h}. The "Short Taylor" bubbles are characterized by a length l lower than 3.5, the "Middle Taylor" bubbles have a length l included between 3.5 and 7, the "Long Taylor" bubbles have a length l that ranges between 7 and 20 and the "Taylor-Annular" bubbles have a length l larger than 20 (see Tab. 4.3).

Since l is also linked to the value assumed by the void fraction (see Eq. (4.7)) it is possible to find a relationship between the dimensions of the Taylor bubbles and α. It is possible to observe that, in the case of "Short Taylor" bubbles the void

fraction stays lower than 0.7; for the "Middle Taylor" bubbles the void fraction ranges between 0.7 and 0.82, and for the "Long Taylor" bubbles the void fraction is included between 0.82 and 0.9. For "Taylor - Annular" bubbles, the void fraction is generally higher than 0.9. A further difference of the "Taylor - Annular" regime from Taylor slugs is represented by the presence of a characteristic liquid ring located close to the tail of each bubble, which is slightly visible in fig. 4.16 representing a series of Taylor bubbles, while becomes more clear from the analysis of the motion pictures obtained collecting all the bubble frames.

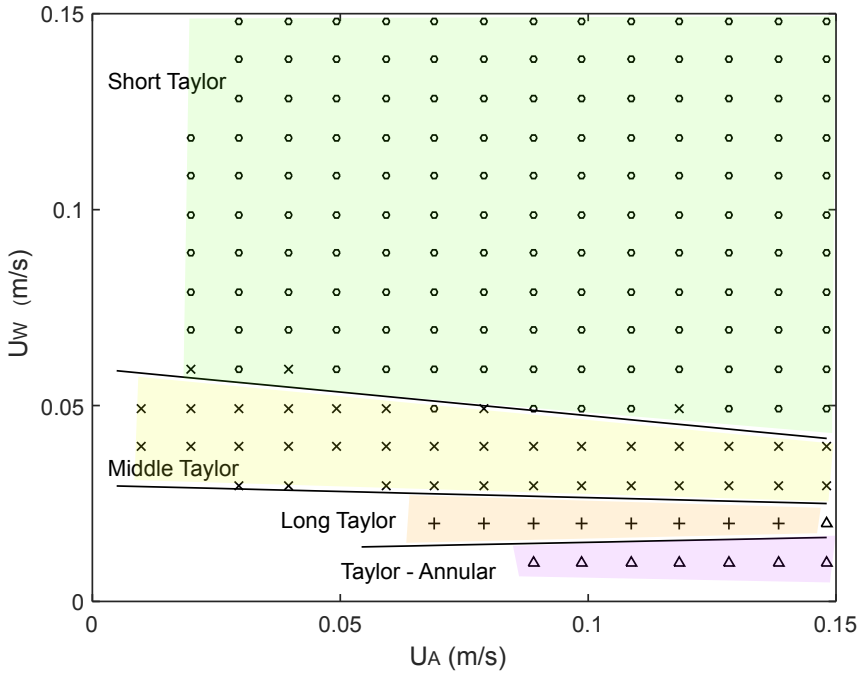

Figure 4.15: Experimental flow pattern map observed. In light green the area of superficial flow velocities in which the Short Taylor regime has been observed, in light yellow the one belonging to Middle Taylor regimes, in orange is outlined the Long Taylor regimes and finally in light purple the Taylor-Annular regime.

As it is visible from the flow pattern map depicted in fig. 4.15, in the range of superficial velocities (U_W) and (U_A) investigated here, the flow regimes are strongly dependent to the superficial velocity of water (U_W) while the superficial velocity of the air (U_A) is of minor importance. For superficial velocities of water lower than 0.02 m/s only the Taylor - Annular regime is observed, Middle Taylor bubbles appear only for superficial velocities of water ranging between 0.02 and 0.06 m/s and for water superficial velocity values larger than 0.06 m/s only Short Taylor bubbles are detected. In Table 4.2 and Table 4.3 for each flow regime, the average values of the main physical quantities which can be introduced in order to

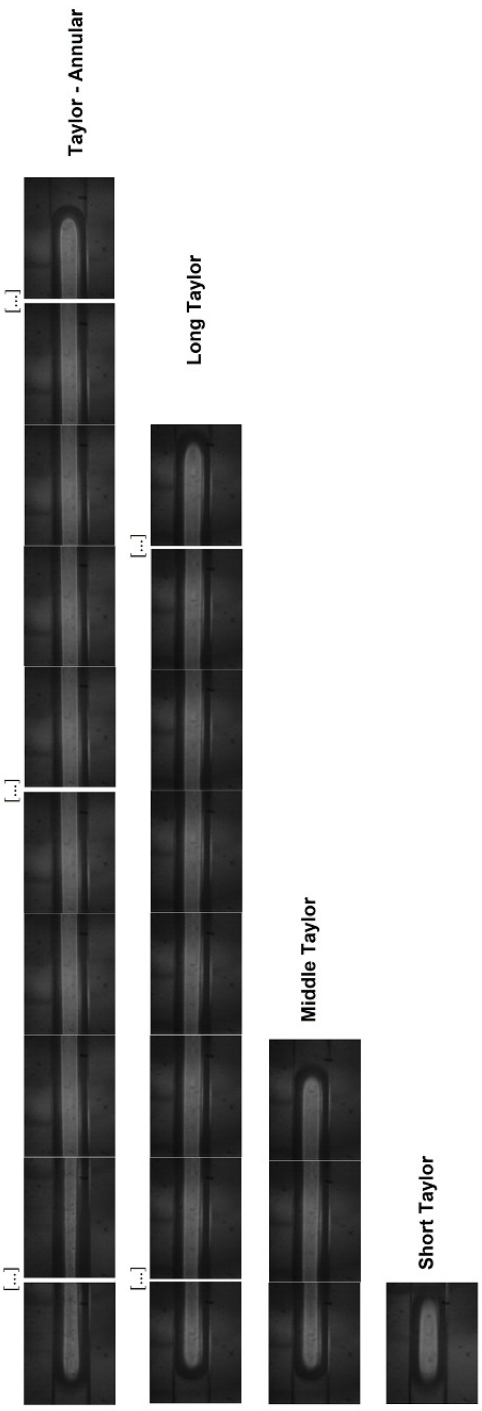

Figure 4.16: Example of bubbles belonging to the four different flow patterns observed, obtained by merging different frames. For clarity of image, some frames are skipped in the reconstruction of "Long Taylor" and Taylor-Annular bubbles.

characterize the bubbles (void fraction and bubble velocity in Tab. 4.2 and length of the bubble in Tab. 4.3) are reported as a function of the imposed superficial velocities of water and air.

Table 4.2: Range of superficial velocity of air and water for which the different flow patterns are established and average values of bubbles velocity for the different flow patterns in the reported range of superficial velocities and measured void fraction α.

Flow Pattern	(m/s) U_W	(m/s) U_A	(-) α	(m/s) $\overline{W_B}$	(-) $\bar{\alpha}$
Taylor - Annular	≤ 0.02	≥ 0.09	> 0.9	0.099	0.92
Long Taylor	0.02	≥ 0.07	$0.81 < \alpha < 0.9$	0.100	0.84
Middle Taylor	$0.02 < U_W \leq 0.06$	≥ 0.01	$0.7 < \alpha < 0.82$	0.106	0.77
Short Taylor	≥ 0.05	≥ 0.01	< 0.7	0.131	0.5

In particular in Table 4.3, the uncertainty related to the bubbles length is estimated by means of the ratio CV_b between the standard deviation of the length of the bubbles (δ(l)) and the average bubble length value ($\overline{L_B}$) (Peng et al., 2015):

$$CV_{\mathrm{b}} = \frac{\delta(l)}{\overline{L_B}} \tag{4.8}$$

Table 4.3: Averaged values of the length of the bubbles and dimensionless length of the bubbles over the range of superficial velocity of water and air analyzed for each flow regime.

Flow Pattern	(-) l	(µm) $\overline{L_B}$	(%) CV_{b}	(-) $\bar{l}$
Taylor - Annular	> 20	9935	< 25	35.4
Long Taylor	$7 < l < 20$	4009	< 25	14.3
Middle Taylor	$3.5 < l < 7$	1201	$25 < CV_{\mathrm{b}} < 13$	4.3
Short Taylor	< 3.5	480	$16 < CV_{\mathrm{b}} < 7$	1.7

It has been observed that the velocity of the bubbles is related to the imposed flow rates of the incoming flows. In particular, the velocity of the bubbles is dependent from the sum of the superficial velocities of air and water and raises with the increasing of the flow rates of both incoming flows. The experimental data obtained in this thesis confirm this trend, as evidenced in fig. 4.17. This result is in agreement with the results obtained by Santos and Kawaji (2010) for larger values of the imposed superficial velocities. The data collected in this work underline that the length of the bubble is strongly dependent from the water superficial velocity; this is underlined by the data depicted in the flow pattern map of fig. 4.15 and by the data of Tables 4.2 and 4.3. This trend is also

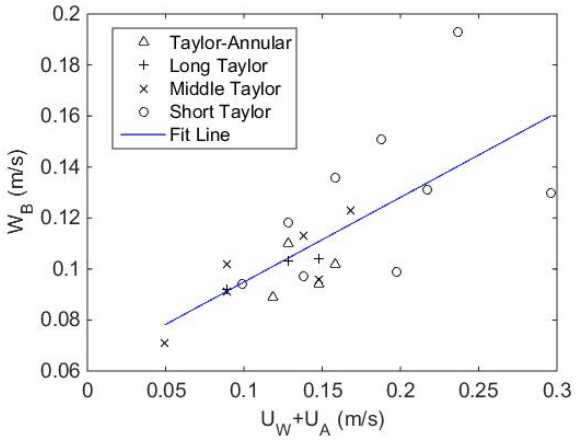

Figure 4.17: Velocity of the bubbles for the different flow patterns as a function of the sum of superficial velocities of air and water.

highlighted by fig. 4.18 in which the length of the bubble is plotted as a function of the superficial velocity of the water. As it is visible from fig. 4.18, the length of the bubbles decreases exponentially with the increasing of the superficial velocity of the water. The minimum length of the bubble is found for the higher superficial velocities of water and air and was equal to 324 µm. However, particular care has to be taken regarding to the results related to "Taylor-Annular" and "Long Taylor" bubbles. For capillary number values lower than 0.0005 (U_W < 0.04 m/s) a high variability of the bubbles length appears. This is underlined by the increase of the CV_b values reported in Tab. 4.3 and from the values assumed by the standard deviation linked to the length of the bubbles $\delta(l)$ depicted by means of bars in fig. 4.18. On the contrary for Ca > 0.0005 the CV_b is always lower than 20 % reaching values below the 10 % for the higher capillary numbers. These results are in good agreement with the observations made by Peng et al. (2015) which found a threshold value of the capillary number for stabilization of the bubble length equal to 0.0008 for an air-water mixture in a T-junction having a rectangular cross-section of 300 µm x 500 µm.

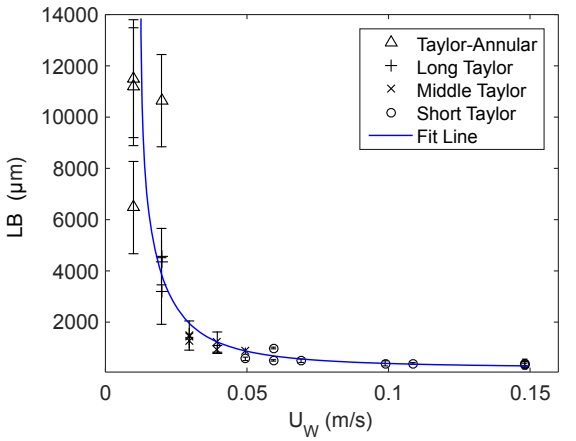

Figure 4.18: Relationship between the length of the bubbles and the superficial velocity of the water for some points belonging to each flow pattern condition. (0.02 m/s ≤ U_A ≤ 0.15 m/s) In blue is drawn the fitting.

As a consequence of the trends evidenced, it is possible to demonstrate that also the volumetric void fraction depends only on the superficial velocity of the water. In particular, the void fraction α decreases linearly with the increasing of the water flow rate as evidenced by fig. 4.19.

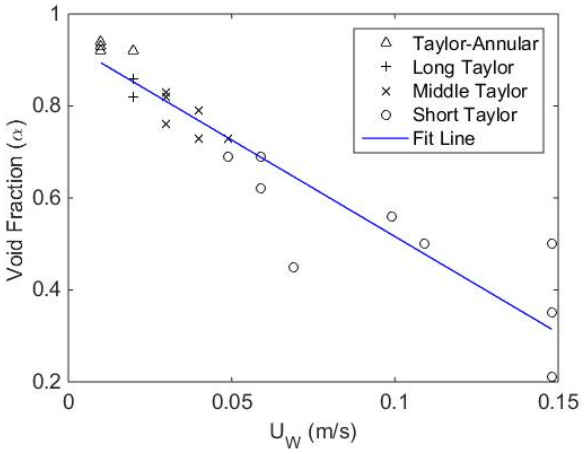

Figure 4.19: Void fraction determined experimentally as a function of the superficial velocity of water.

In addition, in accordance to the remarks made by Chung and Kawaji (2004) and Saisorn and Wongwises (2010), a direct linear relationship can be found between the volumetric void fraction α and the homogeneous void fraction β defined as the ratio of the gaseous superficial velocity and the sum of liquid and gaseous superficial velocities (Eq. (4.9)).

$$\beta = \frac{U_A}{U_A + U_W} \tag{4.9}$$

The result is evidenced by the data collected in fig. 4.20, where a dispersion of the experimental data with respect to the linear relationship between α and β is observed when α and β become lower than 0.6 (low void fractions).

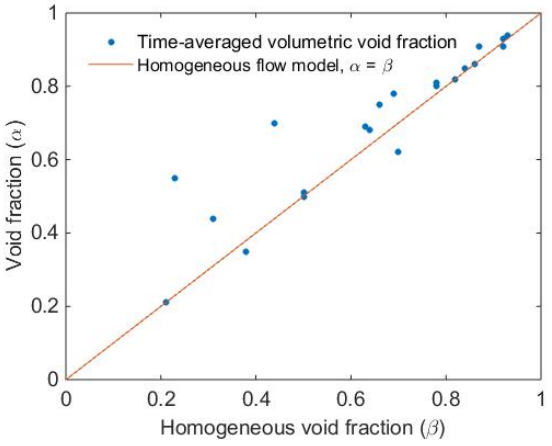

Figure 4.20: Time-averaged volumetric void fraction as a function of the homogeneous void fraction.

In fig. 4.21 the relationship between the measured static pressure on the air inlet branch (P_A) and the sum of the superficial velocities is shown. It is evident that the pressure of the air inlet branch increases with the increasing of both the superficial velocities of air and water. As remarked by Santos and Kawaji (2010), for a fixed value of the air flow rate imposed, the pressure needed in order to reach the steady state condition along the air branch increases considerably when the water flow rate is higher with respect to the air flow rate. In fact, in this case the water flow rate tends to block the entrance of the air in the T-junction which ask larger values of the air pressure to continue to generate air bubbles.

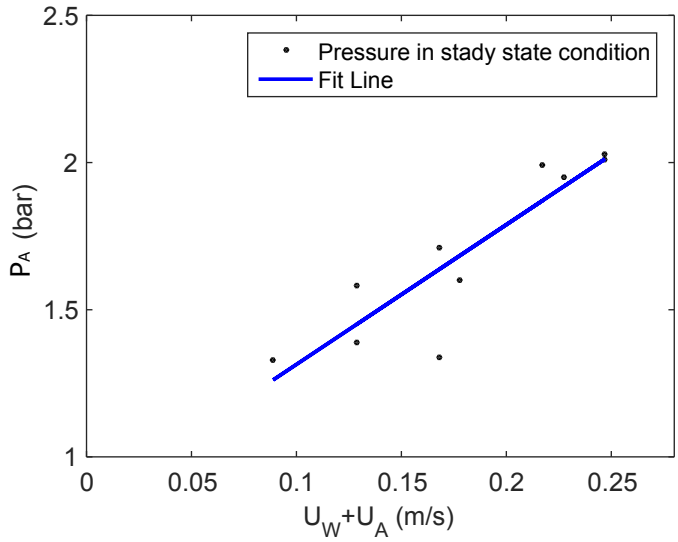

Figure 4.21: Relationship between the static pressure along the branch of the inlet air supply and the sum of the superficial velocities of the water and air flows for some points belonging to different flow rate conditions. In blue is drawn the fitting line of the same.

The results reported in this thesis are in good agreement with the results shown in other similar works. Therefore, the proposed methodology can be profitably used in order to test and design bubble-generators based on micro T-junctions also for different gas/liquid working fluids.

4.6 Conclusions

In this chapter the experimental evaluation of the different flow patterns of an air-water mixture in a micro T-junction having an hydraulic diameter of 281 μm has been shown. In order to extend the results reported in the literature, a flow pattern map composed by 195 experimental observations is reported for a range of superficial velocities of 0.01 m/s and 0.15 m/s for both the water and air flows, corresponding to capillary numbers ranging from 0.0001 up to 0.0019. For this reason, since the Ca is always lower than 0.01 only Taylor bubbles are visualized for all the flow rates under investigations. However, concerning to the length of the bubbles and to the void fraction associated to each couple of flow rates, the Taylor flow pattern has been divided in four different patterns based on the length of the generated air bubbles, namely: "Short Taylor" bubbles, "Middle Taylor" bubbles, "Long Taylor" bubbles and "Taylor-Annular" bubbles.

Short Taylor bubbles are very short bubbles ($l < 3.7$) having a uniform length for each condition of flow rates imposed. The Short Taylor regime covers the largest part of the flow pattern map since it is the only flow pattern observed for superficial velocities of the water higher than 0.06 m/s; it has been demonstrated that the void fraction associated to this regime is lower than 0.7.

For superficial velocities of the water flow between 0.02 m/s and 0.06 m/s Middle Taylor bubbles have been observed. The length of these bubbles is up to 7 times the hydraulic diameter of the microchannel, while the void fraction associated to this regime ranges between $0.7 < \alpha < 0.82$.

For a Ca < 0.0003 (*i.e.* $U_W < 0.02$) only Long Taylor bubbles and Taylor-Annular bubbles have been observed. The long Taylor regime is characterized by long bubbles having variable lengths. In fact, the length of the bubbles is up to 20 times the hydraulic diameter of the microchannel while the non-uniformity of the length of the bubbles is highlighted by CV_b values higher than the 25 %. The void fraction associated to this flow pattern ranges between 0.81 and 0.9.

Taylor-Annular bubbles have a length larger than 20 times the hydraulic diameter of the microchannel, and, as for the Long Taylor bubbles, the CV_b is larger than 25 %, underlying the high non-uniformity of the bubbles' length found in this regime. The void fraction associated to this flow pattern is higher than 0.9. In addition, a water ring close to the tail of the bubbles is clearly visible when the motion picture obtained from the collection of all the frames is visualized.

In summary, a strong dependence from the superficial velocity of the water (*i.e.* Ca) on the trend of the physical quantities associated to the flow pattern observed, such as the length of the bubbles and void fraction, has been evidenced.

In conclusion, all the results achieved and the trends observed, including the transition from the slug Taylor flow pattern to the "Taylor - Annular" flow pattern, are qualitatively in good agreement with the remarks reported in literature for similar microfluidic systems. Therefore, the proposed experimental procedure can be employed in order to provide experimental quantitative results to be used

as design tool for micro T-junction bubble generators and as a system able to generate experimental data on gas-liquid mixture which can be used for the validation of numerical code developed for the analysis of two-phase flows in microfluidics. For this reason, every further development on the experimental investigations that could lead to better and more refined results as to be regarded with remarkable interest.

4.7 Perspecitves

The apparatus and methodologies presented in this chapter, have been applied for the optical evaluation of the flow patterns related to an air-water mixture inside a micro T-junction. Nevertheless, the experimental procedure utilized for this work is not limited to the set of fluids and micro junction taken into account, but it allows also to investigate other kind of fluids, both for the dispersed and continuous phase, in different types of bubble generator having disparate geometries. In this way it will be possible to experimentally investigate the flow patterns obtained for different types of fluids in different conditions of bubbles or droplets generation.

Concerning the setup of the experimental apparatus, a possible improvement is given by the employment of an additional light source put over the sample under investigation. In this way, if the micro device allows to have an optical access from both the sides (the bottom one for the standard illumination and the top one for the supplementary illumination), the employment of an additional light source gives mainly two advantages. First of all, the supplementary light source increases the quantity of light that reach the section under investigation and therefore it allows to use a higher frame rate of the high speed camera. A higher frame rate means that the images are acquired with a reduced time delay between two subsequent frames and consequently a fast physical phenomenon, like the bubbles' detachment, can be studied with more accuracy. In second instance, a supplementary light source in an opposite direction with respect to the principal one gives back images with reduced shadows and as a consequence of that, the edge of the bubble or droplet results to be more defined, therefore, the detection of the same is more accurate. An example of this is shown in fig. 4.22 and 4.23 in which a water droplet in silicone oil is generated in a micro cross-junction. In particular, the image have been acquired using a COB LED lamp of 100 W as the supplementary system of illumination. Due to the additional amount of light, the image depicted in fig. 4.23 has been acquired using a frame rate of high speed camera equal to 5000 fps which correspond to a time delay of 200 μs between the two subsequent frames. Hence, as it is visible from fig. 4.22 and 4.23, the droplet contour is very defined also for the bubble during the instant of the break up. The quality of the images is also underlined by the reduced shadow area in correspondence to the lateral walls of the channel.

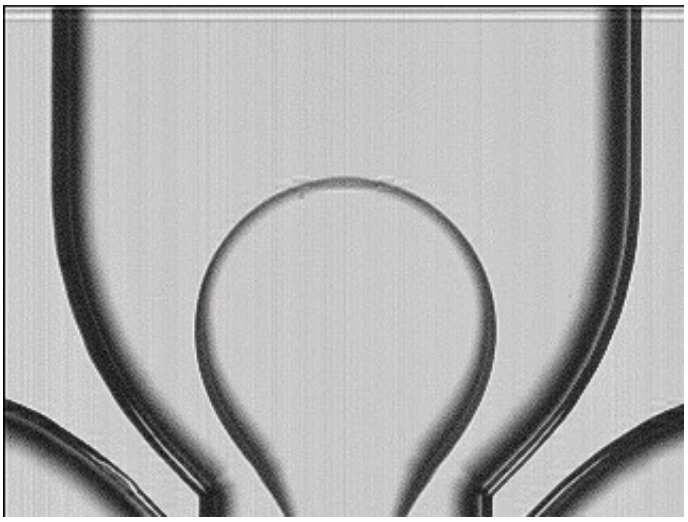

Figure 4.22: Water droplet in silicone oil during the instant of break up.

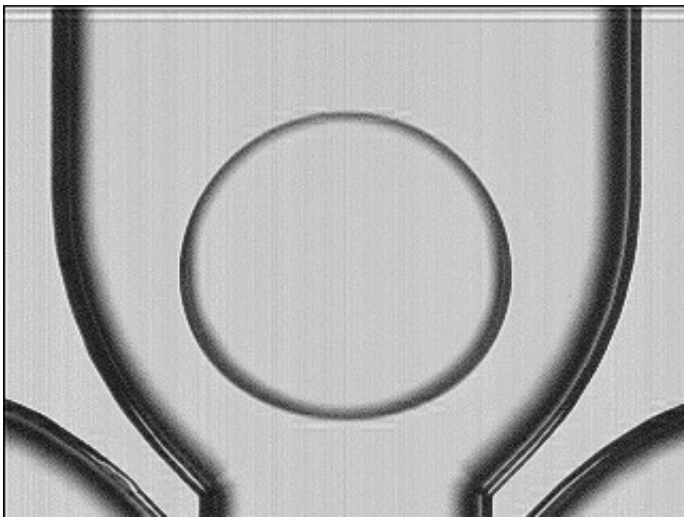

Figure 4.23: Complete detection of a water droplet in silicone oil.

Chapter 5

Conclusions and Perspectives

5.1 General conclusions

In this PhD dissertation, three different optical, non-intrusive, experimental techniques have been used in order to carry out local measurements of velocity and temperature in laminar flows inside microchannels and for the investigation of the two-phase flow patterns generated by an air-water mixture through a micro T-junction.

First of all, a methodology able to check the real cross-section geometry of a "sealed" commercial transparent microchannel has been presented in Chapter 2. This method proposes to use the μPIV technique as an "inverse technique" in order to deduct by the knowledge of the experimental velocity field the geometry of a channel. In this thesis is shown how the systematic comparison between the experimental measurements of the local velocity in a laminar flow and the velocity profiles obtained by the numerical simulation of laminar flows in channels having different shapes can allow to individuate the geometry of the channel cross-section and the existence of local singularities along the wetted perimeter of the microchannel. The accuracy of the proposed methodology has been tested by comparing the cross-section geometry predicted by using the μPIV measurements with the direct observation of the cross-section obtained, after a destructive test, by SEM. It has been demonstrated for a commercial glass microchannel having a declared (by the manufacturer) squared cross-section with a side of 300 μm how the inverse use of the μPIV technique is able to recognize the real cross section of the channel which was effectively slightly trapezoidal with acute angles of 88° and rounded edges close to the smaller base. These results have been confirmed by the SEM analysis. It has been demonstrated in addition that the difference in terms of microchannel cross-section area between its real value (86080 μm^2) determined by the elaboration of SEM images and the cross-section area determined by using the μPIV measurements (*i.e.* 86850 μm^2) is of the order of 1 %. On the contrary, the difference between the real cross

sectional area and the area declared by the manufacturer (90000 μm^2) is of the order of 4.5 %.

Even if this difference can be considered small, especially by considering the dimensions of the channel, a difference of this order of magnitude on the cross-section (also in terms of shape) can be responsible of large deviations in terms of pressure drops and friction factors from the expected values obtained by using the conventional relationships validated for laminar flows. It is possible to conclude that in microfluidics the correct knowledge of the real shape and dimensions of the channels is extremely important in order to give to the experimental measurements a right physical meaning. Thus is underlined by a large number of experimental works published in the past in which the disagreement between experiments and simulations have been mainly attributed to the erroneous assumption on the geometry of the tested microchannels (Celata et al., 2006; Silva et al., 2009; Morini et al., 2011). The proposed method can help experimentalists to make a check of the real geometry of a microchannel avoiding the use of expensive and intrusive techniques, like SEM. In particular, the proposed methodology represents a convenient tool for all the situations in which the experimental velocity measurements are used in order to validate numerical models for laminar flows in microchannels. The main limitations of the proposed technique is that an optical access to the channel is required and, at the present stage, a rough knowledge of the geometry of the channel is needed. However, by combining the simple direct observation of the cross-section by using an optical microscope and the development of the routine used by this methodology, it will be possible to extend in future this technique also to conditions in which the cross-section of the microchannel is not known in advance.

The third Chapter of this PhD thesis is focused on the local temperature measurements in liquid flows through microchannels. From an experimental point of view, direct local temperature measurements in microflows are probably one of the most difficult and interesting tasks in microfluidics. One of the most promising local temperature measurement technique for microfluidics applications is the TLC thermography based on the use as active temperature sensors of non-encapsulated TLC particles dispersed in the fluid. In this dissertation, an experimental investigation on the shear stress sensitivity of the temperature signal of non-encapsulated TLC particles has been shown. Three kinds of non-encapsulated TLC particles which differ themselves for their working temperature range, (*i.e.*, $\Delta T = 1$ K, $\Delta T = 5$ K and $\Delta T = 10$ K) have been tested. It has been demonstrated that a reliable local temperature measurement can be obtained by using non-encapsulated TLC particles dispersed in a water flow until the shear rate stays lower than 400 s^{-1}, which corresponds to shear stresses of around 0.3 - 0.4 Pa depending on the temperature of the working fluid. In addition, it has been observed that when the shear rate is increased beyond 400 s^{-1} an increasing number of TLC particles begin to collapse. More specifically, when the shear rate reaches the value of 400 s^{-1} the ratio between the destroyed particles and

the intact ones is around 35 %. On the contrary, this ratio tends to 100 % for shear rates higher to 4000 s^{-1}, which correspond to shear stresses in the range of around 3 - 4 Pa depending to the temperature of the TLC particles. The broken TLC particles lose their original compact structure becoming consequently no more available for temperature measurements. However, it has been demonstrated that for low values of the shear rate the TLCs signal is not significantly affected by the presence of a neighbouring velocity field. The results reported in this thesis demonstrate that the non-encapsulated TLC particles can be safely used for the measurement of the local fluid temperature in a microchannel for all the microfluidic applications characterized by low mass flow rates of liquids with a Reynolds number lower than 10.

Under these conditions, a preliminary combined experimental evaluation of velocity and temperature fields in a straight microchannel has been made by using non-encapsulated TLC particles as both local temperature sensors and tracers for APTV. It has been demonstrated that the local temperature measurement is characterized by an associated uncertainty of ± 0.5 K over a temperature working range of 7.5 K. The uncertainties related to the velocity measurements are evaluated as the standard deviation of the velocity along the y- and z-axis, where the velocity is zero for a Poiseuille flow. The obtained uncertainty values are equal to ± 5 μm/s (2 % with respect to the maximum velocity value) for the in-plane velocity vectors and ± 29 μm/s (11.7 % with respect to the maximum velocity value) for the out-of-plane velocity vectors. The maximum velocity obtained from the APTV measurements is equal to 250 μm/s, 6.4 % lower with respect to the theoretical one equal to 267 μm/s.

Finally, in the fourth Chapter of this thesis an experimental optical evaluation of the different flow patterns of an air-water mixture generated by means of a micro T-junction obtained from channels having a hydraulic diameter of 281 μm has been shown. The measurements have been performed for superficial velocity values of both the flows (air and water) ranging between 0.01 m/s and 0.15 m/s, which corresponds to Capillary numbers (Ca) ranging from 0.0001 up to 0.0019. As clarified in literature, for low values of the Capillary number as those considered in this investigation, only Taylor bubbles can be obtained. The observation of the Taylor bubbles has suggested to divide the Taylor bubble flow pattern in four sub-regions: "Short Taylor" bubbles, "Middle Taylor" bubbles, "Long Taylor" bubbles and "Taylor-Annular" bubbles. In order to individuate the boundaries of each region, particular care has been taken in order to be able to reconstruct the geometry of the bubbles and of the liquid slugs between two consecutive bubbles. A Matlab script has been made in order to reconstruct the evolution of the bubbles contour from the acquired images. By means of this image post-processing it has been observed that for Capillary numbers lower than 0.0005, bubbles with high non-uniformity of their length are generated. Hence, in order to stabilize the length of the bubbles, higher Ca numbers (*i.e.* higher superficial velocity of the water) must be imposed. This result is in good

agreement with the observations made recently by Peng et al. (2015) which found for an air-water mixture in a T-junction obtained by using microchannels with a rectangular cross-section of 300 μm x 500 μm, that only for values of the Capillary number larger than 0.0008 air bubbles with an uniform length can be generated. Another result obtained by the tests described in this thesis is that the flow pattern, the void fraction and the bubble length are mainly dependent on the water superficial velocity; on the contrary, the value of the air superficial velocity tends to give a secondary effect on these quantities. In addition, the trends observed of the bubbles edge velocity, the mixture void fraction and the pressure of the air supply system are found to be in good agreement with the observations reported in literature for similar configurations of the bubble generators.

5.2 Perspectives

Microfluidics is an emerging field which involves nowadays different technological fields ranging from biomedical to chemical industry and from electronics to mechanical engineering. The capability to optimize the design of new microfluidics devices in which single-phase or two-phase flows are involved, can be improved if reliable thermal fluid-dynamics data obtained for the typical geometries of the channels used in these devices become available. Many problems occur when accurate local measurements have to be made in small regions; as an example, it is not easy to obtain sensors which can be used within the microfluidic devices without to generate evident disturbances on the internal flows.

In this thesis it has been demonstrated that non-encapsulated TLC microparticles can be used as velocity and temperature sensors if they are dispersed in a laminar water flow characterized by low Reynolds numbers (Re < 10). It has been proved that by means of the use of the Astigmatic Particle Tracking Velocimetry (APTV) these particles are able to detect the local velocity and temperature field in a microchannel. However, even if the use of non-encapsulated TLC particles for the simultaneous measurement of the temperature and velocity distribution for a laminar flow in a microchannel has been preliminary demonstrated in this dissertation, the development of this technique is in its early stage and further improvements are required in order to improve its accuracy. First of all, the signal level of the light reflected from the TLC particles has to be enhanced in order to reduce the uncertainty of the thermometry technique based on the evaluation of the color linked to the reflected light. This enhancement of the light signal can be achieved by using a more powerful illumination source able to emit a light beam with a higher intensity. In addition, a color CCD camera with higher sensitivity will enable an improved detection of the hue and intensity of the color shined by the TLC particles, by improving the accuracy on the color detection and hence on the corresponding temperature. Moreover, also the non-encapsulated particles have margins of improvement. In fact, the non-encapsulated TLC particles used in this thesis, reflect a brilliant color only from their central core, while the peripheral

part of these particles is nearly transparent. Hence, only a little part of them is really used as temperature sensor. Therefore, smaller TLC particles having a larger reflecting core can be developed with evident benefits in terms of accuracy both for temperature and velocity measurements.

The investigation of two-phase flow patterns in microchannels can be made by using optical techniques based on a microscope coupled with a fast CCD camera. In order to obtain high quality images of the flow patterns an upgrade of the illuminating system is also required. It has been demonstrated that the use of a double light source is able to give brighter images with lower shadows along the bubble contour. Moreover, the additional light introduced by the secondary system of illumination can allow to acquire the images with a higher frame rate, enabling consequently a more accurate investigation of faster phenomena, such as the detachment of the bubble at the center of the T-junction due to the squeezing phenomena.

In summary, the results shown in this thesis underline as the optical techniques can have a role of primary importance for the experimental characterization of the innovative micro-devices involving single-phase or two-phase flows. However, this dissertation seem to indicate that many improvements are still possible in terms of hardware (*i.e.* more powerful light sources, use of double-direction light, new TLC particles optimized for temperature measurements) and software (*i.e.* more efficient algorithms for particle tracking, algorithms for bubble contour detection, procedure for the automatic reconstruction of the channel geometry starting from velocity measurements). To take part as active researcher to this research path within the Industry or the Academy will be the next goal of the author of this dissertation.

Appendix A

A1: Additional Pictures

Figure A.1: Picture of threads of fluorescent particles diluted into the working fluid after a long resting time.

Figure A.2: Objectives used in chapter 2 and 4.

Figure A.3: Picture of the thermochromic liquid crystals stored inside a syringe. From this picture is clearly visible the turbidity of the liquid crystals' material when it is in its smectic phase.

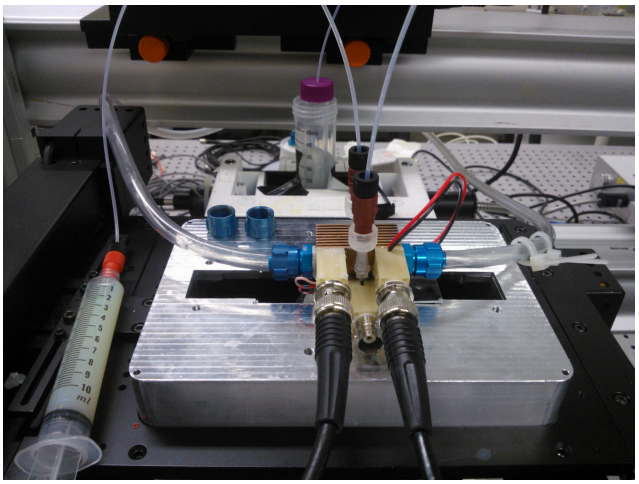

Figure A.4: *On the left* Picture of the microchannel realized in a copper substrate and coupled with a Peltier device. The microchannel is housed in a raised mounting plate due to the insertion of the filter under the objective lens. The objective lens (M = 20× NA = 0.4) coupled with the filtering system (linear glass polarizer and achromatic quarter wave plate) is shown *on the right.*

Figure A.5: System for the calibration of the thermocouples

Appendix B

A2: List of Publications

Journals

1. Puccetti G., Rossi M., Morini G.L. and Kähler C.J.,
   2016, Sensitivity to shear stress of non-encapsulated thermochromic liquid crystal (TLC) particles for microfluidic applications, *Microfluidics and Nanofluidics*, 20(1):1-7.
   DOI 10.1007/s10404-015-1694-x

2. Puccetti G., Tosi M., Pulvirenti B. and Morini G.L.,
   2015, Flow patterns of an air–water mixture at the exit of a micro T-junction, *Experimental Thermal and Fluid Science*, 67:62-29.
   DOI 10.1016/j.expthermflusci.2015.01.010

3. Pulvirenti B., Rostami B, Puccetti G., and Morini G.L.,
   2015, Determination of droplet contours in liquid-liquid flows within microchannels, *IOP: Confernce Series*, 655(1):012028.
   DOI 10.1088/1742-6596/655/1/012028

4. Puccetti G., Pulvirenti B. and Morini G.L.,
   2014, Experimental determination of the 2D velocity laminar profile in glass microchannels using μPIV, *Energy Procedia*, 45:538-547.
   DOI 10.1016/j.egypro.2014.01.058

5. Puccetti G., Pulvirenti B. and Morini G.L.,
   2014, Use of the μPIV technique for an indirect determination of the microchannel cross-section passage geometry, *IOP: Confernce Series*, 501(1):012027
   DOI 10.1088/1742-6596/501/1/012027

6. Vocale P., Puccetti G., Morini G.L. and Spiga M.,
   2014, Numerical investigation of viscous dissipation in elliptic microduct, *IOP: Conference Series*, 547:012023
   DOI 10.1088/1742-6596/547/1/012023

International Conferences

1. Florindo I., Puccetti G., Sphaier L.A. and Morini G.L.,
   2015 Effects of Fabrication Imperfections on Fully Developed Flow in Rectangular Micro-Channels, *ASME 2015 13th International Conference on Nanochannels, Microchannels, and Minichannels*, San Francisco, California, USA, 6–9 July 2015.
   ISBN: 978-0-7918-5687-1

2. Puccetti G., Vocale P., Eberhardt S., Pulvirenti B., Brandner J.J. and Morini G.L.,
   2014 Numerical and experimental analysis of the splitting of water laminar flow into a micro T-junction, *4th European Conference on Microfluidics (μFlu 2014)*, Limerick, Ireland, 10-12 December 2014
   ISBN: 979-10-93567-04-4

3. Vocale P., Puccetti G. Pulvirenti B. and Morini G.L.,
   2014 Experimental and Numerical Analysis of Single Phase Flow in a micro T-junction, *4th Micro and Nano Flows Conference* UCL, London, UK, 7-10 September 2014
   ISBN: 978-1-908549-16-7

4. Puccetti G., Tosi M., Pulvirenti B., Morini G.L.,
   2014 Experimental Analysis of the Air-Water Mixture Flow Patterns in a Micro T-junction, *5th International Conference on Heat Transfer and Fluid Flow in Microscale*, Mareseille, France, 22-25 April 2014

National Conferences

1. Puccetti G., Rossi M., Kähler C.J. and Morini G.L.,
   2015, Non-encapsulated thermoliquid crystal particles: a way for temperature measurements inside microchannels, *33rd UIT Heat Transfer Conference*, L'Aquila, 22-24 June 2015.

2. Pulvirenti B., Rostami B, Puccetti G., and Morini G.L.,
   2015, Determination of droplet contours in liquid-liquid flows within microchannels, *33rd UIT Heat Transfer Conference*, L'Aquila, 22-24 June 2015.

3. Puccetti G., Vocale P., Pulvirenti B. and Morini G.L.,
   2014 Numerical and Experimental Analysis of Laminar Flows through a T-junction Micromixer, *32nd UIT Heat Transfer Conference*, Pisa 23-25 June 2014.

4. Pulvirenti B., Puccetti G. and Morini G.L.,
   2014 Determination of bubble contours in two-phase flows within microchannels, *32nd UIT Heat Transfer Conference*, Pisa 23-25 June 2014.

5. Puccetti G., Pulvirenti B. and Morini G.L.,
2013 Use of μPIV technique for an indirect determination of the microchannel cross-section passage geometry, *31^{st} UIT Heat Transfer Conference*, Como 25-27 June 2013.

6. Puccetti G., Pulvirenti B. and Morini G.L.,
2013 Experimental Determination of the 2D Velocity Laminar Profile in Glass Microchannel Using μPIV, *68^{th} Congresso Nazionale ATI*, Bologna 11-14 September 2013.

Bibliography

Abbate, G., V. Tkachenko, V. Marino, F. Vita, M. Giocondo, A. Mazzulla, and L. De Stefano
2007. Optical characterization of liquid crystals by combined ellipsometry and half-leaky-guided-mode spectroscopy in the visible-near infrared range. *J. App. Phys.*, 101(8):073105–1.

Abdullah, N., A. R. Abu Talib, A. A. Jaafar, M. A. Mohd Salleh, and W. T. Chong
2010. The basics and issues of Thermochromic Liquid Crystal Calibrations. *Exp. Therm. Fluid Sci.*, 34(8):1089–1121.

Abgrall, P. and A.-M. Gué
2007. Lab-on-chip technologies: making a microfluidic network and coupling it into a complete microsystem—a review. *J. Micromech. Microeng.*, 17(5):R15.

Adams, J. E., W. Haas, and J. Wysocki
1969. Optical Properties of Certain Cholesteric Liquid-Crystal Films. *J. Chem. Phys.*, 50(6):2458–2464.

Adrian, R. J.
1991. Particle-Imaging Techniques for Experimental Fluid Mechanics. *Annu. Rev. Fluid Mech.*, 23:261–304.

Adrian, R. J. and C.-S. Yao
1985. Pulsed laser technique application to liquid and gaseous flows and the scattering power of seed materials. *Appl. Opt.*, 24(1):44–52.

Altieri, M. F. and M. Camarca
2001. Point of care testing. *Clinical Pediatric Emergency Medicine*, 2(4):275 – 279.

Anastasiou, A. D., C. Makatsoris, A. Gavriilidis, and A. A. Mouza
2013. Application of μ-piv for investigating liquid film characteristics in an open inclined microchannel. *Exp. Therm. Fluid Sci.*, 44:90 – 99.

Arias, S. and R. González-Cinca
2013. Experimental analysis of the bubble–slug transition in a flow generated

by a T-junction in a minichannel with air/water and air/ethanol mixtures in conditions relevant to microgravity. *Chem. Eng. Sci.*, 91:5–10.

Asako, Y., K. Nakayama, and T. Shinozuka
2005. Effect of compressibility on gaseous flows in a micro-tube. *Int. J. Heat Mass Transfer.*, 48(23–24):4985 – 4994.

Ashauer, M., J. Ende, H. Glosch, H. Haffner, and K. Hiltmann
1997. Thermal characterization of microsystems by means of high-resolution thermography. *Microelectr. J.*, 28(3):327 – 335.

Ashwood, A., S. V. Hogen, M. Rodarte, C. Kopplin, D. Rodríguez, E. Hurlburt, and T. Shedd
2015. A multiphase, micro-scale {PIV} measurement technique for liquid film velocity measurements in annular two-phase flow. *Int. J. Multiphas. Flow*, 68:27 – 39.

Augustsson, P., R. Barnkob, S. T. Wereley, H. Bruus, and T. Laurell
2011. Automated and temperature-controlled micro-piv measurements enabling long-term-stable microchannel acoustophoresis characterization. *Lab. Chip*, 11:4152–4164.

Basson, M. and T. Pottebaum
2012. Measuring the temperature of fluid in a micro-channel using thermochromic liquid crystals. *Exp. Fluids*, 53(3):803–814.

Bavière, R., M. Favre-Marinet, and S. L. Person
2006. Bias effects on heat transfer measurements in microchannel flows. *Int. J. Heat Mass Transfer.*, 49(19–20):3325 – 3337.

Behle, M., K. Schulz, W. Leiner, and M. Fiebig
1996. Color-Based Image Processing to Measure Local Temperature Distributions by Wide-Band Liquid Crystal Thermography. *App. Sci. Res.*, 56:113–143.

Belyakov, V. A., V. E. Demitrienko, and V. P. Orlov
1979. Optics of cholesteric liquid crystals. *Sov. Phys. Usp.*, 22(2):63–88.

Berreman, D. W. and T. J. Scheffer
1970a. Bragg reflection of light from single-domain cholesteric liquid-crystal films. *Phys. Rev. Lett.*, 25(9):577–581.

Berreman, D. W. and T. J. Scheffer
1970b. Bragg reflection of light from single-domain cholesteric liquid-crystal films: Errata. *Phys. Rev. Lett.*, 25(13):902.

Bessette, P. H., X. Hu, H. T. Soh, , and P. S. Daugherty
2007. Microfluidic library screening for mapping antibody epitopes. *Anal. Chem.*, 79(5):2174–2178.

Bianchi, R., F. D. Santos, J. Karam, B. Courtois, F. Pressecq, and S. Sifflet
1998. Cmos-compatible smart temperature sensors. *Microelectr. J.*, 29(9):627 – 636.

Bourdon, C. J., M. G. Olsen, and A. D. Gorby
2004. Power-filter technique for modifying depth of correlation in microPIV experiments. *Exp. Fluids*, 37:263–271.

Bourdon, C. J., M. G. Olsen, and A. D. Gorby
2006. The depth of correlation in micro-PIV for high numerical aperture and immersion objectives. *J. Fluid Eng ASME*, 123(4):883–887.

Bouttier, F. and P. Courtier
2002. Data assimilation concepts and methods march 1999. *Meteorological training course lecture series. ECMWF*.

Brandner, J. J., L. Bohn, T. Henning, U. Schygulla, and K. Schubert
2007. Microstructure heat exchanger applications in laboratory and industry. *Heat Transfer Eng.*, 28(8-9):761–771.

Brody, J., P. Yager, R. Goldstein, and R. Austin
1996. Biotechnology at low reynolds numbers. *Biophys. J.*, 71(6):3430 – 3441.

Brostow, W.
1990. Properties of polymer liquid crystals: choosing molecular structures and blending. *Polymer*, 31:979–995.

Bruus, H.
2008. *Theoretical Microfluidics*. Oxford University Press.

Buffone, C. and K. Sefiane
2004. {IR} measurements of interfacial temperature during phase change in a confined environment. *Exp. Therm. Fluid Sci.*, 29(1):65 – 74.

Buffone, C. and K. Sefiane
2005. Temperature measurement near the triple line during phase change using thermochromic liquid crystals thermography. *Exp. Fluids*, 39:99–110.

Campagnolo, L., M. Nikolić, J. Perchoux, Y. L. Lim, K. Bertling, K. Loubière, L. Prat, A. D. Rakić, and T. Bosch
2013. Flow profile measurement in microchannel using the optical feedback interferometry sensing technique. *Microfluidic Nanofluidic*, 14(1):113–119.

Carey, V. P.
1992. *Liquid-Vapour Phase.Change Phenomena*. Taylor & Franics, United States.

Celata, G., M. Cumo, S. McPhail, L. Tesfagabir, and G. Zummo
2007. Experimental study on compressible flow in microtubes. *Int. J. Heat Fluid Flow*, 28(1):28 – 36.

Celata, G., M. Cumo, S. McPhail, and G. Zummo
2006. Characterization of fluid dynamic behaviour and channel wall effects in microtube. *Int. J. Heat Fluid Fl.*, 27(1):135 – 143.

Chaudhari, A. M., T. M. Woudenberg, M. Albin, and K. E. Goodson
1998. Transient Liquid Crystal Thermometry of Microfabricated PCR Vessel Arrays. *J Microelectromech S*, 7(4):345–355.

Chen, G. S. and H. C. Yeh
2012. Polarization-selective color-filter Fresnel lens in polymer-stabilized cholesteric liquid cystals. *J. App. Phys.*, 112:054501.

Chen, H., A. Abolmatty, and M. Faghri
2011. Microfluidic inverse phase elisa via manipulation of magnetic beads. *Microfluidic Nanofluidic*, 10(3):593–605.

Chen, J., J. Li, and Y. Sun
2012. Microfluidic approaches for cancer cell detection, characterization, and separation. *Lab. Chip*, 12:1753–1767.

Chin, Y.-L., J.-C. Chou, T.-P. Sun, W.-Y. Chung, and S.-K. Hsiung
2001. A novel ph sensitive {ISFET} with on chip temperature sensing using {CMOS} standard process. *Sensor. Actuat. B-Chem.*, 76(1–3):582 – 593.

Choi, H. and X. Li
2007. Fabrication and application of micro thin film thermocouples for transient temperature measurement in nanosecond pulsed laser micromachining of nickel. *Sensor Actuat A-Phys*, 136(1):118 – 124.

Choi, S. R., J. Hong, and D. Kim
2009. A micromachined {AC} thermal sensor for monitoring the liquid–gas interface in a microchannel. *Sensor Actuat A-Phys*, 150(1):40 – 45.

Chung, P.-Y. and M. Kawaji
2004. The effect of channel diameter on adiabatic two-phase flow characteristics in microchannels. *Int. J. Multiphas. Flow*, 30(7-8):735–761.

Churchill, S. W. and H. H. S. Chu
1975. Correlating equations for laminar and turbulent free convection from a vertical plate. *Int. J. Heat Mass Transfer*, 18(11):1323–1329.

Cierpka, C. and C. J. Kähler
2012. Particle imaging techniques for volumetric three-component (3D3C) velocity measurements in microfluidics. *J. Vis.*, 15:1–31.

Cierpka, C., M. Rossi, R. Segura, and C. J. Kähler
2011. On the calibration of astigmatism particle tracking velocimetry for microflows. *Meas. Sci. Technol.*, 22:015401.

Cierpka, C., R. Segura, R. Hain, and C. J. Kähler
2010. A simple single camera 3C3D velocity measurement technique without errors due to depth of correlation and spatial averaging for microfluidics. *Meas. Sci. Technol.*, 21:045401.

Cierpka, C., R. Segura, R. Hain, and C. J. Kähler
2012. A comparative analysis of the uncertainty of astigmatism-μPTV, stereo-μPIV, and μPIV. *Exp. Fluids*, 52:605–6015.

Ciofalo, M., M. Signorino, and M. Simiano
2003. Tomographic particle-image velocimetry and thermography in Rayleigh-Bénard convection using suspended thermochromic liquid crystals and digital image processing. *Exp. Fluids*, 34:156–172.

Colin, S.
2010. *Microfluidics*. ISTE Ltd John Wiley & Sons, UK and USA.

Coppeta, J. and C. Rogers
1998. Dual emission laser induced fluorescence for direct planar scalar behavior measurements. *Exp. Fluids*, 25:1–15.

Crimaldi, J. P.
2008. Planar laser induced fluorescence in aqueous flows. *Exp. Fluids*, 44:851–863.

Cubaud, T. and C.-M. Ho
2004. Transport of bubbles in square microchannels. *Phys. Fluids*, 16(12):4575–4585.

Cubaud, T., U. Ulmanella, and C.-M. Ho
2006. Two-phase flow in microchannels with surface modifications. *Fluid Dyn. Res.*, 38(11):772–786.

Cukurel, B., C. Selcan, and T. Arts
2012. Color theory perception of steady wide band liquid crystal thermometry. *Exp. Therm. Fluid Sci.*, 39:112–122.

Cummings, E. B.
2000. An image processing and optimal nonlinear filtering technique for particle image velocimetry of microflows. *Exp. Fluids*, 29:S042–S050.

Dabiri, D.
2009. Digital particle image thermometry/velocimetry: a review. *Exp. Fluids*, 46(1):191–241.

Dabiri, D. and M. Gharib
1991. Digital particle image thermometry: The method and implmentation. *Exp. Fluids*, 11:77–86.

Dahm, W. J. A., L. K. Su, and K. B. Southerland
1992. A scalar imaging velocimetry technique for fully resolved four-dimensional vector velocity field measurements in turbulent flows. *Phys. Fluids A*, 4(10):2191–2206.

Davis, K. L., K. L. K. Liu, M. Lanan, and M. D. Morris
1993. Spatially resolved temperature measurements in electrophoresis capillaries by raman thermometry. *Anal. Chem.*, 65(3):293–298. PMID: 8447619.

de Baar, J., M. Percin, R. Dwight, B. van Oudheusden, and H. Bijl
2014. Kriging regression of piv data using a local error estimate. *Exp. Fluids*, 55(1).

de Gennes, G. P. and J. Prost
1993. *The Physics of Liquid Crystals*. Clarendon Press, Oxford, UK.

de Vries, H. L.
1951. Rotatory Power and Other Optical Properties of Certain Liquid Crystals. *Acta Cryst.*, 4:219–226.

Demsis, A., B. Verma, S. V. Prabhu, and A. Agrawal
2009. Experimental determination of heat transfer coefficient in the slip regime and its anomalously low value. *Phys. Rev. E*, 80:016311.

Derber, J. C.
1989. A variational continuous assimilation technique. *Mon. Weather Rev.*, 117(11):2437–2446.

Devasenathipathy, S., , J. G. Santiago, and K. Takehara
2002. Particle tracking techniques for electrokinetic microchannel flows. *Anal. Chem.*, 74(15):3704–3713.

Dhavaleswarapu, H. K., S. Garimella, and J. Murthy
2009. Microscale temperature measurements near the triple line of an evaporating thin liquid film. *J. Heat Transfer*, 131(6):061501–061501–7.

Dreher, R. and G. Meier
1973. Optical Properties of Cholesteric Liquid Crystals. *Phys. Rew. A*, 8(3):1616–1623.

Duan, Z. and Y. S. Muzychka
2007. Slip flow in non-circular microchannels. *Microfluidic Nanofluidic*, 3(4):473–484.

Fabien, G., M. Antoni, and K. Sefiane
2011. Use of ir thermography to investigate heated droplet evaporation and contact line dynamics. *Langmuir*, 27(11):6744–6752.

Fan, X., D. Parker, and M. Smith
2006. Labelling a single particle for positron emission particle tracking using direct activation and ion-exchange techniques. *Nucl. Instr. Meth. Phys. Res.*, 562(1):345 – 350.

Fergason, J. L.
1966. Cholesteric Structure-1 Optical Properties. *Mol. Cryst.*, 1:293–307.

Fergason, J. L.
1968. Liquid Crystals in Nondestructive Testing. *App. Opt.*, 7(9):1729–1737.

Filanovsky, I. and W. Lee
1999. Two temperature sensors with signal-conditioning amplifiers realized in bicmos technology. *Sensor. Actuat. A-Phys.*, 77(1):45 – 53.

Frezzotti, A., H. Si Hadj Mohand, C. Barrot, and S. Colin
2015. Role of diffusion on molecular tagging velocimetry technique for rarefied gas flow analysis. *Microfluidic Nanofluidic*, 19(6):1335–1348.

Friedel, M. G.
1922. Les États Mésamorphes de la matière. *Annales de Physique*, 18:273–474.

Fu, T., Y. Ma, D. Funfschilling, C. Zhu, and H. Z. Li
2010. Squeezing-to-dripping transition for bubble formation in a microfluidic T-junction. *Chem. Eng. Sci.*, 65(12):3739–3748.

Fujisawa, N. and S. Funatani
2000. Simultaneous measurement of temperature and velocity in a turbolent theraml convection by the extended range scanning liquid crystal visualization. *Exp. Fluids*, Suppl.:S158–S165.

Fujisawa, N., Y. Nakamura, F. Matsuura, and Y. Sato
2006. Pressure field evaluation in microchannel junction flows through μPIV measurement. *Microfluid Nanofluid*, 2(5):447–453.

Garstecki, P., M. J. Fuerstman, H. A. Stone, and G. M. Whitesides
2006. Formation of droplets and bubbles in a microfluidic t-junction-scaling and mechanism of break-up. *Lab Chip*, 6:437–446.

Garvey, J., D. Newport, F. Lakestani, M. Whelan, and S. Joseph
2007. Full field measurement at the micro-scale using micro-interferometry. *Microfluidic Nanofluidic*, 5(1):77–87.

Goettsche, T., J. Kohnle, M. Willmann, H. Ernst, S. Spieth, R. Tischler, S. Messner, R. Zengerle, and H. Sandmaier
2005. Novel approaches to particle tolerant valves for use in drug delivery systems. *Sensor Actuat. A-Phys.*, 118(1):70 – 77.

Guha, P., S. Ali, C. Lee, F. Udrea, W. Milne, T. Iwaki, J. Covington, and J. Gardner
2007. Novel design and characterisation of {SOI} {CMOS} micro-hotplates for high temperature gas sensors. *Sensor. Actuat B-Chem.*, 127(1):260 – 266.

Gunes, H., S. Sirisup, and G. E. Karniadakis
2006. Gappy data: To krig or not to krig? *J. Comput. Phys.*, 212(1):358 – 382.

Ha, N. Y., Y. Ohtsuka, S. M. Jeong, S. Nishimura, G. Suzaki, Y. Takanishi, K. Ishikawa, and H. Takezoe
2008. Fabbrication of a simultaneous red-green-blue refletctor using single-pitched cholesteric liquid crystals. *Nature Mater.*, 7:43–47.

Hallcrest LCR
2014. *Handbook of Thermochrmic Liquid Crystal Technology*. Hallcrest LCR.

Han, I. Y. and S. J. Kim
2008. Diode temperature sensor array for measuring micro-scale surface temperatures with high resolution. *Sensor. Actuat. A-Phys.*, 141(1):52 – 58.

Hassan, I., M. Vaillancourt, and K. Pehlivan
2005. Two-Phase Flow Regime Transitions in Microchannels: A Comparative Experimental Study. *Microscale Therm. Eng.*, 9(2):165–182.

Haverkamp, V., V. Hessel, H. Löwe, G. Menges, M. J. F. Warnier, E. V. Rebrov, M. H. J. M. de Croon, J. C. Schouten, and M. A. Liauw
2006. Hydrodynamics and Mixer-Induced Bubble Formation in Micro Bubble Columns with Single and Multiple-Channels. *Chem. Eng. Technol.*, 29(9):1025–1026.

Hay, J. L. and D. K. Hollingsworth
1996. A Comparison of Trichromic Systems for Use in the Calibration pf Polymer-Dispersed Thermochromic Liquid Crystals. *Exp. Therm. Fluid Sci.*, 12:1–12.

Hay, J. L. and D. K. Hollingsworth
1998. Calibration of micro-encapsulated liquid crystals using hue angle and a dimensionless temperature. *Exp. Therm. Fluid Sci.*, 18:251–257.

Hetsroni, G., M. Gurevich, A. Mosyak, and R. Rozenblit
2003. Surface temperature measurement of a heated capillary tube by means of an infrared technique. *Meas. Sci. Technol.*, 14(6):807.

Hetsroni, G., A. Mosyak, E. Pogrebnyak, and R. Rozenblit
2011. Infrared temperature measurements in micro-channels and micro-fluid systems. *Int. J. Therm. Sci.*, 50(6):853 – 868.

Hoffmann, M., M. Schlüter, and N. Räbiger
2006. Experimental investigation of liquid–liquid mixing in T-shaped micromixers using μ-LIF and μ-PIV. *Chem. Eng. Sci.*, 61(9):2968–2976.

Hu, H. and M. M. Koochesfahani
2006. Molecular tagging velocimetry and thermometry and its application to the wake of a heated circular cylinder. *Meas. Sci. Technol.*, 17(6):1269.

Incropera, F. P., D. P. Dewitt, T. L. Bergman, and A. S. Lavine
2006. *Introduction to Heat Transfer 5th Edition*. John Wiley & Sons.

Jones, B. A. and F. A. Meier
2004. Patient safety in point-of-care testing. *Clin. Lab. Med.*, 24(4):997 – 1022.

Joseph, S. and H. Bunjes
2014. Evaluation of shirasu porous glass (spg) membrane emulsification for the preparation of colloidal lipid drug carrier dispersions. *Eur. J. Pharm. Biopharm.*, 87(1):178 – 186.

Kandlikar, S. G.
2012. History, advances, and challenges in liquid flow and flow boiling heat transfer in microchannels: A critical review. *ASME. J. Heat Transfer.*, 134(3):034001–034001–15.

Kandlikar, S. G., S. Colin, Y. Peles, S. Garimella, R. F. Pease, J. J. Brandner, and D. B. Tuckerman
2013. Heat transfer in microchannels—2012 status and research needs. *ASME. J. Heat Transfer.*, 135(9):091001–091001–18.

Kandlikar, S. G. and W. J. Grande
2003. Evolution of microchannel flow passages–thermohydraulic performance and fabrication technology. *Heat Transfer Eng.*, 24(1):3–17.

Kawahara, A., P.-Y. Chung, and M. Kawaji
2002. Investigation of two-phase flow pattern, void fraction and pressure drop in a microchannel. *Int. J. Multiphas. Flow*, 28(9):1411–1435.

Khalid, A. H. and K. Kontis
2008. Thermographic Phosphors for High Temperature Measurements: Principles, Current State of the Art and Recent Applications. *Sensors*, 8:5673–5744.

Khan, I. U., C. A. Serra, N. Anton, and T. Vandamme
2013. Microfluidics: A focus on improved cancer targeted drug delivery systems. *J. Control. Release*, 172(3):1065 – 1074.

Kim, M. M., A. Giry, M. Mastiani, G. O. Rodrigues, A. Reis, and P. Mandin
2015. Microscale thermometry: A review. *Microelectron. Eng.*, 148:129 – 142.

Klank, H., G. Goranović, J. P. Kutter, H. Gjelstrup, J. Michelsen, and C. H. Westergaard
2002. PIV measurements in a microfluidic 3D-sheathing structure with three-dimensional flow behaviour. *J. Micromech. Microeng.*, 12:862–869.

Koochesfahani, M. M. and D. G. Nocera
2007. Molecular tagging velocimetry. *Handbook of experimental fluid dynamics*, Pp. 362–382.

Kuang, C., W. Zhao, F. Yang, and G. Wang
2009. Measuring flow velocity distribution in microchannels using molecular tracers. *Microfluidic Nanofluidic*, 7(4):509–517.

Kumar, V., M. Paraschivoiu, and K. Nigam
2011. Single-phase fluid flow and mixing in microchannels. *Chem. Eng. Sci.*, 66(7):1329 – 1373.

Lagerwall, J. P. F. and G. Scalia
2012. A new era for liquid crystal research: Applications of liquid crystals in soft matter nano-, bio-, and microtechnology. *Curr. App. Phys.*, 12:1387–1412.

Lammerink, T. S., N. R. Tas, M. Elwenspoek, and J. H. Fluitman
1993. Proceedings of eurosensors vi micro-liquid flow sensor. *Sensor. Actuat. A-Phys.*, 37:45 – 50.

Lee, C.-Y., C.-L. Chang, Y.-N. Wang, and L.-M. Fu
2011. Microfluidic Mixing: A Review. *Int. J. Mol. Sci.*, 12(5):3263–3287.

Lee, P.-S., S. V. Garimella, and D. Liu
2005. Investigation of heat transfer in rectangular microchannels. *Int. J. Heat Mass Transfer*, 48(9):1688–1704.

Lee, S. J. and S. Kim
2009. Advanced particle-based velocimetry techniquesfor microscale flows. *Microfluid Nanofluid*, 6:577–588.

Lehmann, O.
1889. Über fleissende Krystalle. *Z. Phys. Chem.*, 4:462–472.

Lindken, R., M. Rossi, S. Große, and J. Westerweel
2009. Micro-Particle image Velocimetry (μPIV): Recent developments, applications, and guidelines. *Lab. Chip*, 9:2551–2567.

Lindken, R., J. Westerweel, and B. Wieneke
2006. Stereoscopic micro particle image velocimetry. *Exp. Fluids*, 41:161–171.

Liu, D., S. V. Garimella, and S. T. Wereley
2005. Infrared micro-particle image velocimetry in silicon-based microdevices. *Exp. Fluids*, 38:385–392.

Liu, T.-L. and C. Pan
2016. Infrared thermography measurement of two-phase boiling flow heat transfer in a microchannel. *App. Therm. Eng.*, 94:568 – 578.

Mauger, C., L. Méès, M. Michard, and M. Lance
2014. Velocity measurements based on shadowgraph-like image correlations in a cavitating micro-channel flow. *Int. J. Multiphas. Flow*, 58:301 – 312.

Maynes, D. and R. A. Webb
2002. Velocity profile characterization in sub-millimeter diameter tubes using molecular tagging velocimetry. *Exp. Fluids*, 32(1):3–15.

McKnight, T. E., C. T. Culbertson, S. C. Jacobson, and J. M. Ramsey
2001. Electroosmotically Induced Hydraulic Pumping with Integrated Electrodes on Microfluidic Devices. *Anal. Chem.*, 73:4045–4049.

Mehendale, S., A. Jacobi, and R. Shah
2000. Fluid flow and heat transfer at micro- and meso-scales with application to heat exchanger design. *ASME. Appl. Mech. Rev*, 53(7):175 – 193.

Meinhart, C. D. and S. T. Wereley
2003. The theory of diffraction-limited resolution in microparticle image velocimetry. *Meas. Sci. Technol.*, 14:1047–1053.

Meinhart, C. D., S. T. Wereley, and M. H. B. Gray
2000a. Volume illumination for two-dimensional particle image velocimetry. *Meas. Sci. Technol.*, 11:809–814.

Meinhart, C. D., S. T. Wereley, and J. G. Santiago
1999. PIV measurements of a microchannel flow. *Exp. Fluids*, 27:414–419.

Meinhart, C. D., S. T. Wereley, and J. G. Santiago
2000b. A PIV Algorithm for Estimating Time-Averaged Velocity Fields. *J. Fluid Eng ASME*, 122:285–289.

Meinhart, C. D. and H. Zhang
2000. The Flow Structure Inside a Microfabricated Inkjet Printhead. *J. Microelectromech. S.*, 9:67–75.

Melamed, L. and D. Rubin
1971. Selected Optical Properties of Mixtures of Cholesteric Liquid Crystals. *App. Opt.*, 10(5):1103–1107.

Miribel-Català, P., E. Montané, S. Bota, M. Puig-Vidal, and J. Samitier
2001. Mosfet-based temperature sensor for standard {BCD} smart power technology. *Microelectr. J.*, 32(10–11):869 – 873.

Mishan, Y., A. Mosyak, E. Pogrebnyak, and G. Hetsroni
2007. Effect of developing flow and thermal regime on momentum and heat transfer in micro-scale heat sink. *Int. J. Heat Mass Transfer.*, 50(15–16):3100 – 3114.

Morini, G. L.
2004. Single-phase convective heat transfer in microchannels: a review of experimental results. *Int. J. Therm. Sci.*, 43(7):631 – 651.

Morini, G. L.
2008a. *Entrance Region, Encyclopedia of Micro and Nano flows*. Springer.

Morini, G. L.
2008b. Misure di velocità in mini- e micro-canali mediante la tecnica μpiv. *Tecniche ottiche e termografiche in termofluidodinamica, L'Aquila 2008*.

Morini, G. L., M. Lorenzini, and S. Salvigni
2006. Friction characteristics of compressible gas flows in microtubes. *Exp. Therm. Fluid Sci.*, 30(8):733 – 744.

Morini, G. L. and M. Spiga
1998. SLIP FLOW IN RECTANGULAR MICROTUBES. *Microscale Thermophysical Engineering*, 2(4):273–282.

Morini, G. L. and Y. Yang
2013. Guidelines for the determination of single-phase forced convection coefficients in microchannels. *J. Heat Transfer*, 135(10):101004.

Morini, G. L., Y. Yang, H. Chalabi, and M. Lorenzini
2011. A critical review of the measurement techniques for the analysis of gas microflows through microchannels. *Exp. Therm. Fluid. Sci.*, 35:843–865.

Motosuke, M., D. Akutsu, and S. Honami
2009. Temperature measurement of microfluids with high temporal resolution by laser-induced fluorescence. *J. Mech. Sci. Technol.*, 23:1821–1828.

Mutyala, M. S. K., J. Zhao, J. Li, H. Pan, C. Yuan, and X. Li
2014. In-situ temperature measurement in lithium ion battery by transferable flexible thin film thermocouples. *J. Power Sources*, 260:43 – 49.

Muwanga, R. and I. Hassan
2006. Local Heat Transfer Measurements in Microchannels Using Liquid Crystal Termography: Methodology Development and Validation. *J. Heat Transfer*, 128:617–626.

Newport, D., J. Garvey, T. Dalton, V. Egan, and M. Whelan
2004. Development of interferometric temperature measurement procedures for microfluid flow. *Microscale Therm. Eng.*, 8(2):141–154.

Nguyen, N.
1997. Micromachined flow sensors—a review. *Flow Meas. Instrum.*, 8(1):7 – 16.

Nichols, J. H.
2007. Point of care testing. *Clin. Lab. Med.*, 27(4):893 – 908.

Noh, J. H., H.-L. Liang, I. Drevensek-Olenik, and J. P. F. Lagerwall
2014. Tunable multicoloured patterns from photonic cross-communication between cholesteric liquid crystal droplets. *J. Mater. Chem. C*, 2:806–810.

Oddy, M. H., J. G. Santiago, and J. C. Mikkelsen
2001. Electrokinetic Instability Micromixing. *Anal. Chem.*, 73:5822–5832.

Olsen, M. G. and R. J. Adrian
2000a. Brownian motion and correlation in particle image velocimetry. *Opt. Laser Technol.*, 32:621–627.

Olsen, M. G. and R. J. Adrian
2000b. Out-of-focus effects on particle image visibility and correlation in microscopic particle image velocimetry. *Exp. Fluids*, 29(1):S166–S174.

Onofri, F.
2006. Three interfering beams in laser doppler velocimetry for particle position and microflow velocity profile measurements. *Appl. Opt.*, 45(14):3317–3324.

Oseen, C. W.
1933. The Theory of Liquid Crystals. *Trans. Faraday Soc.*, 29(140):883–899.

Otsu, N.
1979. A Threshold Selection Method from Gray-Level Histograms. *IEEE Trans. Syst. Man Cyber.*, 9(1):62–66.

Ovryn, B.
2000. Three-dimensional forward scattering particle image velocimetry applied to a microscopic field-of-view. *Exp. Fluids*, 29(1):S175–S184.

Ozawa, M., U. Müller, I. Kimura, and T. Takamori
1992. Flow and temperature measurement of natural convection in a hele-shaw cell using thermo-sensutive liquid-crystal tracer. *Exp. Fluids*, 12:213–222.

Özisik, M. N. and H. R. B. Orlande
2000. *Inverse heat transfer: fundamentals and applications.* Taylor & Francis, CRC Press.

Park, H. G., D. Dabiri, and M. Gharib
2001. Digital particle image velocimetry/thermometry and application to the wake of a heated circular cylinder. *Exp Fluids*, 30:327–338.

Park, J. S., C. K. Choi, and K. D. Kihm
2004. Optically sliced micro-PIV using confocal laser scanning microscopy (CLSM). *Exp. Fluids*, 37:105–119.

Paul, P. H., M. G. Garguilo, , and D. J. Rakestraw
1998. Imaging of pressure- and electrokinetically driven flows through open capillaries. *Anal. Chem.*, 70(13):2459–2467.

Peng, D., F. Xin, L. Zhang, H. Yu, and W. Zhang
2015. Experiments and modeling on bubble uniformity of taylor flow in t-junction microchannel. *Chem. Eng. Sci.*, 128:11 – 20.

Peters, F., L. Lobry, and E. Lemaire
2010. Pressure-driven flow of a micro-polar fluid: Measurement of the velocity profile. *J. Rheol.*, 54(2):311–325.

Pottebaum, T. S. and M. Gharib
2006. Using oscillations to enhance heat transfer for a circular cylinder. *Int. J. Heat Mass Transfer*, 49:3190–3210.

Powell, R. L.
2008. Experimental techniques for multiphase flows. *Phys. Fluids*, 20(4).

Pratt, W. K.
2001. *Digital Image Processing: PIKS Inside, Third Edition*. John Wiley and Sons, Inc.

Puccetti, G., B. Pulvirenti, and G. L. Morini
2014. Use of the μPIV technique for an indirect determination of the microchannel cross-section passage geometry. *IOP: Confernce Series*, 501:012027.

Puccetti, G., M. Rossi, C. J. Kähler, and G. L. Morini
2015. Non-encapsulated thermoliquid crystal particles: a way for temperature measurements inside microchannels. *33rd UIT Heat Transfer Conference, L'Aquila, June 22-24, 2015*.

Raben, S. G., J. J. Charonko, and P. P. Vlachos
2012. Adaptive gappy proper orthogonal decomposition for particle image velocimetry data reconstruction. *Meas. Sci. Technol.*, 23(2):025303.

Rao, Y. and S. Zang
2010. Calibrations and the measurement uncertainty of wide-band liquid crystal thermography. *Meas. Sci. Technol.*, 21:015105.

Reichle, R. H.
2008. Data assimilation methods in the earth sciences. *Adv. Water Resour.*, 31(11):1411 – 1418. Hydrologic Remote Sensing.

Reinitzer, F.
1888. Beiträge zur Kenntniss des Cholesterins. *Weiner Monatschr Für Chem.*, 9:421–441.

Robinson, A. R. and P. F. Lermusiaux
2000. Overview of data assimilation. *Harvard reports in physical/interdisciplinary ocean science*, 62:1–13.

Roesgen, T. and R. Totaro
2002. A statistical calibration technique for thermochromic liquid crystals. *Exp. Fluids*, 33:732–734.

Ross, D., M. Gaitan, and L. E. Locascio
2001. Temperature measurement in microfluidic systems using a temperature-dependent fluorescent dye. *Anal. Chem.*, 73(17):4117–4123.

Rossi, M. and C. J. Kähler
2014. Optimization of astigmatic particle tracking velocimeters. *Exp. Fluids*, 55:1809.

Rossi, M., R. Lindken, B. P. Hierckb, and J. Westerweel
2010a. Tapered microfluidic chip for the study of biochemical and mechanical response at subcellular level of endothelial cells to shear flow. *Lab Chip*, 9:1403–1411.

Rossi, M., R. Lindken, and J. Westerweel
2010b. Optimization of multiplane μPIV for wall shear stress and wall topography characterization. *Exp. Fluids*, 48(2):211–223.

Rossi, M., R. Segura, C. Cierpka, and C. J. Kähler
2012. On the effect of particle image intensity and image preprocessing on the depth of correlation in micro-PIV. *Exp. Fluids*, 52:1063–1075.

Russ, J. C.
2002. *The Image Processing Handbook*. CRC Press Inc. Boca Raton.

Sadaghiani, A. K. and A. Koşar
2016. Numerical and experimental investigation on the effects of diameter and length on high mass flux subcooled flow boiling in horizontal microtubes. *Int. J. Heat Mass Transfer.*, 92:824 – 837.

Sage, I.
2011. Thermochromic liquid crystals. *Liq. Cryst.*, 38(11):1551–1561.

Saisorn, S. and S. Wongwises
2010. The effects of channel diameter on flow pattern, void fraction and pressure drop of two-phase air–water flow in circular micro-channels. *Exp. Therm. Fluid Sci.*, 34(4):454–462.

Sakai, Y., S. Wada, H. Matsumoto, T. Suyama, O. Ohno, and I. Anno
2003. Nondestructive evaluation of blood flow in a dialyzer using x-ray computed tomography. *J. Artif. Organs*, 6(3):197–204.

Sakakibara, J. and R. J. Adrian
1999. Whole field measurement of temperature in water using two-color laser induced fluorescence. *Exp. Fluids*, 26:7–15.

Sakakibara, J. and R. J. Adrian
2004. Measurement of temperature field of a Rayleigh-Bénard convection using two-color laser-induced fluorescence. *Exp. Fluids*, 37:331–340.

Saltzman, W. M. and W. L. Olbricht
2002. Building drug delivery into tissue engineering design. *Nat. Rev. Drug Discov.*, 1:177–186.

Samouda, F., S. Colin, C. Barrot, L. Baldas, and J. J. Brandner
2015. Micro molecular tagging velocimetry for analysis of gas flows in mini and micro systems. *Microsys. Technol.*, 21(3):527–537.

Santiago, J. G., S. T. Wereley, C. D. Meinhart, D. J. Beebe, and R. J. Adrian
1998. A particle image velocimetry system for microfluidics. *Exp. Fluids*, 25:316–319.

Santos, R. M. and M. Kawaji
2010. Numerical modeling and experimental investigation of gas–liquid slug formation in a microchannel T-junction. *Int. J. Multiphas. Flow*, 36(4):314–323.

Sato, Y., S. Inaba, K. Hishida, and M. Maeda
2003. Spatially averaged time-resolved particle-tracking velocimetry in microspace considering Brownian motion of submicron fluorescent particles. *Exp. Fluids*, 35:167–177.

Schembri, F., H. Bodiguel, and A. Colin
2015. Velocimetry in microchannels using photobleached molecular tracers: a tool to discriminate solvent velocity in flows of suspensions. *Soft Matter*, 11:169–178.

Schöler, L., B. Lange, K. Seibel, H. Schäfer, M. Walder, N. Friedrich, D. Ehrhardt, F. Schönfeld, G. Zech, and M. Böhm
2005. Monolithically integrated micro flow sensor for lab-on-chip applications. *Microelectron. Eng.*, 78–79:164 – 170.

Segura, R.
2014. *Thermo-liquid crystal (TLC) thermography and astigmatism particle tracking velocimetry (APTV) for the simultaneous time-resolved 3D measurements of microscopic temperature and velocity flow fields.* Shaker Verlag GmbH.

Segura, R., C. Cierpka, M. Rossi, S. Joseph, H. Bunjes, and C. J. Kähler
2013. Non-encapsulated thermo liquid crystals for digital particle tracking thermography/velocimetry in microfluids. *Microfluid Nanofluid*, 14(3-4):445–456.

Segura, R., M. Rossi, C. Cierpka, and C. J. Kähler
2015. Simultaneous three-dimensional temperature and velocity field measurements using astigmatic imaging of non-encapsulated thermo-liquid crystals (TLC) particles. *Lab Chip*, 15:660–663.

Serizawa, A., Z. Feng, and Z. Kawara
2002. Two-phase flow in microchannels. *Exp. Therm. Fluid Sci.*, 26(6 - 7):703 – 714.

Shah, R. K. and A. L. London
1978. *Laminar flow forced convections in ducts (pp. 196-222) in Adv. Heat Transfer.* Academic Press Inc.

Shao, N., A. Gavriilidis, and P. Angeli
2009. Flow regimes for adiabatic gas–liquid flow in microchannels. *Chem. Eng. Sci.*, 64(11):2749–2761.

Shinohara, K., Y. Sugii, A. Aota, A. Hibara, M. Tokeshi, T. Kitamori, and K. Okamoto
2004. High-speed micro-PIV measurements of transient flow in microfluidic devices. *Meas. Sci. Technol.*, 15:1965–1970.

Si Hadj Mohand, H.
2015. *Micro-vélocimétrie par marquage moléculaire adaptée aux écoulements gazeux confinés.* PhD thesis, Université de Toulouse.

Silva, G., N. Leal, and V. Semiao
2009. Micro-PIV and CFD characterization of flows in a microchannel: Velocity profiles, surface roughness and Poiseuille numbers. *Int. J. Heat Fluid Fl.*, 29(4):1211–1220.

Sinton, D.
2004. Microscale flow visualization. *Microfluid Nanofluid*, 1:2–21.

Smith, C. R., D. R. Sabatino, and T. J. Praisner
2001. Temperature sensing with thermochromic liquid crystals. *Exp. Fluids*, 30:190–201.

Smith, J. D., C. D. Cappa, W. S. Drisdel, R. C. Cohen, and R. J. Saykally
2006. Raman thermometry measurements of free evaporation from liquid water droplets. *J. Am. Chem. Soc.*, 128(39):12892–12898.

Someya, S., S. Bando, Y. Song, B. Chen, and M. Nishio
2005. DeLIF measurement of ph distribution around dissolving CO_2 droplet in high pressure vessel. *Int. J. Heat Mass Transfer*, 48:2508–2515.

Someya, S., Y. Li, K. Ishii, and K. Okamoto
2011. Combined two-dimensional velocity and temperature measurements of natural convection using a high-speed camera and temperature-sensitive particles. *Exp. Fluids*, 50:65–73.

Stasiek, J. A. and T. A. Kowalewski
2002. Thermocromic liquid crystals applied for heat transfer research. *Opto Eletron. Rev.*, 10(1):1–10.

Stauffer, D. R. and N. L. Seaman
1994. Multiscale four-dimensional data assimilation. *J. Appl. Meteorol.*, 33(3):416–434.

Stone, S. W., C. D. Meinhart, and S. T. Wereley
2002. A microfluidic-based nanoscope. *Exp. Fluids*, 33:613–619.

Sui, Y., P. Lee, and C. Teo
2011. An experimental study of flow friction and heat transfer in wavy microchannels with rectangular cross section. *Int. J. Therm. Sci.*, 50(12):2473 – 2482.

Tabeling, P.
2005. *Introduction to Microfluidics*. Oxford University Press.

Tang, G., Z. Li, Y. He, and W. Tao
2007. Experimental study of compressibility, roughness and rarefaction influences on microchannel flow. *Int. J. Heat Mass Transfer.*, 50(11–12):2282 – 2295.

Taylor, J. A. and E. S. Yeung
1993. Imaging of Hydrodynamic and Electrokinetic Flow Profiles in Capillaries. *Anal. Chem.*, 65:2928–2932.

Thomson, S. and D. Maynes
2001. Spatially resolved temperature measurements in a liquid using laser induced phosphorescence. *ASME. J. Fluids Eng.*, 123(2):293 – 302.

Tieu, A. K., M. R. Mackenzie, and E. B. Li
1995. Measurements in microscopic flow with a solid-state LDA. *Exp. Fluids*, 19:293–294.

Tseng, F.-G., I.-D. Yang, K.-H. Lin, K.-T. Ma, M.-C. Lu, Y.-T. Tseng, and C.-C. Chieng
2002. Fluid filling into micro-fabricated reservoirs. *Sensor Actuat. A-Phys.*, 97-98:131–138.

van Dinther, A., C. Schroën, F. Vergeldt, R. van der Sman, and R. Boom
2012. Suspension flow in microfluidic devices — a review of experimental techniques focussing on concentration and velocity gradients. *Adv. Colloid Interface Sci.*, 173:23 – 34.

van Steijn, V., M. T. Kreutzer, and C. R. Kleijn
2007. μPIV study of the formation of segmented flowin microfluidic T-junctions. *Chem. Eng. Sci.*, 62(4):7505–7514.

Vehring, R. and G. Schweiger
1992. Optical determination of the temperature of transparent microparticles. *Appl. Spectrosc.*, 46(1):25–27.

Vejrazka, J. and P. Marty
2007. An Alternative Technique for the Interpretation of Temperature Measurements Using Thermochromic Liquid Crystals. *Heat Transfer Eng.*, 28:154–162.

Venturi, D.
2006. On proper orthogonal decomposition of randomly perturbed fields with applications to flow past a cylinder and natural convection over a horizontal plate. *J. Fluid Mech.*, 559:215–254.

Venturi, D. and G. E. Karniadakis
2004. Gappy data and reconstruction procedures for flow past a cylinder. *J. Fluid Mech.*, 519:315–336.

Vocale, P., G. Puccetti, B. Pulvirenti, and G. L. Morini
2014. Experimental and Numerical Analysis of Single Phase Flow in a micro T-junction. *4^{th} Micro and Nano Flows Conference UCL, London, UK, 7-10 September 2014.*

Vogt, J. and P. Stephan
2012. Using microencapsulated fluorescent dyes for simultaneous measurement of temperature and velocity fields. *Meas. Sci. Technol.*, 23:105306.

Wagner, E. and P. Stephan
2006. Frequency response of a surface thermometer based on uncapsulated thermochromic liquid crystals. *Exp. Therm. Fluid Sci.*, 31:687–699.

Wang, G. R.
2005. Laser induced fluorescence photobleaching anemometer for microfluidic devices. *Lab. Chip.*, 5:450–456.

Wang, Y., F. Houshmand, D. Elcock, and Y. Peles
2013. Convective heat transfer and mixing enhancement in a microchannel with a pillar. *Int. J. Heat Mass Transfer.*, 62:553 – 561.

Wereley, S. and C. Meinhart
2005. *Micron-Resolution Particle Image Velocimetry, Microscale Diagnostic Techniques*, K. S. Breuer edition. Springer Berlin Heidelberg.

Wereley, S. T., L. Gui, and C. D. Meinhart
2002. Advanced Algorithms for Microscale Particle Image Velocimetry. *AIAA J.*, 40(6):1047–1055.

Westerweel, J.
1997. Fundamentals of digital particle image velocimetry. *Meas. Sci. Technol.*, 8(12):1379–1392.

Whitesides, G. M.
2006. The origins and the future of microfluidics. *Nature*, 442:368–373.

Wong, P. K., Y. K. Lee, and C. M. Ho
2003. Deformation of DNA molecules by hydrodynamic focusing. *J. Fluid Mech.*, 497:55–65.

Wu, J., W. Cao, W. Wen, D. C. Chang, and P. Sheng
2009. Polydimethylsiloxane microfluidic chip with integrated microheater and thermal sensor. *Biomicrofluidics*, 3(1).

Wu, S., Q. Lin, Y. Yuen, and Y.-C. Tai
2001. {MEMS} flow sensors for nano-fluidic applications. *Sensor Actuat A-Phys*, 89(1–2):152 – 158.

Yager, P., T. Edwards, E. Fu, K. Helton, K. Nelson, M. R. Tam, and B. H. Weigl
2006. Microfluidic diagnostic technologies for global public health. *Nature*, 442:412–418.

Yamamoto, K. and S. Ogata
2013. Effects of T-junction size on bubble generation and flow instability for two-phase flows in circular microchannels. *Int. J. Multiphas. Flow*, 49:24–30.

Yoshida, H.
2005. The wide variety of possible applications of micro-thermofluid control. *Microfluidic Nanofluidic*, 1(4):289–300.

Zhang, X., H. Choi, A. Datta, and X. Li
2006. Design, fabrication and characterization of metal embedded thin film thermocouples with various film thicknesses and junction sizes. *J. Micromech. Microeng.*, 16(5):900.

Zhao, C.-X.
2013. Multiphase flow microfluidics for the production of single or multiple emulsions for drug delivery. *Adv. Drug Deliv. Rev.*, 65(11-12):1420–1446.

Zhao, C.-X. and A. P. Middelberg
2011. Two-phase microfluidic flows. *Chem. Eng. Sci.*, 66(7):1394–1411.

Zhao, W., F. Yang, J. Khan, K. Reifsnider, and G. Wang
2015. Corrections on lifpa velocity measurements in microchannel with moderate velocity fluctuations. *Exp. Fluids*, 56(2):1–10.

Zhao, W., F. Yang, J. Khan, K. Reifsnider, and G. Wang
2016. Measurement of velocity fluctuations in microfluidics with simultaneously ultrahigh spatial and temporal resolution. *Exp. Fluids*, 57(1):1–12.

Zheng, X. and Z. H. Silber-Li
2008. Measurement of velocity profiles in a rectangular microchannel with aspect ratio α= 0.35. *Exp. Fluids*, 44:951–959.

Ziaie, B., A. Baldi, M. Lei, Y. Gu, and R. A. Siegel
2004. Hard and soft micromachining for biomems: review of techniques and examples of applications in microfluidics and drug delivery. *Adv. Drug Deliv. Rev.*, 56(2):145 – 172.